Ground-based OH(3,1) rotational temperature observations:

A basis for the analysis of differently caused fluctuations of atmospheric temperatures: – solar cycle influences, long-term behaviour, planetary wave activity, and gravity wave activity –

Habilitationsschrift

vorgelegt der

Bergischen Universität
Wuppertal

Fakultät 4 – Mathematik und Naturwissenschaften

von

Dr. rer. nat. Christoph Kalicinsky

Wuppertal 2022

Abstract

Temperatures are a key parameter in atmospheric sciences. Compared to other atmospheric parameters and constituents, temperatures are relatively easy to measure, at least at the surface. Furthermore, temperature time series enable the analysis of a large variety of phenomena. In order to study all of these different phenomena and also the coupling between different parts of the atmosphere, temperature observations in every region of the globe and at every height in the atmosphere from the surface up to the thermosphere are of great interest. Part of the interest is certainly based on the recent temperature increase that is typically related to the anthropogenic climate change. Besides this human-induced global warming, other temperature related phenomena as, for example, atmospheric waves, which become apparent in quasi-periodic temperature fluctuations, are also of great importance for the understanding of the atmospheric dynamics. This improved understanding also improves the predictability of the future evolution.

OH airglow emissions are widely used to determine temperatures, the temperature evolution and temperature related phenomena in the mesopause region from ground. GRIPS (GRound-based Infrared P-branch Spectrometers) instruments have been used in Wuppertal since the beginning of the 1980s to monitor the mesopause temperatures at an altitude of about 87 km. The Wuppertal time series is one of the largest and continuously recorded time series in the world. The OH(3,1) band emissions are observed every night, except for nights with cloudy conditions. Hence, records of the temperature variations in every possible night as well as a long-term record of nightly mean temperatures are available for the Wuppertal station. These temperature time series allow for a large variety of scientific investigations and enable the analysis of temperature fluctuations on very different time scales from short-period variations (e.g. gravity waves, planetary waves) to long-period variations (e.g. 11-year cycle of solar activity). Results of these two different types of temperature fluctuations derived from OH(3,1) rotational temperatures are presented in the following.

The long-term behaviour of the OH(3,1) rotational temperatures observed from Wuppertal can be describe by two main components: 1) the 11-year cycle of solar activity; 2) a long-periodic oscillation. The observation of a temperature fluctuation that coincides with the 11-year cycle of solar activity is typical for mesopause temperatures. This is observed at many stations around the globe. The derived sensitivity of about $4\ \mathrm{K}\,(100\,\mathrm{SFU})^{-1}$ for the Wuppertal time series is also in the middle of the range reported in literature. The observation of a long-periodic temperature oscillation with a period of about two decades is, to my knowledge, the first one in this altitude region. This quasi-bidecadal oscillation has an amplitude of about 2 K and contributes significantly to the variance of the time series of annual mean temperatures. The additional analysis of a time series of plasma scale heights (PSH), which can be used as temperature proxy at an altitude of about 80 km in summer, showed that the quasi-bidecadal oscillation behaves opposite in the region slightly above and below the mesopause temperature minimum in summer. This behaviour can be explained by a vertical periodic displacement of the temperature profile which leads to opposite effects at different constant altitudes depending on the vertical temperature gradient.

Besides the analysis of the long-term variation of temperatures in the mesopause region, studies of the analysis of short-term fluctuations are also presented. Here the focus is on two wave types, the planetary waves and the gravity waves. The main focus of the presented work is on the long-term evolution of these two different wave types, which are very important as a driver for the residual circulation in the stratosphere and mesosphere. The planetary wave activity also shows a quasi-bidecadal oscillation which is very similar to that of the OH(3,1) rotational temperatures themselves. In contrast to this, the behaviour of the gravity wave activity shows a trend-break with a maximum activity in about 2004, where the planetary wave activity and the temperatures show a minimum. Thus, the behaviour is opposite to each other.

Contents

List of Figures

List of Tables

1. Introduction

Temperature observations in the mesopause region at about 87 km height are limited in two ways. First, temperatures are obtained from satellite observations and therefore the length of the time series is limited, because the start of the satellite era was not that long ago (satellite observations of temperatures and other atmospheric constituents started at about 1979, e.g. Adler et al., 2017; Indira Rani et al., 2021) and the typical lifetime of a satellite can be comparably short (e.g. MIPAS-Envisat[1] 2002 – 2012; e.g. Glatthor et al., 2017; Höpfner et al., 2018), which is the main drawback here. Second, they are obtained using ground-based instruments and, consequently, these observations are only obtained for one local position. In contrast to satellite observations, ground-based instruments give the opportunity to monitor the mesopause region with the same (or a rebuilt) instrument for a very long time, since the instrument can be repaired and maintained which enhances the lifetime. Hence, a very long and at the same time homogeneous time series can be obtained.

An easy way to monitor the mesopause region is to measure OH band emissions and calculate temperatures from these emissions. Such observations are performed at different locations at the globe, for example, at Antarctica (e.g. French and Mulligan, 2010), in Brazil (e.g. Clemesha et al., 2005), Spain (e.g. García-Comas et al., 2017), Germany (e.g. Bittner et al., 2000; Schmidt et al., 2013), Russia (e.g. Perminov et al., 2014), Ireland (e.g. Mulligan and Lowe, 2008), Sweden (e.g. Kim et al., 2017) or Norway (e.g. Holmen et al., 2014). One of the longest time series of OH observations has been recorded in Wuppertal, Germany, since 1980 (e.g Bittner et al., 2000; Offermann et al., 2010; Kalicinsky et al., 2016). The observations were performed in each night with good weather conditions. Because of these exceptional long time of observations the Wuppertal time series is a very unique temperature record.

The continuous measurements of temperatures in the mesopause region allow for the anal-

---

[1] The Michelson Interferometer for Passive Atmospheric Sounding - Envisat (MIPAS-Envisat) is an infrared limb emission sounder operated onboard the Envisat satellite in the time period 2002 – 2012 (Fischer et al., 2008).

ysis of different aspects of atmospheric variabilities and dynamics. These variabilities start at very short timescales of several minutes and go to long-term variations with periods of several years. Examples for variations on shorter timescales are gravity and planetary waves with periods beginning with minutes for gravity waves and ending up at periods of several days for planetary waves. Well-known long-term variations are, for example, a possible long-term trend and the 11-year cycle of solar activity, which can also be observed in mesopause temperatures.

Gravity waves are excited in the lower atmosphere and propagate upwards. As the atmospheric density decreases with height the amplitudes of the waves grow exponentially to compensate for this decrease (Andrews et al., 1987). Gravity wave breaking events and the deposition of momentum then drive the residual circulation from the summer to the winter pole in the mesosphere and, additionally, contribute to the circulation from the equator to the summer pole in the stratosphere (e.g. Andrews et al., 1987; Fritts and Alexander, 2003; Vincent, 2015). The gravity waves are also responsible for temperature fluctuations with rather short periods (in the range from minutes to hours) in the mesopause region which can be observed by ground-based instruments measuring OH airglow emissions (e.g. Offermann et al., 2009, 2011; Vargas et al., 2015; Sedlak et al., 2016; Rourke et al., 2017; Wüst et al., 2018; López-González et al., 2020). A recent overview on capabilities and challenges of observing gravity waves by using OH airglow emissions is given by Wüst et al. (2022).

Planetary waves are also generated in the lower atmosphere and propagate upwards. By contrast to the gravity waves, planetary wave breaking and dissipation is mainly responsible for the circulation in the stratosphere going from the equator to the winter pole (e.g. Andrews et al., 1987; Vincent, 2015). The planetary waves exhibit longer horizontal wavelengths as gravity waves and, thus, they have longer periods (typically in the range of days to weeks). These waves can also cause temperature fluctuations in the mesopause region that were observed by instruments monitoring the OH airglow emissions (e.g. Espy et al., 2005; Höppner and Bittner, 2007; Murphy et al., 2007; Offermann et al., 2009; Zhao et al., 2019).

The two different issues, long-term trend and sensitivity to the 11-year cycle of solar activity, have been, for example, addressed by Beig (2011a,b) who reviewed a number of different studies. The linear trends reported in these different studies range from not significant to a cooling of about -3 $\mathrm{K\,decade^{-1}}$. The sensitivities to the 11-year cycle of solar activity lie between about 1 to 6 $\mathrm{K\,(100\,SFU)^{-1}}$, whereby the majority of the results are in the range between 2 to 5 $\mathrm{K\,(100\,SFU)^{-1}}$. In a new study by French et al. (2020) an updated collection of linear trends and sensitivities for many observation sites is given. These updated results confirm previous studies.

At the surface also long-periodic oscillations have been observed for different meteorological parameters such as temperature and precipitation that show a prominent period of about 20 years (e.g. King et al., 1974; Willet, 1974; King, 1975; Wei et al., 2015, 2019). This quasi-bidecadal oscillation of temperatures has also been observed in higher altitudes in the stratosphere (e.g. Coughlin and Tung, 2004; Qu et al., 2012). In the mesosphere and mesopause region the oscillation was not observed in temperature time series until my studies. However, it should be mentioned that other researchers observed a quasi-bidecadal oscillation in other parameters such as pressure (e.g. von Cossart and Taubenheim, 1986) and planetary wave activity (e.g. Jarvis, 2006; Höppner and Bittner, 2007).

The following work gives a summary of my own studies and studies I contributed to that deal with the long-term and short-term variability derived from OH(3,1) rotational temperatures. Additionally, further studies I contributed to and that deal with the vertical structure of the long-term variability are included in this overview to explain more details. The work is structured as follows. In Sect. 2 the OH(3,1) measurements and other data sets that have been analysed are explained and the methods used for the analysis are described. The results from my studies are summarised in Sect. 3 and the interrelationships between the different studies are explained. This section is subdivided into two parts: 1) the long-term (trend, oscillation, 11-year solar cycle) and 2) the short term variations (planetary and gravity waves). A summary of the results is given in Sect. 4 together with a detailed discussion of the results that also includes new studies that have been published after my own work and refer to my work.

2. Data and methods

2.1. Data

2.1.1. OH rotational temperatures

Excited hydroxyl molecules emit radiation in the near infrared in the upper mesosphere. The main formation of these hydroxyl molecules is via the reaction of H and O_3:

$$H + O_3 \longrightarrow OH^*(\nu\prime \leq 9) + {O_2}^*,$$

where $\nu\prime$ is the upper vibrational level. The OH band emissions have been measured and monitored since their first observation and description by Meinel (1950), which gives them also the name OH-Meinel band emissions. The centre altitude of this emission layer and the altitude dependencies on the vibrational level has been obtained from different observations. Rocket-borne observations revealed a centre altitude of about 87 km and a width of the layer of about 9 km (Baker and Stair Jr., 1988). This altitude is not a completely fixed value but it varies on different time scales (e.g. García-Comas et al., 2017, and references therein). Nonetheless, different studies showed that the value of 87 km is a good approximation for the mean altitude of the layer. This is especially true for the OH(3,1) band which will be used in the following. SCIAMACHY[1] satellite observations of the OH(3,1) band showed a clear semi-annual variation of the emission altitude with typical variations between 86 and 88 km, but no obvious long-term trend is reported (-10° to 30° N; von Savigny, 2015). SABER[2] observations of the OH(3,1) band emissions over Maynooth (Ireland) exhibit larger variations of the layer altitude between about 84 and 88 km (years 2004/2005; Mulligan and Lowe,

---

[1] The SCanning Imaging Absorption spectroMeter for Atmospheric CHartographY (SCIAMACHY) is a passive remote sensing instrument operated onboard the Envisat satellite in the time interval 2002 – 2012. The instrument performed nadir and occultation measurements and also observed scattered solar radiation and airglow emissions in limb geometry (Bovensmann et al., 1999).

[2] The Sounding of the Atmosphere using Broadband Emission Radiometry (SABER) instrument is a limb-scanning infrared radiometer operated onboard the Thermosphere Ionosphere Mesosphere Energetics Dynamics (TIMED) satellite since 2002 (e.g. Mlynczak, 1997; Russell III et al., 1999; Yee et al., 2003).

2008). Further satellite observations showed that the centre altitude depends on the upper vibrational level $\nu\prime$ and that an upward shift by about 0.4 to 0.5 km occurs for a $\Delta\nu\prime = 1$ (von Savigny et al., 2012; Noll et al., 2016). In the study by Noll et al. (2016) the centre altitudes derived from SABER observations over Chile vary from 86.2 km ($\nu\prime = 2$) to 89.0 km ($\nu\prime = 9$) with a centre altitude of the OH(3,1) band emissions of about 86.6 km.

The OH(3,1) emissions used in this work are all measured by GRIPS (GRound-based Infrared P-branch Spectrometer) instruments. Three different instruments have been used to perform the measurements: GRIPS-I, GRIPS-II, and GRIPS-N. The observations at the station in Wuppertal started in 1980 and have been continuously performed since 1987. They were mainly carried out by GRIPS-II until mid of 2011, when a detector failure stopped the measurements. GRIPS-II is a Czerny-Turner spectrometer with a Ge detector cooled by liquid nitrogen (see Bittner et al., 2000, 2002, for instrument description). In the years 1993 to 1996 parts of the measurements have been performed by GRIPS-I, because of problems with GRIPS-II and a refurbishment of the instrument. Both instruments were operated side by side and they were intercompared at least once per year to determine systematic differences and correct them (Bittner et al., 2000). Thus, continuous measurements were ensured. At the beginning of the year 2011 a new instrument was operated next to GRIPS-II. In the first half of 2011 simultaneous measurements were performed that showed no differences between the two instruments. Hence, after the detector failure of GRIPS-II the new instrument was able to continue the measurements. Unfortunately, the new instrument had several technical problems in the following years that led to larger data gaps in 2012 and 2013. Finally, a reconstruction was performed to set up the GRIPS-N instrument. GRIPS-N is a Czerny-Turner spectrometer such as GRIPS-II. It is equipped with a thermoelectrically cooled InGaAs detector to enable an easier handling compared to a detector cooled by liquid nitrogen. The optical and spectral properties of GRIPS-N and GRIPS-II are very similar and therefore the measurements of both instruments are nearly identical. The new GRIPS-N instrument was operated without further problems since the beginning of 2014 (see Kalicinsky et al., 2016, for first data and comparisons). The GRIPS-I instrument is a Ebert-Fastie spectrometer with a Ge detector that is cooled with liquid nitrogen (see Bittner et al., 2000, 2002, for instrument description). The instrument was used as backup for GRIPS-II in Wuppertal in the 1980s and 1990s as described above. At the end of 2003 GRIPS-I was installed at the observatory in Hohenpeissenberg to start a new time series of OH(3,1) band emissions at a second location. GRIPS-I successfully performed measurements until November 2017. All instruments measure every single night, except in nights with cloudy conditions. On average this results in

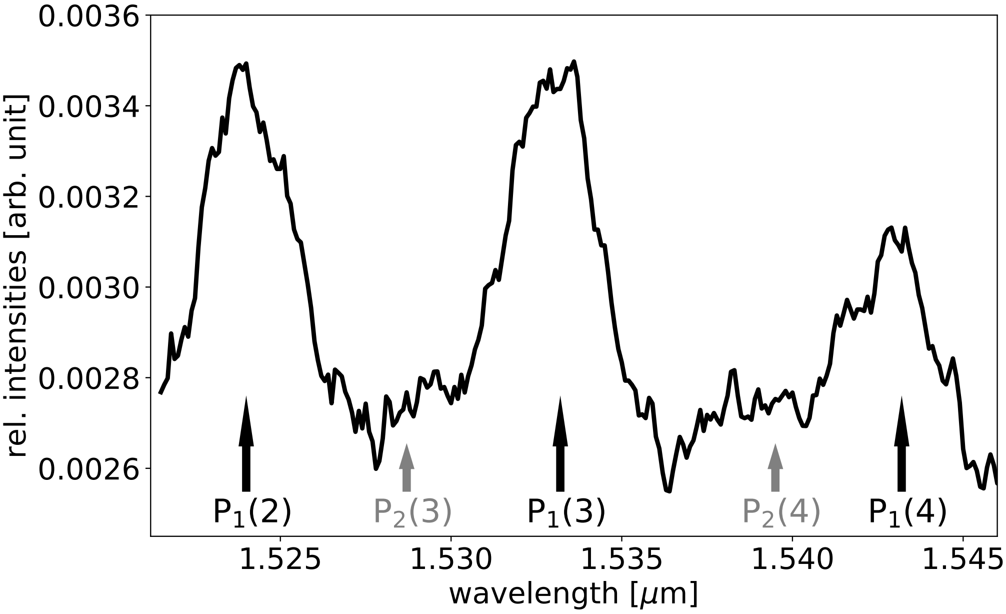

Figure 2.1: Typical spectrum of OH(3,1) P$_1$(2), P$_1$(3), and P$_1$(4) lines. The spectrum was measured with the GRIPS-N instrument at Wuppertal in the night from 1 July 2022 to 2 July 2022.

about 220 nights of measurements per year (Oberheide et al., 2006; Offermann et al., 2010) All three instruments measure the same emission lines of the OH(3,1) band, namely the P$_1$(2), P$_1$(3), and P$_1$(4) lines. The peaks of these emissions lines are located in the wavelength range from 1.524 to 1.543 µm. Figure 2.1 shows a typical example for the GRIPS-N instrument. The intensities of these lines are then used to derive rotational temperatures. The relationship between the intensity I of a line and the corresponding rotational temperature T_{rot} can be described as:

$$\ln \frac{I}{2(2J'+1)A(\nu',J'->\nu'',J'')} = const - \frac{F(J')}{kT_{rot}}, \tag{2.1}$$

where J and ν are the rotational and vibrational quantum numbers, A are the Einstein coefficients, k is the Boltzmann constant, and $F(J')$ is the rotational term value (e.q. Mies, 1974; Sivjee and Hamwey, 1987; Bittner et al., 2000; Schmidt et al., 2013). When all three lines are considered and $\ln \frac{I}{2(2J'+1)A(\nu',J'->\nu'',J'')}$ is plotted versus $F(J')$, the slope of the fitted line is determined by the rotational temperature T_{rot} (see Sivjee and Hamwey, 1987, for more details of the temperature retrieval). The Einstein coefficients are taken from Mies (1974) and the numerical values for $F(J')$ are taken from Krassovsky et al. (1962). Because of the semi-logarithmic relationship only the relative intensities of the three lines are necessary for the calculation of T_{rot}. Hence, changes in the detector sensitivity or the atmospheric transmission have no impact on the temperature determination (Bittner et al., 2002).

Because of non-LTE (Local Thermodynamic Equilibrium) effects, the OH rotational temperatures may deviate from the kinetic temperatures, especially for higher vibrational states. Therefore, the OH(3,1) band is a good choice since the non-LTE effects appear to be smaller compared to other bands and as a consequence the rotational temperatures are closer to the kinetic temperatures (Noll et al., 2015). The OH(3,1) rotational temperatures have been compared with kinetic temperatures in different studies. Oberheide et al. (2006) (time interval 2003–2005) and Offermann et al. (2010) (April 2002–August 2008) used SABER temperatures (retrieval data V 1.04/1.06 and V 1.07, respectively) for comparisons with the GRIPS-II measurements in Wuppertal. For both comparisons higher temperatures were obtained for the ground-based observations (warm bias). However, the differences (ground-based minus satellite) of 7.4 K and 3.4 K, respectively, lie within the combined systematic error bars of the instruments. Additionally, Offermann et al. (2010) obtained a warm bias of 4.6 K for the GRIPS-I instrument in Hohenpeissenberg (October 2003–August 2008), which is also smaller than the combined errors. von Savigny et al. (2004) compared the GRIPS-I and GRIPS-II OH(3,1) rotational temperatures with corresponding OH(3,1) rotational temperatures derived from SCIAMACHY and showed a warm bias of the ground-based instruments of 2.6 K and 2.7 K, respectively. Again these mean differences were much smaller than the standard deviations. Thus, despite a possible warm bias the OH(3,1) rotational temperatures can be used to study the temperatures in the upper mesosphere. In particular, studies that only examine variability are much safer, as variability is less affected than absolute temperatures. (Noll et al., 2015).

The OH(3,1) rotational temperatures of the ground-based instruments were also compared with SABER temperature observations with a special focus on the long-term variability (Kalicinsky et al., 2018). Figure 2.2a shows mean seasonal cycles of the OH(3,1) rotational temperatures in two different time intervals, 2002–2006 and 2012–2016. Additionally, the difference of these two seasonal cycles is displayed in the lower panel of Fig. 2.2a. As the centre altitude of the OH layer is at approximately 87 km, this altitude was used for the comparison. The mean seasonal cycles of the SABER kinetic temperatures at this altitude and in the same time intervals are shown in Fig. 2.2b. The absolute values show the warm bias of the ground-based observations as all the other comparisons before also showed. Despite this, the differences between the two seasonal cycles and therefore the long-term variability in the analysed time

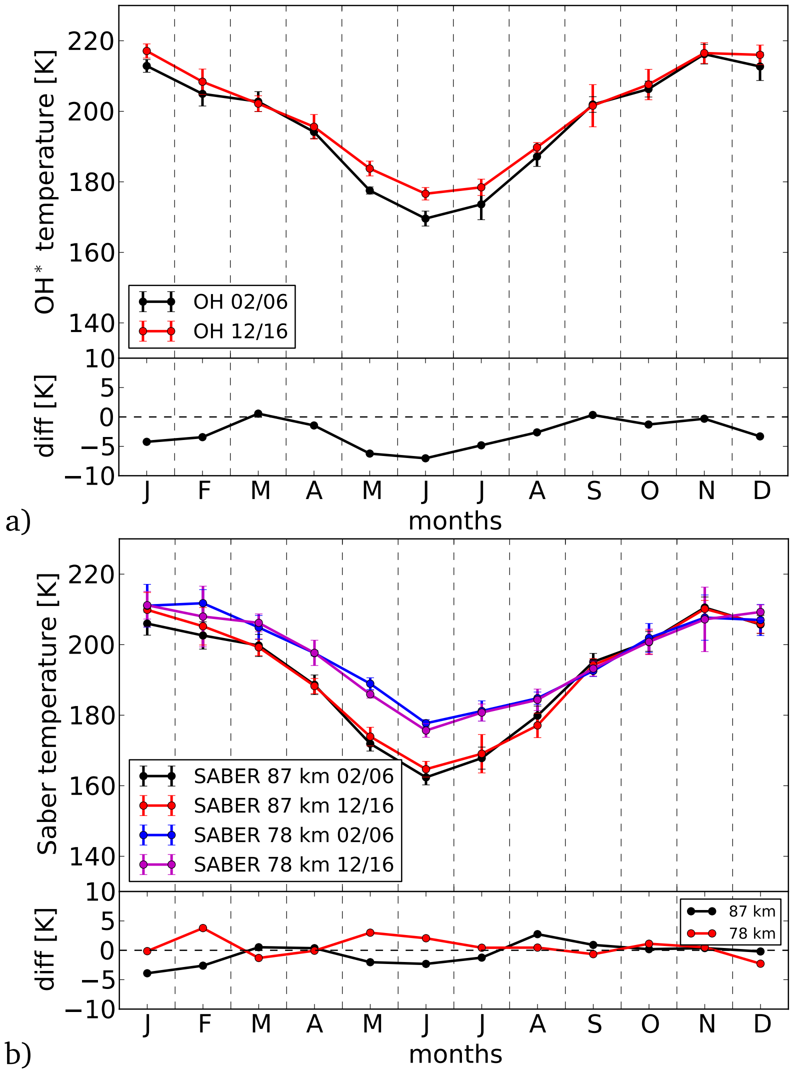

Figure 2.2: Comparison of the OH(3,1) rotational temperatures seasonal cycles between GRIPS-II/N and SABER observations. a) The mean OH(3,1) rotational temperature seasonal cycle for the years 2002–2006 is shown in black and for 2012–2016 in red. The lower panel shows the difference ((2002–2006) - (2012–2016)). b): The mean seasonal cycles of SABER temperatures in the region 47°–53° and 0°–12°E at 87 km are shown in black (2002–2006) and red (201—2016) and at 78 km in blue (2002–2006) and magenta (2012–2016). Additionally, the differences of the seasonal cycles at the two altitudes are shown in the lower panel. The figures are taken from Kalicinsky et al. (2018).

intervals are very similar for both temperature time series. Both exhibit clear negative differences in the months May, June, July as well as in winter (DJF). In the months March and April and in autumn (SON) only small differences are present and the two seasonal cycles in the two time intervals show nearly the same values. Only in August there are larger deviations between the two different data sets, because the OH(3,1) rotational temperatures show a negative and the SABER temperatures show a positive difference. This is maybe caused by the fact that the altitude of 87 km is not a completely fixed altitude and can vary throughout the year. However, the OH(3,1) rotational temperatures are a very good proxy for the long-term variability of the kinetic temperatures at an altitude of about 87 km.

2.1.2. Plasma scale heights

The procedure to derive the plasma scale heights (PSH) is described in detail by Peters and Entzian (2015) and here only a brief summary is given. The PSHs are derived from indirect phase height measurements. The transmitter station that emits a radio signal is located in Allouis (47° N, 2° E, France) and the receiving station is located in Kühlungsborn (50° N, 12° E, Germany). Because of this setup, the reflection point is located over the Eifel. The indirect phase heights are derived from interference measurements of a ground and a sky wave and the corresponding observations of field strength extrema. The daily variation of the phase height is between about 75 km and 87 km. It sinks in the forenoon till midday and increases in the afternoon. The main information on averages comes from altitudes around about 82 km in winter and equinoxes and 80 km in summer. Two important parameters are derived from these phase height observations: 1) the standard phase heights (SPH) and 2) the plasma scale heights (PSH). The phase height varies during the day depending on the solar zenith angle at the reflection point. The heights plotted versus $\ln(Ch(\chi))$ (Ch is the Chapman function and χ is the solar zenith angle) give a straight line. The SPH is then defined as the height at $\ln(Ch(\chi)) = 1.6$, i.e. a solar zenith angle $\chi = 78.8°$. The PSH is determined by the slope of the same line. It is defined as the altitude difference for a change of $\ln(Ch(\chi))$ by one, i.e. the plasma scale heights are on the order of a few kilometres. The PSHs depend on the temperature of the ionized gas NO and under thermal equilibrium on the neutral gas temperature. Many different comparisons showed that the PSH positively correlate with local temperatures in the summer months (e.g. Entzian, 1967; Lauter, 1974; von Cossart and Taubenheim, 1976; Peters et al., 2017), whereas an anomaly disturbs this correlation in winter months (see e.g. Kalicinsky et al. (2018) and Fig. 2.3).

Similar as for the OH(3,1) rotational temperatures, the PSH seasonal cycles were compared with that of the SABER kinetic temperatures. Here the focus concentrates on the summer months as the PSHs are a temperature proxy in summer only. Figure 2.3 shows the mean seasonal cycles for the time intervals 2002–2006 and 2012–2016 as black and red curve, respectively. In the lower panel of Fig. 2.3 the difference of these two seasonal cycles is

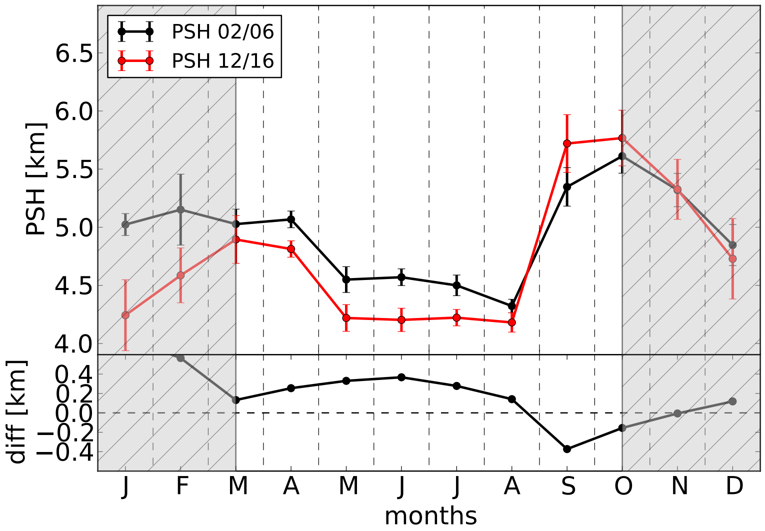

Figure 2.3: PSH seasonal cycles for the time intervals 2002–2006 and 2012–2016. The mean seasonal cycles for the years 2002–2006 are shown in black and for 2012–2016 in red. The lower panel shows the difference ((2002–2006) - (2012–2016)). The winter months are overlayed with a grey area. The figure is taken from Kalicinsky et al. (2018).

shown. As in the case of the PSH observations the main information on averages comes from altitudes at about 80 km ranging down to 78 km in summer, Fig. 2.2b shows the seasonal cycles of the SABER kinetic temperatures at 78 km in the same time intervals for comparison. The differences of the two seasonal cycles (lower panels in Fig. 2.2b and Fig. 2.3) show a reasonable agreement for both data sets, i.e. the long-term variability is the same. From April to August both data sets exhibit positive differences, except for the zero difference in case of the SABER observations in April. In September both data sets show a negative difference. Thus, the sign agrees very well, albeit the differences are more obvious for the PSH observations. However, the PSHs are a good proxy for the long-term variability of the kinetic temperatures at the analysed altitudes.

2.1.3. SABER satellite observations

The Sounding of the Atmosphere using Broadband Emission Radiometry (SABER) instrument is operated onboard the Thermosphere Ionosphere Mesosphere Energetics Dynamics (TIMED) satellite since 2002 (e.g. Mlynczak, 1997; Russell III et al., 1999; Yee et al., 2003). SABER is a 10-channel broadband limb-scanning infrared radiometer that measures in the spectral range from 1.27 µm to 17 µm. The measurements of the instrument are used to derive vertical profiles of temperature and volume mixing ratios of several trace gases.

Temperature retrieval results of the version 2.0 product were used in the presented comparisons. The operational temperature retrieval uses the 15 µm CO_2 emission together with CO_2 volume mixing ratios to derive the temperature information. The results are provided in the altitude range from 15 to 110 km. The precision and accuracy of the temperatures for single profiles worsen with increasing altitude. The precision starts at 0.3 K at 15 km, increases to 3.6 K at 90 km and, finally, reaches about 15.0 K at 110 km. Thus, the uppermost altitudes have much larger uncertainties. The total accuracy has a similar behaviour with the values of 1.4 K, 5.4 K and about 29 K, respectively (SABER, 2022). As in the comparisons of SABER temperatures with OH(3,1) rotational temperatures and PSHs only mean values in larger regions (latitude-longitude box 47° – 53°N and 0° – 12°E) calculated from a larger number of profiles were used, the corresponding uncertainties are typically much smaller.

2.1.4. Reanalysis data sets

In the present work two different reanalysis data sets were used. The first is the reanalysis data set from the National Centers for Environmental Prediction (NCEP) and the National Center for Atmospheric Research (NCAR), in short NCEP/NCAR Reanalysis 1 (Kalnay et al., 1996). The project uses a state-of-the-art analysis/forecast system and performs data assimilation using past data from 1948 to the present. The resulting data set provides temperatures at 17 pressure levels between 1000 and 10 hPa on a 2.5° × 2.5° global grid.

The second reanalysis data set is The Modern-Era Retrospective Analysis for Research and Applications Version 2 (MERRA-2) starting in the year 1980 (Gelaro et al., 2017). MERRA-2 uses an upgraded version of the GEOS-5 (Goddard Earth Observing System Model, Version 5) data assimilation system. The updates include model updates (Molod et al., 2012, 2014) and updates of the Global Statistical Interpolation (GSI) scheme (Wu et al., 2002). The horizontal grid of MERRA-2 is 0.625° × 0.5° (longitude × latitude) which corresponds to 576 and 361 points, respectively. The data are provided on a pressure grid with 42 levels between 1000 and 0.1 hPa. Thus, the data set reaches into the mesosphere. More information on the data products are given by Bosilovich et al. (2016).

2.1.5. Model simulations

The model simulation results used in this work were provided by two different atmospheric models: 1) HAMMONIA and 2) ECCHAM6. The HAMburg Model of the Neutral and Ionized Atmosphere (HAMMONIA) (Schmidt et al., 2006) is an improved model on the basis of the

ECHAM5 general circulation model (Roeckner et al., 2006). The vertical range of the model now ends at 2×10^{-7} hPa and, additionally, the model is coupled to MOZART3 (Model for Ozone and Related Chemical Tracers, version 3; Kinnison et al., 2007). The spectral resolution of the simulation used here is T31 with 119 vertical layers. The 34-year long simulation run is performed with fixed boundary conditions (including aerosol, ozone climatology). Further details about this simulation run are given by Schmidt et al. (2010).
The ECMWF/Hamburg (ECHAM6) model (Stevens et al., 2013) is the successor of ECHAM5, which is the base model of HAMMONIA. The model has improved with respect to the representation of radiative transfer in the solar part of the spectrum, a new description of atmospheric aerosol, and a new representation of the surface albedo in comparison to the previous version. The model vertically extends up to 0.01 hPa. The simulations were performed at T63 spectral resolution with 47 vertical layers. All boundary conditions were fixed to constant values, where the average from 1979 to 2008 was taken. The total length of the simulation run is 400 years.

2.2. Methods

2.2.1. Annual mean temperatures

Studies analysing the long-term trend or the long-term behaviour of the OH(3,1) rotational temperatures are typically based on annual mean temperatures. Since the OH(3,1) temperature time series has several data gaps over the course of one year due to cloudy conditions, a simple arithmetic mean is not advisable. Instead of an arithmetic mean a fit that describes the seasonal variations is used to determine the annual mean temperatures. These seasonal variations include three main components: an annual cycle, a semi-annual cycle, and a ter-annual cycle (Bittner et al., 2000). The fit is given by:

$$T(t) = T_0 + \sum_{i=1}^{3} A_i \cdot \sin\left(\frac{2 \cdot \pi \cdot i}{365.25}(t + \phi_i)\right), \tag{2.2}$$

where T_0 is the annual mean temperature, t is the time in days of the year, and A_i, ϕ_i are the amplitudes and phases of the sinusoids. This technique has been used in several studies using the Wuppertal or other OH rotational temperatures time series (e.g. Bittner et al., 2002; Offermann et al., 2010; Perminov et al., 2014; Kalicinsky et al., 2016) and is a suitable way to obtain the best estimate of T_0. Figure 2.4 shows an example of OH(3,1) rotational

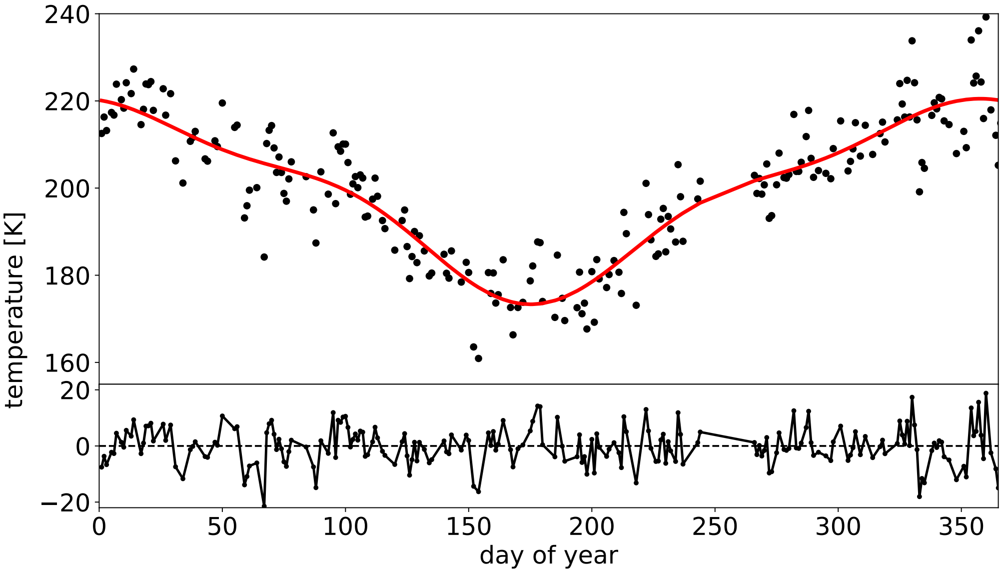

Figure 2.4: OH(3,1) rotational temperatures in the year 2016 and fitted seasonal variations. The rotational temperatures are shown in black in the upper panel and the fit of the seasonal variations to the data is displayed as red curve. The lower panel shows the residual temperatures (data – fit).

temperatures for the year 2016 as black dots. The fit of the seasonal variations to the data using Eq. 2.2 is shown as red curve. The largest variation in the course of one year is the annual cycle, but also the semi-annual and ter-annual cycles contribute to the total variation. For example, the narrower minimum in summer and the wider maximum in winter is largely caused by the semi-annual cycle. The fit can be used to detrend the OH(3,1) rotational temperatures within one year. In this way residual temperatures are obtained (see lower panel of Fig. 2.4) that can be further analysed with respect to temperature fluctuations with periods of a few to several days (see Sect. 3.2.1).

2.2.2. Multiple linear regression and least squares fits

A very useful method to analyse OH(3,1) rotational temperatures is the linear regression or multiple linear regression. This method is very suitable to investigate influences that can be described by a time series of one parameter. One example is the influence of the sun. The variation of the solar radiation can be described e.g. by the solar radio flux F10.7cm or the Mg-II index. The solar influence has been determined for the Wuppertal OH(3,1) or other OH temperature time series in different studies using a linear regression (e.g. Offermann et al., 2010; Perminov et al., 2014; Kalicinsky et al., 2016). The analysis of linear trends of the annual mean temperatures or other parameters is also a linear regression with the time. Such analyses have also been performed in different studies using OH temperatures (e.g. Bittner et al., 2002; Offermann et al., 2010; Perminov et al., 2014; Kalicinsky et al., 2016). Because of possible correlations between the different parameters used for single linear regressions, it is advisable to use an iterative procedure until convergence of the results is reached (e.g. Offermann et al., 2010) or to analyse all dependencies at once with a multiple linear regression (e.g. Kalicinsky et al., 2016). In order to analyse periodic variations of OH(3,1) rotational temperatures least squares fits of sinusoids to the time series proofed as suitable. In practice these fits are typically combined with the multiple linear regression terms described above (e.g. Kalicinsky et al., 2016, 2018).

2.2.3. Lomb–Scargle periodogram

OH(3,1) temperature time series typically exhibit data gaps. Most of these gaps are caused by cloudy conditions, which lead to measurement gaps within one night or to the lack of the complete night (e.g. Bittner et al., 2000; Oberheide et al., 2006). Due to instrument problems or reconstructions some years are largely affected by missing data and cannot be used for long-term analyses (e.g. Kalicinsky et al., 2016). Since most of the commonly used methods to analyse periodicities such as FFT (fast Fourier transform) or wavelet transform rely on an equidistant grid, the OH(3,1) rotational temperature time series need to be prepared, e.g. by interpolation, before the analysis. Thus, another processing step is necessary that could potentially influence the results.

This drawback can be avoided by using the Lomb-Scargle periodogram (LSP). The LSP was developed by Lomb (1976) and Scargle (1982) and is a method that can handle unequally spaced data time series. The periodogram is defined as

$$P_X(\omega) = \frac{1}{2}\left\{ \frac{\left[\sum_j X_j \cos\omega(t_j-\tau)\right]^2}{\sum_j \cos^2\omega(t_j-\tau)} + \frac{\left[\sum_j X_j \sin\omega(t_j-\tau)\right]^2}{\sum_j \sin^2\omega(t_j-\tau)} \right\}, \tag{2.3}$$

where X_j are the measurements at the times t_j, ω is the angular frequency ($\omega = 2\pi f$), and the time offset τ is defined as

$$\tan(2\omega\tau) = \frac{\left(\sum_j \sin 2\omega t_j\right)}{\left(\sum_j \cos 2\omega t_j\right)}. \tag{2.4}$$

The analysed time series has to have zero mean before the calculation of the periodogram powers. The LSP, as defined in Eq. 2.3, has two useful properties. Firstly, it is invariant to a shift of the origin of time and, secondly, it is equivalent to the least squares fitting of sinusoids to the data set (e.g. Horne and Baliunas, 1986). The definition of the periodogram is the same (except for a factor of 1/2) as the reduction in sum of squares (sum of squares of the original data minus sum of squares of residual data) when least squares fitting of a sinusoid is applied to the data (see Scargle, 1982, Appendix C). This means that the maximum power occurs at the same frequency that leads to the optimal least squares fit of a sinusoid to the data, i.e. the sum of squares of the residual data has a minimum and consequently the reduction in sum of squares has also a maximum.

The significance of the LSP is typically analysed with the so called false alarm probability (FAP). This FAP gives the probability that a peak with a certain height (power) occurred just by chance, e.g. due to noise. The levels for different FAPs are typically determined using Monte-Carlo simulations (see e.g. Horne and Baliunas, 1986; Cumming et al., 1999). Depending on the normalisation of the periodogram (e.g. sample variance, variance of the residuals) the maximum peak heights observed in these simulations follow different distributions (see Schwarzenberg-Czerny, 1998; Cumming et al., 1999; Zechmeister and Kürster, 2009). The complete procedure to calculate FAP levels is e.g. explained by Kalicinsky et al. (2016, 2020) and some more details are given in Sect. 2.2.4.

2.2.4. Moving LSP approach

Many periodic variations observed in temperature time series show also variations in some of the defining parameters, i.e. the amplitude and the period are not constant with time. This means that standard methods such as FFT or LSP that analyse the complete time interval at once only observe a mean situation and cannot resolve the temporal changes. In contrast, a wavelet transform is able to resolve temporal changes and it is often used to analyse any kind of periodicities observed in airglow observations (e.g. Bittner et al., 2000; Das and Sinha, 2008; Höppner and Bittner, 2009; Takahashi et al., 2013; Reid et al., 2014; Nyassor et al., 2018). One drawback of the wavelet transform is the equidistant grid that is needed for the analysis. Thus, in the case of data gaps these gaps have to be eliminated before the analysis by some kind of interpolation or assimilation technique (e.g. Bittner et al., 2000; Das and Sinha, 2008; Höppner and Bittner, 2009; Reid et al., 2014). As described in Sect. 2.2.3 the LSP can handle time series with data gaps. This is then combined with a moving window to additionally resolve the temporal changes. This idea is not completely new. Other airglow studies also use some kind of windowed LSP, but some these studies only use the LSP for independent time windows following each other such as different parts of a night (e.g Reid et al., 2014) or months of a year (e.g. Egito et al., 2018). Some other studies report on the analysis of radar observations of winds using a periodogram analysis with a moving window, but either the significance evaluation is missing (e.g. Yoshida et al., 1999) or the windows are only partly overlapping (e.g. Luo et al., 2000). In this work the LSP is combined with a window that is moved with the minimum possible step (the sampling step). Additionally, an empirical relationship to easily calculate significance levels was derived, which is useable for all different kinds of situations, e.g. changes of the window or frequency range or the number of data gaps. In this way the developed method enables an easy and very fast usage. The complete technique is described and tests with artificial and measurement data are shown by Kalicinsky et al. (2020). Here a summary is given.

First, a window length for the approach is chosen. Here it is advisable to chose a medium length to get a trade-off between the capability to resolve temporal changes of periods or amplitudes and a safe detection of longer period oscillations. In the first case the window length should not be too long as a mean state over the complete window length is determined and possible short term fluctuations of periods or amplitudes are largely smoothed for long time windows. In the second case the window length should not be chosen too short, because an oscillation with a somewhat longer period may show only less than one full cycle in the defined window. For the analysis of planetary wave activity during one year a window length of 60 days is a reasonable choice as many observed oscillations exhibit periods less than that and also temporal changes are resolved properly. The approach starts at the beginning of the time series and the LSP is calculated for all data points in the first window. Then the window is shifted by the minimum possible step (sampling step) and the next LSP is calculated. This procedure is repeated until the end of the time series is reached.

An important issue with respect to the analysis of periodicities is a significance analysis. For the LSP this significance analysis is typically done using the FAP, which needs time-consuming Monte-Carlo simulations. At a single frequency and for a normalisation of the periodogram with the sum of squares of the time series the probability that a peak of height z exceeds a value of z_0 is given by

$$\mathrm{Prob}(z > z_0) = (1 - z_0)^{\frac{N-3}{2}}, \tag{2.5}$$

where N is the number of data points (Zechmeister and Kürster, 2009). This probability can be calculated for every single frequency and any number of data points. But the important question is how large is the probability that one peak somewhere in the complete analysed frequency range Δf exceeds a value by chance. This probability is called the false alarm probability (FAP) and is

$$\text{FAP} = 1 - (1 - \text{Prob}(z > z_0))^{N_i}, \tag{2.6}$$

where N_i is the number of independent frequencies (see e.g. Horne and Baliunas, 1986; Cumming et al., 1999; Zechmeister and Kürster, 2009, for further discussion on FAP). Unfortunately, the number of independent frequencies (≈ number of frequencies where peaks can occur) cannot be analytically described. Monte-Carlo simulations are a suitable way to determine N_i (e.g. Cumming et al., 1999), but such simulations are time-consuming. Kalicinsky et al. (2020) wanted to avoid this by establishing a derived empirical relationship. They showed that the number of independent frequencies relies on two main parameters: 1) the window length; 2) the frequency range. As the resolving power (width of the peaks) is inversely proportional to the window length (e.g Cumming et al., 1999; Zechmeister and Kürster, 2009), a longer window leads also to a larger number of independent frequencies and vice versa. Additionally, the possibility to observe a peak of height z by chance is larger when the frequency range Δf is larger too. Kalicinsky et al. (2020) derived the empirical relationship for the number of independent frequencies

$$N_i = \left(2.92dd^{-1} \cdot \Delta f - 0.203d^{-1}\right) \cdot T, \tag{2.7}$$

where T is the window length. In the study they used windows from 30 to 90 d and frequency ranges from 1/2 – 1/5 d^{-1} to 1/2 – 1/90 d^{-1}, as these are suitable parameter choices for the analysis of planetary wave activity. However, the results can also be transferred to other situations, e.g. for gravity wave analyses (days change to minutes), by just transferring the values in terms of sampling steps from one situation to the other. Additionally, Kalicinsky et al. (2020) analysed the dependency on the number of data gaps and found only a very small decrease of N_i with increasing number of data gaps of a few per cent. This means a change of the FAP of a few per mille only. With this new empirical relationship it is possible to calculate a FAP for every situation (e.g. change of window length or frequency range, missing data points at the edges of the window and therefore smaller effective window) in an easy and very fast way.

The performance of the approach was tested with different artificial time series. These artificial time series included different types of oscillations and variations of the defining parameters. In Kalicinsky et al. (2020) one time series with an oscillation that exhibits a varying period and another time series with an oscillation that had a varying amplitude was used for tests. Finally, a time series composed as a superposition of the two former ones was used for the last test. During these tests also noise and data gaps were included into the artificial time series to simulate real measurement conditions. Figure 2.5 shows the two latter examples, the oscillation with varying amplitude and the superposition of this oscillation with a second oscillation with varying period. The original time series and the single components of them are shown in the two upper panels (Fig. 2.5a and Fig. 2.5d) and the results for the normalised power and the amplitude of the oscillations determined by the moving LSP approach are presented in the middle and lower panels (Figs. 2.5b, c and Figs. 2.5e, f). The maximum amplitude of both oscillations was always 1 K which is correctly detected by the approach. The slightly smaller amplitude for the oscillation with the varying amplitude (see Fig. 2.5c) stems from the fact that the length of the time window of 60 days introduces some smoothing and the maximum amplitude of 1 K is only reached in a small time interval in the middle of the time series. The normalised power shown in Fig. 2.5b and Fig. 2.5e also reflects the contribution of the oscillations to the complete signal very well. In the case of the oscillation with varying amplitude the contribution increases to the middle of the time series and then decreases again as the amplitude does. For the superposition of the two oscillations the partitioning of the contributions is also captured well. In the middle the contribution of each single oscillation is nearly identical as both have an amplitude of about 1 K here and at the beginning and end only the oscillation with varying period plays a role. The remaining part to explain the total variance in both cases is always the noise. In total, the method is capable to detect all different kinds of signals and the additional noise and the data gaps only introduce some noise to the results, but they do not largely influence the results.

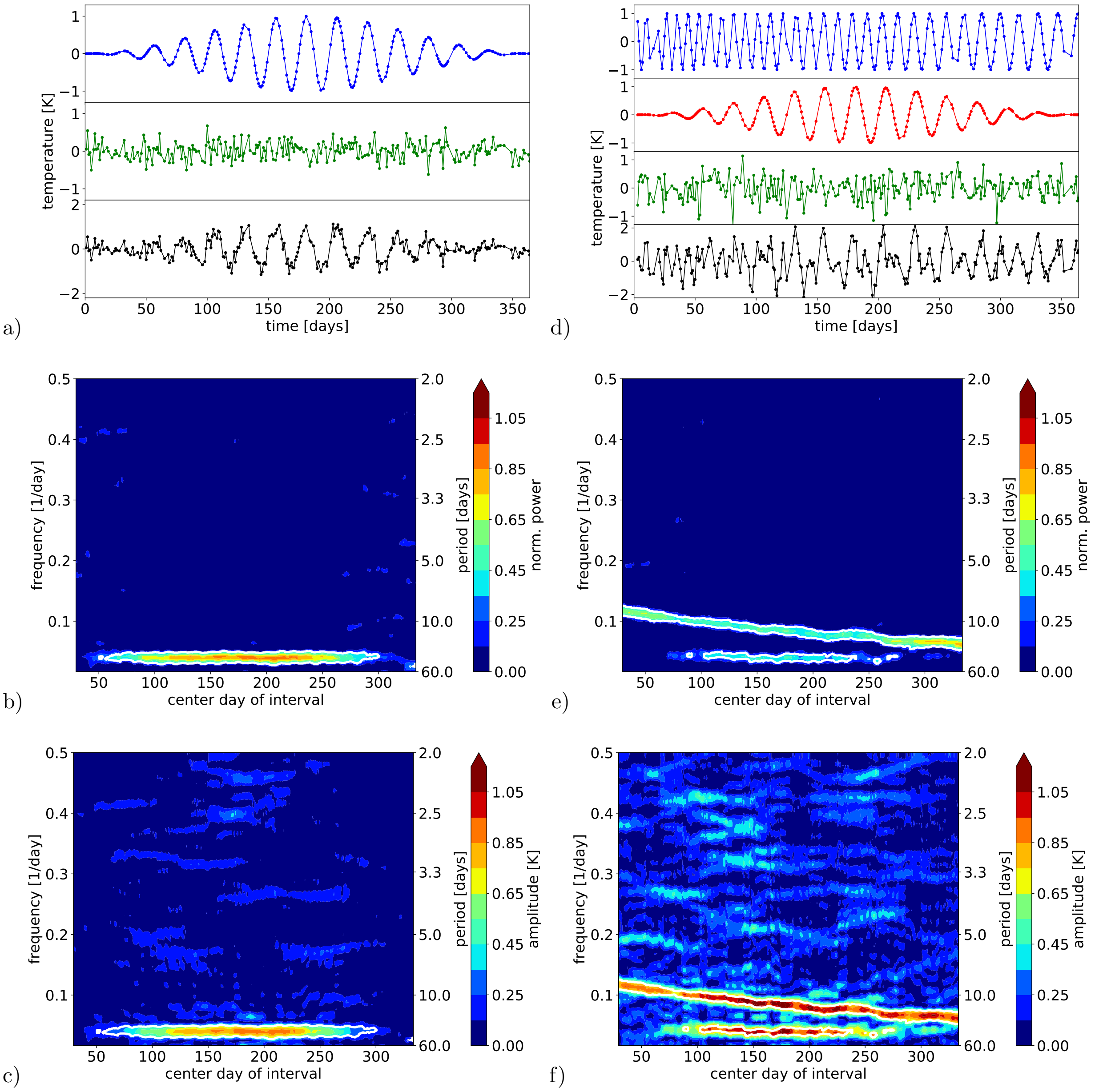

Figure 2.5: Different examples for the results of the moving LSP approach: Periodic signal with varying amplitude (a – c) and periodic signal with increasing amplitude plus a periodic signal with varying amplitude (d – e). a) The upper panel shows the periodic signal with varying amplitude, the middle panel shows the noise and the lower panel the sum of both. Additionally, data gaps are included (b, c) Results for the normalised power and amplitude. These results are displayed at the centre day of the corresponding time window, which has a length of 60 days. The white contours mark the significant results. (d) The upper two panels show the two signals, the periodic signal with varying period and the periodic signal with varying amplitude. In the third panel the noise and in the lower panel the sum of all are displayed. (e, f) Same as for (b, c). Figure taken from Kalicinsky et al. (2018)

3. Results

3.1. Long-term variations

In addition to the many rather short-term temperature variations, e.g. annual, semi-annual, and ter-annual cycles (compare Sect. 2.2.1), or on even shorter time scales in the case of wave activities (compare Sects. 3.2.1 and 3.2.2), the OH(3,1) rotational temperatures and thus mesopause temperatures show also clear long-term variations. These variations occur on time scales of years to decades and have an important influence on the temperatures in the mesopause region. Examples are the influence of the well-known 11-year cycle of solar activity, a possible long-term trend, and long-periodic oscillations with periods of several years. In this section these different long-term influences on the OH(3,1) rotational temperatures are presented and discussed.

3.1.1. 11-year cycle of solar activity

The 11-year cycle of solar activity is well known and can be seen in the sunspot number or other solar proxy data such as the F10.7cm solar radio flux (typically given in solar flux units (SFU); 1 SFU = 10^{-22} $\mathrm{Wm^2Hz^{-1}}$). Numerous publications about the correlation of the 11-year cycle of solar activity and temperatures in the mesopause region exist. A review of previous studies is given by Beig (2011b, see Fig. 2 and corresponding section). In the northern middle to higher latitudes the reported sensitivity to the 11-year cycle is in the range of 1 to 6 $\mathrm{K\,(100SFU)^{-1}}$. A study published by Perminov et al. (2014) also showed a sensitivity of 3.5 ± 0.8 $\mathrm{K\,(100SFU)^{-1}}$ for the mesopause temperatures measured at Zvenigorod (56°N, 37°E; 2000–2012), confirming the former results.
Earlier studies of the OH(3,1) rotational temperatures at Wuppertal station also showed sensitivities in this range. Only the study by Bittner et al. (2002) found no clear solar signature which could be caused by the shorter length of the time series in this study. In the following

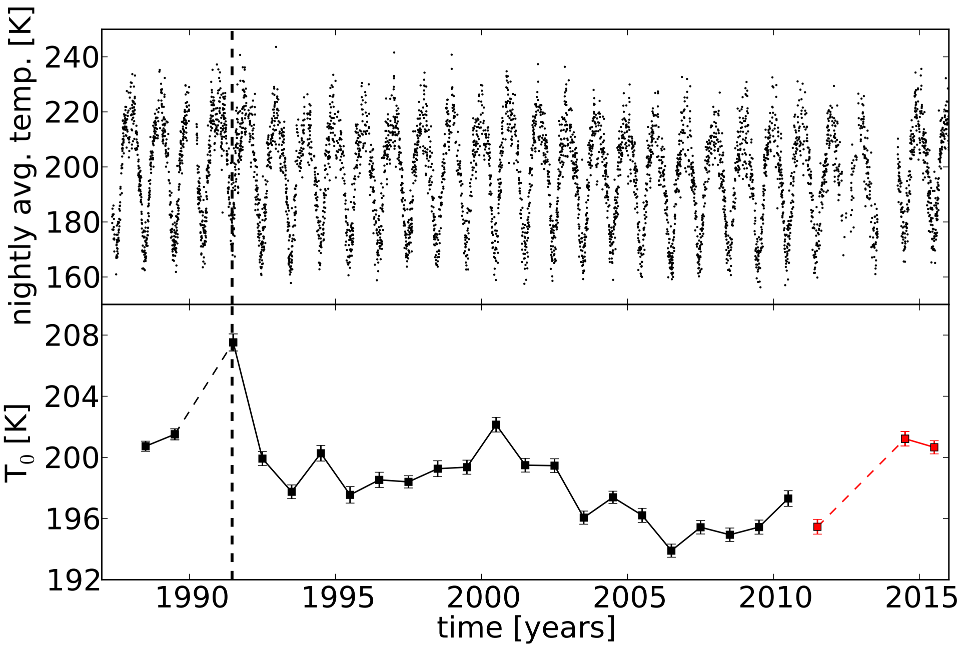

Figure 3.1: OH(3,1) rotational temperatures from 1988 to 2015. The upper panel shows the nightly average temperatures as black dots. In the lower panel the annual average temperatures are shown as black squares for the older GRIPS-I/II instruments and with red squares for the new GRIPS-N instrument. The error bars mark the 1σ uncertainties the temperatures. The vertical dashed line shows the date of Mt Pinatubo eruption. All annual average temperatures are shown in the middle of the years whereas the numbers at the x-axis mark the beginning of the years. The figure is taken from Kalicinsky et al. (2016).

studies by Offermann et al. (2004) and Offermann et al. (2010) almost the same sensitivities of 3.4 and 3.5 $\mathrm{K}(100\,\mathrm{SFU})^{-1}$ were obtained, respectively. These values perfectly agree with the findings by Perminov et al. (2014) and lie in the middle of the range given by Beig (2011b), where the results by Offermann et al. (2010) are included.

Figure 3.1 shows the OH(3,1) rotational temperatures analysed by Kalicinsky et al. (2016). The upper panel shows the nightly average temperatures and the lower panel the annual average temperatures determined using the fit procedure described in Sect. 2.2.1. These annual average temperatures were used to analyse the long-term behaviour of the temperatures in the mesopause region. Compared to the previous studies by Offermann et al. (2004) and Offermann et al. (2010) the length of the time series increased by at least 7 years (13 years compared to Offermann et al. (2004)). Thus, in this analysis now almost three maxima of the 11-year solar cycle were included: 1990/1991, 2001/2002, and 2014/2015. Obviously, the OH(3,1) rotational temperatures show local maxima at the times of maximum solar activity.

Table 3.1: Summary of the derived sensitivities to the 11-year cycle of solar activity.

description of the long-term behaviour	sensitivity [K/(100SFU)]
linear trend	4.2 ± 0.9
trend break	3.3 ± 0.9
Hale cycle	5.0 ± 0.7
long-periodic oscillation	4.1 ± 0.8
partly linear trends	3.9 ± 0.3

Kalicinsky et al. (2016) derived a sensitivity to the 11-year solar cycle of 3–5 $\mathrm{K}\,(100\,\mathrm{SFU})^{-1}$ depending on the fits applied to the data. They used four different descriptions of the long-term behaviour of the OH(3,1) rotational temperatures: 1) a linear trend, 2) a trend break (two phases with a linear trend each), 3) the Hale cycle (solar polar magnetic field), and 4) a long-periodic oscillation. All of these were used together with the influence of the 11-year cycle of solar activity to describe the complete long-term behaviour. The fit of the linear trend plus the 11-year solar cycle, as also done in Offermann et al. (2010), led to a sensitivity of 4.2 ± 0.9 $\mathrm{K}\,(100\,\mathrm{SFU})^{-1}$. The best fit was obtained with the combination of a long-periodic oscillation and the 11-year solar cycle. This resulted in a sensitivity of 4.1 ± 0.8 $\mathrm{K}\,(100\,\mathrm{SFU})^{-1}$. The results of all descriptions are summarised in Tab. 3.1. Thus, all results, except for the description using the Hale cycle, are in very good agreement with previous studies of the Wuppertal temperature time series and also with the other studies. Kalicinsky et al. (2016) judged the description using the Hale cycle as not very suitable. Further details to the trend itself and a possible trend break or long-periodic oscillation are discussed in Sects. 3.1.2 and 3.1.3.

Another important issue is the stability of the sensitivity to the 11-year solar cycle. The different studies of the Wuppertal OH(3,1) rotational temperature time series, which include an increasing number of data points, already suggest that the sensitivity is a fairly stable parameter. Kalicinsky et al. (2016) additionally analysed the stability in more detail. For this purpose they derived the sensitivity to the 11-year cycle of solar activity in consecutive 11-year time intervals starting with the interval 1988 – 1998. The time interval was shifted by 1 year until the end of the complete time series. Time intervals with missing data points at the beginning or the end were excluded from the analysis. In each time interval the sensitivity was derived together with a linear trend (option 1, see above). The results of this analysis are shown in Fig. 3.2. The upper panel shows the sensitivities, which were derived piecewise in 11-year time intervals, together with the range of the best fitting result of 4.1 ± 0.8 $\mathrm{K}\,(100\,\mathrm{SFU})^{-1}$. Obviously, the sensitivity is fairly stable throughout the complete time

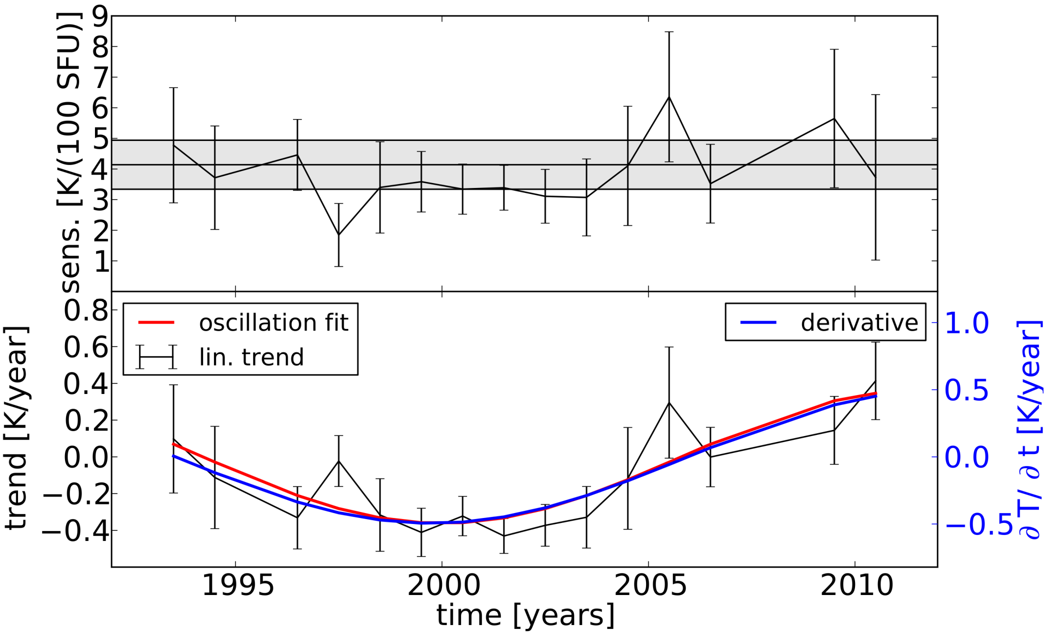

Figure 3.2: Stability of the solar influence and linear trends derived piecewise in consecutive 11-year time intervals. The upper panel shows the sensitivity to the 11-year cycle of solar activity derived for 11-year time intervals displayed at the centres of the time intervals. The error bars mark the 1σ uncertainties and the grey shaded area shows the results of the best fit: $4.1 \pm 0.8\,\mathrm{K}\,(100\,\mathrm{SFU})^{-1}$. The lower panel shows the linear trends derived for the 11-year time intervals with the corresponding 1σ uncertainties. The red curve shows a fit of an oscillation to these results and the blue curve shows the derivative of the derived temperature oscillation (see Sect. 3.1.3) with a second axis to the right. The figure is adapted from Kalicinsky et al. (2016).

interval and only small variations can be seen. These variations are typically smaller than the corresponding 1σ uncertainties, which shows that no significant long-term change of the sensitivity is observed. The mean sensitivity of the derived results is $3.9 \pm 0.3\,\mathrm{K}\,(100\,\mathrm{SFU})^{-1}$, which nearly perfectly agrees with the other results derived in the study. Thus, from this different studies a significant change of the sensitivity to the 11-year cycle of solar activity can be excluded.

Kalicinsky et al. (2018) also studied a possible seasonal difference by comparing winter and summer results. They defined the three months May, June, and July around the temperature minimum in June as the mesopause summer (compare Fig. 2.4). Consequently, the winter is defined by the months November, December, and January. The fit used by Kalicinsky et al. (2018) to describe the OH(3,1) rotational temperatures included the sensitivity to the 11-

year solar cycle and a long-periodic oscillation (option 4, see above). The results for summer and winter were 3.5 ± 1.5 K$(100\,\text{SFU})^{-1}$ and 3.5 ± 0.8 K$(100\,\text{SFU})^{-1}$, respectively. Thus, they agree well with each other and also with the results for the annual mean temperatures of previous studies, additionally showing the stability of the sensitivity throughout the year.

3.1.2. Long-term temperature trend

Besides the influence of the 11-year cycle of solar activity, another type of long-term evolution of the mesopause temperatures is a possible linear trend. Such linear trends have often been analysed and presented in the literature. Beig (2011a) gives an overview over this topic and reports about trends from no cooling up to a cooling of 3 K$\,\text{decade}^{-1}$. More recent studies showed similar results. Hall et al. (2012) analysed meteor radar observations over Svalbard (78° N, 16° E) at an altitude of 90 km in the time interval 2001 – 2012 and derived a negative trend of -4 ± 2 K$\,\text{decade}^{-1}$. Perminov et al. (2014) presented a trend of -2.2 ± 0.9 K$\,\text{decade}^{-1}$ for the measurements at Zvenigorod (56° N, 37° E) in nearly the same time interval 2000 – 2012. She et al. (2015) analysed combined Na LIDAR observations at Fort Collins (41° N, 105° W) and Logan (42° N, 112° W) in a larger time interval from 1990 – 2014 and in a larger altitude range. The authors found an insignificant trend of -0.64 ± 0.99 K$\,\text{decade}^{-1}$ at 85 km altitude. This negative trend then enlarges with increasing height up to an maximum of -2.8 ± 0.58 K$\,\text{decade}^{-1}$ in the altitude range between 91 and 93 km and afterwards the cooling trend decreases and turns into a warming trend above 103 km.

Previous studies of the OH(3,1) rotational temperatures at Wuppertal led to different results depending on the analysed time interval. Bittner et al. (2002) (1980 – 1998) could not found any evidence for a significant trend in the data. Offermann et al. (2004) (1981 – 2002) reported a trend value which is likely positive with a value of about 0.5 K$\,\text{decade}^{-1}$, but similar to the study by Bittner et al. (2002) this trend was also not significant. Offermann et al. (2010) analysed a different time interval from 1988 to 2008 and derived a negative trend of -2.3 ± 0.6 K$\,\text{decade}^{-1}$. Furthermore, they reported on a possible trend break close to 1997 with a less negative trend before this year and a stronger negative trend thereafter. Thus, the OH(3,1) rotational temperatures did not show a stable linear trend during the complete time series but variations depending on the analysed time interval.

Kalicinsky et al. (2016) extended the analysed time interval to 1988 – 2015, thus, 7 years longer than in Offermann et al. (2010). They fitted performed a multiple linear regression using the time (linear trend) and solar radio flux and they obtained a linear trend of -0.89 ± 0.55 K$\,\text{decade}^{-1}$. Compared to the previous study by Offermann et al. (2010) the trend value

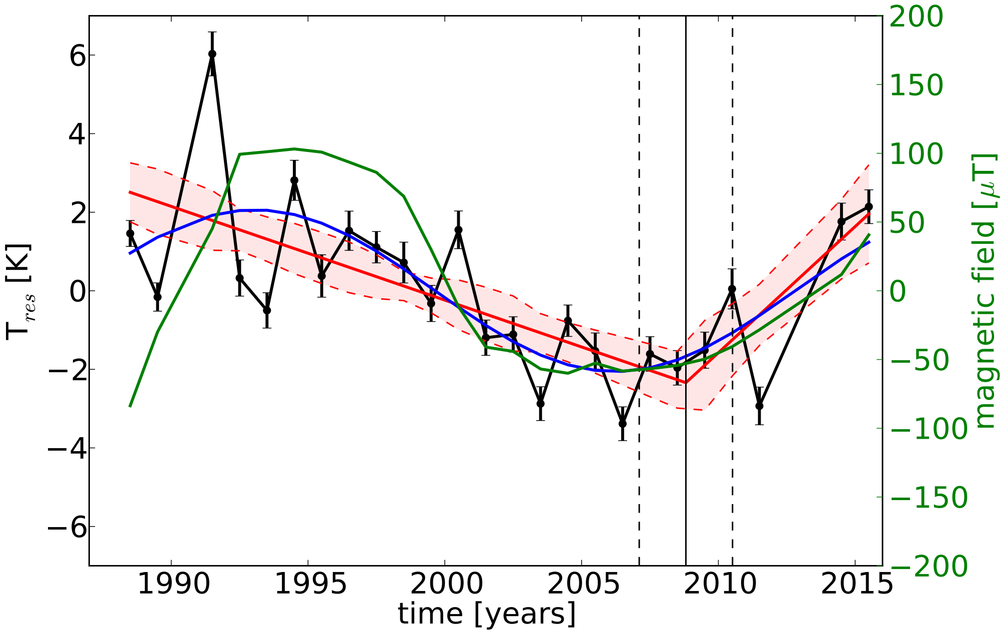

Figure 3.3: Trend break in OH(3,1) rotational time series. The black circles show the time series of residual temperature after removing the influence of the 11-year solar cycle and subtracting the mean. The red lines show the fit of the trend break and the reddish area marks the 1σ uncertainty of the complete fit. The break point is displayed by the vertical black line and the corresponding uncertainties are shown as vertical dashed black lines. The blue curve shows a sinusoidal fit to the residual temperatures. Additionally, the solar polar magnetic field strength values are shown as a green curve with a second axis to the right. Displayed are the average values for the solar North Pole and South Pole with the magnetic field orientation of the North Pole ((N–S)/2). The data were provided by the Wilcox Solar Observatory (for an instrument description see Scherrer et al. (1977)). The figure is taken from Kalicinsky et al. (2016).

still is negative but more then halved. This can be explained by the fact that one linear trend for the whole time series is not enough to explain all long-term variations. Furthermore, a trend break at the end of the 2000s was indicated in the residual temperatures (original data - fit curve). Therefore, they repeated the analysis and exchanged the linear trend term in the fit with a trend break description with two linear parts with different slopes. The result of this analysis is shown in Fig. 3.3. The OH(3,1) rotational temperatures (after subtracting the solar influence and the mean) are shown as black circles and the red lines show the two linear trends with the trend break marked by the vertical black line. The break point is located in the year 2008 (2008.8 ± 1.7 years). Before the break point the linear trend is -2.4 ±

0.7 $\mathrm{K\,decade^{-1}}$ and therefore the same as already derived in Offermann et al. (2010). After the break in 2008 the trend turns positive and the result of the fit is 6.4 ± 3.3 $\mathrm{K\,decade^{-1}}$. Taking into account that a linear trend at the beginning of the time series until the end of the 1990s seems to be much smaller than in the 2000s (compare also Offermann et al. (2010)) an oscillation as possible description of the long-term evolution of the temperatures is an option, too. The blue curve in Fig. 3.3 shows a sinusoidal fit to the temperature residual to account for this possible periodic behaviour. The derived parameters of the oscillation are a period of 26.3 ± 3.2 years and an amplitude of 2.04 ± 0.43 K. This oscillation gives a very good description of the residual temperatures. The idea of an oscillation as main part of the long-term evolution beside the influence of the 11-year solar cycle is already supported by the analysis, which was performed piecewise and is shown in Sect. 3.1.1 and in Fig. 3.2. In this analysis the multiple linear regression using time (linear trend) and solar radio flux (sensitivity to the 11-year solar cycle) was performed in consecutive 11-year time windows. The derived linear trends for these 11-year time windows are shown in the lower panel of Fig. 3.2 in black. The trend values can be nearly perfectly described by an oscillation as can be seen by the red curve which shows a sinusoid fitted to these values. The obtained period is about 25 years. Since the partially derived linear trends are a smoothed derivative of the OH(3,1) rotational temperature time series itself (after removing the solar influence), the observed oscillation shows that the temperatures themselves can be described by an oscillation as well (in combination with the 11-year cycle of solar activity) as shown with the blue curve in Fig. 3.3. The idea of an oscillation as important part of the temperature time series is further analysed in discussed in the following sections.

3.1.3. Long-periodic temperature oscillation

Kalicinsky et al. (2016) analysed different options to describe the long-term evolution of the Wuppertal OH(3,1) rotational temperature time series. One component was always the influence of the 11-year cycle of solar activity. The other components varied from a linear trend or trend break (see Sect. 3.1.2) to long-periodic oscillations. It turned out that a fit including the solar influence and a long-periodic oscillation is possibly the best way to describe the complete long-term behaviour. The result of this fit is shown in Fig. 3.4a. The OH(3,1) rotational temperatures are shown as black circles and the fit curve is shown in red in the upper panel. The lower panel shows the residual temperatures (original data - fit). Obviously, no further long-term variation is visible. The resulting fit parameters were an amplitude of 1.95 ± 0.44 K and a period of 24.8 ± 3.3 years. These values are in very good agreement with

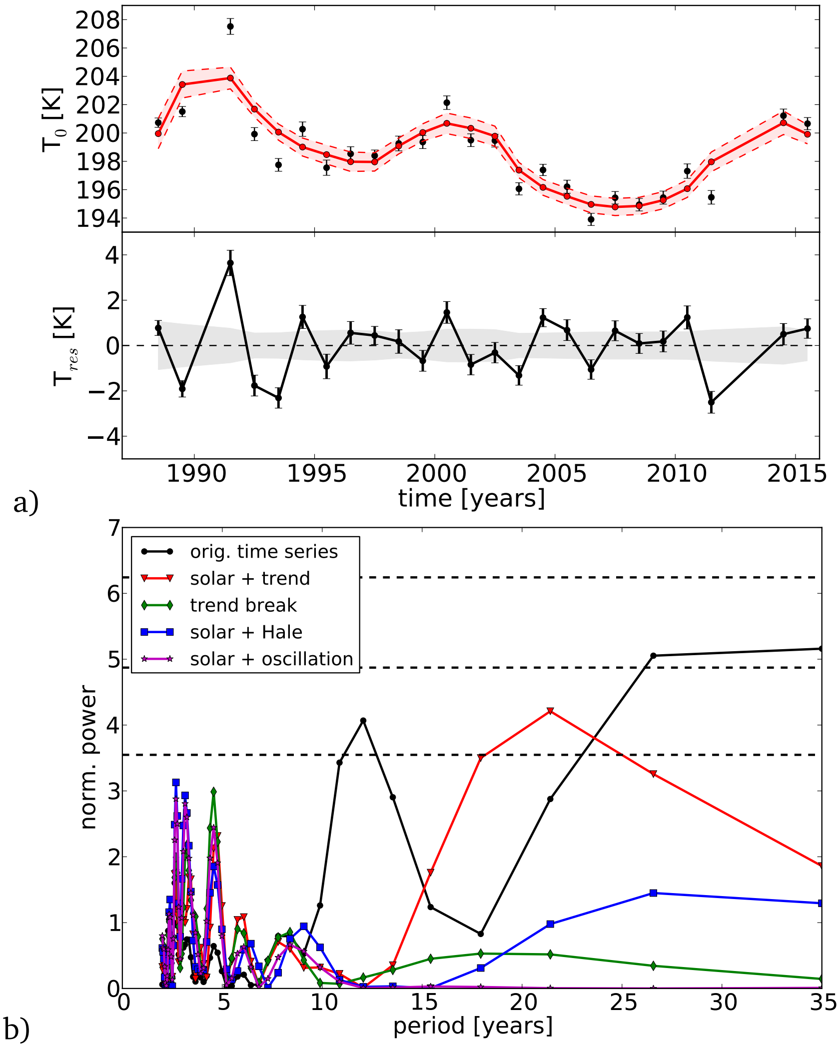

Figure 3.4: Best description of OH(3,1) rotational temperature time series and LSPs of the time series and residuals. a) In the upper panel the OH(3,1) rotational temperatures are shown as black circles with corresponding 1σ uncertainties. The red line shows the best fitting curve including a long-periodic oscillation and the correlation to the 11-year solar cycle. The reddish area marks the 1σ uncertainty of the fit curve. The lower panel shows the residual temperatures after subtracting the fit from the original data. The grey area again shows the 1σ uncertainty of the fit curve. b) LSPs for the original time series (black) and different residual temperatures after subtracting different fit curves. Red: trend; green: trend break; blue: Hale cycle; magenta: long-periodic oscillation (all together with correlation to the 11-year solar cycle). The dashed black horizontal lines display the levels for false alarm probabilities of 0.01, 0.1, and 0.5 (top to bottom). The figure a) is taken from Kalicinsky et al. (2016) and figure b) is adapted from Kalicinsky et al. (2016).

the values obtained before during the trend break analysis (see Sect. 3.1.2).

Due to the fact that Höppner and Bittner (2007) observed a similar quasi-bidecadal oscillation for the planetary wave activity that showed reasonable agreement with the Hale cycle (reversal of the solar polar magnetic field), Kalicinsky et al. (2016) tested the possibility of the Hale cycle as driving mechanism as well. The solar polar magnetic field strength is shown in Fig. 3.3 as green curve with a second axis to the right. In the analysis the oscillation term in the complete fit term was replaced by a regression term using the Hale cycle. But, it turned out that this description had some deficiencies, especially at the beginning and the end of the time series. Thus, the fit including the oscillation was still better and Kalicinsky et al. (2016) excluded the Hale cycle acting as input parameter in this and the following study (Kalicinsky et al., 2018).

The LSPs for the different residual temperatures confirm the fact that the fit including the oscillation is enough to explain all long-term variations. Figure 3.4b shows the LSP for the original data series as black curve. The two main peaks are at about 11 years and larger than 25 years. The LSPs for the different residual temperatures are shown in different colours. Only for the fit including the long-periodic oscillation and the influence of the 11-year solar cycle (magenta curve in Fig. 3.4b) there are no indications for variability with periods larger than 10 years in the residual temperatures any more. All other descriptions show more or less prominent signals in this period range.

The fitted long-periodic oscillation perfectly agrees with the results of the partially derived trends (see Fig. 3.2). As already mentioned these trends show a smoothed derivative of the temperature residual after subtracting the solar influence. When this temperature residual can be described with an oscillation, the derivative is consequently an oscillation as well shifted by $\frac{\pi}{2}$. Figure 3.2 shows the derivative of the quasi-bidecadal oscillation as the blue curve in the lower panel. Obviously, this curve perfectly agrees with the oscillation fitted to the partially derived trends (red curve in Fig. 3.2). Because of the smoothing effect, the maximum values are slightly smaller for the partially derived trends than for the real local derivative. In total, both different approaches describing the long-term evolution of the OH(3,1) rotational temperatures lead to the same results for the solar influence and the observed quasi-bidecadal oscillation.

Kalicinsky et al. (2018) additionally analysed the difference for the summer and winter months. As mentioned above, they defined the summer months for the OH(3,1) rotational temperatures as MJJ and, consequently, the winter months as NDJ. A fit of a long-periodic oscillation together with the influence of the 11-year solar cycle to the two different data series was applied. In contrast to the sensitivity to the solar cycle, which is the same in both seasons, the oscillations differ in some aspects. Kalicinsky et al. (2018) showed that in both seasons a quasi-bidecadal oscillation is observed. Although the periods agree well, the amplitude is nearly twice as large as in summer compared to winter. Thus, in summer the oscillation clearly dominates the complete long-term evolution of the temperatures, whereas in winter months the sensitivity to the 11-year solar cycle plays the major role.

The observed quasi-bidecadal oscillation also explains the different linear trends observed in previous studies for different time intervals. In Bittner et al. (2002) and Offermann et al. (2004) no significant trend was observed, which is at least partly caused by the rather short length of the used time series 1980 – 1998 and 1981 – 2002, respectively. On the other hand, this would be in accordance with the quasi-bidecadal oscillation which has a minimum at the beginning of the 1980s and a maximum at the beginning of the 1990s. Thus, a linear trend in the above mentioned time intervals would be rather small and likely little positive as also indicated by Offermann et al. (2004). Care has to be taken concerning the values by Bittner et al. (2002) and Offermann et al. (2004) because of the data gaps in the mid of the 1980s and since the studies do not fit the linear trend together with the influence of the 11-year solar cycle (see Offermann et al., 2004) or do not mention the details of the procedure (see Bittner et al., 2002). In Offermann et al. (2010), where the authors analysed the time interval 1988 – 2008, both components were considered at the same time and a linear trend of -2.3 ± 0.6 $\mathrm{K\,decade^{-1}}$ was derived. A fit of a line to the quasi-bidecadal oscillation in the same time interval also led to the same slope of -2.2 ± 0.3 $\mathrm{K\,decade^{-1}}$ (Kalicinsky et al., 2016). The same is true for the longest time interval analysed in Kalicinsky et al. (2016). Here, also a fit of a line to the oscillation alone led to the same result as the complete fit including a linear trend and the influence of the 11-year solar cycle to the complete data series. The values were -0.97 ± 0.32 $\mathrm{K\,decade^{-1}}$ and -0.89 ± 0.55 $\mathrm{K\,decade^{-1}}$, respectively.

In total, the quasi-bidecadal oscillation is the second major part of the long-term evolution of the OH(3,1) rotational temperatures observed from Wuppertal. Because of its existence all different kind of linear trends can be observed depending on the analysed time interval.

3.1.4. Theory of vertical displacement

Kalicinsky et al. (2018) performed a more detailed analysis of the quasi-bidecadal oscillation and additionally analysed plasma scale height (PSH) observations in the time interval 1959 – 2016 located close to the OH(3,1) rotational temperature observations. These plasma scale heights are a proxy for the temperatures at altitudes around 80 km in summer (e.g. Pe-

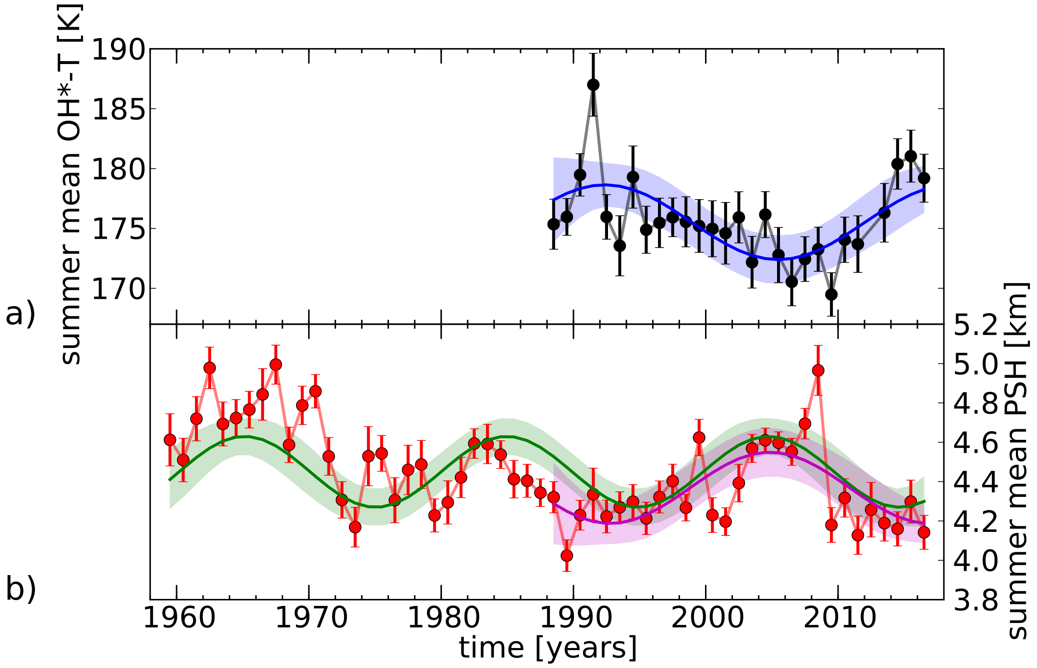

Figure 3.5: Quasi-bidecadal oscillation in the summer mean OH(3,1) rotational temperatures and the PSH time series. a) The summer mean (MJJ) OH(3,1) rotational temperatures in the time interval 1988 – 2016 are shown with black circles. b) The summer mean values of PSH in the time interval 1959 – 2016 are shown as red circles. All error bars show two times the standard error of the mean values. The coloured curves display fits of sinusoids to the time series in different time intervals: blue and magenta: 1988 – 2016; green: 1959 – 2016. The coloured shaded areas mark two times the 1σ uncertainties of the fits. The figure is taken from Kalicinsky et al. (2018).

ters et al., 2017; Kalicinsky et al., 2018). Due to this only summer values for the OH(3,1) rotational temperatures and PSH were used. Because of the temperature minimum of the OH(3,1) rotational temperatures in June the summer is defined as the months May, June, and July (MJJ) (compare e.g. Fig. 2.2 and Fig. 2.4).

Figure 3.5 shows the time series of OH(3,1) rotational temperatures as the black curve in the upper panel and the time series of PSH as red curve in the lower panel. The coloured curves with the shaded areas show sinusoids fitted to these two time series. Obviously, both time series show a clear quasi-bidecadal oscillation. The resulting values for the period derived in the same time interval (1988 – 2016) are 26.2 ± 3.8 for the OH(3,1) rotational temperatures and 24.1 ± 3.2 for PSH. Hence, there is a remarkable agreement of the oscillation periods, but the phase is opposite to each other, i.e. the PSH values show a minimum at the time of a maximum in the OH(3,1) rotational temperatures and vice versa. Kalicinsky et al. (2018)

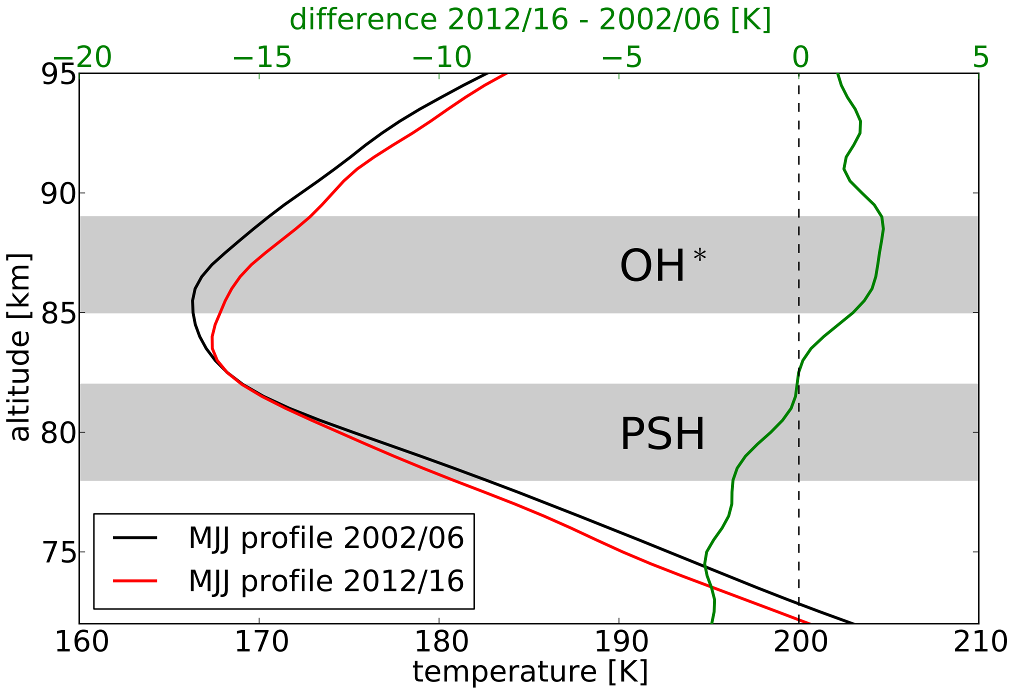

Figure 3.6: The vertical displacement of the temperature profile in SABER observations. The mean summer SABER temperature profile (MJJ) in the region 47° - 53° N and 0° - 12° E in the time interval 2002 - 2006 is shown as black curve and in the time interval 2012 - 2016 as red curve. The grey horizontal bars show the centre regions of OH(3,1) rotational temperatures and PSH, respectively. Additionally, the difference between the profile of the second and the first interval is shown with a second axis on the top. The figure is taken from Kalicinsky et al. (2018).

also analysed the influence of the 11-year cycle of solar activity and observed only a very weak effect on the long-periodic oscillations, i.e. the oscillations obtained under consideration of the solar cycle influence agree within the uncertainties with the oscillations shown here without consideration of the solar cycle influence.

A possible explanation of the observed anticorrelation is a periodic vertical displacement of the whole temperature profile. To understand this phenomenon it has to be kept in mind that the two observations are located at two different altitudes. The centre altitude of the OH(3,1) rotational temperatures is about 87 km and therefore above the temperature minimum in the mesopause region in summer (compare Fig. 3.6). By contrast to this, the centre altitude of the PSH observations is 80 km. This altitude range lies below the temperature minimum (compare Fig. 3.6). As a consequence both observations took place in regions with opposite vertical temperature gradients, positive for the OH(3,1) rotational temperatures and negative for PSH. When the temperature profile vertically shifts from a first time interval

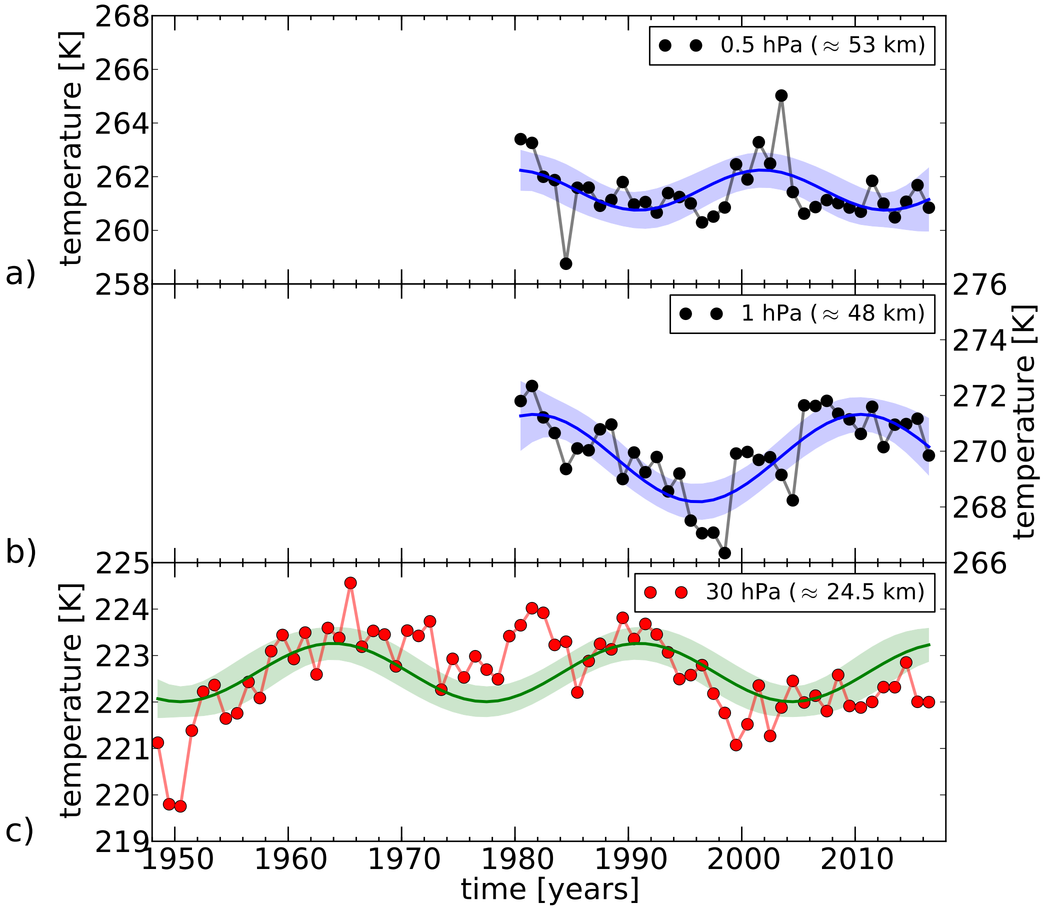

Figure 3.7: Quasi-bidecadal oscillation observed in the MERRA-2 and NCEP/NCAR reanalysis data sets. a), b) The summer mean values (MJJ) of the MERRA-2 temperatures at 0.5 hPa (≈ 53 km) and at 1 hPa (≈ 48 km) in the time interval 1980 to 2016 are shown as black circles. c) The summer mean values of NCEP/NCAR temperatures at 30 hPa (≈ 24.5 km) in the time interval 1948 to 2016 are shown as red circles. All time series show the average values in the region 47°-53°N and 0°-12°E. The temperatures in panel a) and b) have been detrended by subtracting a straight line. The blue and green curves show the main periodic oscillation fitted to the data series. The shaded areas display two times the 1σ uncertainties of the sinusoidal fits. The figure is taken from Kalicinsky et al. (2018).

(black in Fig. 3.6) to a second time interval (red in Fig. 3.6), the temperature difference (second profile - first profile) is opposite in the two regions. This is shown in Fig. 3.6 with two mean profiles in the time intervals 2002 - 2006 (around the minimum of the oscillation at the OH(3,1) altitude) and 2012 - 2016 that were derived from SABER observations. Obviously, the red curve is a downward shifted version of the black curve and the temperature minimum is about 2 km lower for the red curve compared to the black one. Because of the opposite gradients in the regions of the OH(3,1) rotational temperatures and the PSH observations, the difference between the two profiles (green curve in Fig. 3.6) has an opposite sign in the two regions and therefore shows the expected behaviour confirming the theory of a periodic vertical displacement.

Furthermore, the reanalysis data sets MERRA-2 and NCEP/NCAR, which cover much longer time periods compared to SABER, also revealed quasi-bidecadal oscillations in the mesosphere and stratosphere. Figure 3.7 shows some examples at different altitudes in the latitudinal and longitudinal region of the OH(3,1) rotational temperature and PSH observations. The NCEP/NCAR reanalysis temperatures at 30 hPa (see Fig. 3.7c), i.e. in the stratosphere, shows a quasi-bidecadal oscillation (period 27.0 ± 1.4 years), which is very similar to that observed for the OH(3,1) rotational temperatures with a maximum at the beginning of the 1990s and a minimum in beginning to mid-2000s. The MERRA-2 time series at 0.5 hPa (see Fig. 3.7a)) shows an oscillation (period 21.9 ± 2.6 years) that is in phase with the oscillation of PSH. In the stratopause region at about 1 hPa (see Fig. 3.7b) the situation is not completely clear. Although a nearly quasi-bidecadal oscillation (period 28.8 ± 2.7 years) is observed the phase is neither matching that of the oscillation of the OH(3,1) rotational temperatures nor that of the oscillation of PSH. Note here that for the MERRA-2 data an additional linear trend has to be taken into account. The observed anticorrelation between the mesosphere and stratosphere temperature oscillations again stems from the opposite vertical temperature gradients in this two regions. Hence, a shift of the oscillations by about a half period length occurs when the vertical gradient of the temperature profile changes sign. The complete behaviour of the vertical structure of this mechanism is illustrated in Fig. 3.8. The time intervals are chosen such that a warming in the lower thermosphere and mid-stratosphere together with a cooling in the mesosphere occurs when a transition from the first (black) to the second time interval (red) takes place. As in the upper stratosphere and stratopause region the situation is not completely clear and warming and cooling can occur here. Therefore this region is denoted as transition region.

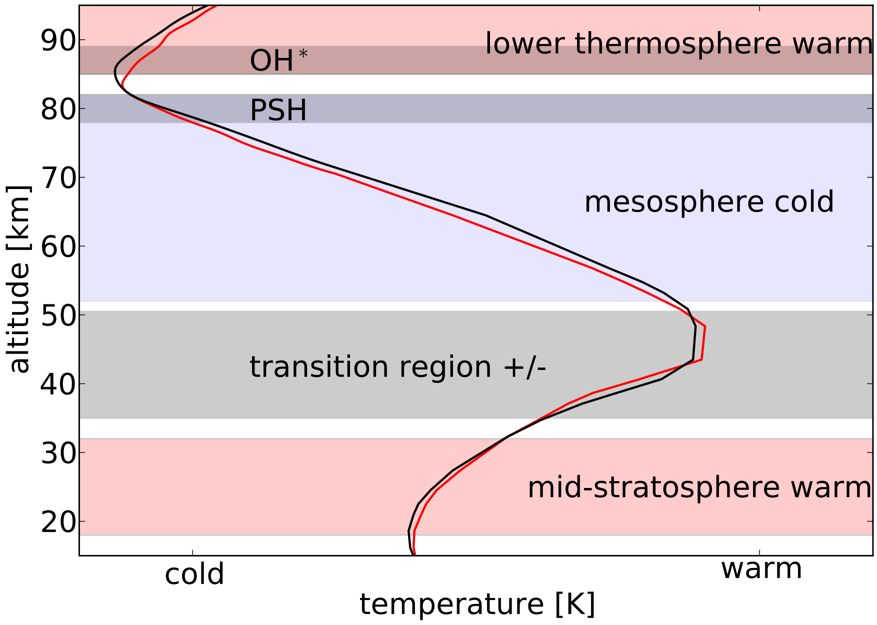

Figure 3.8: Sketch of the vertical displacement of the temperature profile. The summer mean temperature profiles (MJJ) in two different time intervals are shown in black (first interval) and red (second interval). The temperature difference at a constant altitude between the two time intervals is marked by the coloured areas in blue for cold and red for warm. Additionally, the centre regions of PSH and OH(3,1) rotational temperatures are marked by darker dyed horizontal bars. The figure is taken from Kalicinsky et al. (2018).

3.1.5. Vertical structure and further properties of the long-periodic oscillation

The vertical structure of the quasi-bidecadal oscillation with adjacent regions that behave opposite to each other was already known to us in the context of much smaller periods. Offermann et al. (2015) analysed SABER observations and HAMMONIA model simulations with respect to multi-annual oscillations in the range from 2 to 6 years. In this study they showed that oscillations exist in the complete altitude range from the ground up to 110 km that show a fairly constant period over all altitudes. In the analysed period range they found three oscillations with the periods 2.4, 3.4, and 5.5 years. The amplitudes and the phases of these oscillations varied with altitude. The amplitude showed alternating minima and maxima and the phase showed steep changes by about 180° at the altitudes of the amplitude minima. In between two minima the phase was constant. This means that the oscillations of two adjacent altitude regimes behaved opposite to each other. Hence, the behaviour is

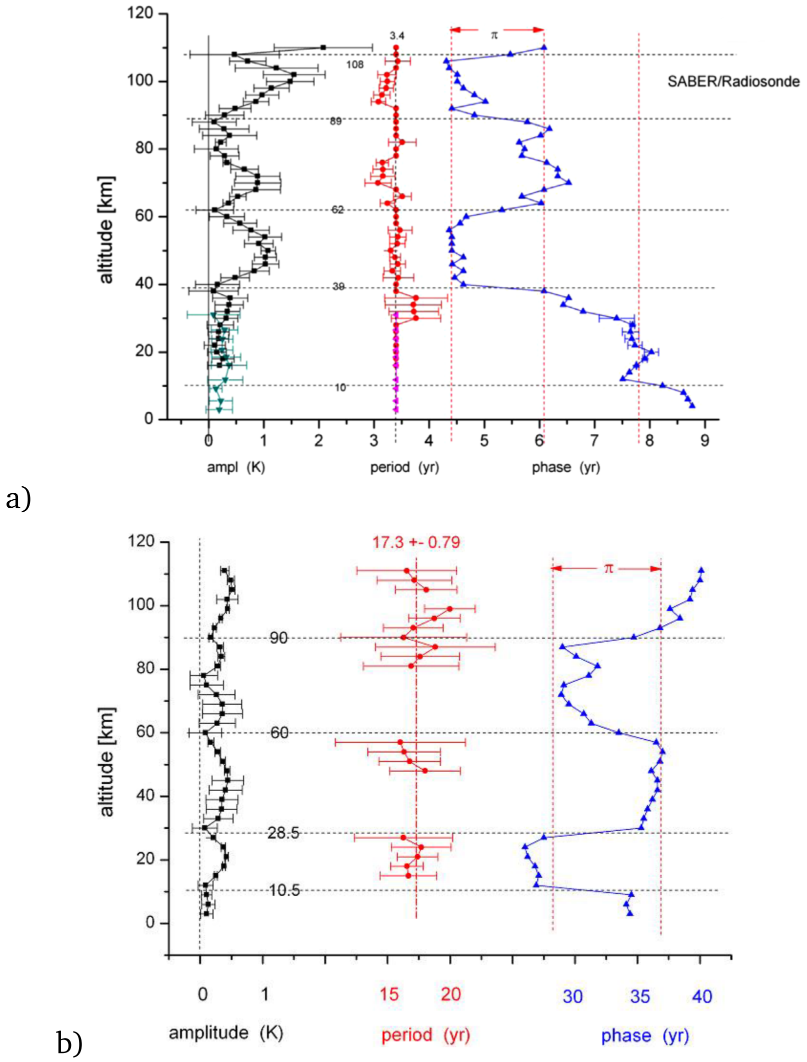

Figure 3.9: Vertical structure of oscillations with different periods. a) The amplitudes, the periods, and the phase of the oscillations near the mean period of about 3.4 years derived from SABER observations and radiosonde measurements in the region of Wuppertal. The results for the SABER data are shown in black and red, whereas the results for the radiosonde data are show in cyan and pink. The phases show relative values. Period data that could not be derived are shown without error bars and they were prescribed in the analysis using the mean period to derive estimates for the amplitudes and phases. The figure is adapted from Offermann et al. (2015). b) The amplitudes, the periods, and the phase of the oscillations near the mean period of about 17.3 years derived from HAMMONIA simulations in the region of Wuppertal. The phases show relative values. Missing period data could not be derived and were prescribed in the analysis using the mean period to derive estimates for the amplitudes and phases. The figure is taken from Offermann et al. (2021).

the same as already shown here for the OH(3,1) rotational temperatures and the PSH observations. In a following study Offermann et al. (2021) additionally extended the analysis to much longer periods using HAMMONIA and ECHAM model simulations. In this study the same vertical structure was observed for several other oscillations with periods in the range from 5 to more than 200 years. Two examples are shown in Fig. 3.9, one for a shorter period of 3.4 years in Fig. 3.9a and one for a longer period of 17.3 years in Fig. 3.9b. Both examples show results for the region of Wuppertal. Obviously, the two results agree very well with each other, especially in the upper altitude regime above about 40 km. The altitude regions with constant phase and the altitudes where the steep changes occur are nearly identical for both different periods stemming from completely different data sources. In the lower altitude part some differences occur between the model simulations and the observations.

The results derived from these two data sets also agree well with the findings presented in the former subsection and summarised in Fig. 3.8. For the quasi-bidecadal oscillation the first altitude region above about 85 km is in phase and behaves opposite to the second altitude region below about 85 km, which is almost identical to the results presented here. This second region ends at an altitude of about 52 km in the case of the quasi-bidecadal oscillation (see Fig. 3.8) and at an altitude of about 60 km in the two other cases (see Fig. 3.9). Below these altitudes a third region with a constant phase establishes. In the case of the quasi-bidecadal oscillation and the SABER observations it extends down to below 20 km. Note here that the change of the phase at an altitude of about 30 km in the case of the SABER observations is about 2π in Fig. 3.9a, i.e. there is no change in phase. In a shorter altitude range between 39 km and 30 km some oscillations with a phase that is shifted by about π can be observed, but these observations fall into the altitude regime denoted as transition region before (compare Fig. 3.8) and a correct determination might be difficult in this region. In the case of the HAMMONIA simulation results shown in Fig. 3.9b the lower altitude part shows one additional change of the phase by about π at an altitude of about 28 km that is not observed for the observational data sets. However, there is a remarkable agreement when keeping in mind the difference of the data sets, the period lengths that were analysed, and the fact, that the OH(3,1) rotational temperatures and the PSH observations are summer mean values and the other data yearly means.

The further analysis of the HAMMONIA and ECHAM model simulations showed that at distinct periods oscillations in a large altitude range could be derived. In contrast to this, at periods in between no oscillations have been found. Figure 3.10 shows the vertically resolved LSPs for the ECHAM simulations (the figure is comparable to Fig. 7 in Offermann

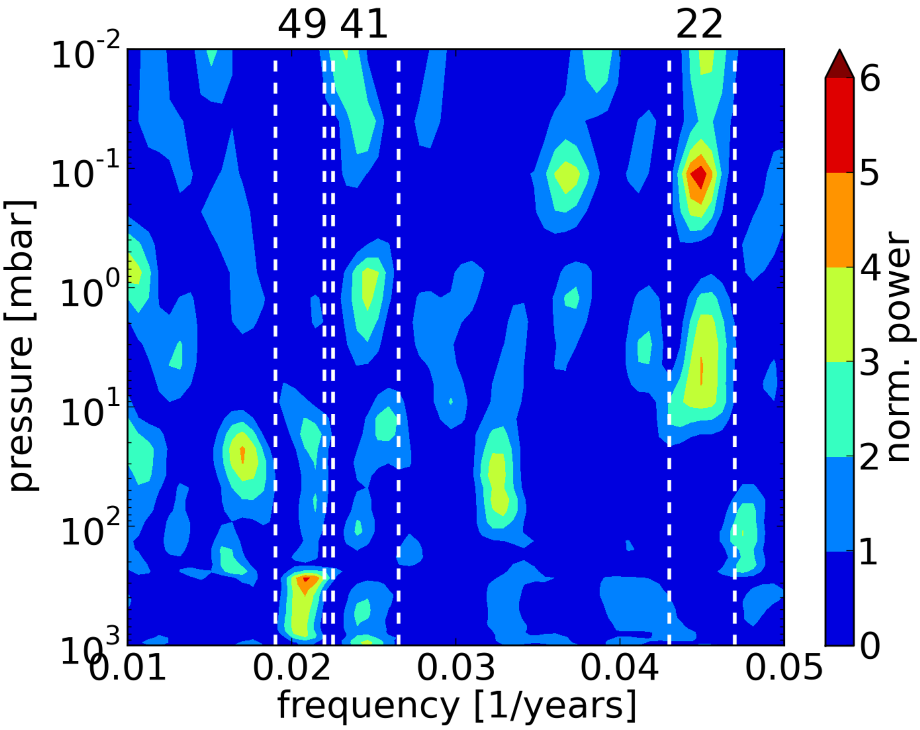

Figure 3.10: Vertically resolved LSPs for the ECHAM simulations. The LSPs for the ECHAM simulations are calculated in the frequency range from 0.01 to 0.05 years^{-1} (periods: 20 – 100 years) and in the altitude range from ground (1000 mbar) to 0.01 mbar for each altitude separately. The normalised power is depicted colour coded. The vertical dashed lines mark the region around a period of 22, 41, and 49 years.

et al. (2021)). As only some distinct periods seem to be preferred and oscillations at other periods are not detected, the normalised power shows a pattern of vertical stripes. At some distinct periods in a large part of the altitude range (e.g. at periods of 22 years in the upper atmosphere and 49 years in the lower atmosphere) or in nearly the complete altitude range (e.g. at a period of about 41 years) higher values of the normalised power can be seen, i.e. oscillations are detected. Additionally, they are horizontal gaps where the normalised powers are very low, i.e. here the amplitudes of the oscillations are very small. Thus, there is a clear structure concerning the observed periods and a vertical pattern of the corresponding amplitudes. The fact that some periods are preferred and others not can additionally be shown by a vertically averaged LSP. This mean LSP is shown in Fig. 3.11 as blue curve. Because of the anticorrelated behaviour in different altitude regimes, the LSPs were calculated separately for each altitude level and averaged afterwards instead of averaging the temper-

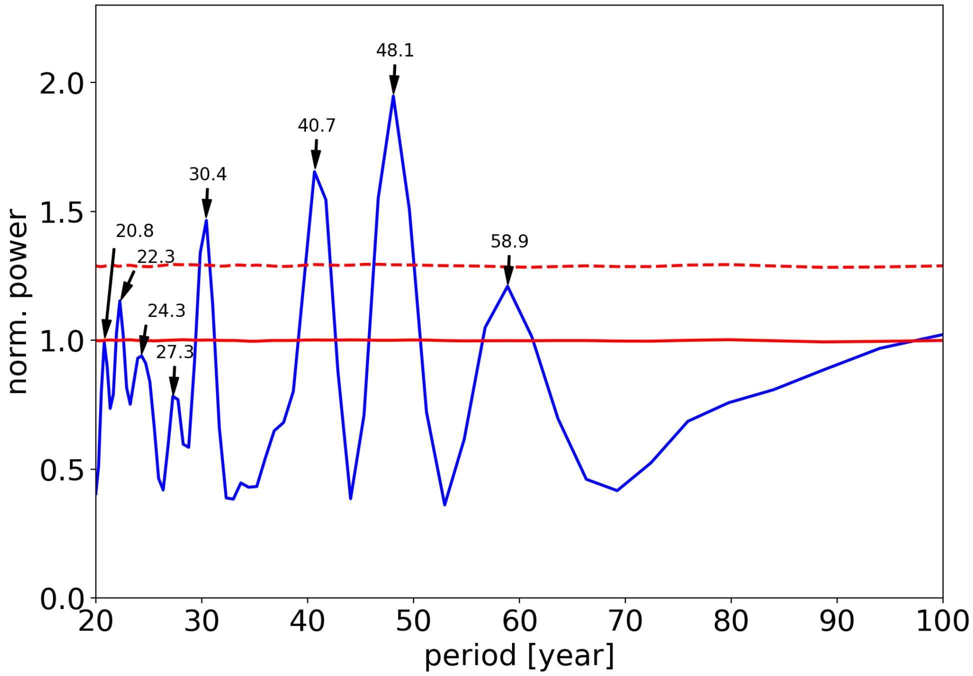

Figure 3.11: Vertically averaged LSP for the ECHAM simulations. The mean LSP over all simulation altitudes is shown as blue curve. The red line shows a mean LSP for independent Gaussian noise at all altitudes and the red dashed line shows this mean plus 2σ. The figure is taken from Offermann et al. (2021).

atures themselves, which would have a cancelling effect. At distinct periods a clear peak in the averaged LSP is visible (periods are given with numbers in Fig. 3.11). In the case of independent Gaussian noise at the different altitudes one would expect that the signals cancel each other. This is shown with the red line which shows the mean result from 10000 random representations. One of these representations simulated one atmosphere with its 47 altitude layers (same number as in the simulations). At each layer noise from a Gaussian distribution was used as temperature data. The vertically averaged LSP was then calculated in the same way as for the ECHAM simulations for each of the 10000 representations. The red line is the mean of all resulting LSPs of these representations and the red dashed line shows the upper 2σ level (for more details see Offermann et al., 2021). At some periods a significant peak is observed in the averaged LSP (e.g. at about 41 and 49 years; compare Fig. 3.10), which shows the existence of an oscillation with this period in a large altitude range. The peak at about 22 years is the largest in the period range from 20 to 30 years but not significant at the 2σ level. This is a consequence of the vertical distribution of this oscillation,

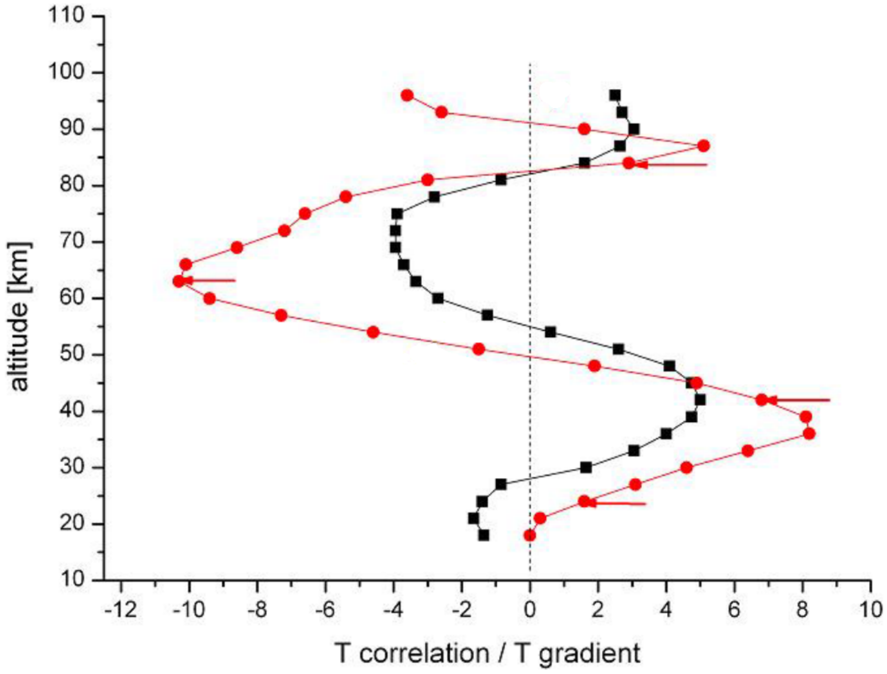

Figure 3.12: Comparison between temperature correlation and vertical temperature gradient. The correlation coefficients (reference level 42 km) are multiplied by 5 and the temperature gradients are approximated by the differences in consecutive temperatures (K per 3 km). The red arrows show the altitudes of the amplitude maxima. The figure is adapted from Offermann et al. (2021).

which does not show a large amplitude in the troposphere and lower stratosphere (compare Fig. 3.10). Since a large number of altitude levels lie in this region, the average over all altitudes certainly weakens. Nonetheless, the quasi-bidecadal oscillation is clearly visible, especially in the vertically resolved result from the stratosphere upwards (see Fig. 3.10). Taking into account the uncertainties and the fact that the time series of the observational data are much shorter, which worsens the resolution, the quasi-bidecadal oscillation observed for the OH(3,1) rotational temperatures and PSH agrees with the findings presented here and in Offermann et al. (2021).

Offermann et al. (2021) also analysed the vertical displacement theory. They used correlations of the temperature time series at single altitude with the reference time series at the altitude level of 42 km. The resulting correlation coefficients are shown in Fig. 3.12 as black squares. In this way a vertical profile showing the regions of correlation (positive correlation coefficient) and anticorrelation (negative correlation coefficient) with respect to the reference level was obtained. A comparison with the vertical temperature gradients, that are displayed as red full circles in Fig. 3.12, shows a large similarity, i.e. the changes from correlation to anticorrelation occur in the region of the change of sign of the vertical temperature gradient. The maximum amplitudes of the oscillations were also observed at the maxima of the vertical temperature gradients (compare arrows in Fig. 3.12). This analysis additionally supports the idea of a vertical displacement as mechanism causing the oscillations. Compared to the former results derived from the measurements, the correlation coefficients show very similar altitude regions that behave in phase and in anti-phase, respectively. Only at the lower altitudes in the troposphere and lower stratosphere still a slight difference is observed. The same difference was already recognised during the comparisons of the vertical phase profiles (see Fig. 3.9).

Offermann et al. (2021) also analysed the seasonal difference of the observed oscillations using the HAMMONIA simulation results. Figure 3.13 shows FFT results for the January and July temperature time series as examples for winter and summer. Obviously, the periods at which oscillations were detected are very similar in both seasons, e.g. large amplitudes can be seen at a period of about 20 years in both cases. The vertical structure of the amplitudes is largely different. In winter the amplitudes at altitudes above about 80 km are very small or virtually non-existent. In summer the situation is completely opposite. Here, only above 80 km oscillations with larger amplitudes were observed. Furthermore, the maximum amplitudes are larger in winter than in summer. A difference between summer and winter was already observed during the analysis of the OH(3,1) rotational temperatures. Kalicinsky et al. (see 2018) showed that the amplitude of the quasi-bidecadal oscillation observed for the OH(3,1) rotational temperatures is nearly twice as large in summer than in winter. This is in very good agreement with the results for the HAMMONIA simulations. In the altitude region around 87 km and at a frequency smaller than 0.05 year^{-1} (period larger than 20 years) also significantly larger amplitudes are observed in summer compared to winter. In this case the temperature profile likely is the most important cause, as the lowest temperatures in the mesopause region occur in summer and, thus, the gradient change is most clear and pronounced at this time.

The simulations used in the presented studies were carried out under special conditions. The most important external influences such as the solar activity, the ocean, and the greenhouse gases had constant boundary conditions in the case of the HAMMONIA simulations (see Offermann et al., 2015) and the ECHAM simulations (see Offermann et al., 2021), i.e. no long-term changes of green house gas concentration, sea surface temperatures, abd solar radiation. This means that these external sources cannot act as a driver for long-term changes

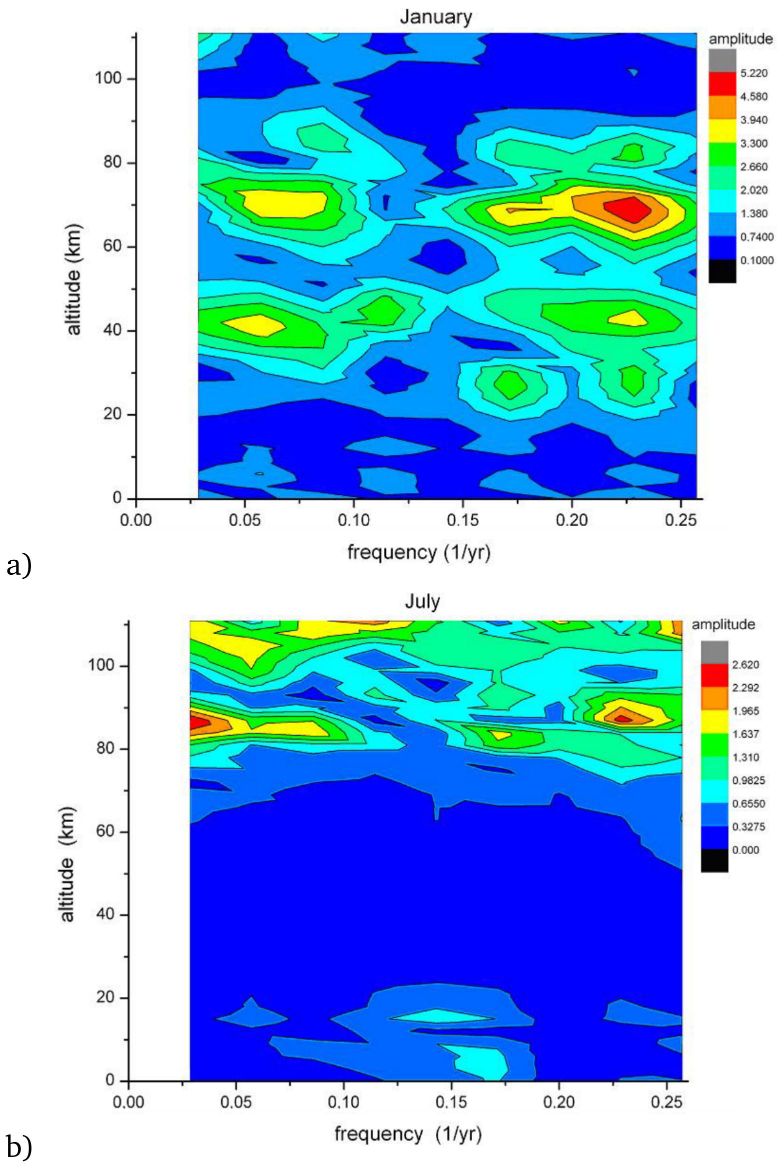

Figure 3.13: Comparisons between FFT results for summer and winter. a) Vertically resolved FFT results for winter (January) simulations results of HAMMONIA. b) Vertically resolved FFT results for summer (July) simulation results. The figures are taken from Offermann et al. (2021).

and periodic variations as observed for the simulated atmospheric temperatures. Hence, one might think about self-excited oscillations here. However, a possible excitation by land surface processes is possible (Offermann et al., 2021). Also interactions between these possible self-excited oscillations and a matching external forcing (same or nearly same period) are imaginable which then may lead to a synchronisation of the internal and external variabilities. In this way oscillations in the atmosphere at some periods may enhance in amplitude whereas oscillations at other periods do not (Kalicinsky et al., 2018). A complete analysis of such interactions will be a future subject of research and rely on model simulations with different boundary conditions for all different possible external forcing, which will be a huge effort.

3.2. Short-term temperature variations

3.2.1. Planetary waves

One typical type of short-term temperature variations observed in the mesopause region is a variation with a period larger than 1 day up to a few months. Such a variation appears as (periodic) variation around the fit curve describing the seasonal variations (annual, semi-annual, and ter-annual cycle) of the OH(3,1) rotational temperatures (see Fig. 3.14a). The observed temperature variations in this period range are likely connected to planetary waves that are typically excited in the lower atmosphere and propagate upwards (see e.g. Holton, 1984; Smith, 2003; Espy et al., 2005; Murphy et al., 2007; Vincent, 2015; Zhao et al., 2019, and references therein). The moving LSP approach (described in Sect. 2.2.4) is an excellent method to analyse the residuals of OH(3,1) rotational temperatures (data minus seasonal fit; see Sect. 2.2.1) and detect such periodic variations.
An example is shown in Fig. 3.14. Figure 3.14a shows the OH(3,1) rotational temperatures of the year 1989 together with the fit of the seasonal variations and the resulting residual temperatures. Figure 3.14b shows the moving LSP results for these residual temperatures. Several significant periodic fluctuations are detected for this year as marked with the white contour lines. For example, an oscillation with a period of about 40 days and an amplitude of 5 to 7 K was observed at the beginning of the year. Furthermore, there are significant oscillations with a period of about 50 days around day 250, with a period of about 10 days around day 300, and with a period of about 16 days around day 300. The amplitudes here reach values of up to 5 K. The same year has already been analysed by Bittner et al. (2000) using the maximum entropy method to assimilate data gaps and a wavelet transform to detect the significant fluctuations. The significant periodic fluctuations presented here and in Kalicinsky et al. (2020) are also clearly observed by Bittner et al. (2000) using a different method. This agreement between the results obtained with fairly different methods give additional confidence in two aspects. First, the presented results are real and no artefacts are

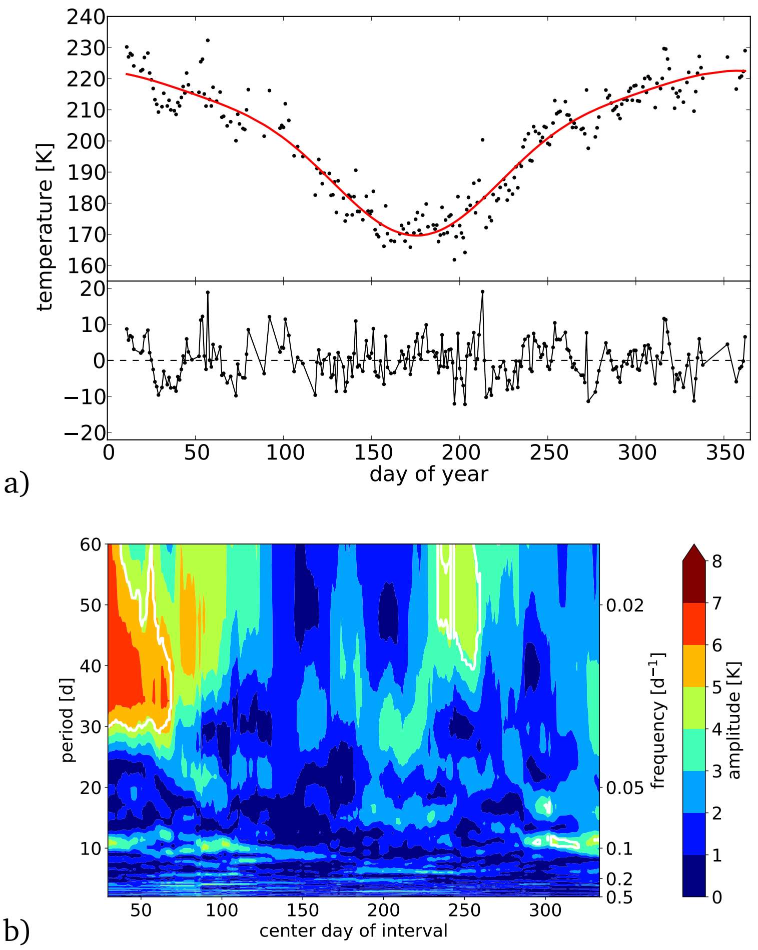

Figure 3.14: GRIPS-II OH(3,1) rotational temperatures of 1989 and moving LSP result of the temperature residual. a) The GRIPS-II OH(3,1) rotational temperatures are shown as black curve and the fit of the seasonal variations is shown as red curve. In the lower panel the resulting residual when subtracting the fit from the data is displayed. b) The amplitudes o f the moving LSP result are shown colour coded and the white lines mark the significant results. The time window used for the analysis is 60 d and the results are shown at the centre days of these windows. The figure a) is taken from Kalicinsky et al. (2020) and figure b) is adapted from Kalicinsky et al. (2020)

caused by one of the methods. Second, the new approach is well suited to derive information on the periodicities contained in data series. In contrast to the procedure used by Bittner et al. (2000), this new approach does no longer need data preprocessing, that may introduce unwanted effects. The moving LSP approach can handle the data set as it is, including data gaps. This is a large improvement with respect to the time consumption of the analysis and leads to a reduction of possible error sources.

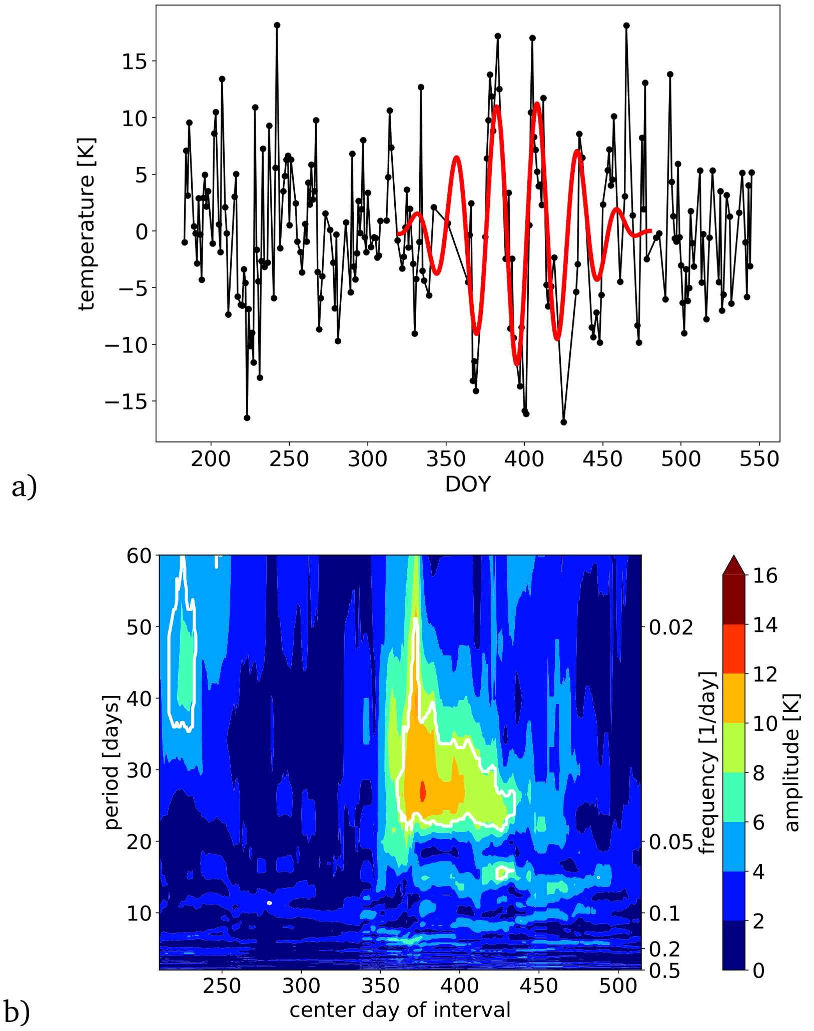

Figure 3.15: Observation of temperature fluctuation with large amplitude in winter 1997/1998 . a) The temperature residual after subtracting the seasonal variations is shown as black curve. The red curve shows a fit to the middle of the data series. Details see text. b) Moving LSP result for the winter 1997/1998. The time window used for the analysis is 60 d and the results are shown at the centre days of these windows. The count of the days start at the beginning of 1997. The amplitude is shown colour coded and the white lines mark the significant results.

The moving LSP approach can now be used to quickly analyse time series with respect to periodic fluctuations. A prominent example of such a periodic fluctuation is shown in Fig. 3.15. The temperature residual for the winter 1997/1998 (July 1997 – June 1998) after subtracting the seasonal variations is shown as black curve in Fig. 3.15a and the corresponding moving LSP result for these temperatures is depicted in Fig. 3.15b. Obviously, a periodic fluctuation with a period near 26 days is observed in mid-winter. This periodic fluctuation shows a very large amplitude of more than 10 K in the centre. During the complete event the amplitude enlarges from the beginning to a maximum in the centre and then decreases again. This behaviour is shown with a fit to the residual temperatures in Fig. 3.15a. The fit curve is shown in red and consists of two parts. Firstly, a sinusoid with constant period describes the periodic variation with time. Secondly, a $\sin^2$ term at a second constant period is used to account for the modulation of the amplitude. The period of the main oscillation is about 26 days and the maximum amplitude is about 12 K. The fit curve nicely resembles the behaviour of the temperature residual in mid-winter 1997/1998. A very similar temperature behaviour was observed by Zhao et al. (2019) for OH(3,1) temperature measurements over Antarctica in austral winter 2014. The authors additionally used satellite observations from the stratosphere up to the lower thermosphere to further investigate the observed temperature fluctuations. The main characteristics and global structure of the observed event are consistent with the 28-day Rossby wave. The observations of the OH(3,1) rotational temperatures at Wuppertal in the winter 1997/1998 may be a similar phenomenon and also related to the 28-day Rossby wave. But further investigations and supporting data are necessary to proof this hypothesis.

Besides the analysis of events restricted in time such as the shown wave events, it is also possible to analyse the temporal evolution of the planetary wave activity. The standard deviation of the temperature residuals can be used as a proxy for the planetary wave activity. After subtracting the seasonal variations from the temperature time series the remaining temperature variations can be seen as, at least partly, caused or largely influenced by planetary scale waves (e.g. Bittner et al., 2000; Offermann et al., 2006; Höppner and Bittner, 2007). Höppner and Bittner (2007) already showed that the standard deviations follow a long-periodic behaviour similar to the Hale cycle, thus, they exhibit a quasi-bidecadal oscillation. Kalicinsky et al. (2016) also repeated parts of this analysis in the course of their study. The main results are shown in Fig. 3.16 (not presented in Kalicinsky et al. (2016)). Figure 3.16a shows the change in the yearly standard deviations of the temperature residuals (standard deviations minus mean value). The temperature residuals and, thus, the standard deviations are determined for each year separately. Obviously, the standard deviations show a clear long-term behaviour and some fluctuations with periods of a few years. Figure 3.16b shows the LSP of the standard deviations to analyse the periodicities. In the long-periodic range larger than 10 years only one clear peak at about 20 years is visible. In the range below 10 years some more peaks can be seen, for example at about 2.5 years. This period range showing

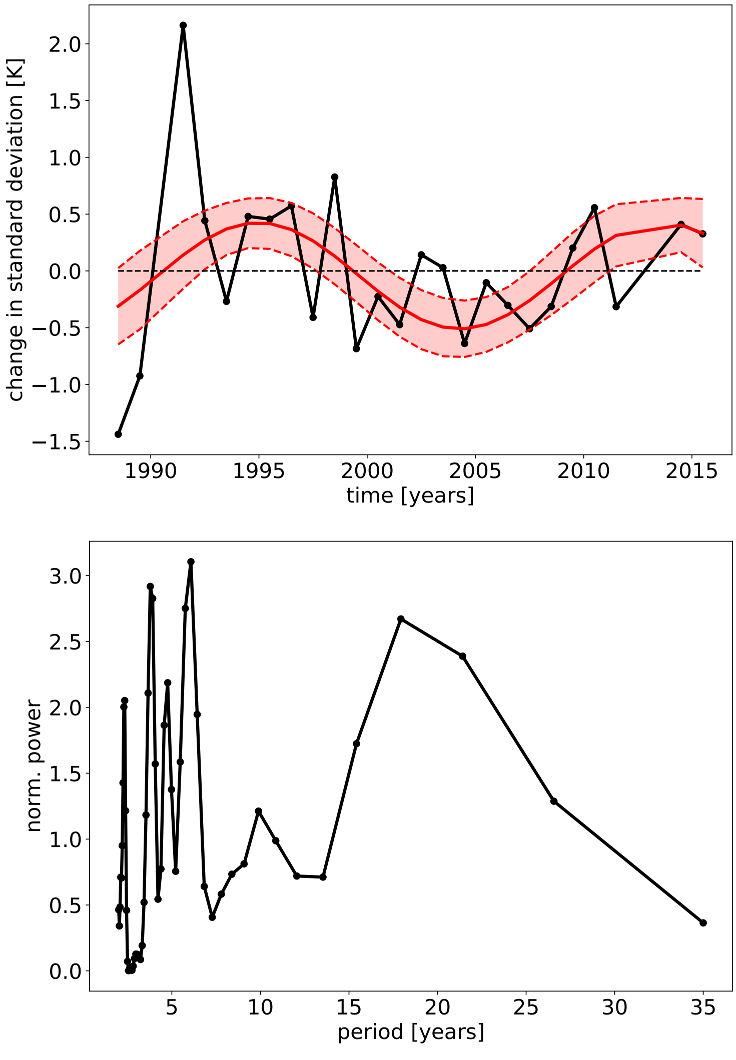

Figure 3.16: Temporal evolution of the planetary wave activity in the time interval 1988 – 2015. a) The change in the yearly standard deviation of the temperature residuals (data minus seasonal fit) is shown as black curve. The red curve shows a sinusoid fitted to the data series and the reddish area marks the 1σ uncertainty of the fit. b) LSP of the standard deviation changes.

a quasi-biennial oscillation has already been discussed by Bittner et al. (2000) and Höppner and Bittner (2007). Here, the focus is on the longest period of about 20 years. A fit to the standard deviations lead to the results for the period of about 19 years (18.6 ± 2.9 years) and an amplitude of about 0.5 K (0.47 ± 0.20 K). The fit is shown as red curve in Fig. 3.16a. The determined period agrees within the combined uncertainties with the period determined for the OH(3,1) rotational temperatures (see Sect. 3.1.3). Especially at the beginning of the time series the standard deviations are either very high in the year 1991 or low in the years 1988 and 1989 compared to the other years. The reason for this is unknown, but in the year 1991 the eruption of Mt Pinatubo could have had an influence. However, the derived period slightly differs when the year of the Mt Pinatubo eruption is excluded from the analysis. Without the first three years a period that is two years larger is determined and, thus, it is even closer to the period of the temperature oscillation. Besides the agreement of the period, the phase of the oscillations observed for the standard deviations and the OH(3,1) rotational temperatures agree well. Both show a maximum in beginning to mid-1990s and a minimum in mid to end of the 2000s.

The sensitivity to the way of calculating the standard deviations was also tested. Shown are the standard deviations for the complete temperature residual in each year. Because of the data gaps in the time series and to avoid a possible bias to times with a denser sampling, one can also calculate standard deviations on a monthly basis. The yearly standard deviation is then the mean of this monthly values. This has possibly an effect on single monthly standard deviations when the number of observations in a month is very low. To avoid a larger impact on the yearly mean a weight considering the number of observations is considered in the calculation of the mean (compare Offermann et al., 2006). The results of all three different ways (complete year, weighted and non-weighted yearly mean of monthly means) agree very well for the determined periods, amplitudes and phases of the oscillations. Thus, an influence of the calculation of the standard deviations on the periodicity can be excluded.

3.2.2. Gravity waves

In addition to planetary waves also other type of waves with shorter periods can be analysed with the OH(3,1) rotational temperatures. For this purpose the single observations are necessary instead of the nightly mean observations, that have been used to detect planetary waves. These observations during a night include observations of different types of waves, e.g gravity waves. Offermann et al. (2011) used the standard deviation of the temperatures during a night as a measure for the gravity wave activity. A similar procedure was already done in previous studies in the 1990s by Fetzer and Gille (1994) and Wu and Waters (1996). The nightly standard deviations contain different contributions: some noise (instrument and atmosphere), the contribution of gravity waves and dissipating gravity waves, and possibly tides and very fast planetary waves (Offermann et al., 2011). In their study Offermann et al. (2011) compared the standard deviations to FFT results. These FFT results were calculated for separated 21 min windows during the night in the period range between 2.6 and 20.8

min (the two end points of the spectra were not used). From the FFT results an equivalent standard deviation was calculated to express the amplitudes of the short-period waves (periods 3 - 10 min) in terms of one single parameter. A comparison between the two standard deviations showed that the short-period fluctuations show the same behaviour during the course of a year and for the whole time interval used for the study (mid-1994 to end-2009). In a correlation analysis of both standard deviations it turned out that the short-period fluctuations contribute to a large extent (up to 40%) to the complete standard deviation of a night. Thus, the simply calculated nightly standard deviation is a good proxy for short-period waves. This is in accordance with other observations. Short-period waves have been intensively studied using airglow imagers in the years before (e.g. Hecht, 2004; Hecht et al., 2007; Medeiros et al., 2007; Nielsen et al., 2009, and references therein). Two different major types of waves have been identified: bands and ripples. The band structures are larger than ripples with periods of about 4 – 40 min compared to 3 – 10 min (Hecht, 2004). Also the origin is different: 1) band structures show gravity waves travelling from the lower atmosphere to the mesosphere; 2) ripples originate from interactions of wind shears with gravity waves that lead to Kelvin-Helmholtz instabilities or from convective instabilities (for more details see Offermann et al., 2011, and references therein). Thus, the ripples indicate dissipating gravity waves. The FFT spectra (3–10 min) include contributions of both and, thus, the nightly standard deviations show also both gravity waves and dissipating gravity waves. Offermann et al. (2011) also analysed the seasonal variations of the wave activity. The monthly means of the nightly standard deviations are shown as black curve in Fig. 3.17. The main result was that the seasonal cycle of the nightly standard deviations show two clear maxima, one in spring and one in autumn. Both maxima are located shortly before the circulation turn around in the stratosphere and mesosphere. This is in good agreement with model simulations for turbulent eddy coefficients K_{ZZ} (red dots in Fig. 3.17) that indicate wave dissipation, which leads to eddy diffusion of potential temperature and constituents (more details are given in Offermann et al., 2011). The correspondence of the standard deviations and the eddy coefficients additionally suggest that the nightly standard deviations are related to both gravity waves and dissipating gravity waves. Certainly, also longer-period (gravity) waves contribute to the complete standard deviation. The third curve in Fig. 3.17 shows the turbopause height as derived by Offermann et al. (2011). High amplitudes of gravity waves are expected when the turbopause is low and vice versa. Due to this fact the axis for the turbopause is reversed in Fig. 3.17. Again a good correspondence between all curves can be seen indicating a large wave activity in the months around the turn arounds

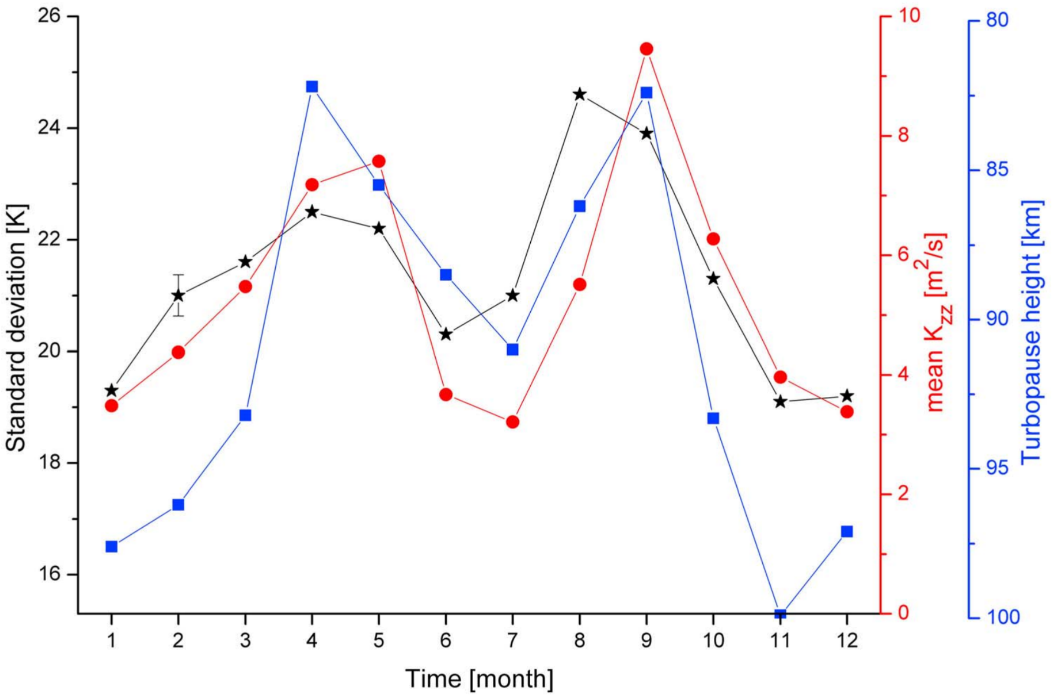

Figure 3.17: Seasonal cycle of the (gravity) wave activity. The monthly means of the nightly temperature standard deviations are shown as black curve at an altitude of approximately 87 km The red curve shows the turbulent eddy coefficients K_{ZZ} as derived by the WACCM 3.5 model. Nineteen years of free model runs have been averaged, and resulting monthly means are shown for 85 km altitude. The blue curve shows the turbopause height (see Offermann et al., 2007). The figure is taken from Offermann et al. (2011).

that lead to enhanced production of turbulence.

In the context of the results presented in the former sections the long-term development of the wave activity is the most important issue. Offermann et al. (2011) analysed this development in the time interval from mid-1994 to end-2009. Figure 3.18 shows the yearly means of the nightly temperature standard deviations as black curve. The results are shown at the beginning of the analysed time intervals, i.e. 01.01.1995 – 31.12.1995 is shown at 1995.0. Additionally, the results for the time intervals shifted by one half year are shown. For the whole time interval an increase of the standard deviation and thus the gravity wave activity can be observed. A linear fit results in a slope of $0.32 \pm 0.13\ \mathrm{K\,year^{-1}}$. Thus, a significant total increase of the activity can be determined. Obviously, a single linear trend is not sufficient to completely describe the long-term development. In the year 2004 a maximum is observed with increasing values before and decreasing values after this maximum. In Fig. 3.18 two single lines are fitted to the different time intervals 1994 – 2004 and 2004 – 2009. The

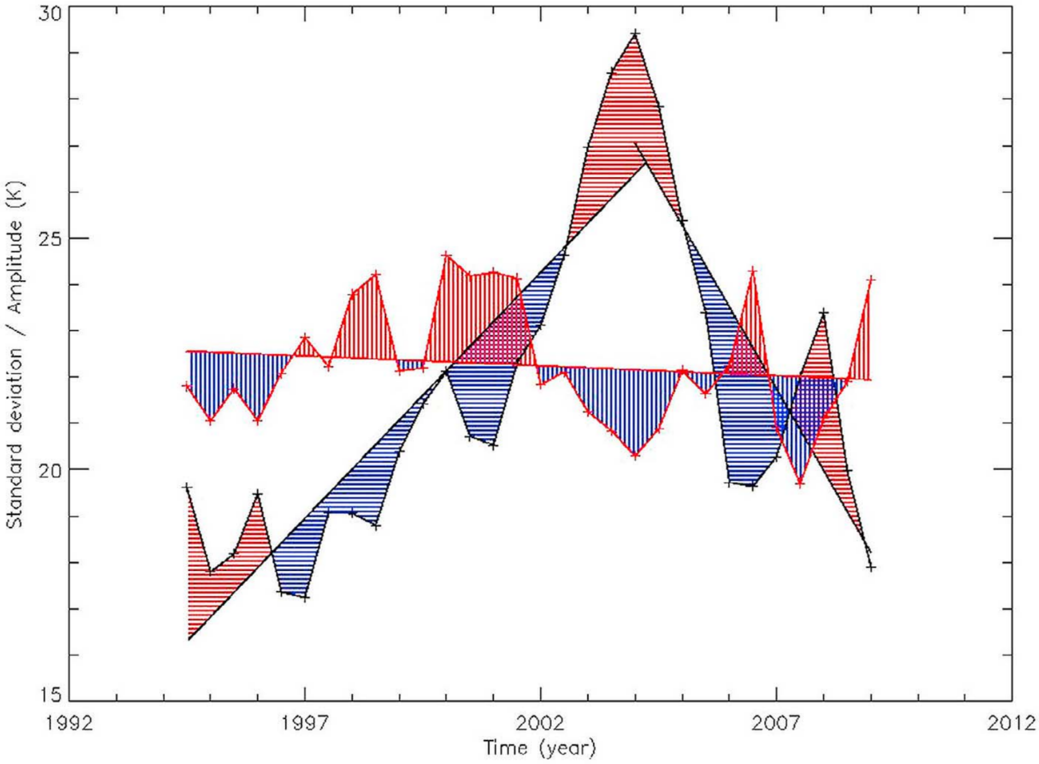

Figure 3.18: Long-term development of short-period (gravity) wave activity. The yearly means of the nightly temperature standard deviations are shown as black curve. The data points are displayed at the beginning of the analysed time intervals, i.e. 01.01.1995 – 31.12.1995 is shown at 1995.0. The red curve shows the amplitudes of the annual cycle determined with the seasonal fit. To obtain an increased resolution the time intervals have additionally been shifted by one half year. The straight lines show linear fits to the data series and the residuals to these lines are shaded red when positive and blue when negative. The figure is taken from Offermann et al. (2011).

obvious trend break is surprisingly very similar to the trend break or oscillation observed for the OH(3,1) rotational temperatures and the planetary wave activity but with opposite phase. The temperature oscillation/trend break shows a minimum in the mid to end-2000s (compare e.g. Fig. 3.3 and Fig. 3.5) and also the planetary wave activity shows a minimum in mid-2000s (compare Fig. 3.16 a). This is a remarkable correspondence between these different atmospheric parameters that is not fully understood until now. Likely there are interconnections between the gravity waves influencing the circulation and related parameters and the temperatures changes possibly influencing circulation and winds and therefore wave filtering.

The red curve in Fig. 3.18 shows the amplitude of the annual cycle derived using the seasonal fit. The behaviour of this curve is somehow opposite to that of the wave activity. The complete trend is negative with a slope of -0.042 $\mathrm{K\,year^{-1}}$. In Fig. 3.18 the areas between the displayed fits and the original data were filled with red when above the line and with blue when below. The blue and red areas for the standard deviations and the amplitudes are also opposite to each other, i.e. a wave activity larger than the fit (red area) corresponds to a amplitude lower than the fit (blue area). The correspondence of this two parameters can likely be explained by changes of the mesospheric circulation that is driven by gravity waves. A variation of the gravity wave activity leads to a change of the circulation. This circulation change can also be observed in radar wind observations at Juliusruh (Keuer et al., 2007). The good correspondence between the gravity wave activity and the zonal wind speed illustrates the influence of the gravity waves on the circulation (see Offermann et al., 2011, for more details). Consequently, the amplitude of the seasonal cycle changes too, as this parameter and the seasonal cycle as a whole is largely influenced by the circulation in the mesosphere.

4. Summary and discussion

The two main parts of the long-term behaviour of the OH(3,1) rotational temperatures are the sensitivity to the 11-year cycle of solar activity and a quasi-bidecadal oscillation. The sensitivity of the OH(3,1) rotational temperatures to the 11-year solar cycle is in Wuppertal still the same as in other previous studies of the Wuppertal time series and shows a large stability with time. Kalicinsky et al. (2016, 2018) derived a value of about 4 ± 1 K (100SFU)$^{-1}$, which is in good agreement with previous studies for the Wuppertal time series (e.g. Offermann et al., 2010) and also other observations at other locations (e.g. Beig, 2011b). Recent studies still show very similar results of sensitivities in the range between 3 and 5 K (100SFU)$^{-1}$ (see French et al., 2020, and references therein) and therefore confirm the results for the Wuppertal OH(3,1) rotational temperatures.

Besides the sensitivity to the 11-year cycle of solar activity, Kalicinsky et al. (2016, 2018) observed a quasi-bidecadal oscillation as second major part of the long-term variability. In contrast to this, in other studies analysing mesopause temperatures typically only one long-term linear trend is determined (e.g. French et al., 2020, and references therein). Kalicinsky et al. (2016) also derived a linear trend in their study and observed a large change of the value compared to the previous study, because the longer time interval now includes also the increasing part of the oscillation (-0.089 K decade^{-1} in 1988 – 2015 (Kalicinsky et al., 2016) compared to -2.3 K decade^{-1} in 1988 – 2008 (Offermann et al., 2010)). Both values are in good agreement with other previous studies (e.g. Beig, 2011a, and references therein) and also recent studies that have been published in the last years (e.g. French et al., 2020, and references therein). All studies report on values between no or not significant trend and a trend of -3 K decade^{-1}. Due to the oscillation a trend-break was observed in about 2008, i.e. the trend before this date is negative and positive afterwards. Such a trend-break is not often reported in the recent literature and, to my knowledge, the observation of a quasi-bidecadal oscillation of temperatures in the mesopause region at the Wuppertal station was the first publication showing this result. However, many of the other studies are either located in another hemisphere or they do not cover the complete year but only winter observations where the oscillation is much weaker. Hence, the observation of such a long-periodic oscillation can be very difficult or even not possible.

In a few recent publications a trend-break or change is reported (Perminov et al., 2018; Yuan et al., 2019). Yuan et al. (2019) analysed LIDAR observations at Fort Collins and Logan (USA) in the time interval 1990 – 2018. They observed a large negative trend when the complete time interval is analysed, but the trend becomes statistically insignificant when only the time after 2000 is considered. Thus, the linear trend is different in the last years compared to the beginning of the time series. The authors argument that the eruption of Mt Pinatubo in June 1991 influenced the trend in the first part of the observation interval (the effect disappeared after 2000), because the episodic warming in the beginning of the 1990s (see She et al., 1998, 2015, for details) led to a larger negative trend. This large and long-lasting effect of the Mt. Pinatubo is at least questionable as, to my knowledge, the LIDAR temperature time series is the only time series that observes such a huge temperature effect in the mesopause region (about 9 K at 86 km and about 13 K at 100 km) with a maximum in 1993 that is potentially caused by the Mt Pinatubo eruption (She et al., 1998). Other studies of the volcanic effect in the altitude region below 80 km by Keckhut et al. (1995) and at about 100 km by Thulasiraman and Nee (2002) showed half as large temperature increases and only in the years 1992 and 1993. In a very recent study by Wallis et al. (2022) the authors analysed HALOE temperature observations with respect to the temperature behaviour after the Mt Pinatubo eruption. This data suggest a more rapid reaction of the mesopause temperatures and a smaller total effect that disappears faster than seen by She et al. (1998, 2015). Wallis et al. (2022) also performed model simulations that show the strongest response about half a year after the eruption and nearly no effect after 2 years.

Perminov et al. (2018) analysed OH rotational temperatures observed at Zvenigorod (Russia) in the time interval 2000 – 2016. Compared to their previous study of the time series that considered the time interval 2000 – 2012 (Perminov et al., 2014) they observed a largely reduced linear trend of only -0.7 K decade^{-1} instead of -2.2 K decade^{-1}. Thus, including the data of the last years led to a reduction of the negative trend. This is exactly the same phenomenon as it was observed for the Wuppertal OH(3,1) rotational temperatures and it can only be explained by a trend-break or a long-periodic oscillation. Perminov et al. (2018) also stated that a consideration of long-periodic oscillations with periods of more than two decades is probably more useful than a single linear trend. In a very recent study Perminov et al. (2021) found a quasi-bidecadal oscillation in the OH(6,2) intensities observed from Zvenigorod that show a similar behaviour to the OH(3,1) rotational temperatures at Wuppertal. Hence, other authors picked up the results by Kalicinsky et al. (2016, 2018) and confirmed the existence of a quasi-bidecadal oscillation in atmospheric parameters in the mesopause region.

By means of additional data, namely the time series of PSH, Kalicinsky et al. (2018) showed that the temperature behaviour above and below the temperature minimum in the summer mesopause region is opposite to each other, i.e. when the OH(3,1) rotational temperatures increase the PSH decrease and vice versa. They proposed a periodic vertical displacement as mechanism for this anticorrelated temperature behaviour in regions with opposite vertical temperature gradient. Such a vertical displacement can be explained with shrinking/contraction or expansion of the atmosphere. As Yuan et al. (2019) stated, a contraction of the stratosphere and mesosphere guides the large negative gradient in the mesosphere to lower altitudes which causes a cooling at constant geometric altitude. However, the authors do not report a significant downward movement of the low mesopause (LM) (130 ± 160 m decade^{-1}) with respect to the long-term behaviour, i.e. the summer mesopause at about 87 km stays almost around a constant altitude in the last three decades or it moves down at slow pace. Lübken et al. (2013) simulated a slightly larger decrease of the pressure heights at 82 km and 92 km of about 600 – 800 m from 1980 to 2009. The downward movement of the summer mesopause seen in the SABER temperature observations of about 2 km in one decade (2002/06 – 2012/16; see Fig. 3.6 and Sec. 3.1.4) is much larger than these observed and simulated long-term downward movements. Thus, the long-term downward movement is probably not enough to explain this observed decrease of about 2 km. Likely, there is an additional overlaying process. A cooling of the stratosphere and mesosphere is typically assigned to increasing CO_2 concentrations in the atmosphere and, additionally, to contributions of other species such as O_3 (e.g. Laštovička and Bremer, 2004; Berger and Lübken, 2011; Laštovička et al., 2012; Qian et al., 2013; Lübken et al., 2013, and references therein). Peters et al. (2017) showed by means of the radio reflection height observations, which are used to derive the PSH, that the complete mesosphere cools over the last decades. A slight cooling of the upper mesosphere can also be seen in the PSH time series where a little decrease over the whole time period is indicated, but the fluctuations caused by the quasi-bidecadal oscillation prevail (compare Fig. 3.5). However, the OH(3,1) rotational temperature observations do not show an additional linear trend. As the CO_2 increase does not show any periodic behaviour, this can be excluded as source for the quasi-bidecadal oscillation. The same is true for the O_3 impact on the temperatures. Additionally, the fact that the quasi-bidecadal oscillation can be derived from surface observations (e.g. Wei et al., 2015, 2019; Offermann et al., 2021) is not compatible with a CO_2 increase, because this increase would have an opposite effect in the troposphere than in the stratosphere and mesosphere. Hence, it cannot cause a periodic contraction and expansion of the whole atmosphere which would explain the observed structure of the oscillation. Concluding, the process causing the quasi-bidecadal oscillation has to be an overlaying process which source is not completely known. A self-excited oscillation is possible since the oscillation is also observed in simulations with constant boundary conditions.

Besides the quasi-bidecadal oscillation of the temperatures, also the planetary wave activity show this oscillation which is in phase with the temperature oscillation. Furthermore, the gravity wave activity shows a trend-break in about 2004 with increasing activity before and decreasing activity after this date. This is opposite to the behaviour of the temperatures and the planetary wave activity, which both show a minimum in the mid-2000s. A possible connection between the temperature oscillation and the oscillation and trend-break observed in the wave activities is still not known. However, all parameters are connected with each other, since the planetary and gravity waves drive the residual circulations in the stratosphere and mesosphere, respectively (e.g. Andrews et al., 1987; Vincent, 2015). Thus, the wind pattern and the circulation is influenced when the waves change and a change in the upward and downward movement influences adiabatic heating and cooling. Furthermore, the wind direction and speed is crucial for the filtering of waves and thus for the propagation or non-propagation to the upper atmosphere. Lastly, also temperature changes and therefore changes of horizontal temperature gradients can influence the winds in the atmosphere. But with temperature observations alone this connection cannot be completely resolved, but will be subject of future projects.

Bibliography

Adler, R., Gu, G., Sapiano, M., Wang, J.-J., and Huffman, G.: Variations and Trends During the Satellite Era (1979–2014), Surv. Geophys., 38, 679–699, doi:10.1007/s10712-017-9416-4, 2017.

Andrews, D., Holton, J., and Leovy, C.: Middle atmosphere dynamics, Academic Press, London, 1987.

Baker, D. J. and Stair Jr., A. T.: Rocket measurements of the altitude distribution of the hydroxyl airglow, Phys. Scripta, 37, 611–622, 1988.

Beig, G.: Long-term trends in the temperature of the mesosphere/lower thermosphere region: 1. Anthropogenic influences, J. Geophys. Res., 116, doi:10.1029/2011JA016646, 2011a.

Beig, G.: Long-term trends in the temperature of the mesosphere/lower thermosphere region: 2. Solar response, J. Geophys. Res., 116, doi:10.1029/2011JA016766, 2011b.

Berger, U. and Lübken, F.-J.: Mesospheric temperature trends at mid-latitudes in summer, Geophys. Res. Lett., 38, doi:10.1029/2011GL049528, 2011.

Bittner, M., Offermann, D., and Graef, H. H.: Mesopause temperature variability above a midlatitude station in Europe, J. Geophys. Res., 105, 2045–2058, doi:10.1029/1999JD900307, 2000.

Bittner, M., Offermann, D., Graef, H. H., Donner, M., and Hamilton, K.: An 18-year time series of OH* rotational temperatures and middle atmosphere decadal variations, J. Atmos. Sol. Terr. Phy., 64, 1147–1166, doi:10.1016/S1364-6826(02)00065-2, 2002.

Bosilovich, M. G., Lucchesi, R., and Suarez, M.: MERRA-2: File Specification, `http://gmao.gsfc.nasa.gov/pubs/office_notes`, GMAO Office Note No. 9 (Version 1.1), 2016.

Bovensmann, H., Burrows, J. P., Buchwitz, M., Frerick, J., Noël, S., Rozanov, V. V., Chance, K. V., and Goede, A. P. H.: SCIAMACHY: Mission Objectives and Measurement Modes, J. Atmos. Sci., 56, 127 – 150, doi:10.1175/1520-0469(1999)056<0127:SMOAMM>2.0.CO;2, 1999.

Clemesha, B., Takahashi, H., Simonich, D., Gobbi, D., and Batista, P.: Experimental evidence for solar cycle and long-term change in the low-latitude MLT region, J. Atmos. Sol.-Terr. Phys., 67, 191–196, doi:10.1016/j.jastp.2004.07.027, 2005.

Coughlin, K. and Tung, K.: 11-Year solar cycle in the stratosphere extracted by the empirical mode decomposition method, Adv. Space Res., 34, 323–329, doi:10.1016/j.asr.2003.02.045, 2004.

Cumming, A., Marcy, G. W., and Butler, R. P.: The lick planet search: detectability and mass thresholds, Astrophys. J., 526, 890–915, doi:10.1086/308020, 1999.

Das, U. and Sinha, H. S. S.: Long-term variations in oxygen green line emission over Kiso, Japan, from ground photometric observations using continuous wavelet transform, J. Geophys. Res., 113, D19 115, doi:10.1029/2007JD00951, 2008.

Egito, F., Buriti, R. A., Fragoso Medeiros, A., and Takahashi, H.: Ultrafast Kelvin waves in the MLT airglow and wind, and their interaction with the atmospheric tides, Ann. Geophys, 36, 231–241, doi:10.5194/angeo-36-231-2018, 2018.

Entzian, G.: Quasi-Phasenmessungen im Langwellenbereich (100–200 kHz) zur indirekten Bestimmung von Plasmaparametern in der Hochatmosphäre (60–90 km), Diss. Univ. Rostock, 1967.

Espy, P. J., Hibbins, R. E., Riggin, D. M., and Fritts, D. C.: Mesospheric planetary waves over Antarctica during 2002, Geophys. Res. Lett., 32, doi:10.1029/2005GL023886, 2005.

Fetzer, E. and Gille, J. C.: Gravity-wave variance in LIMS temperatures. Part I: Variability and comparison with background winds, J. Atmos. Sci., 51, 2461–2483, doi:10.1175/1520-0469(1994)051<2461:GWVILT>2.0.CO;2, 1994.

Fischer, H., Birk, M., Blom, C., Carli, B., Carlotti, M., von Clarmann, T., Delbouille, L., Dudhia, A., Ehhalt, D., Endemann, M., Flaud, J. M., Gessner, R., Kleinert, A., Koopman, R., Langen, J., López-Puertas, M., Mosner, P., Nett, H., Oelhaf, H., Perron, G., Remedios, J., Ridolfi, M., Stiller, G., and Zander, R.: MIPAS: an instrument for atmospheric and climate research, Atmos. Chem. Phys., 8, 2151–2188, doi:10.5194/acp-8-2151-2008, 2008.

French, W. J. R. and Mulligan, F. J.: Stability of temperatures from TIMED/SABER v1.07 (2002–2009) and Aura/MLS v2.2 (2004–2009) compared with OH(6-2) temperatures observed at Davis Station, Antarctica, Atmospheric Chemistry and Physics, 10, 11 439–11 446, doi:10.5194/acp-10-11439-2010, 2010.

French, W. J. R., Mulligan, F. J., and Klekociuk, A. R.: Analysis of 24 years of mesopause region OH rotational temperature observations at Davis, Antarctica – Part 1: long-term trends, Atmos. Chem. Phys., 20, 6379–6394, doi:10.5194/acp-20-6379-2020, 2020.

Fritts, D. C. and Alexander, M. J.: Gravity wave dynamics and effects in the middle atmosphere, Rev. Geophys., 41, doi:10.1029/2001RG000106, 2003.

García-Comas, M., López-González, M. J., González-Galindo, F., de la Rosa, J. L., López-Puertas, M., Shepherd, M. G., and Shepherd, G. G.: Mesospheric OH layer altitude at midlatitudes: variability over the Sierra Nevada Observatory in Granada, Spain (37° N, 3° W), Annales Geophysicae, 35, 1151–1164, doi:10.5194/angeo-35-1151-2017, 2017.

Gelaro, R., McCarty, W., Suárez, M. J., Todling, R., Molod, A., Takacs, L., Randles, C. A., Darmenov, A., Bosilovich, M. G., Reichle, R., Wargan, K., Coy, L., Cullather, R., Draper, C., Akella, S., Buchard, V., Conaty, A., da Silva, A. M., Gu, W., Kim, G.-K., Koster, R., Lucchesi, R., Merkova, D., Nielsen, J. E., Partyka, G., Pawson, S., Putman, W., Rienecker, M., Schubert, S. D., Sienkiewicz, M., and Zhao, B.: The Modern-Era Retrospective Analysis for Research and Applications, Version 2 (MERRA-2), J. Clim., 30, 5419 – 5454, doi:10.1175/JCLI-D-16-0758.1, 2017.

Glatthor, N., Höpfner, M., Leyser, A., Stiller, G. P., von Clarmann, T., Grabowski, U., Kellmann, S., Linden, A., Sinnhuber, B.-M., Krysztofiak, G., and Walker, K. A.: Global carbonyl sulfide (OCS) measured by MIPAS/Envisat during 2002–2012, Atmos. Chem. Phys., 17, 2631–2652, doi:10.5194/acp-17-2631-2017, 2017.

Hall, C. M., Dyrland, M. E., Tsutsumi, M., and Mulligan, F. J.: Temperature trends at 90 km over Svalbard, Norway (78°N 16°E), seen in one decade of meteor radar observations, J. Geophys. Res., 117, doi:10.1029/2011JD017028, 2012.

Hecht, J. H.: Instability layers and airglow imaging, Rev. Geophys., 42, doi:10.1029/2003RG000131, 2004.

Hecht, J. H., Liu, A. Z., Walterscheid, R. L., Franke, S. J., Rudy, R. J., Taylor, M. J., and Pautet, P.-D.: Characteristics of short-period wavelike features near 87 km altitude from airglow and lidar observations over Maui, J. Geophys. Res., 112, 2007.

Holmen, S., Dyrland, M., and Sigernes, F.: Mesospheric temperatures derived from three decades of hydroxyl airglow measurements from Longyearbyen, Svalbard (78°N), Acta Geophys., 62, 302–315, doi:10.2478/s11600-013-0159-4, 2014.

Holton, J. R.: The Generation of Mesospheric Planetary Waves by Zonally Asymmetric Gravity Wave Breaking, J. Atmos. Sci., 41, 3427 – 3430, doi:10.1175/1520-0469(1984)041<3427:TGOMPW>2.0.CO;2, 1984.

Höpfner, M., Deshler, T., Pitts, M., Poole, L., Spang, R., Stiller, G., and von Clarmann, T.: The MIPAS/Envisat climatology (2002–2012) of polar stratospheric cloud volume density profiles, Atmos. Meas. Tech., 11, 5901–5923, doi:10.5194/amt-11-5901-2018, 2018.

Höppner, K. and Bittner, M.: Detection of solar activity signatures in OH* temperature fluctuations possibly related to the differential rotation of the Sun, J. Atmos. Sol.-Terr. Phy., 71, 1287–1292, doi:10.1016/j.jastp.2009.04.008, 2009.

Horne, J. H. and Baliunas, S. L.: A prescription for period analysis of unevenly sampled time series, Astrophys. J, 302, 757–763, 1986.

Höppner, K. and Bittner, M.: Evidence for solar signals in the mesopause temperature variability?, J. Atmos Sol.-Terr. Phys., 69, 431–448, doi:10.1016/j.jastp.2006.10.007, 2007.

Indira Rani, S., Arulalan, T., George, J., Rajagopal, E., Renshaw, R., Maycock, A., Barker, D., and Rajeevan, M.: IMDAA: High-Resolution Satellite-Era Reanalysis for the Indian Monsoon Region, J.Clim., 34, 5109–5133, doi:10.1175/JCLI-D-20-0412.1, 2021.

Jarvis, M.: Planetary wave trends in the lower thermosphere—Evidence for 22-year solar modulation of the quasi 5-day wave, J. Atmos. Sol.-Terr. Phys., 68, 1902–1912, doi:10.1016/j.jastp.2006.02.014, 2006.

Kalicinsky, C., Knieling, P., Koppmann, R., Offermann, D., Steinbrecht, W., and Wintel, J.: Long-term dynamics of OH* temperatures over central Europe: trends and solar correlations, Atmos. Chem. Phys., 16, 15 033–15 047, doi:10.5194/acp-16-15033-2016, 2016.

Kalicinsky, C., Peters, D. H. W., Entzian, G., Knieling, P., and Matthias, V.: Observational evidence for a quasi-bidecadal oscillation in the summer mesopause region over Western Europe, J. Atmos. Sol. Terr. Phys., 178, 7–16, doi:10.1016/j.jastp.2018.05.008, 2018.

Kalicinsky, C., Reisch, R., Knieling, P., and Koppmann, R.: Determination of time-varying periodicities in unequally spaced time series of OH* temperatures using a moving Lomb–Scargle periodogram and a fast calculation of the false alarm probabilities, Atmos. Meas. Tech., 13, 467–477, doi:10.5194/amt-13-467-2020, 2020.

Kalnay, E., Kanamitsu, M., Kistler, R., Collins, W., Deaven, D., Gandin, L., Iredell, M., Saha, S., White, G., Woollen, J., Zhu, Y., Chelliah, M., Ebisuzaki, W., Higgins, W., Janowiak, J., Mo, K., Ropelewski, C., Wang, J., Leetmaa, A., Reynolds, R., Jenne, R., and Joseph, D.: The NCEP/NCAR 40-year reanalysis project, Bull. Am. Meteorol. Soc., 77, 437–471, doi:10.1175/1520-0477(1996)077<0437:TNYRP>2.0.CO;2, 1996.

Keckhut, P., Hauchecorne, A., and Chanin, M. L.: Midlatitude long-term variability of the middle atmosphere: Trends and cyclic and episodic changes, J. Geophys. Res.: Atmos., 100, 18 887–18 897, doi:10.1029/95JD01387, 1995.

Keuer, D., Hoffmann, P., Singer, W., and Bremer, J.: Long-term variations of the mesospheric wind field at mid-latitudes, Ann. Geophys., 25, 1779–1790, doi:10.5194/angeo-25-1779-2007, 2007.

Kim, G., Kim, J.-H., Kim, Y., and Lee, Y.: Long-term trend of mesospheric temperatures over Kiruna (68°N, 21°E) during 2003–2014, J. Atmos. Sol.-Terr. Phys., 161, 83–87, doi:10.1016/j.jastp.2017.06.018, 2017.

King, J.: Sun-weather relationships, Aeronautics and Astronautics, 13, 10–19, 1975.

King, J., Hurst, E., Slater, A., Smith, P., and Tamkin, B.: Agriculture and sunspots, Nature, 252, 131–134, 1974.

Kinnison, D. E., Brasseur, G. P., Walters, S., Garcia, R. R., Marsh, D. R., Sassi, F., Harvey, V. L., Randall, C. E., Emmons, L., Lamarque, J. F., Hess, P., Orlando, J. J., Tie, X. X., Randel, W., Pan, L. L., Gettelman, A., Granier, C., Diehl, T., Niemeier, U., and Simmons, A. J.: Sensitivity of chemical tracers to meteorological parameters in the MOZART-3 chemical transport model, J. Geophys. Res., 112, doi:10.1029/2006JD007879, 2007.

Krassovsky, V. I., Shefov, N. N., and Yarin, V. I.: Atlas of the airglow spectrum 3000–12400 Å, Planetary and Space Science, 9, 883–915, doi:10.1016/0032-0633(62)90008-9, 1962.

Lauter, E.: Mesospheric properties as seen from D-region electron density behaviour, Z. Meteorol., 24, 65–79, 1974.

Laštovička, J. and Bremer, J.: An Overview of Long-Term Trends in the Lower Ionosphere Below 120 km, Surv. Geophys., 25, doi:10.1023/B:GEOP.0000015388.75164.e2, 2004.

Laštovička, J., Solomon, S. C., and Qian, L.: Trends in the Neutral and Ionized Upper Atmosphere, Space Sci. Rev., 168, 113–145, doi:10.1007/s11214-011-9799-3, 2012.

Lomb, N. R.: Least-squares frequency analysis of unequally spaced data, Astrophys. Space Sci., 39, 447–462, 1976.

Luo, Y., Manson, A. H., Meek, C. E., Meyer, C. K., and Forbes, J. F.: The quasi 16-day oscillations in the mesosphere and lower thermosphere at Saskatoon (52° N, 107° W), 1980–1996, J. Geophys. Res., 105, 2125–2138, doi:10.1029/1999JD900979, 2000.

López-González, M., García-Comas, M., Rodríguez, E., López-Puertas, M., Olivares, I., Jerónimo-Zafra, J., Robles-Muñoz, N., Pérez-Silvente, T., Shepherd, M., Shepherd, G., and Sargoytchev, S.: Gravity wave activity in the middle atmosphere from SATI airglow observations at northern mid-latitude: Seasonal variation and comparison with tidal and planetary wave-like activity, J. Atmos. Sol.-Terr. Phys., p. 105329, doi:10.1016/j.jastp.2020.105329, 2020.

Lübken, F.-J., Berger, U., and Baumgarten, G.: Temperature trends in the midlatitude summer mesosphere, J. Geophys. Res.: Atmos., 118, 13,347–13,360, doi:10.1002/2013JD020576, 2013.

Medeiros, A. F., Takahashi, H., Buriti, R. A., Fechine, J., Wrasse, C. M., and Gobbi, D.: MLT gravity wave climatology in the South America equatorial region observed by airglow imager, Ann. Geophys., 25, 399–406, doi:10.5194/angeo-25-399-2007, 2007.

Meinel, A. B.: OH emission band in the spectrum of the night sky. I, Astrophys. J., 111, 555–564, 1950.

Mies, F. H.: Calculated vibrational transition probabilities of OH($X^2\Pi$), J. Molec. Spec., 53 (2), 150–188, doi:10.1016/0022-2852(74)90125-8, 1974.

Mlynczak, M. G.: Energetics of the mesosphere and lower thermosphere and the SABER experiment, Adv. Space Res., 20, 1177–1183, doi:10.1016/S0273-1177(97)00769-2, 1997.

Molod, A., Takacs, L., Suarez, M., Bacmeister, J., Song, I.-S., and Eichmann, A.: The GEOS-5 Atmospheric General Circulation Model: Mean Climate and Development from MERRA to Fortuna, NASA Technical Report Series on Global Modeling and Data Assimilation, NASA TM—2012 -1 04606, Vol. 28, 2012.

Molod, A., Takacs, L., Suarez, M., and Bacmeister, J.: Development of the GEOS-5 atmospheric general circulation model: evolution from MERRA to MERRA-2, Geosci. Model Dev. Discuss., 7, 7575–7617, doi:10.5194/gmdd-7-7575-2014, 2014.

Mulligan, F. J. and Lowe, R. P.: OH-equivalent temperatures derived from ACE-FTS and SABER temperature profiles - a comparison with OH* (3,1) temperatures from Maynooth (53.2°N, 6.4°W), Ann. Geophys., 26, 1–17, doi:10.5194/angeo-26-795-2008, 2008.

Murphy, D., French, W., and Vincent, R.: Long-period planetary waves in the mesosphere and lower thermosphere above Davis, Antarctica, J. Atmos. Sol.-Terr. Phys., 69, 2118–2138, doi:10.1016/j.jastp.2007.06.008, 2007.

Nielsen, K., Taylor, M., Hibbins, R., and Jarvis, M.: Climatology of short-period mesospheric gravity waves over Halley, Antarctica (76°S, 27°W), J. Atmos. Sol.-Terr. Phys., 71, 991–1000, doi:10.1016/j.jastp.2009.04.005, 2009.

Noll, S., Kausch, W., Kimeswenger, S., Unterguggenberger, S., and Jones, A. M.: OH populations and temperatures from simultaneous spectroscopic observations of 25 bands, Atmospheric Chemistry and Physics, 15, 3647–3669, doi:10.5194/acp-15-3647-2015, 2015.

Noll, S., Kausch, W., Kimeswenger, S., Unterguggenberger, S., and Jones, A. M.: Comparison of VLT/X-shooter OH and O_2 rotational temperatures with consideration of TIMED/SABER emission and temperature profiles, Atmos. Chem. Phys., 16, 5021–5042, doi:10.5194/acp-16-5021-2016, 2016.

Nyassor, P. K., Buriti, R. A., Paulino, I., Medeiros, A. F., Takahashi, H., Wrasse, C. M., and Gobbi, D.: Determination of gravity wave parameters in the airglow combining photometer and imager data, Ann. Geophys., 36, 705–715, doi:10.5194/angeo-36-705-2018, 2018.

Oberheide, J., Offermann, D., Russell III, J. M., and Mlynczak, M. G.: Intercomparison of kinetic temperature from 15 μm CO2 limb emissions and OH*(3,1) rotational temperature in nearly coincident air masses: SABER, GRIPS, Geophys. Res. Lett., 33, doi:10.1029/2006GL026439, 2006.

Offermann, D., Donner, M., Knieling, P., and Naujokat, B.: Middle atmosphere temperature changes and the duration of summer, J. Atmos. Sol.-Terr. Phy., 66, 437–450, doi:10.1016/j.jastp.2004.01.028, 2004.

Offermann, D., Jarisch, M., Donner, M., Steinbrecht, W., and Semenov, A.: OH temperature re-analysis forced by recent variance increases, J. Atmos. Sol.-Terr. Phys., 68, 1924–1933, doi:10.1016/j.jastp.2006.03.007, 2006.

Offermann, D., Jarisch, M., Schmidt, H., Oberheide, J., Grossmann, K., Gusev, O., Russell III, J., and Mlynczak, M.: The “wave turbopause”, J. Atmos. Sol. Terr. Phys., 69, 2139–2158, doi:10.1016/j.jastp.2007.05.012, 2007.

Offermann, D., Gusev, O., Donner, M., Forbes, J. M., Hagan, M., Mlynczak, M. G., Oberheide, J., Preusse, P., Schmidt, H., and Russell III, J. M.: Relative intensities of middle atmosphere waves, J. Geophys. Res.: Atmos., 114, doi:10.1029/2008JD010662, 2009.

Offermann, D., Hoffmann, P., Knieling, P., Koppmann, R., Oberheide, J., and Steinbrecht, W.: Long-term trends and solar cycle variations of mesospheric temperature and dynamics, J. Geophys. Res., 115, doi:10.1029/2009JD013363, 2010.

Offermann, D., Wintel, J., Kalicinsky, C., Knieling, P., Koppmann, R., and Steinbrecht, W.: Long-term development of short-period gravity waves in middle Europe, J. Geophys. Res., 116, doi:https://doi.org/10.1029/2010JD015544, 2011.

Offermann, D., Goussev, O., Kalicinsky, C., Koppmann, R., Matthes, K., Schmidt, H., Steinbrecht, W., and Wintel, J.: A case study of multi-annual temperature oscillations in the atmosphere: Middle Europe, J. Atmos. Sol.-Terr. Phys., 135, 1–11, doi:10.1016/j.jastp.2015.10.003, 2015.

Offermann, D., Kalicinsky, C., Koppmann, R., and Wintel, J.: Very long-period oscillations in the atmosphere (0–110 km), Atmos. Chem. Phys., 21, 1593–1611, doi:10.5194/acp-21-1593-2021, 2021.

Perminov, V., Semenov, A., Pertsev, N., Medvedeva, I., Dalin, P., and Sukhodoev, V.: Multi-year behaviour of the midnight OH* temperature according to observations at Zvenigorod over 2000–2016, Adv. Space Res., 61, 1901–1908, doi:10.1016/j.asr.2017.07.020, 2018.

Perminov, V., Pertsev, N., Dalin, P., Zheleznov, Y. A., Sukhodoev, V., and Orekhov, M. D.: Seasonal and Long-Term Changes in the Intensity of O_2 ($b^1\sum$) and OH($X^2\Pi$) Airglow in the Mesopause Region, Geomagn. Aeron., 61, 589–599, doi:10.1134/S0016793221040113, 2021.

Perminov, V. I., Semenov, A. I., Medvedeva, I. V., and Zheleznov, Y. A.: Variability of mesopause temperature from hydroxyl airglow observations over mid-latitudinal sites, Adv. Space Res, 54, 2511–2517, doi:10.1016/j.asr.2014.01.027, 2014.

Peters, D. H. and Entzian, G.: Long-term variability of 50 years of standard phase-height measurement at Kühlungsborn, Mecklenburg, Germany, Adv. Space Res., 55, 1764–1774, doi:10.1016/j.asr.2015.01.021, 2015.

Peters, D. H., Entzian, G., and Keckhut, P.: Mesospheric temperature trends derived from standard phase-height measurements, J. Atmos. Sol.-Terr. Phys., 163, 23–30, doi:10.1016/j.jastp.2017.04.007, 2017.

Qian, L., Marsh, D., Merkel, A., Solomon, S. C., and Roble, R. G.: Effect of trends of middle atmosphere gases on the mesosphere and thermosphere, J. Geophys. Res.: Space Phys., 118, 3846–3855, doi:10.1002/jgra.50354, 2013.

Qu, W., Zhao, J., Huang, F., and Deng, S.: CORRELATION BETWEEN THE 22-YEAR SOLAR MAGNETIC CYCLE AND THE 22-YEAR QUASICYCLE IN THE EARTH'S ATMOSPHERIC TEMPERATURE, Astronom. J., 144, 6, doi:10.1088/0004-6256/144/1/6, 2012.

Reid, I. M., Spargo, A. J., and Woithe, J. M.: Seasonal variations of the nighttime O(1S) and OH(8-3) airglow intensity at Adelaide, Australia, J. Geophys. Res.-Atmos., 119, 6991–7013, doi:10.1002/2013JD020906, 2014.

Roeckner, E., Brokopf, R., Esch, M., Giorgetta, M., Hagemann, S., Kornblueh, L., Manzini, E., Schlese, U., and Schulzweida, U.: Sensitivity of Simulated Climate to Horizontal and Vertical Resolution in the ECHAM5 Atmosphere Model, J. Clim., 19, 3771 – 3791, doi:10.1175/JCLI3824.1, 2006.

Rourke, S., Mulligan, F. J., French, W. J. R., and Murphy, D. J.: A Climatological Study of Short-Period Gravity Waves and Ripples at Davis Station, Antarctica (68°S, 78°E), During the (Austral Winter February–October) Period 1999–2013, J. Geophys. Res.: Atmos., 122, 11,388–11,404, doi:10.1002/2017JD026998, 2017.

Russell III, J. M., Mlynczak, M. G., Gordley, L. L., Tansock Jr., J. J., and Esplin, R. W.: Overview of the SABER experiment and preliminary calibration results, in: Optical Spectroscopic Techniques and Instrumentation for Atmospheric and Space Research III, edited by Larar, A. M., vol. 3756, pp. 277 – 288, International Society for Optics and Photonics, SPIE, 1999.

SABER: SABER Temperature and CO2 Retrieval Accuracies, URL `http://saber.gats-inc.com/temp_errors.php`, 2022.

Scargle, J. D.: Studies in astronomical time series analysis. II. Statistical aspects of spectral analysis of unevenly spaced data, Astrophys. J, 263, 835–853, 1982.

Scherrer, P. H., Wilcox, J. M., Svalgaard, L., Duvall Jr., T. L., Dittmeier, P. H., and Gustafson, E. K.: The mean magnetic field of the sun – Observations at Stanford, Sol. Phys., 54, 353–361, 1977.

Schmidt, C., Höppner, K., and Bittner, M.: A ground-based spectrometer equipped with an InGaAs array for routine observations of OH(3-1) rotational temperatures in the mesopause region, J. Atmos. Sol. Terr. Phys., 102, 125–139, doi:10.1016/j.jastp.2013.05.001, 2013.

Schmidt, H., Brasseur, G. P., Charron, M., Manzini, E., Giorgetta, M. A., Diehl, T., Fomichev, V. I., Kinnison, D., Marsh, D., and Walters, S.: The HAMMONIA Chemistry Climate Model: Sensitivity of the Mesopause Region to the 11-Year Solar Cycle and CO2 Doubling, J. Clim., 19, 3903 – 3931, doi:10.1175/JCLI3829.1, 2006.

Schmidt, H., Brasseur, G. P., and Giorgetta, M. A.: Solar cycle signal in a general circulation and chemistry model with internally generated quasi-biennial oscillation, J. Geophys. Res., 115, doi:10.1029/2009JD012542, 2010.

Schwarzenberg-Czerny, A.: The distribution of empirical periodograms: Lomb–Scargle and PDM spectra, Mon. Not. R. Astron. Soc., 301, 831–840, doi:10.1111/j.1365-8711.1998.02086.x, 1998.

Sedlak, R., Hannawald, P., Schmidt, C., Wüst, S., and Bittner, M.: High-resolution observations of small-scale gravity waves and turbulence features in the OH airglow layer, Atmospheric Measurement Techniques, 9, 5955–5963, doi:10.5194/amt-9-5955-2016, 2016.

She, C. Y., Thiel, S. W., and Krueger, D. A.: Observed episodic warming at 86 and 100 km between 1990 and 1997: Effects of Mount Pinatubo Eruption, Geophys. Res. Lett., 25, 497–500, doi:10.1029/98GL00178, 1998.

She, C.-Y., Krueger, D. A., and Yuan, T.: Long-term midlatitude mesopause region temperature trend deduced from quarter century (1990–2014) Na lidar observations, Ann. Geophys., 33, 363–369, doi:10.5194/angeo-33-363-2015, 2015.

Sivjee, G. G. and Hamwey, R. M.: Temperature and chemistry of the polar mesopause OH, J. Geophys. Res., 92, 4663–4672, 1987.

Smith, A. K.: The Origin of Stationary Planetary Waves in the Upper Mesosphere, J. Atmos. Sci., 60, 3033 – 3041, doi:10.1175/1520-0469(2003)060<3033:TOOSPW>2.0.CO;2, 2003.

Stevens, B., Giorgetta, M., Esch, M., Mauritsen, T., Crueger, T., Rast, S., Salzmann, M., Schmidt, H., Bader, J., Block, K., Brokopf, R., Fast, I., Kinne, S., Kornblueh, L., Lohmann, U., Pincus, R., Reichler, T., and Roeckner, E.: Atmospheric component of the MPI-M Earth System Model: ECHAM6, J. Adv. Model. Earth Sys., 5, 146–172, doi:10.1002/jame.20015, 2013.

Takahashi, H., Shiokawa, K., Egito, E., Murayama, Y., Kawamura, S., and Wrasse, C. M.: Planetary wave induced wind and airglow oscillations in the middle latitude MLT region, J. Atmos. Sol.-Terr. Phy., 98, 97–104, doi:10.1016/j.jastp.2013.03.014, 2013.

Thulasiraman, S. and Nee, J. B.: Further evidence of a two-level mesopause and its variations from UARS high-resolution Doppler imager temperature data, J. Geophys. Res.: Atmos., 107, doi:10.1029/2000JD000118, 2002.

Vargas, F., Swenson, G., and Liu, A.: Evidence of high frequency gravity wave forcing on the meridional residual circulation at the mesopause region, Adv. Space Res., 56, 1844–1853, doi:10.1016/j.asr.2015.07.040, 2015.

Vincent, R. A.: The dynamics of the mesosphere and lower thermosphere: a brief review, Prog. Earth Planet. Sci., 2, doi:10.1186/s40645-015-0035-8, 2015.

von Cossart, G. and Taubenheim, J.: Ein Modell der Mesopausenregion zur Interpretation indirekter Phasenmessungen und zur Abschätzung von Ionosphären- und Neutralgasparametern, Z. Meteorol., 26, 219–230, 1976.

von Cossart, G. and Taubenheim, J.: Indications of a quasi-20-year cycle of middle atmosphere temperatures, Adv. Sp. Res., 6, 73–75, 1986.

von Savigny, C.: Variability of OH(3-1) emission altitude from 2003 to 2011: Long-term stability and the universality of the emission rate–altitude relationship, J. Atmos. Sol. Terr. Phys., 127, 120–128, doi:10.1016/j.jastp.2015.02, 2015.

von Savigny, C., Eichmann, K.-U., Llewellyn, E. J., Bovensmann, H., Burrows, J. P., Bittner, M., Höppner, K., Offermann, D., Taylor, M. J., Zhao, Y., Steinbrecht, W., and Winkler, P.: First near-global retrievals of OH rotational temperatures from satellite-based Meinel band emission measurements, Geophys. Res. Lett., 31, doi:10.1029/2004GL020410, 2004.

von Savigny, C., McDade, I. C., Eichmann, K.-U., and Burrows, J. P.: On the dependence of the OH* Meinel emission altitude on vibrational level: SCIAMACHY observations and model simulations, Atmos. Chem. Phys., 12, 8813 – 8828, doi:10.5194/acp-12-8813-2012, 2012.

Wallis, S., Hoffmann, C. G., and von Savigny, C.: Estimating the impact of the 1991 Pinatubo eruption on mesospheric temperature by analyzing HALOE (UARS) temperature data, Ann. Geophys., 40, 421–431, doi:10.5194/angeo-40-421-2022, 2022.

Wei, M., Qiao, F., and Deng, J.: A Quantitative Definition of Global Warming Hiatus and 50-Year Prediction of Global-Mean Surface Temperature, J. Atmos. Sci., 72, 3281 – 3289, doi:10.1175/JAS-D-14-0296.1, 2015.

Wei, M., Qiao, F., Guo, Y., Deng, J., Song, Z., Shu, Q., and Yang, X.: Quantifying the importance of interannual, interdecadal and multidecadal climate natural variabilities in the modulation of global warming rates, Clim. Dyn., 53, doi:10.1007/s00382-019-04955-2, 2019.

Willet, H.: Recent statistical evidence in support of predictive significance of solar-climatic cycles, Monthly Weather Review, 102, 679–686, 1974.

Wu, D. L. and Waters, J. W.: Gravity-wave-scale temperature fluctuations seen by the UARS MLS, Geophys. Res. Lett., 23, 3289–3292, doi:10.1029/96GL02924, 1996.

Wu, W.-S., Purser, R., and Parrish, D.: Three-dimensional variational analysis with spatially inhomogeneous covariances, Mon. Wea. Rev., 130, 2905–2916, 2002.

Wüst, S., Offenwanger, T., Schmidt, C., Bittner, M., Jacobi, C., Stober, G., Yee, J.-H., Mlynczak, M. G., and Russell III, J. M.: Derivation of gravity wave intrinsic parameters and vertical wavelength using a single scanning OH(3-1) airglow spectrometer, Atmospheric Measurement Techniques, 11, 2937–2947, doi:10.5194/amt-11-2937-2018, 2018.

Wüst, S., Bittner, M., Espy, P. J., French, W. J. R., and Mulligan, F. J.: Hydroxyl airglow observations for investigating atmospheric dynamics: results and challenges, Atmos. Chem. Phys. Disc., 2022, 1–33, doi:10.5194/acp-2022-528, 2022.

Yee, J., Talaat, E., Christensen, A., Killeen, T., Russell III, J., and Woods, T.: TIMED instruments, Johns Hopkins APL Tech. Dig., 24, 156–164, 2003.

Yoshida, S., Tsuda, T., Shimizu, A., and Nakamura, T.: Seasonal variations of 3.0 $\sim$ 3.8-day ultra-fast Kelvin waves observed with a meteor wind radar and radiosonde in Indonesia, Earth Planets Space, 51, 675–684, doi:10.1186/BF03353225, 1999.

Yuan, T., Solomon, S. C., She, C.-Y., Krueger, D. A., and Liu, H.-L.: The Long-Term Trends of Nocturnal Mesopause Temperature and Altitude Revealed by Na Lidar Observations Between 1990 and 2018 at Midlatitude, J. Geophys. Res.: Atmos., 124, 5970–5980, doi:10.1029/2018JD029828, 2019.

Zechmeister, M. and Kürster, M.: The generalised Lomb–Scargle periodogram – A new formalism for the floating-mean and Keplerian periodograms, Astron. Astrophys., 496, 577–584, doi:10.1051/0004-6361:200811296, 2009.

Zhao, Y., Taylor, M. J., Pautet, P.-D., Moffat-Griffin, T., Hervig, M. E., Murphy, D. J., French, W. J. R., Liu, H. L., Pendleton Jr, W. R., and Russell III, J. M.: Investigating an Unusually Large 28-Day Oscillation in Mesospheric Temperature Over Antarctica Using Ground-Based and Satellite Measurements, J. Geophys. Res., 124, 8576–8593, doi:10.1029/2019JD030286, 2019.

A. Appendix

A.1. Contributions to publications

First author

1. **Kalicinsky, C.**, Knieling, P., Koppmann, R., Offermann, D., Steinbrecht, W., and Wintel, J.: Long-term dynamics of OH* temperatures over central Europe: trends and solar correlations, Atmos. Chem. Phys., 16, 15033–15047, https://doi.org/10.5194/acp-16-15033-2016, 2016.

   Contributions: I designed the complete study and I did the complete analysis of the time series. Furthermore, I created all figures shown in the publication and I also wrote the complete first draft of the textual content.

2. **Kalicinsky, C.**, Peters, D. H. W., Entzian, G., Knieling, P., and Matthias, V.: Observational evidence for a quasi-bidecadal oscillation in the summer mesopause region over Western Europe, J. Atmos. Sol.-Terr. Phys., 178, 7–16, https://doi.org/10.1016/j.jastp.2018.05.008, 2018.

   Contributions: I designed the complete study and I did the complete analysis of the different data series, that have been provided by the co-authors. Furthermore, I created all figures shown in the publication and I also wrote the complete first draft of the textual content, except the part describing the plasma scale heights.

3. **Kalicinsky, C.**, Reisch, R., Knieling, P., and Koppmann, R.: Determination of time-varying periodicities in unequally spaced time series of OH* temperatures using a moving Lomb–Scargle periodogram and a fast calculation of the false alarm probabilities, Atmos. Meas. Tech., 13, 467–477, https://doi.org/10.5194/amt-13-467-2020, 2020.

   Contributions: I designed the complete study and conceptualised the new approach, which is presented and tested in the publication. Together with the student assistant Robert Reisch, I performed all necessary simulations and analysed the simulation results. Furthermore, I created all figures shown in the publication and I also wrote the complete first draft of the textual content.

Co-author

4. Offermann, D., Wintel, J., **Kalicinsky, C.**, Knieling, P., Koppmann, R. and Steinbrecht, W.: Long-term development of short-period gravity waves in middle Europe, J. Geophys. Res., 116, D00P07, https://doi.org/10.1029/2010JD015544, 2011.

   Contributions: I performed data processing of the OH(3,1) rotational temperatures for Wuppertal (GRIPS-II) and Hohenpeissenberg (GRIPS-I). In this processing I calculated nightly mean temperatures and corresponding standard deviations individually for each single night (one data file per night with partly different formats) to compile an easy to use data collection of these important parameters. The standard deviations are for example shown in Figs. 5 and 9. Furthermore, they were analysed by Dirk Offermann in more detail and thus used to create further figures. I also created the Fig. 12 of the publication, where I analysed the long-term development of the standard deviations at Wuppertal. Finally, I contributed to the first draft of the textual content describing this figure and to the final textual content of the publication.

5. Offermann, D., Goussev, O., **Kalicinsky, C.**, Koppmann, R., Matthes, K., Schmidt, H., Steinbrecht, W., and Wintel, J.: A case study of multi-annual temperature oscillations in the atmosphere: Middle Europe, J. Atmos. Sol.-Terr. Phy., 135, 1–11, https://doi.org/10.1016/j.jastp.2015.10.003, 2015.

Contributions: I analysed parts of the SABER data to confirm the vertical structure of the results, which have been completely new to us at that moment (not shown in the publication). Furthermore, I contributed to the interpretation of the results and to the final textual content the paper.

6. Offermann, D., **Kalicinsky, C.**, Koppmann, R., and Wintel, J.: Very long-period oscillations in the atmosphere (0–110 km), Atmos. Chem. Phys., 21, 1593–1611, https://doi.org/10.5194/acp-21-1593-2021, 2021.

   Contributions: I performed the analysis of the temperature data using the Lomb-Scargle periodogram (LSP). The main results are presented in Fig. 8, which I created for the publication. I also wrote a first draft of textual content to this LSP part. Furthermore, I analysed the data using the LSP to confirm the FFT results presented in the paper in Fig. 7 (not shown in the publication). Finally, I contributed to the interpretation of the results and to the final textual content the paper.

Atmos. Chem. Phys., 16, 15033–15047, 2016
www.atmos-chem-phys.net/16/15033/2016/
doi:10.5194/acp-16-15033-2016

Atmospheric Chemistry and Physics
Open Access

Long-term dynamics of OH* temperatures over central Europe: trends and solar correlations

Christoph Kalicinsky[1], **Peter Knieling**[1], **Ralf Koppmann**[1], **Dirk Offermann**[1], **Wolfgang Steinbrecht**[2], and **Johannes Wintel**[1]

[1]Institute for Atmospheric and Enviromental Research, University of Wuppertal, Wuppertal, Germany
[2]DWD, Hohenpeissenberg Observatory, Germany

Correspondence to: Christoph Kalicinsky (kalicins@uni-wuppertal.de)

Received: 6 April 2016 – Published in Atmos. Chem. Phys. Discuss.: 7 June 2016
Revised: 26 October 2016 – Accepted: 27 October 2016 – Published: 6 December 2016

Abstract. We present the analysis of annual average OH* temperatures in the mesopause region derived from measurements of the Ground-based Infrared P-branch Spectrometer (GRIPS) at Wuppertal (51° N, 7° E) in the time interval 1988 to 2015. The new study uses a temperature time series which is 7 years longer than that used for the latest analysis regarding the long-term dynamics. This additional observation time leads to a change in characterisation of the observed long-term dynamics.

We perform a multiple linear regression using the solar radio flux F10.7 cm (11-year cycle of solar activity) and time to describe the temperature evolution. The analysis leads to a linear trend of $(-0.089 \pm 0.055)\,\mathrm{K\,year^{-1}}$ and a sensitivity to the solar activity of $(4.2 \pm 0.9)\,\mathrm{K}\,(100\,\mathrm{SFU})^{-1}$ (r^2 of fit 0.6). However, one linear trend in combination with the 11-year solar cycle is not sufficient to explain all observed long-term dynamics. In fact, we find a clear trend break in the temperature time series in the middle of 2008. Before this break point there is an explicit negative linear trend of $(-0.24 \pm 0.07)\,\mathrm{K\,year^{-1}}$, and after 2008 the linear trend turns positive with a value of $(0.64 \pm 0.33)\,\mathrm{K\,year^{-1}}$. This apparent trend break can also be described using a long periodic oscillation. One possibility is to use the 22-year solar cycle that describes the reversal of the solar magnetic field (Hale cycle). A multiple linear regression using the solar radio flux and the solar polar magnetic field as parameters leads to the regression coefficients $C_{\mathrm{solar}} = (5.0 \pm 0.7)\,\mathrm{K}\,(100\,\mathrm{SFU})^{-1}$ and $C_{\mathrm{hale}} = (1.8 \pm 0.5)\,\mathrm{K}\,(100\,\mu\mathrm{T})^{-1}$ ($r^2 = 0.71$). The second way of describing the OH* temperature time series is to use the solar radio flux and an oscillation. A least-square fit leads to a sensitivity to the solar activity of $(4.1 \pm 0.8)\,\mathrm{K}\,(100\,\mathrm{SFU})^{-1}$, a period $P = (24.8 \pm 3.3)$ years, and an amplitude $C_{\sin} = (1.95 \pm 0.44)\,\mathrm{K}$ of the oscillation ($r^2 = 0.78$). The most important finding here is that using this description an additional linear trend is no longer needed. Moreover, with the knowledge of this 25-year oscillation the linear trends derived in this and in a former study of the Wuppertal data series can be reproduced by just fitting a line to the corresponding part (time interval) of the oscillation. This actually means that, depending on the analysed time interval, completely different linear trends with respect to magnitude and sign can be observed. This fact is of essential importance for any comparison between different observations and model simulations.

1 Introduction

The mesopause of the Earth is one of the most variable regions in the atmosphere. There are numerous different influences such as the solar radiation and different types of waves (e.g. tides, planetary waves, gravity waves) that affect the temperature in this region. Thus, the temperature undergoes large variations on very different timescales from minutes to years. The largest variation observed in temperature is the variation in 1 year. This seasonal variation is characterised by an annual, a semi-annual, and a ter-annual component (see e.g. Bittner et al., 2000) and shows maximum to minimum temperature differences of up to 60 K throughout the year (see Fig. 1). The second largest temperature variations are caused by different types of waves. The induced temperature fluctuations occur on timescales from days up to months in the case of planetary waves (e.g. Bittner et al., 2000; Offermann et al., 2009; Perminov et al., 2014) and on the timescale of several minutes in the case of gravity waves (e.g. Offermann et al., 2011; Perminov et al., 2014). Beside these rather short-term fluctuations the temperature in the mesopause region also exhibits long-term variations on a timescale of several years. Although the amplitudes of these long-term variations are much smaller, the long-term change of the mesopause temperatures is, nevertheless, clearly existent and important. Several previous studies showed the existence of an 11-year modulation of the temperature in coincidence with the 11-year cycle of solar activity which is visible in the number of sunspots and the solar radio flux F10.7 cm (for a review of solar influence on mesopause temperature see Beig, 2011a). The reported sensitivities in the middle to high latitudes of the Northern Hemisphere lie between 1 to 6 K $(100\,\mathrm{SFU})^{-1}$. Another type of long-term change is linear trends in the analysed time interval. In the mesopause region of the Northern Hemisphere such trends range from about zero up to a cooling of $3\,\mathrm{K\,decade}^{-1}$ (for a review of mesopause temperature trends see Beig, 2011b). Trend breaks also seem to be possible where the linear trend switches its sign (positive or negative trend) or the magnitude of the trend significantly changes (for an example of the latter case see Offermann et al., 2010). In cases of such changes in trend (e.g. caused due to changes in trend drivers) a piecewise linear trend approach can be used, in which different linear trends are determined for different time intervals (e.g. Lastovicka et al., 2012).

Beside these variations of the mesopause temperature, Höppner and Bittner (2007) found a quasi 22-year modulation of the planetary wave activity which they derived from mesopause temperature measurements. This observed modulation coincides with the reversal of the solar polar magnetic field, the so-called Hale cycle. The solar polar magnetic field reverses every approximately 11 years at about solar maximum, thus the maximum positive and negative values of magnetic field strength occur between two consecutive solar maxima (e.g. Svalgaard et al., 2005). Several studies exist showing a quasi 22-year modulation of different meteorological parameters such as temperature, rainfall, and temperature variability that are in phase with the Hale cycle or the double sunspot cycle (e.g. Willet, 1974; King et al., 1974; King, 1975; Qu et al., 2012), but no physical mechanism is found for these coincidences. The double sunspot cycle is another type of Hale cycle with a period of about 22 years which is phase-shifted compared to the Hale cycle of the solar polar magnetic field. The maxima and minima of the double sunspot cycle occur at maxima of the sunspot number (e.g. King, 1975; Qu et al., 2012). However, a number of possible influences, also showing a 22-year modulation, are named: galactic cosmic rays (GCR), solar irradiation, and solar wind (e.g. White et al., 1997; Zieger and Mursula, 1998; Scafetta and West, 2005; Miyahara et al., 2008; Thomas et al., 2013; Mursula and Zieger, 2001).

Because of this large number of influences and possible interactions the analysis of the temperatures is not easy to interpret, but due to the different timescales of the variations the different types of influences and phenomena can sometimes be distinguished. In this paper we focus on the long-term variations of the mesopause temperature on timescales larger than 10 years. We use OH* temperatures, which have been derived from ground-based measurements of infrared emissions at a station in Wuppertal (Germany), for our analyses.

The paper is structured as follows. In Sect. 2 we describe the instrument and measurement technique and show the OH* temperature observations, Sect. 3 introduces the Lomb–Scargle periodogram and its properties, and in Sect. 4 we analyse the OH* temperatures regarding solar correlations, long-term trends, and long periodic oscillations. A discussion of the obtained results is given in Sect. 5, and we summarise and conclude in Sect. 6.

2 Observations

2.1 Instrument and measurements

Excited hydroxyl (OH*) molecules in the upper mesosphere/mesopause region emit radiation in the visible and near infrared. The emission layer is located at about 87 km height with a layer thickness of approximately 9 km (full width at half maximum) (e.g. Baker and Stair Jr., 1998; Oberheide et al., 2006). The GRIPS-II (Ground-based Infrared P-branch Spectrometer) instrument is a Czerny–Turner spectrometer with a Ge detector cooled by liquid nitrogen. It measures the emissions of the P1(2), P1(3), and P1(4) lines of the OH*(3,1) band in the near infrared (1.524–1.543 µm) (for extensive instrument description see Bittner et al., 2000, 2002). The measurements are taken from Wuppertal (51° N, 7° E) every night with a time resolution of about 2 min. Thus, a continuous data series throughout the year is obtained with data gaps caused by cloudy conditions only. This results in approximately 220 nights of measurements per year (Oberheide et al., 2006; Offermann et al., 2010). The relative intensities of the three lines are used to derive rotational temperatures in the region of the OH* emission layer (see Bittner et al., 2000, and references therein).

At the beginning of 2011 a newly built instrument was operated next to the GRIPS-II instrument. Simultaneous measurements conducted over a few months showed no significant differences between the two instruments. Unfortunately a detector failure stopped the GRIPS-II measurements in mid-2011, but the new instrument was able to continue the time series of nightly OH* temperatures. Unfortunately, the new instrument had several technical problems in the following period which led to larger data gaps in the years 2012 and 2013. Finally, a reconstruction was performed to set up the GRIPS-N instrument, a Czerny–Turner spectrom-

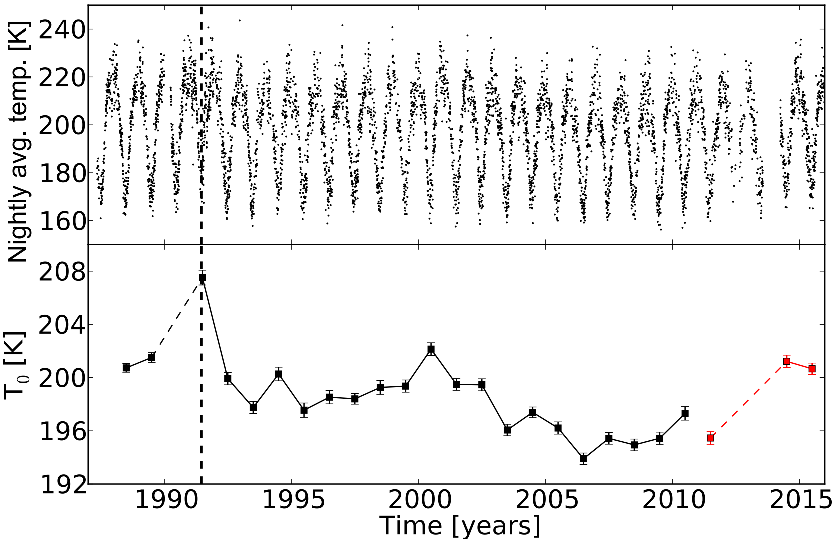

Figure 1. OH* temperature time series derived from GRIPS-II and GRIPS-N measurements at Wuppertal. The upper panel shows the nightly average temperatures and the lower panel shows the annual average temperatures T_0. Each T_0 is plotted in the middle of the corresponding year and the dates given at the x axis show the beginning of the years. The annual average temperatures partly or completely derived from the new instrument between 2011 and 2015 are shown in red in the lower panel. The error bars show the estimated 1σ uncertainties σ_{T_0} of the temperatures T_0 (based on the standard deviation of the residuals). The vertical dashed line marks the date of Mt Pinatubo eruption.

eter, equipped with a thermoelectrically cooled InGaAs detector. The optical and spectral properties of GRIPS-N and GRIPS-II are very similar, thus the measurements of both instruments are nearly identical. The new GRIPS-N instrument was operated without further problems since the beginning of 2014. Hence, for the years 2014 and 2015 a complete set of measurements is available with only the typical data gaps due to cloudiness.

2.2 Data processing

The nightly average OH* temperatures derived from the GRIPS-II and GRIPS-N measurements in Wuppertal are shown in the upper panel of Fig. 1 for the time interval 1988 to 2015. As mentioned above the data series show larger gaps of several months due to technical problems in the years 2012 and 2013 and, additionally, a data gap of 3 months at the beginning of 1990. These years have to be excluded from the analysis, since a reasonable determination of an annual average temperature in the presence of such large data gaps is not possible.

By far the largest variation in this temperature series is the variation over the course of a year. In order to evaluate the data with respect to long-term dynamics with periods well above 1 year the seasonal variation has to be eliminated first. Since the temperature series exhibits data gaps mostly due to cloudy conditions, a simple arithmetic mean for each year is not advisable. We follow the method used before in several analyses (e.g. Bittner et al., 2002; Offermann et al., 2004, 2006, 2010; Perminov et al., 2014) and perform a harmonic analysis based on least-square fits for each year separately. As described in Bittner et al. (2000) the seasonal variation is characterised by an annual, a semi-annual, and a ter-annual cycle. Thus, the temperature variation over 1 year is described by

$$T = T_0 + \sum_{i=1}^{3} A_i \cdot \sin\left(\frac{2 \cdot \pi \cdot i}{365.25}(t + \phi_i)\right), \qquad (1)$$

where T_0 is the annual average temperature, t is the time in days of the year, and A_i, ϕ_i are the amplitudes and phases of the sinusoids. By fitting this equation to the temperature data we can obtain the best possible estimate of the annual average temperature T_0 for each year. A year in this case denotes a calendar year. The resulting annual average temperatures are shown in the lower panel of Fig. 1 with data gaps in the years 1990, 2012, and 2013 (illustrated by the dashed lines). The seasonal variation of the year 2009 is shown in Fig. 2 as a typical example. As described above a detector failure in mid-2011 stopped the GRIPS-II measurements. The following measurements were performed with a new instrument. The first year of full data coverage with GRIPS-N was 2014. Due to this the corresponding T_0 for 2011 and 2014–2015 are marked in red in Fig. 1.

2.3 Comparison with other observations

Since there is a data gap of two years (2012–2013) in the GRIPS-II and GRIPS-N measurements in Wuppertal and the last data points are derived from measurements by a new instrument, one has to ensure that the T_0 from 2011 to 2015 fits the whole picture of long-term temperature evolution.

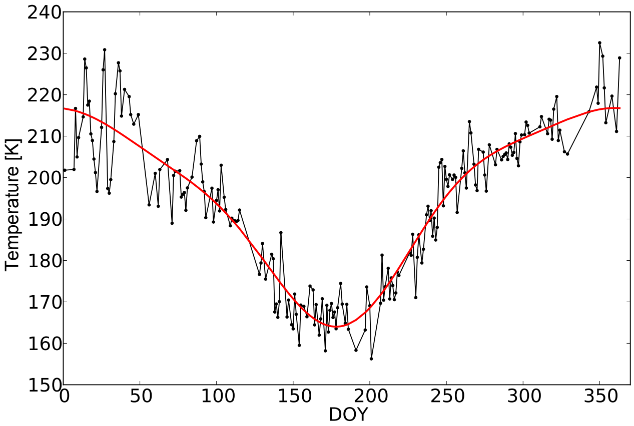

Figure 2. GRIPS-II nightly average temperatures of 2009 plotted at the day of year (DOY). The measurement data are shown in black and the harmonic fit using Eq. (1) is shown as the red curve.

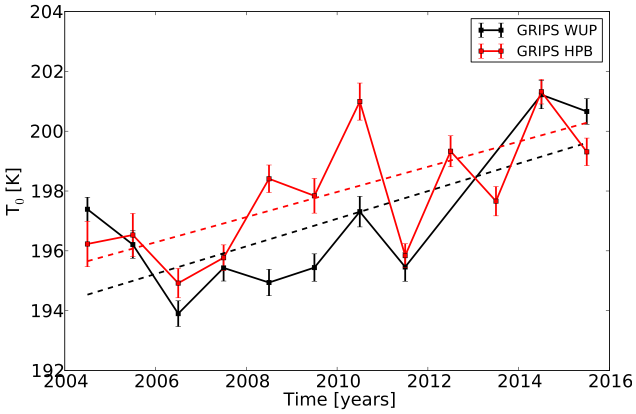

Figure 3. OH* annual average temperatures for the two stations Wuppertal and Hohenpeissenberg in the time interval 2004–2015. The temperatures for Wuppertal (WUP) are shown in black and the temperatures for Hohenpeissenberg (HPB) in red. The dashed lines show the linear fits to the corresponding time series. The linear fit for the Hohenpeissenberg time series only considers measurements at times Wuppertal measurements are also available.

We compare the Wuppertal observations with observations of OH* temperatures taken from Hohenpeissenberg (48° N, 11° E) to check this. The instrument GRIPS-I in Hohenpeissenberg measures in the same spectral range and uses the same data processing technique to determine OH* temperatures. GRIPS-I is an Ebert–Fastie spectrometer with a liquid-nitrogen-cooled Ge detector (see e.g. Bittner et al., 2002). The measurements at Hohenpeissenberg started end of 2003.

Figure 3 shows the comparison for the two measurement stations. A significant correlation between the two time series can be found with a correlation coefficient $r = 0.72$. The comparably low value of r is caused by the differences between 2007 to 2009, where the temperatures at Wuppertal partly decrease (increase) and the Hohenpeissenberg temperatures increase (decrease) at the same time. These differences are most likely caused by local effects. Furthermore, the largest absolute difference in 2010 is caused by an exceptional warm summer observed at Hohenpeissenberg. This warm summer is also observed at the nearby station in Oberpfaffenhofen (see Schmidt et al., 2013, their Fig. 12.) but not at Wuppertal.

The linear increase for each time series is shown in Fig. 3 as dashed lines in black and red. In order to get the most appropriate comparison the linear fit to the Hohenpeissenberg time series only considers data points at times where measurements at Wuppertal are also available. The linear increase during the last 12 years at Wuppertal is $(0.46 \pm 0.17)\,\mathrm{K\,year^{-1}}$ and the increase at Hohenpeissenberg is $(0.42 \pm 0.16)\,\mathrm{K\,year^{-1}}$. Both values agree very well, but the two lines are shifted towards each other indicating an offset between the two stations. This offset is about 0.9 K with Hohenpeissenberg being warmer. In a former study Offermann et al. (2010) obtained a mean offset between the two stations of 0.8 K for the time interval 2004–2008. Thus, this comparison agrees well the former study. Offermann et al. (2010) suggested that the latitudinal difference between the stations is responsible for this small difference. The temperature differences between the minima in 2006 and the maxima in 2014 also agree very well for both stations. The values are (7.3 ± 0.7) K at Wuppertal and (6.4 ± 0.7) K at Hohenpeissenberg. Since we analysed the relative evolution of the temperature series at Wuppertal, the last data points were found to fit the whole picture of the long-term development of OH* temperatures. Thus, the temperature increase observed at Wuppertal in recent years is reliable and confirmed by the temperature increase observed at Hohenpeissenberg.

The latest analysis of the OH* temperatures at Wuppertal regarding long-term dynamics was performed for the time interval 1988–2008 (Offermann et al., 2010). The current study now considers a time series which is 7 years longer than that used before. The clear temperature increase over the last years has encouraged us to perform a new analysis regarding the long-term dynamics.

3 Lomb–Scargle periodogram and false alarm probability

Analysing periodicities in the time series of T_0 using the common fast Fourier transform (FFT) or wavelet analysis is not possible, since the time series exhibits data gaps and these methods rely on equidistant data. A frequently used method in such a situation is the Lomb–Scargle periodogram (LSP), which can handle time series with uneven spacing. The periodogram was developed by Lomb (1976) and Scargle (1982) and is equivalent to the fitting of sinusoids (Horne et al., 1986). It can be calculated for every frequency f, which is another advantage compared to the discrete FFT, which is evaluated at discrete frequencies only. We use the algorithm by Townsend (2010) for the fast calculation of the periodogram.

An important quantity for the interpretation of a LSP is the so called false alarm probability (FAP). The FAP gives the probability that a peak of height z in the periodogram is caused just by chance, e.g. by noise. As already pointed out by Scargle (1982), the cumulative distribution function (CDF) can be used to determine the FAP. If we take different samples of noise, calculate the LSP for each sample and then determine the height z of the maximum peak, the CDF of all these heights z gives the probability that there is a height Z smaller or equal to z. Consequently, the value $1-\text{CDF}$ gives the probability that there is a height Z larger than z by chance. Thus, $1-\text{CDF}$ gives the FAP. Another important point in this context is the normalisation of the periodogram, since the normalisation affects the type of distribution of the periodogram, thus the description of the FAP (for a more detailed discussion see e.g. Horne et al., 1986; Schwarzenberg-Czerny, 1998; Cumming et al., 1999; Zechmeister and Kürster, 2009). We use the normalisation by the total variance of the data, which leads to a beta distribution in the case of Gaussian noise (Schwarzenberg-Czerny, 1998). Since a mean has to be subtracted from the data before calculating the LSP, the total variance is determined using $N-1$ degrees of freedom with N being the number of data points. This leads to a maximum value for a peak in the periodogram of $(N-1)/2$ in the case of a single sinusoid. The FAP can be described by

$$\text{FAP} = 1 - \left[1 - \left(\frac{2z}{N-1}\right)^{(N-3)/2}\right]^{N_i}, \tag{2}$$

where N is the number of data points and N_i is the number of independent frequencies (Schwarzenberg-Czerny, 1998; Cumming et al., 1999; Zechmeister and Kürster, 2009). The number of independent frequencies N_i has to be determined using simulations, since it is not possible to easily describe this quantity analytically (Cumming et al., 1999). It depends on several factors, e.g. the number of data points N and the spacing of the data points. Horne et al. (1986) showed the partly large effect of the spacing (randomly or clumps of points) on N_i. Therefore, we perform simulations to determine N_i for the special situation of our observations. We take random values from a Gaussian distribution and the spacing of our observations as input. Then we calculate the LSP for ten thousand such noise samples in the same way as for the real data and determine the height z of the maximum peak for each LSP. Every LSP is evaluated in the frequency range from Nyquist-frequency $f = 1/2\,\text{year}^{-1}$ to $f = 1/T\,\text{year}^{-1}$, where T in our case is 35 years, since we want to search for periodicities in range of the time window of the data series of 28 years. Periodicities in this range are surely accompanied with larger uncertainties, but the LSP gives a reasonable overview over the periodicities, even the large ones, included in the time series. The LSP is calculated at $4T_{\text{dur}}\Delta f = 53$ evenly spaced frequencies in the mentioned frequency range, where T_{dur} is the duration of observations. Cumming et al. (1999) pointed out that this is an adequate sampling to observe all possible peaks. The upper panel of Fig. 4 shows the resulting empirical CDF of z for our sampling. The number of data points in this case is $N = 25$ and the data series includes the data gaps in 1990 and 2012–2013. The lower panel of Fig. 4 displays the FAP (1 − CDF) as a black curve. The fit of the theoretical curve using Eq. (2) to this data points is shown in red. The fit leads to a number of independent frequencies $N_i = 32.4$. With knowledge of N_i we can calculate the FAP for every peak height z and determine confidence levels for the LSP.

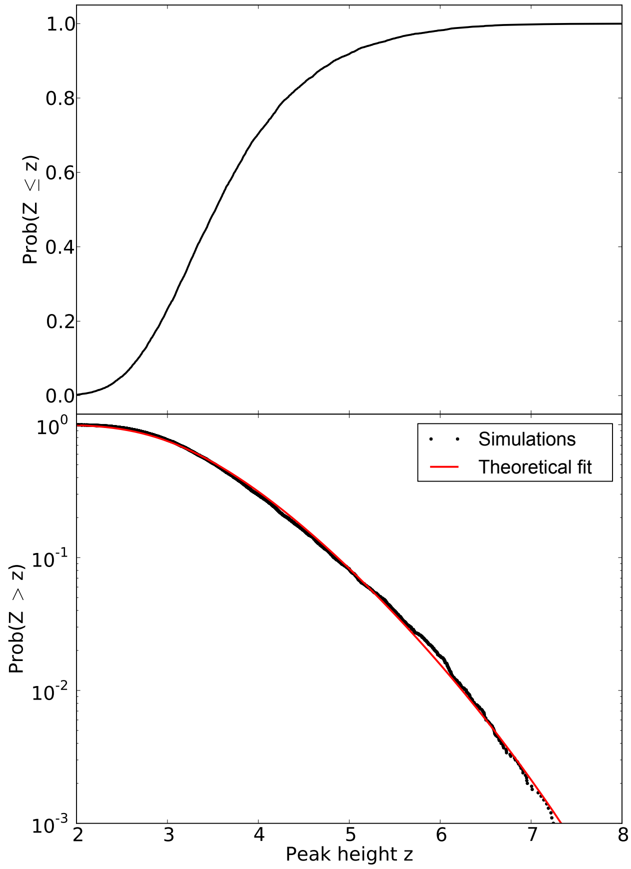

Figure 4. Distribution for peak heights z determined using random values from a Gaussian distribution as input for the calculation of LSP (for details see Sect. 3). The upper panel shows the empirical CDF, thus, the probability that there is a height Z smaller or equal to z. The FAP (probability that a height Z larger z occurs just by chance) is shown in the lower panel. The simulation results are shown in black and a fit to the theoretical curve from Eq. (2) is shown in red. Note the logarithmic scale of the y axis of the lower panel. This calculations are done for a data sampling same as that of the time series from 1988 to 2015 including data gaps. The fit leads to a number of independent frequencies $N_i = 32.4$.

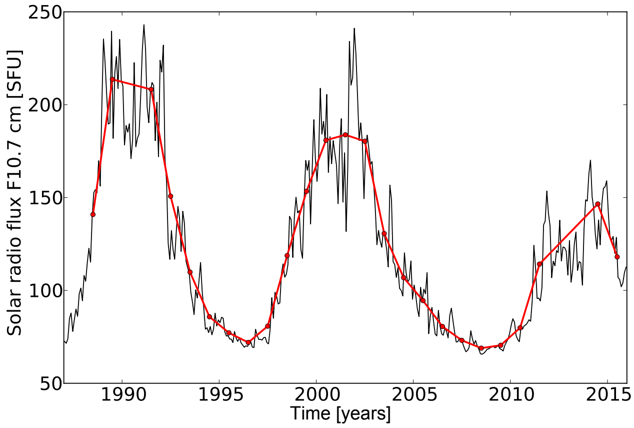

Figure 5. Monthly average values of the solar radio flux F10.7 cm. The red dots mark the annual average values corresponding to the times of the GRIPS data points. The data were provided by Natural Resources Canada, Space Weather Canada.

4 Analysis of long-term dynamics: linear trend, solar correlations, long periodic, and multi-annual oscillations

4.1 Linear trend and 11-year solar cycle

We analyse the long-term trend and the correlation with the 11-year cycle in solar activity by means of a multiple linear regression. For this and the following analyses the time coordinate is shifted such as the first data point (1988.5) is set to zero. The annual average temperatures are described by

$$T_0(t,\mathrm{SF}) = C_{\mathrm{trend}} \cdot t + C_{\mathrm{solar}} \cdot \mathrm{SF} + b, \tag{3}$$

where C_{trend} and C_{solar} are the two regression coefficients, t is the time in years, b is a constant offset, and SF is the solar radio flux F10.7 cm in solar flux units (SFU). The solar radio flux is shown in Fig. 5 for the time interval from 1988 to 2015. The monthly average values of the solar radio flux F10.7 cm were provided by Natural Resources Canada (Space Weather Canada) and were obtained from http://www.spaceweather.gc.ca/solarflux/sx-5-mavg-en.php. There are three solar maxima in this time interval at about 1991, 2001, and 2014. This corresponds well to the annual average temperatures T_0, which also show local maxima at these points. The calculated regression coefficients determined by fitting Eq. (3) using the method of ordinary least squares are $C_{\mathrm{trend}} = (-0.089 \pm 0.055)\,\mathrm{K\,year}^{-1}$ and $C_{\mathrm{solar}} = (4.2 \pm 0.9)\,\mathrm{K}\,(100\,\mathrm{SFU})^{-1}$. The p values (for the null hypothesis test) are 0.12 for C_{trend} and below 0.01 for C_{solar}. The 1σ uncertainties for the parameters given here (and in the following cases) are based on the standard deviation of the residuals to account for variations not captured by the fit. The whole fit has a $r^2 = 0.6$. Figure 6 shows the results for this analysis. The upper panel of the figure shows the temperature time series in black and the fit according to Eq. (3) in red. Additionally, the residual T_{res} is shown in the lower panel. Obviously, a fit taking into account a linear trend and the correlation with the 11-year solar cycle is a relatively poor fit to the temperature time series. When comparing the fit with the temperature time series, one has to additionally keep in mind that the general shape of the fit cannot change, since it depends on the time and solar flux values, which are fixed. The temperature residual still shows a temperature decrease until about 2005 and a temperature increase afterwards. In particular, the large increase at the end of the time series is not captured by the fit. Although there is an increase in solar activity in the same time interval, it is by far not enough to completely explain the observed temperature increase until 2015.

The obvious differences between fit and data series can also be seen in the LSPs in Fig. 7. The LSP is used here to analyse at which periods the determined fit reduces the variance of the original data series. The periodogram for the annual average temperatures T_0 is shown in black and the periodogram for the residual T_{res} after subtracting the fit is shown in red. The LSP for the residual is normalised using the variance of the residual. All variances calculated for residuals in this study are adjusted to account for the reduction of degrees of freedom, which is caused by the subtraction of a fit, using the number of fit parameters. The peak at about 11 years in the LSP for T_0, which indicates the correlation with the 11-year solar cycle, disappeared after subtracting the fit. In contrast, the large broad peak at the end of the periodogram is not completely removed and the probability that the peak is caused accidentally is only 25 %. Since the fit subtracted from the data may contain functions non-orthogonal to the LSP components, which are sinusoids, the remaining peak cannot be interpreted as an oscillation with a period of 20 years that remains or is even a component of the original data series. The peak is likely influenced by the fit subtracted from the data series, e.g. since the subtraction of a linear trend filters out low-frequency components. However, the clear signal in the long periodic range that remains in the periodogram shows that the fit determined by using Eq. (3) is not sufficient to remove all long-term variations. There are two possibilities to describe the long-term variation of the temperature series in a better way. Firstly, one can introduce a trend break so that there is a linear decrease in the first part and a linear increase in the second part of the series. Secondly, one can use a long periodic oscillation, which can introduce a trend break with a smoother transition. We will investigate these two possibilities in the next subsections.

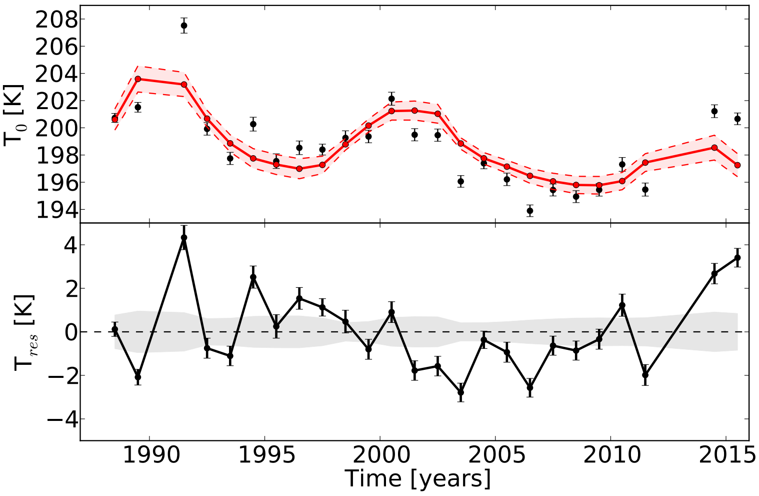

Figure 6. The upper panel of the figure shows the time series of annual average OH* temperatures in black and the fit corresponding to Eq. (3) with the regression coefficients $C_{\text{trend}} = (0.089 \pm 0.055)\,\text{K year}^{-1}$ and $C_{\text{solar}} = (4.2 \pm 0.9)\,\text{K}\,(100\,\text{SFU})^{-1}$ in red. The black error bars show the uncertainties of the temperatures σ_{T_0} and the reddish area defined by the dashed red lines shows the 1σ uncertainty σ_{fit} of the fit. In the lower panel the residual T_{res} of the two is shown. The black error bars show the uncertainties of the temperatures σ_{T_0} and the gray area around the zero line shows the uncertainty of the fit.

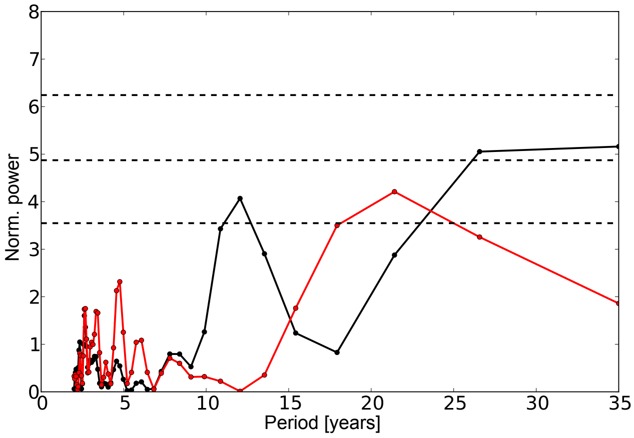

Figure 7. The Lomb–Scargle periodogram for the time series of annual OH* temperatures (see Fig. 1 lower panel) is shown in black and the LPS for the residual after subtracting the fit according to Eq. (3) (see Fig. 6 lower panel) is shown in red. The LSP is evaluated at 53 evenly spaced frequencies in the range $f = 1/2\,\text{year}^{-1}$ to $f = 1/35\,\text{year}^{-1}$. The dashed black horizontal lines display the levels for false alarm probabilities of 0.01, 0.1, and 0.5 (top to bottom). The false alarm probabilities are calculated according to Eq. (2) using $N_i = 32.4$ and the number of data points $N = 25$.

4.2 Trend break

The trend break and the correlation with the 11-year solar cycle are analysed by describing the annual average temperatures as

$$T_0(t, \text{SF}) = C_{\text{solar}} \cdot \text{SF} + \text{trend}_{\text{2phase}}(t), \tag{4}$$

where $\text{trend}_{\text{2phase}}(t)$ is a trend term using two lines to introduce the trend break. The trend term is written as

$$\text{trend}_{\text{2phase}}(t) = \begin{cases} C_{\text{trend1}} \cdot t + b_1 & : t \leq \text{BP} \\ C_{\text{trend2}} \cdot t + b_2 & : t > \text{BP} \end{cases}, \tag{5}$$

where BP is the break point (in years). Since the two different lines need to be equal at the break point, this leads to the condition

$$\begin{aligned} & C_{\text{trend1}} \cdot \text{BP} + b_1 = C_{\text{trend2}} \cdot \text{BP} + b_2 \\ & \Leftrightarrow b_2 = b_1 + (C_{\text{trend1}} - C_{\text{trend2}}) \cdot \text{BP}. \end{aligned} \tag{6}$$

Thus, Eq. (5) can be rewritten as

$$\begin{aligned} & \text{trend}_{\text{2phase}}(t) \\ & = \begin{cases} C_{\text{trend1}} \cdot t + b_1 & : t \leq \text{BP} \\ C_{\text{trend2}} \cdot t + (b_1 + (C_{\text{trend1}} - C_{\text{trend2}}) \cdot \text{BP}) & : t > \text{BP} \end{cases}. \end{aligned} \tag{7}$$

The description of the concept and the condition can be seen in Ryan and Porth (2007). Equation (4) now describes the annual average temperatures by using the correlation with the solar flux and a trend term with two different phases, where both phases have a linear temperature behaviour. These two phases are coupled by the variable break point BP.

We determine the best estimates for the parameters C_{solar}, C_{trend1}, C_{trend2}, b_1, and BP by means of a least-square fit. The fit leads to a sensitivity to the solar flux of $C_{\text{solar}} = (3.3 \pm 0.9)\,\text{K}\,(100\,\text{SFU})^{-1}$. After subtracting this solar dependence and the mean, the resulting residual, and the best fit of the trend term are shown in Fig. 8 as black and red lines respectively. Additionally, the position of the break point and the corresponding uncertainties are marked as a vertical black line and vertical dashed black lines respectively. We observe a trend

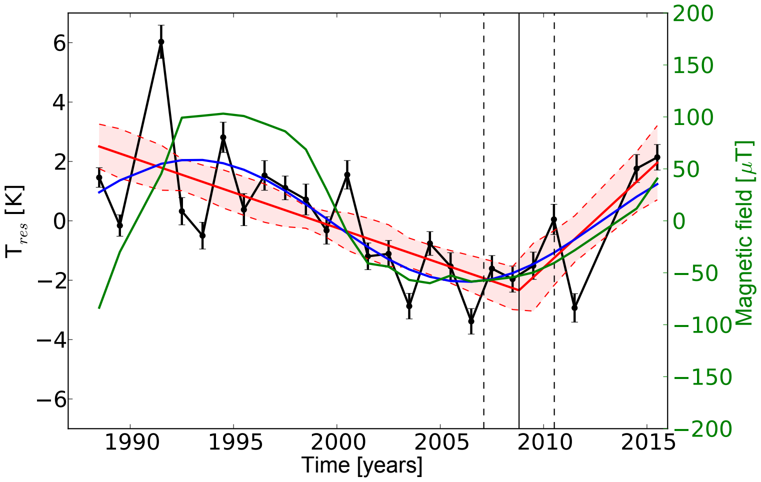

Figure 8. Residual for the temperature time series after removing the 11-year solar cycle ($C_{\text{solar}} = (3.3 \pm 0.9)$ K $(100\,\text{SFU})^{-1}$) and subtracting the mean. The black error bars show the uncertainties σ_{T_0}. The red lines show the fit according to Eq. (7) and the blue curve the fit according to Eq. (8). The reddish area defined by the red dashed lines shows the 1σ uncertainty σ_{fit} of the complete fit according to Eq. (7). The break point BP is marked by the vertical black line and the corresponding uncertainties are shown as vertical dashed black lines. Additionally, the annual average values of the solar polar magnetic field strength are displayed as a green curve with a second axis to the right. Shown are the average values for the solar North Pole and South Pole with the magnetic field orientation of the North Pole ((N–S)/2). The data were provided by the Wilcox Solar Observatory (for an instrument description see Scherrer et al., 1977).

break in the middle of 2008 (BP = (2008.8 ± 1.7) year). Before the trend break in 2008 there is a negative temperature trend $C_{\text{trend1}} = (-0.24 \pm 0.07)\,\text{K}\,\text{year}^{-1}$ and after the break point the trend is positive with a slope $C_{\text{trend2}} = (0.64 \pm 0.33)\,\text{K}\,\text{year}^{-1}$. The r^2 of the whole fit is 0.74. The LSP for the residual after subtracting the trend break fit is shown in Fig. 9 in red. The former large peak at the right end of the periodogram for the original data series (black curve) is nearly completely removed after subtracting the trend break fit. Thus, the fit using two linear trends and a trend break explains a very large portion of the long-term variation of the OH* temperature series.

4.3 Long-term oscillation

We analyse the possibility of an oscillation instead of a trend break. In order to get an idea about the oscillation we fit a sinusoid of the form

$$T_{\text{res}}(t) = A \cdot \sin\left(\frac{2 \cdot \pi}{P}(t + \phi)\right) + b \tag{8}$$

to the temperature residual after subtracting the solar dependence and the mean (see Fig. 8 black curve). A denotes the amplitude, P the period, and ϕ the phase. Additionally, we fit an offset b, since the mean of the temperature residual is not necessarily identical to the zero crossing of the oscillation. The resulting oscillation is shown in Fig. 8 as a blue curve. The important estimated parameters of the fit are an amplitude $A = (2.06 \pm 0.43)$ K and a period of about 26 years ($P = (26.3 \pm 3.2)$ years). It is clear that this oscillation and the fit using the two linear phases and a trend break (red lines in Fig. 8) are nearly identical for the time interval after 2008. Before 2008 the blue curve oscillates about the red line. Additionally, the oscillation introduces a much smoother transition from decreasing to increasing temperatures. The decrease in variance is larger for the oscillation than for the fit using two linear phases. The variances of the two resulting differences, T_{res} minus linear trends (red lines) and oscillation (blue curve) are 2.64 and 2.44 K^2. Offermann et al. (2010) already suggested a trend break in the temperature series at about 1997. The oscillation would account for

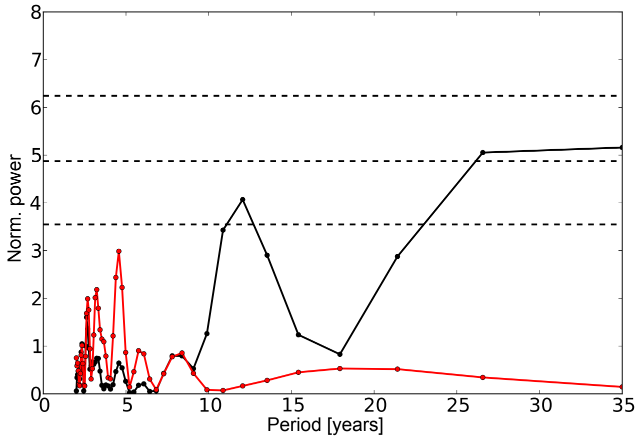

Figure 9. The Lomb–Scargle periodogram for the time series of annual OH* temperatures (see Fig. 1 lower panel) is shown in black and the LPS for the residual after subtracting the fit according to Eq. (4) is shown in red. For details see description of Fig. 7.

such a second trend break in the temperature series in the mid-1990s, about 1993.

Very prominent is the fact that the oscillation has a period of about 26 years with a minimum at about 2006 and a maximum at about 1993. This type of oscillation with very similar parameters can be found on the sun. The original solar cycle (Hale cycle) is a cycle with a period of about 22 years and describes the reversal of the magnetic field of the sun. The solar polar magnetic field of the sun is shown in Fig. 8 as a green curve with a second axis to the right. The solar polar field strength data were provided by the Wilcox Solar Observatory and were obtained from http://wso.stanford.edu/Polar.html. We used the low pass filtered values. Evidently, the oscillation fitted to T_{res} and the Hale cycle of the magnetic field are very similar in the time interval shown. The correlation coefficient for a linear regression between the magnetic field and the temperature residual (black curve in Fig. 8) is $r = 0.55$. The corresponding slope is $(1.74 \pm 0.56)\,\mathrm{K}\,(100\,\mu\mathrm{T})^{-1}$ (p value < 0.01). This is a remarkable accordance between the observed oscillation in atmospheric temperature and solar polar magnetic field.

The long periodic oscillation describes the largest part of the temperature variability after detrending the temperature series with respect to the 11-year solar cycle. Thus, we analyse the temperature series T_0 by means of a multiple linear regression again to fit all dependencies simultaneously. We include the solar polar magnetic field in the equation, which replaces the linear trend. Hence, Eq. (3) transforms to

$$T_0(\mathrm{SF}, B_{\mathrm{solar}}) = C_{\mathrm{solar}} \cdot \mathrm{SF} + C_{\mathrm{hale}} \cdot B_{\mathrm{solar}} + b, \tag{9}$$

where B_{solar} denotes the solar polar magnetic field and C_{hale} the corresponding regression coefficient. The analysis leads to the results for the regression coefficients $C_{\mathrm{solar}} = (5.0 \pm 0.7)\,\mathrm{K}\,(100\,\mathrm{SFU})^{-1}$ and $C_{\mathrm{hale}} = (1.8 \pm 0.5)\,\mathrm{K}\,(100\,\mu\mathrm{T})^{-1}$. The fit to the temperature time series has a $r^2 = 0.71$. This value is larger than the value for the fit including the 11-year solar cycle and one linear trend, which has a $r^2 = 0.6$ (see Sect. 4.1), but it is slightly lower than the $r^2 = 0.74$ of the trend break fit (see Sect. 4.2). An additional linear trend added to Eq. (9) does not significantly change the results. The obtained linear trend is insignificant in this case; therefore, it is excluded. The resulting fit and the residual are shown in Fig. 10. The fit curve (red colour) shows good agreement with the long-term variation of the temperature (black dots), but there are still some differences, especially at the beginning and the end of the time series. Additionally, the temperature residual (lower panel of Fig. 10) seems to show a long periodic oscillation. The LSP for the residual (red curve in Fig. 11) shows that the former large peak at the long periodic end of the periodogram (black curve) is largely reduced after subtracting the fit, which shows that the description using the 11-year solar cycle and the Hale cycle explains most of the variance in the long periodic range. It is possible that an oscillation with similar parameters to the Hale cycle, which are slightly changed (in amplitude, phase, and/or period), can describe the annual average temperatures even better.

We analyse this possibility and add an oscillation to the temperature description, which replaces the solar polar magnetic field. Since the oscillation and the 11-year solar cycle are non-orthogonal functions, here we fit all dependencies simultaneously. The equation transforms to

$$T_0(\mathrm{SF}, t) = C_{\mathrm{solar}} \cdot \mathrm{SF} + C_{\sin} \cdot \sin\left(\frac{2 \cdot \pi}{P}(t + \phi)\right) + b, \tag{10}$$

where $C_{\sin}$ is the amplitude, P is the period, ϕ is the phase of the oscillation, and t is the time in years. The results of the least-square fit are $C_{\mathrm{solar}} = (4.1 \pm 0.8)\,\mathrm{K}\,(100\,\mathrm{SFU})^{-1}$ for the sensitivity to the solar activity, $C_{\sin} = (1.95 \pm 0.44)\,\mathrm{K}$ for the amplitude, and $P = (24.8 \pm 3.3)$ years for the period of the oscillation. The obtained oscillation is hereafter denoted "the 25-year oscillation". The fit has a $r^2 = 0.78$. Compared to the trend break fit (see Sect. 4.2) the increase in r^2 is not significant, thus both descriptions are likely and lead to equivalent results. The fit and the residual are shown in Fig. 12. The temperature residual (lower panel of Fig. 12) no longer shows obvious long-term variations; neither a linear trend nor an oscillation. Only some variations with periods of the order of several years remain. The LSP for the temperature residual, which is shown in Fig. 13, confirms this. All long-term variations with periods larger than about 10 years are now removed from the temperature series. There are only peaks in the range up to a period of about 8 years. Thus, the description of the annual average temperature including the 11-year solar cycle and an oscillation with a period of 25 years is sufficient to explain all long-term variations. No further linear trend can be found in the data series.

4.4 Stability of solar sensitivity

In the former sections a constant sensitivity to the solar activity for the complete observations was assumed. In order to study whether this assumption is correct and the oscillation derived in Sect. 4.3 is still obtained if the solar sensitivity is allowed to vary, we analyse the time series of annual temperatures again. For the analysis we use time intervals of 11 years (approximately the length of one solar cycle). We start with the interval 1988–1998 and always shift the time interval by 1 year, ending with the interval 2005–2015. Time intervals that do not cover a 11-year window because of missing data at the end or beginning of the interval are excluded from the analysis. All possible time intervals are analysed separately. The temperatures in each interval are described by Eq. (3) and the coefficients C_{trend} and C_{solar} are determined. By doing this, we assume a linear trend in each time interval, but the trend and the sensitivity to the solar activity are allowed to vary from one interval to the next.

The results of the analysis are shown in Fig. 14. The sensitivity to the solar activity is shown in the upper panel of the figure in black, and the grey shaded area marks the range

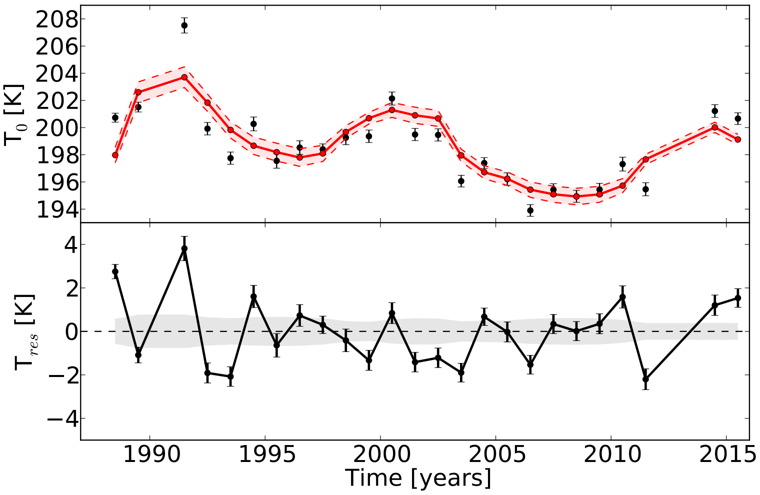

Figure 10. The upper panel of the figure shows the time series of annual average OH* temperatures in black and the fit corresponding to Eq. (9) with the regression coefficients $C_{\mathrm{hale}} = (1.8 \pm 0.5)\,\mathrm{K}\ (100\,\mu\mathrm{T})^{-1}$ and $C_{\mathrm{solar}} = (5.0 \pm 0.7)\,\mathrm{K}\ (100\,\mathrm{SFU})^{-1}$ in red. In the lower panel the residual T_{res} of the two is shown. For description of displayed uncertainties see Fig. 6.

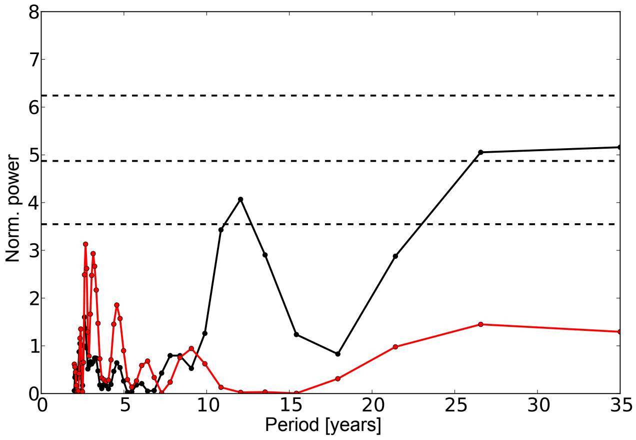

Figure 11. The Lomb–Scargle periodogram for the time series of annual OH* temperatures (see Fig. 1 lower panel) is shown in black and the LPS for the residual after subtracting the fit according to Eq. (9) (see Fig. 10 lower panel) is shown in red. For details see description of Fig. 7.

for the sensitivity derived in Sect. 4.3 for the fit using the solar cycle and an oscillation ($(4.1 \pm 0.8)\,\mathrm{K}\ (100\,\mathrm{SFU})^{-1}$). The sensitivities derived for the 11-year time intervals show some variations but considering the uncertainties no significant changes can be observed. The mean of the derived sensitivities is $(3.9 \pm 0.3)\,\mathrm{K}\ (100\,\mathrm{SFU})^{-1}$, which agrees very well with the value derived before.

The lower panel of Fig. 14 shows the derived linear trends in black. We fit a sinusoid to these trend values (red line in figure) that results in the values $A = (0.36 \pm 0.06)\,\mathrm{K}$ for the amplitude and $P = (23.2 \pm 2.5)$ years for the period. This oscillation found in the trend values should be equal to the derivative of the 25-year oscillation derived in Sect. 4.3 with a reduced amplitude, since 11-year time intervals are used, so no local derivative is obtained. This agreement is indeed the case. The observed period of the trend oscillation agrees within the uncertainties with the 25-year oscillation derived in the former section and the phase is also correct. The 25-year oscillation of the temperature is shown in the lower panel of Fig. 14 in blue and the corresponding derivative in green (with a second axis to the right). It appears that the green and red curve are nearly identical. In total the analysis method using 11-year time intervals leads to the same results as the fit including the sensitivity to the solar cycle and an oscillation to the whole data series. So this analysis confirms the results obtained in Sect. 4.3.

5 Discussion

5.1 11-year solar cycle

There are numerous publications about the correlation of the 11-year cycle of solar activity and temperatures in the mesopause region. A review is given by Beig (2011a, see Fig. 2 and corresponding section). The sensitivity to the solar activity in the northern middle to high latitudes reported in this review is about 1–6 K $(100\,\mathrm{SFU})^{-1}$. In a more recent study on mesopause temperatures measured at Zvenigorod (56° N, 37° E; 2000–2012) by Perminov et al. (2014) a sensitivity of $(3.5 \pm 0.8)\,\mathrm{K}\ (100\,\mathrm{SFU})^{-1}$ is found. This value perfectly agrees with the result of a former analysis of the GRIPS measurements at Wuppertal (1988–2008), where a sensitivity of $(3.5 \pm 0.2)\,\mathrm{K}\ (100\,\mathrm{SFU})^{-1}$ was also found (Offermann et al., 2010). In our study we obtained results in the range 3–5 K $(100\,\mathrm{SFU})^{-1}$. Depending on the analysis

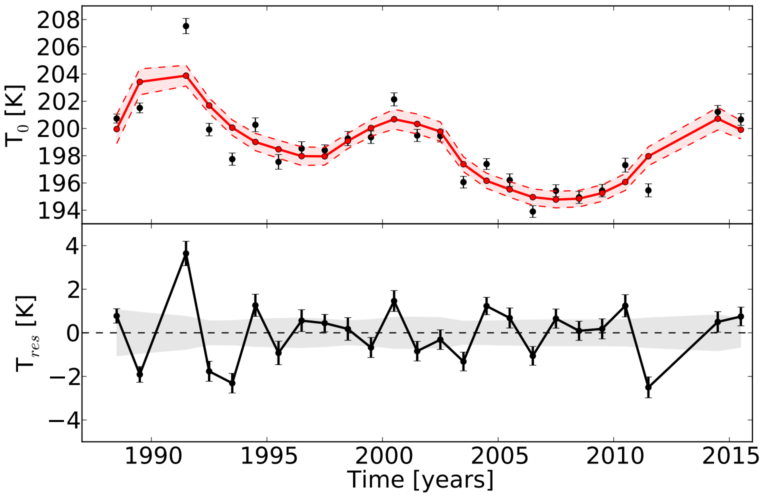

Figure 12. The upper panel of the figure shows the time series of annual average OH* temperatures in black and the fit corresponding to Eq. (10) with the coefficients $C_{\text{solar}} = (4.1 \pm 0.8)\,\text{K}\ (100\,\text{SFU})^{-1}$, $C_{\sin} = (1.95 \pm 0.44)\,\text{K}$, and $P = (24.8 \pm 2.1)$ years in red. In the lower panel the residual T_{res} of the two is shown. For description of displayed uncertainties see Fig. 6

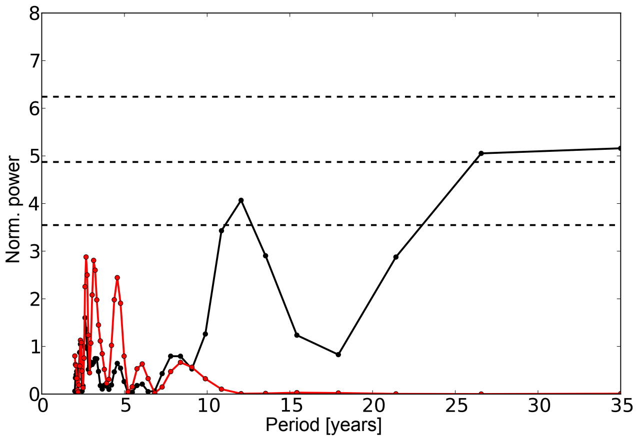

Figure 13. The Lomb–Scargle periodogram for the time series of annual OH* temperatures (see Fig. 1 lower panel) is shown in black and the LPS for the residual after subtracting the fit according to Eq. (10) (see Fig. 12 lower panel) is shown in red. For details see description of Fig. 7.

method the results differ slightly from each other, but they nearly all agree within the uncertainties (only the value derived by using the Hale cycle seems to be a little too large). Since the parameters for the fits (solar radio flux, solar polar magnetic field, oscillation, and time) are not completely independent of each other, the derived coefficients are only approximations of the true values. A much longer time series, including more solar maxima, would be necessary to finally derive the true coefficients. Thus, small differences in the derived values are expected, especially in the case of the multiple linear regression including the solar radio flux and the linear trend, since this regression leads to a result that cannot completely explain all long-term trends and oscillations in the time series. Nearly all derived values for the sensitivity of the OH* temperatures to the 11-year solar cycle are slightly larger than the one derived in the former analysis of the GRIPS measurements at Wuppertal. However, the time intervals are different for the analyses, which can lead to different results for the derived sensitivities. This aspect was already discussed by Offermann et al. (2010).

Besides the fact that the derived values are in the expected range for the northern middle to high latitudes, one new aspect with respect to the correlation between 11-year solar cycle and mesopause temperatures has become apparent. In the present study the correlation was determined for three solar maxima including the comparably weak latest solar cycle 24. Our study shows that the significant correlation between OH* temperatures and the 11-year solar cycle is still evident in this case.

5.2 Linear trend and trend break

Temperature trends in the mesopause region are reported in a number of papers, and a review about numerous results is given by Beig (2011b, see Fig. 2 and corresponding section). The temperature trends reported there range between no trend up to a cooling of about 3 K decade^{-1}. Recent studies by different authors lead to the following results. Combined Na lidar observations at Fort Collins (41° N, 105° W) and Logan (42° N, 112° W) in the time interval 1990–2014 lead to an insignificant trend of $(-0.64 \pm 0.99)\,\text{K}\,\text{decade}^{-1}$ at 85 km and the negative trend increases with increasing height up to an maximum of $(-2.8 \pm 0.58)\,\text{K}\,\text{decade}^{-1}$ at 91 and 93 km (She et al., 2015). The analysis by Perminov et al. (2014) for the measurements at Zvenigorod (56° N, 37° E) showed a trend of $(-2.2 \pm 0.9)\,\text{K}\,\text{decade}^{-1}$

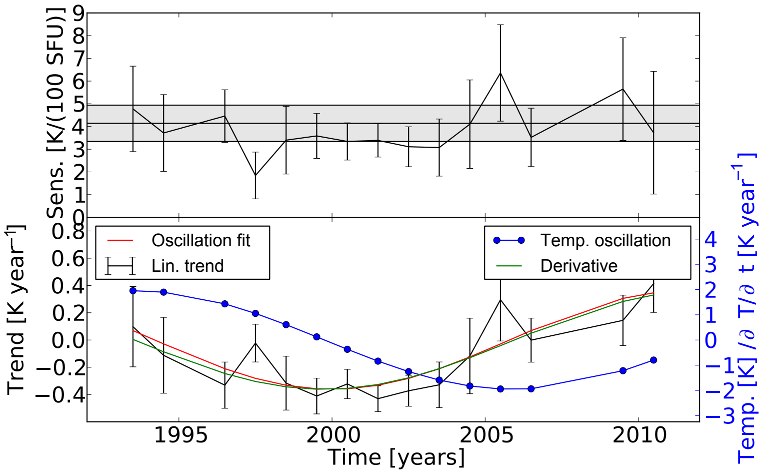

Figure 14. The upper panel shows the sensitivity to the solar activity derived for different 11-year time intervals. All values are displayed at the middle of the corresponding time interval. The error bars show the 1σ uncertainties. The grey shaded area marks the range of the sensitivity derived in Sect. 4.3 for the fit using the solar cycle and one oscillation ($C_{\text{solar}} = (4.1 \pm 0.8)\,\text{K}\,(100\,\text{SFU})^{-1}$). The lower panel of the figure shows the corresponding linear trends for each time interval in black. A sinusoid fitted to these values is shown in red. The result for the 25-year temperature oscillation (see Sect. 4.3) is shown as a blue curve and the corresponding derivative of the oscillation is shown as a green curve with a second axis to the right.

for the time interval 2000–2012. Hall et al. (2012) derived a trend of $(-4 \pm 2)\,\text{K}\,\text{decade}^{-1}$ from meteor radar observations over Svalbard (78° N, 16° E) at 90 km for the time interval 2001–2012. In a former study of the Wuppertal OH* temperature series (1988–2008) a negative trend of $(-2.3 \pm 0.6)\,\text{K}\,\text{decade}^{-1}$ was found (Offermann et al., 2010). The multiple linear regression using the solar radio flux and time as parameters in this paper results in a cooling trend of $(-0.89 \pm 0.55)\,\text{K}\,\text{decade}^{-1}$ for the Wuppertal OH* temperatures from 1988 to 2015 (see Sect. 4.1), which is in good agreement with the observations by She et al. (2015). The value is smaller than the trend derived in the former study of the Wuppertal data. Since there has been an increase in temperature from about 2006, and the former study by Offermann et al. (2010) ended in 2008, this temperature increase leads to a smaller negative trend in our study. However, as shown above, one linear trend is not sufficient to account for all long-term variation in the time series. Due to this we introduced a trend break and found a negative trend before 2008 and a positive trend afterwards. The obtained values are $(-2.4 \pm 0.7)\,\text{K}\,\text{decade}^{-1}$ and $(6.4 \pm 3.3)\,\text{K}\,\text{decade}^{-1}$ (see Sect. 4.2). The time interval used in the former study of the Wuppertal OH* temperature series by Offermann et al. (2010) is nearly identical to the time interval of the first phase, showing the negative temperature trend. The linear temperature trends derived by Offermann et al. (2010) and in this study perfectly agree for this time interval. Due to the additional 7 years of observations this study now clearly shows that the former negative linear trend turned into a positive trend in the last years. This finding is contrary to the other recent studies (She et al., 2015; Perminov et al., 2014; Hall et al., 2012; Mokhov and Semenov, 2014), where no trend break in the mid-2000s is reported.

5.3 Long-term oscillation

The observed trend break can also be described using a long periodic oscillation. In Sect. 4.3 we show two different possibilities for such a long periodic oscillation.

Firstly, the solar polar magnetic field (Hale cycle) is used as one parameter in a multiple linear regression with the second parameter being the solar radio flux. The correlation coefficients are $C_{\text{solar}} = (5.0 \pm 0.7)\,\text{K}\,(100\,\text{SFU})^{-1}$ and $C_{\text{hale}} = (1.8 \pm 0.5)\,\text{K}\,(100\,\mu\text{T})^{-1}$ ($r^2 = 0.71$). Especially at the beginning and the end of the time series the fit curve does not perfectly match the observations (see Fig. 10). Additionally, the LSP for the temperature residual after subtracting this fit curve still shows a peak in the long periodic range (red curve in Fig. 11), although this is not significant. Thus, the Hale cycle together with the 11-year solar cycle might not explain all observed long-term dynamics. Because of these facts, we believe that the solar polar magnetic field acting as an input parameter is not very suitable.

Secondly, an independent oscillation is used to describe the OH* temperature time series. A least-square fit using the solar radio flux and an oscillation with free amplitude, period, and phase leads to the coefficients $C_{\text{solar}} = (4.1 \pm 0.8)\,\text{K}\,(100\,\text{SFU})^{-1}$, $C_{\sin} = (1.95 \pm 0.44)\,\text{K}$ for the amplitude, and $P = (24.8 \pm 3.3)$ years for the period. ($r^2 = 0.78$). After subtracting the derived fit curve the LSP for the residual does not show any remaining long periodic signals (see Fig. 13). The obtained 25-year oscillation, shown in Fig. 15 as a black curve with full circles, is phase-

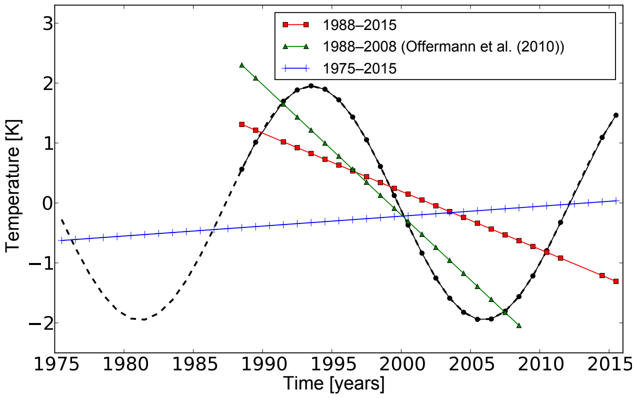

Figure 15. 25-year oscillation of OH* temperatures resulting from the least-square fit using Eq. (10). The coefficients are $C_{\text{sin}} = (1.95 \pm 0.44)$ K, and $P = (24.8 \pm 2.1)$ years. The solid black line with full circles shows the oscillation for the analysed time interval 1988–2015 and the dashed black line shows the continuation of this oscillation back to 1975. The red line with squares displays a linear fit to the oscillation for the time interval 1988–2015, the green line with triangles the fit for the interval 1988–2008, and the blue line with plus signs a fit to the interval 1975–2015.

shifted compared to the Hale cycle and the extrema occur slightly before the extrema of the solar polar magnetic field (compare green curve in Fig. 8 and black curve in Fig. 15, e.g. maximum at about 1993 compared to 1994/1995). This time shift supports the opinion that the Hale cycle is not very likely as an acting input parameter. The nature of the 25-year oscillation is not clear yet, but a self-sustained oscillation in the atmosphere would be a real possibility. Such oscillations were recently discovered by Offermann et al. (2015). An oscillation with a period of about 20 to 25 years is found in various atmospheric parameters such as temperature (Qu et al., 2012; Wei et al., 2015), geopotential height (Coughlin and Tung, 2004a, b), and planetary wave activity (Jarvis, 2006; Höppner and Bittner, 2007). It is also seen in two atmospheric models (HAMMONIA, WACCM). A detailed discussion is, however, beyond the scope of this paper.

The most important point here is that no additional linear trend can be maintained. All long-term dynamics of the Wuppertal OH* temperature time series can be described as a combination of the 11-year solar cycle and a 25-year oscillation. With the knowledge of this 25-year oscillation the linear trends derived in this study (see Sect. 4.1) and a former study of the Wuppertal OH* temperature time series can be reproduced. Figure 15 demonstrates that very different trends can be obtained if specific time intervals of the (sinusoidal) data are used. By fitting a line to the corresponding part (time interval) of the data we obtain the linear trend. The linear trend for the time interval analysed in this study (1988–2015) is $(-0.097 \pm 0.032)\,\text{K year}^{-1}$, which is the same as the linear trend $C_{\text{trend}} = (-0.089 \pm 0.055)\,\text{K year}^{-1}$ derived by using a multiple linear regression with time and solar radio flux as parameters (see Sect. 4.1). This linear trend is shown in Fig. 15 as a red line with squares. Offermann et al. (2010) derived a linear trend for the time interval 1988–2008 of $(-0.23 \pm 0.06)\,\text{K year}^{-1}$. A linear fit to the data for this time interval leads to a slope of $(-0.22 \pm 0.03)\,\text{K year}^{-1}$ (green line with triangles in Fig. 15). Thus, the 25-year oscillation "explains" the derived linear trends of this and the former study as well as the obvious trend break observed in the data series. This means that all different kinds of linear trends are possible depending on the time interval which is analysed. If we continue the oscillation back to 1975 (black dashed line in Fig. 15) and fit a line to these data for the whole time interval (1975–2015; blue line with plus signs) in Fig. 15, this leads to a slope of $(0.017 \pm 0.018)\,\text{K year}^{-1}$. This continuation is certainly an assumption and cannot be verified by the observations, but it is likely and clearly shows the possible effects. The presence of such a long periodic oscillation that, in combination with the 11-year solar cycle, explains all long-term dynamics without an additional linear trend is very important with respect to any kind of comparison between different observations or model simulations. Each comparison of linear trends is only valid if the same time interval is analysed. Furthermore, the current study suggests that there is no universal linear trend which is valid for all time intervals at this altitude.

5.4 Stability of solar sensitivity

The analysis by using different 11-year time intervals leads to two main results. Firstly, the sensitivity to the solar activity is fairly stable throughout the whole time period 1988–2015. There are some variations in sensitivity but considering the uncertainties there are no significant changes. The mean of the derived values is $(3.9 \pm 0.3)\,\text{K}\,(100\,\text{SFU})^{-1}$. This value is in nearly perfect agreement with the result of $(4.1 \pm 0.8)\,\text{K}\,(100\,\text{SFU})^{-1}$ for the fit including the 11-year solar cycle and one oscillation using the whole data series at once. So the assumption that the sensitivity to the solar activity is constant during the whole time period is valid for the Wuppertal OH* observations.

Secondly, the derived partial trend values show the same oscillation as the derivative of the 25-year temperature oscillation. Thus, the analysis using the 11-year time intervals confirms the result that, besides the 11-year solar cycle, an oscillation of about 25 years is the second important component of the OH* temperatures observed at Wuppertal.

6 Summary and conclusions

We present the analysis of the OH* temperatures derived from the GRIPS measurements at Wuppertal. We use annual average temperatures in the time interval 1988 to 2015 for our study. The study focuses on the long-term dynamics and leads to the following results.

1. The OH* temperatures show a significant correlation with the solar radio flux. We find a sensitivity to the 11-year solar cycle of 3–5 K $(100\,\mathrm{SFU})^{-1}$.

2. One linear trend during the whole time interval (together with the sensitivity to the 11-year solar cycle) cannot sufficiently explain all long-term dynamics found in the OH* temperatures. We introduce a trend break to better account for these long-term dynamics. The best representation of the temperature series is found if the trend break occurs in mid-2008 ($\mathrm{BP} = (2008.8 \pm 1.7)$ years). Before the break point the linear trend is negative and after the break point the trend turns positive with the slopes of $(-0.24 \pm 0.07)\,\mathrm{K\,year^{-1}}$ and $(0.64 \pm 0.33)\,\mathrm{K\,year^{-1}}$.

3. The reversal of the temperature trend can also be described by a long periodic oscillation. We present two possibilities for this oscillation. Firstly, the solar polar magnetic field of the sun (Hale cycle) is used in a multiple linear regression together with the solar radio flux as second parameter. The derived regression coefficients are $C_{\mathrm{solar}} = (5.0 \pm 0.7)\,\mathrm{K}\ (100\,\mathrm{SFU})^{-1}$ and $C_{\mathrm{hale}} = (1.8 \pm 0.5)\,\mathrm{K}\ (100\,\mu\mathrm{T})^{-1}$ $(r^2 = 0.71)$. Secondly, an independent oscillation is used instead of the Hale cycle. A least-square fit leads to the coefficients $C_{\mathrm{solar}} = (4.1 \pm 0.8)\,\mathrm{K}\ (100\,\mathrm{SFU})^{-1}$, $C_{\sin} = (1.95 \pm 0.44)\,\mathrm{K}$ for the amplitude, and $P = (24.8 \pm 3.3)$ years for the period. The most important point here is that no additional linear trend is needed.

4. Caution has to be applied when estimating linear trends from data sets containing long-term variations. Trend results are quite sensitive to the length of the data interval used. In such a case a piecewise linear trend approach has to be used or the long-term variation has to be described in another appropriate way, e.g. by using an oscillation.

7 Data availability

The GRIPS data used in this study can be obtained by request to the corresponding author or to P. Knieling (knieling@uni-wuppertal.de). The monthly average values of the solar radio flux F10.7 cm were provided by Natural Resources Canada (Space Weather Canada) and were obtained from http://www.spaceweather.gc.ca/solarflux/sx-5-mavg-en.php. The solar polar field strength data were provided by the Wilcox Solar Observatory and were obtained from http://wso.stanford.edu/Polar.html.

Acknowledgements. This work was funded by the German Federal Ministry of Education and Research (BMBF) within the ROMIC (Role Of the Middle atmosphere In Climate) project MALODY (Middle Atmosphere LOng period DYnamics) under Grant no. 01LG1207A. Wilcox Solar Observatory data used in this study was obtained via the web site http://wso.stanford.edu at 2016:04:11_08:31:21 PDT courtesy of J. T. Hoeksema. The Wilcox Solar Observatory is currently supported by NASA. The solar radio flux 10.7 cm data was obtained from the Natural Resources Canada, Space Weather Canada website: http://www.spaceweather.gc.ca/.

Edited by: F.-J. Lübken
Reviewed by: J. Laštovicka and one anonymous referee

References

Baker, D. J., and Stair Jr., A. T.: Rocket measurements of the altitude distributions of the hydroxyl airglow, Phys. Scr., 37, 611, doi:10.1088/0031-8949/37/4/021, 1998.

Beig, G.: Long term trends in the temperature of the mesosphere/lower thermosphere region: 2. Solar response, J. Geophys. Res., 116, A00H12, doi:10.1029/2011JA016766, 2011a.

Beig, G.: Long term trends in the temperature of the mesosphere/lower thermosphere region: 1. Anthropogenic influences, J. Geophys. Res., 116, A00H11, doi:10.1029/2011JA016646, 2011b.

Bittner, M., Offermann, D., and Graef, H. H.: Mesopause temperature variability above a midlatitude station in Europe, J. Geophys. Res., 105, 2045–2058, doi:10.1029/1999JD900307, 2000.

Bittner, M., Offermann, D., Graef, H. H., Donner, M., and Hamilton, K.: An 18-year time series of OH* rotational temperatures and middle atmosphere decadal variations, J. Atmos. Sol. Terr. Phy., 64, 1147–1166, doi:10.1016/S1364-6826(02)00065-2, 2002.

Coughlin, K. and Tung, K. K.: Eleven-year solar cycle signal throughout the lower atmosphere, J. Geophys. Res., 109, D21105, doi:10.1029/2004JD004873, 2004a.

Coughlin, K. T. and Tung, K. K.: 11-Year solar cycle in the stratosphere extracted by the empirical mode decomposition method, Adv. Space Res., 34, 323–329, doi:10.1016/j.asr.2003.02.045, 2004b.

Cumming, A., Marcy, G. W., and Butler, R. P.: The lick planet search: detectability and mass thresholds, Astrophys. J., 526, 890–915, doi:10.1086/308020, 1999.

Hall, C. M., Dyrland, M. E., Tsutsumi, M., and Mulligan, F. J.: Temperature trends at 90 km over Svalbard, Norway (78° N 16° E), seen in one dacade of meteor radar observations, J. Geophys. Res., 117, D08104, doi:10.1029/2011JD017028, 2012.

Horne, J. H. and Baliunas, S. L.: A prescription for period analysis of unevenly sampled time series, Astrophys. J., 302, 757–763, 1986.

Höppner, K. and Bittner, M.: Evidence for solar signals in the mesopause temperature variability?, J. Atmos. Sol.-Terr. Phy., 69, 431–448, doi:10.1016/j.jastp.2006.10.007, 2007.

Jarvis, M. J.: Planetary wave trends in the lower thermosphere – Evidence for 22-year solar modulation of the quasi 5-day wave, J. Atmos. Sol.-Terr. Phy., 68, 1902–1912, doi:10.1016/j.jastp.2006.02.014, 2006.

King, J. W.: Sun-weather relationships, Aeronautics and Astronautics, 13, 10–19, 1975.

King, J. W., Hurst, E., Slater, A. J., Smith, P. A., and Tamkin, B.: Agriculture and sunspots, Nature, 252, 2–3, 1974.

Lastovicka, J., Solomon, S. C., and Qian, L.: Trends in the Neutral and Ionized Upper Atmosphere, Space Sci. Rev., 168, 113–145, doi:10.1007/s11214-011-9799-3, 2012.

Lomb, N. R.: Least-squares frequency analysis of unequally spaced data, Astrophys. Space Sci., 39, 447–462, 1976.

Miyahara, H., Yokoyama, Y., and Masuda, K.: Possible link between multi-decadal climate cycles and periodic reversals of solar magnetic field, Earth Planet. Sc. Lett., 272, 290–295, doi:10.1016/j.epsl.2008.04.050, 2008.

Mokhov, I. I. and Semenov, A. I.: Nonlinear temperature changes in the atmospheric mesopause region of the atmosphere against the background of global climate changes, 1960–2012, Dokl. Earth Sc., 456, 741–744, doi:10.1134/S1028334X14060270, 2014.

Mursula, K. and Zieger, B.: Long term north-south asymmetry in solar wind speed inferred from geomagnetic activity: A new type of century-scale solar oscillation, Geophys. Res. Lett., 28, 95–98, doi:10.1029/2000GL011880, 2001.

Oberheide, J., Offermann, D., Russell III, J. M., and Mlynczak, M. G.: Intercomparison of kinetic temperature from 15 µm CO_2 limb emissions and OH*(3,1) rotational temperature in nearly coincident air masses: SABER, GRIPS, Geophys. Res. Lett., 33, L14811, doi:10.1029/2006GL026439, 2006.

Offermann, D., Donner, M., Knieling, P., and Naujokat, B.: Middle atmosphere temperature changes and the duration of summer, J. Atmos. Sol.-Terr. Phy., 66, 437–450, doi:10.1016/j.jastp.2004.01.028, 2004.

Offermann, D., Jarisch, M., Donner, M., Steinbrecht, W., and Semenov, A. I.: OH temperature re-analysis forced by recent variance increases, J. Atmos. Sol.-Terr. Phy., 68, 1924–1933, doi:10.1016/j.jastp.2006.03.007, 2006.

Offermann, D., Gusev, O., Donner, M., Forbes, J. M., Hagan, M., Mlynczak, M. G., Oberheide, J., Preusse, P., Schmidt, H., and Russel III, J. M.: Relative intensities of middle atmosphere waves, J. Geophys. Res., 114, D06110, doi:10.1029/2008JD010662, 2009.

Offermann, D., Hoffmann, P., Knieling, P., Koppmann, R., Oberheide, J., and Steinbrecht, W.: Long-term trend and solar cycle variations of mesospheric temperature and dynamics, J. Geophys. Res., 115, D18127, doi:10.1029/2009JD013363, 2010.

Offermann, D., Wintel, J., Kalicinsky, C., Knieling, P., Koppmann, R., and Steinbrecht, W.: Long-term development of short-period gravity waves in middle Europe, J. Geophys. Res., 116, D00P07, doi:10.1029/2010JD015544, 2011.

Offermann, D., Goussev, O., Kalicinsky, C., Koppmann, R., Matthes, K., Schmidt, H., Steinbrecht, W., and Wintel, J.: A case study of multi-annual temperature oscillations in the atmosphere: Middle Europe, J. Atmos. Sol.-Terr. Phy., 135, 1–11, doi:10.1016/j.jastp.2015.10.003, 2015.

Perminov, V. I., Semenov, A. I., Medvedeva, I. V., and Zheleznov, Yu. A.: Variability of mesopause temperature from hydroxyl airglow observations over mid-latitudinal sites, Zvenigorod and Tory, Russia, Adv. Space Res., 54, 2511–2517, doi:10.1016/j.asr.2014.01.027, 2014.

Qu, W., Zhao, J., Huang, F., and Deng, S.: Correlation between the 22-year solar magnetic cycle and the 22-year quasicycle in the Earth's atmospheric temperature, Astron. J., 144, 6, doi:10.1088/0004-6256/144/1/6, 2012.

Ryan, S. E. and Porth, L. S.: A tutorial on the piecewise regression approach applied to bedload transport data, Gen. Tech. Rep., RMRS-GTR-189, Fort Collins, CO: U.S. Department of Agriculture, Forest Service, Rocky Mountain Research Station, 2007.

Scafetta, N. and West, B. J.: Estimated solar contribution to the global surface warming using the ACRIM TSI satellite composite, Geophys. Res. Lett., 32, L18713, doi:10.1029/2005GL023849, 2005.

Scargle, J. D.: Studies in astronomical time series analysis. II. Statistical aspects of spectral analysis of unevenly spaced data, Astrophys. J., 263, 835–853, 1982.

Scherrer, P. H., Wilcox, J. M., Svalgaard, L., Duvall Jr., T. L., Dittmeier, P. H., and Gustafson, E. K.: The mean magnetic field of the sun – Observations at Stanford, Sol. Phys., 54, 353–361, 1977.

Schmidt, C., Höppner, K., and Bittner, M.: A ground-based spectrometer equipped with an InGaAs array for routine observations of OH(3-1) rotational temperatures in the mesopause region, J. Atmos. Sol.-Terr. Phy., 102, 125–139, doi:10.1016/j.jastp.2013.05.001, 2013.

Schwarzenberg-Czerny, A.: The distribution of empirical periodograms: Lomb-Scargle and PDM spectra, Mon. Not. R. Astron. Soc., 301, 831–840, doi:10.1111/j.1365-8711.1998.02086.x, 1998.

She, C.-Y., Krueger, D. A., and Yuan, T.: Long-term midlatitude mesopause region temperature trend deduced from quarter century (1990–2014) Na lidar observations, Ann. Geophys., 33, 363–369, doi:10.5194/angeo-33-363-2015, 2015.

Svalgaard, L., Cliver, E. W., and Kamide, Y.: Sunspot cycle 24: Smallest cycle in 100 years?, Geophys. Res. Lett., 32, L01104, doi:10.1029/2004GL021664, 2005.

Thomas, S. R., Owens, M. J., and Lockwood, M.: The 22-year Hale cycle in cosmic ray flux – Evidence for direct heliospheric modulation, Solar Phys., doi:10.1007/s11207-013-0341-5, 2013.

Townsend, R. H. D.: Fast calculation of the Lomb-Scargle periodogram using graphics processing units, Astrophys. J. Suppl. S., 191, 247–253, doi:10.1088/0067-0049/191/2/247, 2010.

Wei, M., Qiao, F., and Deng, J.: A Quantitative Definition of Global Warming Hiatus and 50-Year Prediction of Global-Mean Surface Temperature, J. Atmos. Sci., 72, 3281–3289, doi:10.1175/JAS-D-14-0296.1, 2015.

White, W. B., Lean, J., Cayan, D. R., and Dettinger, M. D.: Response of global upper ocean temperature to changing solar irradiance, J. Geophys. Res., 102, 3255–3266, doi:10.1029/96JC03549, 1997.

Willet, H. C.: Recent statistical evidence in support of predictive significance of solar-climatic cycles, Mon. Weather Rev., 102, 679–686, 1974.

Zechmeister, M. and Kürster, M.: The generalised Lomb-Scargle periodogram – A new formalism for the floating-mean and Keplerian periodograms, Astron. Astrophys., 496, 577–584, doi:10.1051/0004-6361:200811296, 2009.

Zieger, B. and Mursula, K.: Annual variation in near-Earth solar wind speed: Evidence for persistent north-south asymmetry related to solar magnetic polarity, Geophys. Res. Lett., 25, 841–844, doi:10.1029/98GL50414, 1998.

Journal of Atmospheric and Solar-Terrestrial Physics 178 (2018) 7–16

Contents lists available at ScienceDirect

Journal of Atmospheric and Solar-Terrestrial Physics

journal homepage: www.elsevier.com/locate/jastp

Observational evidence for a quasi-bidecadal oscillation in the summer mesopause region over Western Europe

Christoph Kalicinsky[a,*], Dieter H.W. Peters[b], Günter Entzian[b], Peter Knieling[a], Vivien Matthias[b]

[a] *Institute for Atmospheric and Environmental Research, University of Wuppertal, Germany*
[b] *Leibniz-Institute of Atmospheric Physics (IAP), University of Rostock, Ostseebad Kühlungsborn, Germany*

ARTICLE INFO

Keywords:
Mesopause region
Phase height measurements
OH* temperature measurements
Quasi-bidecadal oscillation

ABSTRACT

We analyzed plasma scale height observations (about 80 km altitude) over the Eifel region (50°N, 6°E) observed from Kühlungsborn (54°N, 12°E) in the time interval 1959–2016 and OH* temperatures (center altitude 87 km) observed from Wuppertal (51°N, 7°E) in the time interval 1988–2016. In summer months both time series show a dominant oscillation with a period of about two decades (20–26 years) with amplitudes of about 180 m and 3 K, respectively. These two oscillations are anticorrelated, because their observation altitudes are located above and below the temperature minimum in the mesopause region in summer, i.e. in a region of a positive and negative temperature gradient, respectively. We assume that a periodic vertical displacement of the mean temperature profile (upward and downward shifts following each other) in long-term variability leads to such an anticorrelated temperature evolution at the different observation altitudes. This mechanism is confirmed by SABER observation on board the TIMED satellite.

1. Introduction

The temperature in the mesopause region is characterized by many different variations on different time scales. On short time scales of minutes to months temperatures are influenced by different wave types such as gravity waves, tides, and planetary waves (e.g., Smith, 1997; Bittner et al., 2000; Offermann et al., 2009, 2011; Perminov et al., 2014; Kopp et al., 2015). Furthermore, the temperature variation during one year is characterized by an annual cycle and higher harmonics (e.g., Bittner et al., 2000). Additionally, the temperatures show multi-annual and even decadal variations such as temperature fluctuations coinciding with the 11-year solar cycle and temperature trends (e.g., Beig, 2011a, b, and references therein).

Very long time series of temperatures or temperature proxies in the mesosphere that cover several decades are not very numerous. Among the existing ones the time series of plasma scale heights (PSH) observed from Kühlungsborn (e.g., Peters and Entzian, 2015; Peters et al., 2017) and the time series of OH* temperatures observed from Wuppertal (e.g., Offermann et al., 2010; Kalicinsky et al., 2016) belong to the longest ones as they cover the time intervals 1959–now and 1988 – now, respectively. In the latest studies on OH* temperatures and plasma scale heights (PSH) a variation with a period in the range of two decades was found for both data sets. Kalicinsky et al. (2016) showed that the annual average OH* temperatures (1988–2015) can be described using a fit including the correlation with the 11-year solar cycle (4.1 K/(100 SFU)) and an oscillation with a period of about 25 years. In the case of the PSH observations (1959–2008) Peters et al. (2017) found a significant peak in the spectrum in the period range larger than 16 years. Furthermore, a quasi-periodic variation of the neutral air pressure at 80 km with a period of about 20 years has already been described by von Cossart and Taubenheim (1986) using the same measurements of reflection heights for a shorter time period (1959–1983).

In literature, various other studies can be found that report on the existence of such a long periodic oscillation at other altitudes in the atmosphere. For example, Qu et al. (2012) showed a 22 year oscillation observed in stratospheric temperatures in NCEP/NCAR reanalysis data (Kalnay et al., 1996) at 10 hPa (≈32 km) in the region 30°–50°N in the time interval 1950 to 2000. Coughlin and Tung (2004) extracted an intrinsic mode function with a period of about 25 years in the stratosphere from NCEP/NCAR reanalysis data of geopotential height at 30 hPa (≈24.5 km) in the region 20°–90°N in the time interval 1958–2002 using empirical mode decomposition. Wei et al. (2015) also observed a variation with a period of about two decades of the global mean surface temperatures in the time interval 1850–2014. Beside these variations of atmospheric temperatures a quasi-bidecadal oscillation also exists at the sun, i.e. the reversal of the solar polar magnetic field (Hale cycle) has a period of about two decades (e.g., Svalgaard et al., 2005; Thomas et al., 2014). Furthermore, the oceans also exhibit

---

[*] Corresponding author.
E-mail address: kalicins@uni-wuppertal.de (C. Kalicinsky).

https://doi.org/10.1016/j.jastp.2018.05.008
Received 28 January 2018; Received in revised form 17 May 2018; Accepted 25 May 2018

such a quasi-bidecadal oscillation. One component of the Pacific decadal oscillation (PDO) has a period of about two decades (e.g., Biondi et al., 2001; Mantua and Hare, 2002; Gedalof et al., 2002).

The present study focuses on the two very long time series of PSH and OH* temperatures in the mesospause region and the periodicity and correlation between the observed long-periodic oscillations are analyzed. Additionally, influences of the 11-year solar cycle of the sun are investigated and possible causes for the quasi-bidecadal oscillation are briefly discussed. The paper is structured as follows. In Sect. 2 we describe the observations of OH* rotational temperatures and plasma scale heights. The results of the analysis of these data sets together with results for stratospheric and mesospheric temperatures obtained from reanalysed data sets are presented in Sect. 3. A discussion of possible influences by the sun, plausible external and internal causes for the quasi-bidecadal oscillation, and a description of a mechanism that leads to the anticorrelated temperature evolution is made in Sect. 4. Finally, a summary is given in Sect. 5.

2. Data sets and methods

In this section we introduce the observations of PSH and OH* temperatures and explain the measurements. Additionally, we shortly describe the complementary data sets used in this study and the statistical methods used to analyse periodicities.

2.1. Nightly observations of OH* temperatures

The OH* temperatures are derived from ground-based observations of infrared emission lines using a GRIPS (GRound-based Infrared P-branch Spectrometer) instrument. GRIPS measures 3 emission lines (P1(2), P1(3) and P1(4)) of the OH(3,1) band in the spectral range from 1.524 to 1.543 µm. The relative intensities are used to derive rotational temperatures in the region of the OH emission layer (Bittner et al., 2000, and references therein). This layer is located in the mesopause region at an altitude of about 87 km and has a full width at half maximum (FWHM) of about 9 km (Baker and Stair, 1998; Oberheide et al., 2006). This altitude is not a fixed value as the OH layer altitude varies on different time scales (e.g., García-Comas et al., 2017, and references therein). Nonetheless, the altitude of approximately 87 km is a good value of the mean state of the layer as confirmed by different studies. von Savigny (2015) derived the emission altitude for the OH(3,1) band using SCIAMACHY measurements in the time interval 2003–2011. The altitude typically varies between 86 and 88 km (-10°–30°N, where SCIAMACHY performs measurements throughout the whole year) and no obvious trend is reported. The study by Mulligan and Lowe (2008) showed some larger variations for the layer peak altitude in the years 2004/2005 over Maynooth (53.2°N, 6.4°W, Ireland) obtained from SABER measurements. The altitude varies between approximately 84 to 88 km (maximum in summer) and the FWHM between about 6 and 9 km (lower in summer). In a recent study by Noll et al. (2016) the authors derived the center altitudes for the OH* layer for different upper vibrational levels v′ using SABER measurements over Chile. The center altitude goes from 86.2 km ($v' = 2$) to 89 km ($v' = 9$), thus, it is approximately 86.6 km for the OH(3,1) band. The reported FWHM is 8.6 km. Measurements are carried out every clear night from Wuppertal (51°N, 7°E, Germany). The time series of OH* temperatures starts in mid-1987 and a GRIPS instrument is still in operation to continue the observations. Until mid-2011 the measurements have been carried out by the GRIPS-II instrument (see Bittner et al., 2000, 2002, for an instrument description) and have been continued using the follow-up instrument GRIPS-N (Kalicinsky et al., 2016).

The OH* rotational temperatures have been compared with kinetic temperatures derived from 15 µm CO_2 limb emissions measured by the SABER instrument in former studies by Oberheide et al. (2006) (time interval 2003–2005) and by Offermann et al. (2010) (April 2002–August 2008). The SABER temperature retrieval data versions that have been used for these comparisons were V 1.04/1.06 in the former and V 1.07 in the latter case. For both comparisons higher temperatures were obtained for the ground-based observations (warm bias) and the differences (ground-based minus satellite) were 7.4 K and 3.4 K, respectively, but these differences lie within the combined systematic error bars of the instruments. A comparison between the GRIPS OH* temperatures and corresponding OH* temperatures derived from SCIAMACHY showed a warm bias of 2.7 K (von Savigny et al., 2004). Despite the warm bias the OH* temperatures show the evolution of kinetic temperatures in the mesopause region.

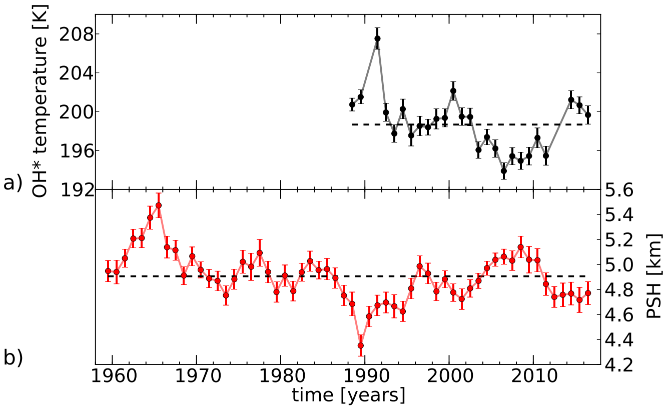

Fig. 1. a): Annual mean OH* temperatures from 1988 to 2016. b): Annual mean plasma scale heights (PSH) from 1959 to 2016. The times given show the beginning of each year and the mean values are displayed in the middle of each year. The error bars show two times the standard error of the fit parameter (for OH*) and two times the standard error of the mean (for PSH). The thin lines connect the mean values. The horizontal black dashed lines show the mean values of each series.

The annual mean temperatures, which show the long-term behavior, are displayed as black full circles in Fig. 1a. Because of the data gaps in the time series, which are mostly caused due to cloudy conditions, the annual mean values are determined using a least squares fit including an annual, a semi-annual and a ter-annual cycle (Bittner et al., 2000, 2002; Offermann et al., 2010; Kalicinsky et al., 2016). Since there are too large data gaps in the years 1991, 2012 and 2013, an annual mean value cannot be determined for these years with sufficient confidence.

2.2. Daily observations of plasma scale height

The plasma scale height (PSH) was derived using indirect phase height measurements between the transmitter Allouis (47°N, 2°E, France, 164 kHz (after February 1986: 162 kHz)) and the receiving station Kühlungsborn (54°N, 12°E, Germany) starting in February 1959. The distance is 1023 km. The reflection point of the signal is located over the Eifel-mountain (50°N, 6°E, Germany). Indirect phase height measurements interpret the received field strength extrema as the interference of ground and sky wave. The phase difference between them allows the calculation of reflection height changes by a layer of constant electron density. If several measuring paths are used, an indirect absolute reflection height is assigned to every field strength extremum. The daily variation of the phase height varies between 87.0 km and 75.2 km, it sinks in the forenoon till midday and increases in the afternoon where the main information is in the mean at 82 km (winter/equinoxes) and 80 km (summer). If the time is converted to $\ln(\mathrm{Ch}(\chi))$ (Ch = Chapman-function, χ = solar zenith distance at the reflection point), the height over $\ln(\mathrm{Ch}(\chi))$ becomes approximately a straight line. From these daily straight lines we obtain two important parameters: the SPH (standard phase height), it is the height at constant $\ln(\mathrm{Ch}(\chi)) = 1.6$, i.e., $\chi = 78.4°$. The SPH-series are anticorrelated to the solar cycle because larger photo-ionization leads to larger electron densities, which reduces the SPH. Furthermore, the statistical analysis of the SPH-series shows a significant overall trend of the order of hundred meters per decade induced by a shrinking stratosphere due to global warming but with strong intra-decadal variability in winter. Peters and Entzian (2015) presented a review of the standard phase height method and discussed results in more details.

The other important parameter is the plasma scale height (PSH), determined by the inclination angle of the straight line mentioned above, i.e., it represents the height difference for $\ln(\mathrm{Ch}(\chi))$ change by one. In this case, after following the height of constant electron density, the scale height of the ionized gas NO, namely the plasma scale height, has to be taken into account (Taubenheim, 1974). The PSH is a function of the temperature of the ionized gas, and under the assumption of thermal equilibrium, it is also a function of the neutral gas temperature. In order to examine this, PSH was compared with CIRA 1965 temperatures (CIRA65, 1965) by Entzian (1967) and Lauter (1974), with rocket temperature measurements by von Cossart and Entzian (1976), and with Lidar temperatures at 82 km altitude by Peters et al. (2017). In all these comparisons, PSH and local temperature correlate significantly for the summer half year. The influence of the winter anomaly (see Sect. 3.1) disturbs this correlation.

The time series of PSH, used here, is part of the release R4 of standard phase height measurements derived under the application of a new diagnostic method and for an extended period, which was performed at the Leibniz-Institute of Atmospheric Physics (Kühlungsborn). The determination of the straight line mentioned above uses seasonal weights and a least squares fit approximation (Peters et al., 2018). The new series cover the period from February 1959 up to January 2017, i.e., 58 years.

The long term behavior of PSH is illustrated in Fig. 1b by annual mean values (arithmetic mean) shown as red full circles. The annual mean values of PSH and OH* temperatures seem to show an anticorrelated behavior, which will be addressed in Sect. 3.1.

2.3. Supplementary data sets and methods

In this study we additionally used different reanalysis data sets of temperatures as well as satellite temperature observations. The satellite temperature observations were made by the SABER instrument aboard the TIMED satellite (e.g., Mlynczak, 1997; Russell III et al., 1999; Yee et al., 2003). The observations of the SABER instrument started 2002. We used the monthly mean values of all available SABER temperatures (day and night; Version 2.0) in the latitude-longitude box 47°–53°N and 0°–12°E. The first reanalysis data set used in this study is NCEP/NCAR Reanalysis 1 (Kalnay et al., 1996). The data set provides temperatures at different pressure levels up to 10 hPa (≈32 km) starting in 1948. The second reanalysis data set is MERRA2 (Gelaro et al., 2017). This data set contains temperatures at pressure levels up to the mesosphere starting in 1980. We used monthly mean values of temperatures in the same grid box as for SABER for both data sets.

The periodicities are analyzed using the Lomb-Scargle-Periodogram (LSP), a statistical method that can handle data gaps and is equivalent to the fitting of sinusoids to the data (Lomb, 1976; Scargle, 1982; Horne and Baliunas, 1986; Townsend, 2010). The unnormalized power gives the reduction in the sum of squares when a sinusoid fit is substracted (with a factor of 1/2). Thus, the power maximizes at that frequency that leads to a minimum in the sum of squares of the residuals for a sinusoid fit to the data with the same frequency (Scargle, 1982). Thus, a normalization with the variance leads to a power that is a measure of the explained variance and that shows a value of (N-1)/2 in the case of a single sinusoid, where N is the number of data points. The significance of the results is evaluated using the false alarm probability (FAP), which gives the probability that a peak above a certain height level can occur by chance, e.g., due to noise. The levels of FAP are determined using simulations of 10,000 noise samples drawn from a Gaussian distribution. For each of these noise samples a LSP is calculated and the height of the maximum peak inside the complete analyzed frequency range is determined. Then the empirical cumulative distribution function (CDF) of these heights is calculated. The CDF gives the probability that a maximum peak below or equal to a certain height value occurs in the case of noise. The FAP is 1 - CDF and this gives the probability that a peak somewhere in the complete frequency range can exceed a certain value (see Schwarzenberg-Czerny, 1998; Cumming et al., 1999; Zechmeister and Kürster, 2009; Kalicinsky et al., 2016, for more details on FAP).

3. Results

In the following subsections the results of the analyses of the different data sets are presented. We focus here on the comparison of the mean seasonal cycles and the quasi-bidecadal oscillation observed for PSH and OH* temperatures. Moreover, we present the results for other mesospheric and stratospheric temperatures in summer, and analyse the possible response to the solar cycle.

3.1. Comparison of the mean seasonal cycle

The mean seasonal cycles of PSH and OH* temperatures are shown in Fig. 2a. These seasonal cycles are determined from time series of monthly mean values for both data sets. Additionally, a detrending procedure (subtraction of the linear regression line) was applied to both time series before calculating the seasonal cycles.

The OH* temperatures (black curve) exhibit a clear seasonal cycle with a pronounced minimum in summer months and a maximum in winter. The seasonal cycle can be described as a combination of annual, semi-annual, and ter-annual cycle, that is able to simulate the narrower minimum in summer and the broader maximum in winter (Bittner et al., 2000).

The seasonal cycle of PSH follows the curve of OH* temperatures from about March to October with lower values in summer. In contrast to the OH* temperatures the PSH significantly drop to a second minimum in winter months. This decrease of PSH is caused by dynamical processes leading to an increase of electron density (caused by enhanced downward transport of NO and, thus, additional ionization) known as winter anomaly (e.g., Lauter, 1974; Peters et al., 2017, and references therein). Since the PSH in winter are largely influenced by additional dynamical processes and not by temperature, only the summer values are used as done before by Peters et al. (2017).

As the annual mean values of OH* temperatures and PSH show a quasi-bidecadal variation, we compared the mean seasonal cycle of the years 2002–2006 with that of 2012–2016 for both data series. The mean solar radio flux F10.7 cm in these two time intervals is nearly the same. The corresponding figures are shown in Fig. 2b and c. Obviously, the largest differences between these two time intervals occur in the summer months, especially May to July, in the case of OH* temperatures. Thus, the differences observed for the annual mean OH* temperatures are mainly driven by the large differences in summer. The comparison for PSH shows a similar picture with large differences in summer. These differences are opposite to those of OH* temperatures, which explains the anticorrelation between the annual mean values of both time series (see Fig. 1).

We compared the PSH and OH* temperature observations with kinetic temperatures of SABER to show that these two quantities serve as good proxies for the relative evolution of the kinetic temperatures at different altitudes. As the center altitude of OH* temperatures is approximately 87 km in summer (see Sect. 2.1), we show this altitude for comparison. The two mean seasonal cycles for the two time intervals are shown in Fig. 2d as black and red curves. Note here that the missing months of the OH* temperatures in 2012 and 2013 are also excluded for SABER temperatures. The two curves and the difference between them correspond well to the observations of OH* temperatures, except for the known offset and a slightly larger deviation in August, which

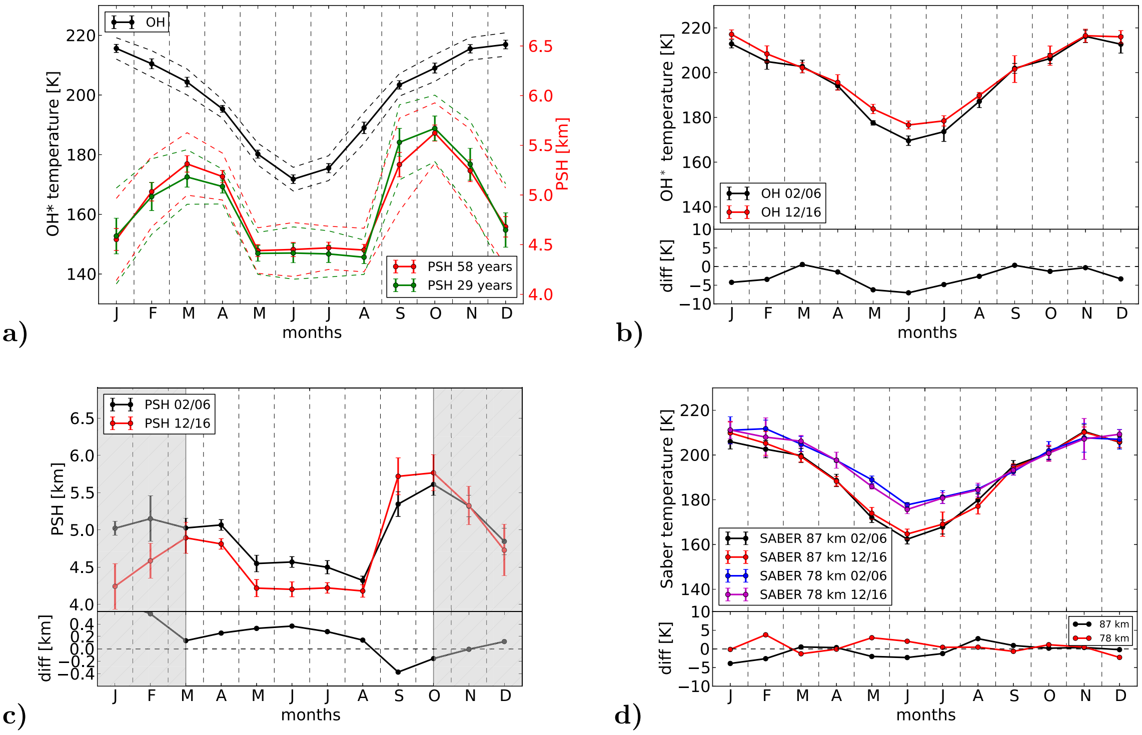

Fig. 2. a): Mean seasonal cycle of OH* temperatures for 29 years (1988–2016) in black, of PSH for 58 years (1959–2016) in red and of PSH for 29 years (1988–2016) in green. The seasonal cycles are derived from monthly mean values where the data series have been detrended before calculating the seasonal cycles. The standard deviation of the monthly mean values (dashed lines) is on average 4.0 K and 0.32 km, respectively. The errors bars show two times the standard error of the mean in all figures. b): Comparison of the mean seasonal cycles of OH* temperatures for the years 2002–2006 (black) and 2012–2016 (red). c): Comparison of the mean seasonal cycles of PSH for the years 2002–2006 (black) and 2012–2016 (red). The winter months are overlayed with a gray area. d): Comparison of the mean seasonal cycles of SABER temperatures in the region 47°–53° and 0°–12°E at 87 km (black and red) and at 78 km (blue and magenta) for the years 2002–2006 and 2012–2016. Additionally, the differences of the seasonal cycles in the different time intervals are shown in the lower panels of b) to d). The difference equals period (2002–2006) minus period (2012–2016). (For interpretation of the references to color in this figure legend, the reader is referred to the Web version of this article.)

may be caused due to the fact that the altitude of 87 km is not fixed (see Sect. 2.1). However, the SABER temperatures at 87 km also show the clear negative temperature differences in summer (MJJ). At the surrounding altitudes (85.5–89.5 km) the SABER temperatures still show negative differences in all of the summer month May, June, and July (for some of the months the range is even larger) and the OH* temperatures are a good proxy for the relative evolution of the kinetic temperatures in this region around 87 km in summer. Consequently, different kinds of averaging the SABER temperatures will lead to OH equivalent temperatures that show these negative differences in summer as the OH* temperatures do. For example, shifts of the center altitude of ±1.5 km and/or variations of the layer width between 6 km and 9 km (see Sect. 2.1) all lead to OH equivalent temperatures that show negative differences in summer months (MJJ) when averaging the SABER temperatures using a Gaussian shaped weighting function as done e.g., by Oberheide et al. (2006).

In the case of PSH the effective altitudes in summer are located around 80 km ranging down to 78 km. The mean seasonal cycles of SABER temperatures at 78 km are shown in Fig. 2d as blue and magenta curves. There is also a reasonable correspondence between the observed differences for temperature and PSH. At the lower altitude of 78 km the difference in summer is opposite to that at 87 km, which is the same behavior as for PSH and OH* temperatures.

Remaining differences, as for example the smaller absolute differences in the case of SABER compared to OH* temperatures, are most likely caused by the averaging procedure of the SABER temperatures (inside the box and during the measurements and retrieval) and they may also be influenced by the averaging of day and nighttime observations for SABER. But the comparisons show that the two time series of PSH and OH* temperatures reflect the relative evolution of kinetic temperatures in the mesopause region at the different altitudes in summer very well.

3.2. Analysis of the quasi-bidecadal oscillation of OH* temperatures and PSH in summer

Because of the winter anomaly that influences the PSH, we concentrate on summer values only. As the clear temperature minimum of the OH* temperatures is in June (see Fig. 2a) and the largest differences between 2002/06 and 2012/16 are in the month May to July, we concentrate on these three months as summer. Nevertheless, we study the robustness of the results by analyzing other combinations of months in Sect. 4.1.

The summer mean values for both data series are shown in Fig. 3. The summer mean values are the average values of the daily/nightly observations in the summer months (MJJ). In the case of PSH 81 days (about 90% coverage) and in the case of the OH* temperatures 56 nights (about 60% coverage) are used on average to calculate one summer mean value. Since there is a data gap in the time series of OH* temperatures in summer 2012, this year has to be excluded from the analysis.

The LSPs for the two complete time series of summer mean values are shown in Fig. 4 as black and red curve, respectively. For both time series a significant peak in the LSP exists between about 20 and 27 years. Note, that the LSP for the OH* summer mean values has a decreased resolution because of the shorter time interval, which leads to much broader peaks. In the frequency space the peak width is approximately 1/T, where T is the time interval length of the observations (e.g., Cumming et al., 1999; Zechmeister and Kürster, 2009). This means that the resolution decreases with decreasing interval length. As

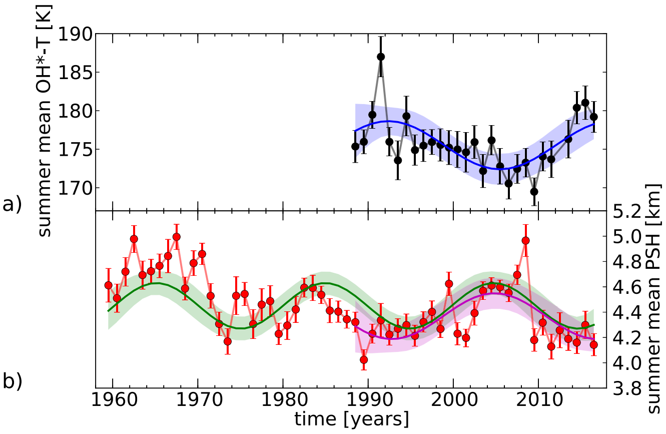

Fig. 3. a): Summer mean values (MJJ) of OH* temperatures in the time interval 1988–2016. b): Summer mean values of PSH in the time interval 1959–2016. The summer mean values are displayed in the middle of each year. The error bars show two times the standard error of the mean. The main sinusoidal oscillation fitted to the data sets is shown as blue curve for OH* temperatures, green curve for 58 years of PSH and magenta curve for 29 years of PSH. The shaded areas display two times the 1σ uncertainties of the fit. (For interpretation of the references to color in this figure legend, the reader is referred to the Web version of this article.)

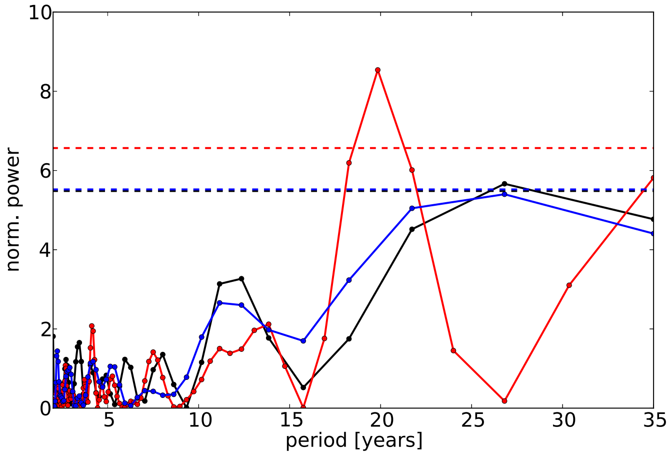

Fig. 4. Lomb-Scargle-Periodograms (LSP) for the summer mean values of OH* temperatures (black), for 58 years of PSH (red) and for 29 years of PSH (blue). The periodogram is calculated at evenly spaced frequencies in the range 1/2 years to 1/35 years and normalized with the variance of the data series. The dashed horizontal lines show the levels of false alarm probabilities (FAP) of 5% in all cases. (For interpretation of the references to color in this figure legend, the reader is referred to the Web version of this article.)

the peak width is constant in the frequency range there is an additional effect in the period range. The peak width and so somehow the uncertainty is larger for larger periods. Beside these significant peaks there are other minor peaks at similar periods in the LSPs, such as at about 10–15 years. The peaks in this range may indicate a response to the 11-year solar cycle. In the case of the annual average OH* temperatures Kalicinsky et al. (2016) already showed the correlation between the solar radio flux F10.7 cm and the temperatures for the time interval 1988–2015. The possible solar influence on the summer mean values is analyzed in Sect. 3.4, and here we focus on the dominant oscillation only. Additionally, we calculated the LSP for the time series of PSH in the time interval 1988–2016 (blue curve in Fig. 4). This LSP is nearly identical to the one for OH* temperatures and by contrast to the LSP for the 58-year time series the largest peak is shifted towards a slightly larger period (FAP of peak >5% and <10%). As the FAP levels refer to the complete analyzed frequency range, it is a worst case comparison. A restriction of the frequency range, e.g., to the period range 10–35 years, will reduce the FAP as it is less likely that a peak somewhere in a frequency range exceeds a certain value, when the frequency range is smaller. Thus, although the analyzed frequency range is very large, the fact that the peaks for the short PSH time series and the OH* temperatures have a FAP around 5% and that both show a peak at the same period is in our opinion a convincing result. The shift of the peak when the PSH time series is shortened is likely a consequence of a non stable period throughout the complete time interval. The result for the complete time interval of PSH (1959–2016) shows a mean state for this interval. When the period is not stable throughout the complete time interval, for different shorter time intervals slightly different periods are obtained.

Table 1
Results for the fits using Eq. (1) and Eq. (2) to the time series of summer mean values (MJJ) of OH* temperatures, PSH, MERRA2 temperatures, and NCEP/NCAR temperatures.

data set	A [K] or [km]	P [years]	ϕ [years]
OH* temperatures 1988–2016	3.1 ± 0.8	26.2 ± 3.8	2.7 ± 2.8
PSH 1988–2016	-0.18 ± 0.05	24.1 ± 3.2	1.8 ± 2.3
PSH 1959–2016	-0.18 ± 0.04	19.8 ± 0.8	-1.4 ± 0.7
MERRA2 0.5 hPa 1980–2016	-0.75 ± 0.24	21.9 ± 2.6	3.1 ± 2.0
MERRA2 1 hPa 1980–2016	-1.6 ± 0.3	28.8 ± 2.7	-0.4 ± 1.4
NCEP/NCAR 30 hPa 1948–2016	0.63 ± 0.14	27.0 ± 1.4	4.3 ± 1.0

The main oscillation is fitted to the data series using the equation

$$\mathrm{T}(t)\ \text{or}\ \mathrm{PSH}(t) = \mathrm{A}\cdot\sin\left(\frac{2\pi}{\mathrm{P}}\cdot((t-1988.5)+\phi)\right)+\mathrm{b}, \tag{1}$$

where A is the amplitude, P the period and ϕ the phase of the sinusoid and b an offset. The important results of the fits are $\mathrm{A} = 3.1 \pm 0.8$ K and $\mathrm{P} = 26.2 \pm 3.8$ years for OH* and $\mathrm{A} = -0.18 \pm 0.04$ km and $\mathrm{P} = 19.8 \pm 0.8$ years for the 58-year time series of PSH (see also Table 1). The given uncertainties are the 1σ uncertainties of the fit parameters based on the standard deviations of the residuals. The resulting fit curves are displayed in Fig. 3a as blue curve and in Fig. 3b as green curve. When using the same time interval from 1988 to 2016 as used for the OH* temperatures also for PSH, the results are $\mathrm{A} = -0.18 \pm 0.05$ km and $\mathrm{P} = 24.1 \pm 3.2$ years (see also Table 1). The corresponding fit is displayed as magenta curve in Fig. 3b. Taking into account the uncertainties the periods derived for the time interval 1988–2016 are the same for PSH and OH* temperatures as already observed in the corresponding LSPs (see Fig. 4). Obviously, the two curves are anticorrelated with corresponding relative maxima and minima. This can also be seen by the good correspondence of the periods and phases and the fact that the amplitude is positive in the case of OH* and negative for PSH (see Table 1). This anticorrelated behavior of the two oscillations is further analyzed and discussed in Sect. 4.3. The difference for the periods when using the different time intervals for the PSH summer mean values most likely indicates that the periodicity is not stable throughout the complete time interval.

3.3. Quasi-bidecadal oscillation in the mesosphere and stratosphere

Since Coughlin and Tung (2004) already showed a mode function with a period of about 25 years extracted from NCEP/NCAR reanalysis data geopotential height (30 hPa; 20°–90°N; 1958–2002), we extend the analysis to the stratosphere by also analyzing NCEP/NCAR data. The summer mean values of the temperatures at 30 hPa (≈24.5 km) in the region 47°–53°N and 0°–12°E from 1948 to 2016 are shown in Fig. 5c. The LSP for the summer mean values shows a significant peak at about 27 years and a second smaller peak at about 11-years (not shown) and, thus, the same behavior as the LSPs for OH* temperatures and PSH. The fit using Eq. (1) to the data series is shown as a green curve.

The main results for the fit parameters are $\mathrm{A} = 0.63 \pm 0.14$ K,

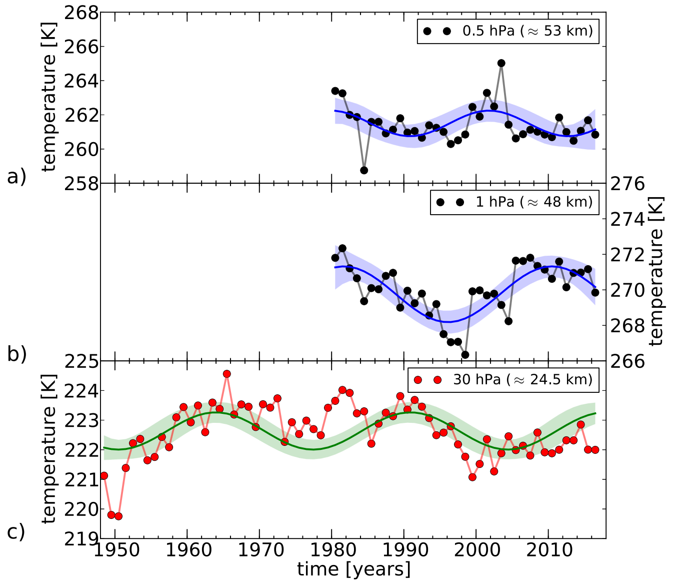

Fig. 5. a), b): Summer mean values (MJJ) of MERRA2 temperatures at 0.5 hPa (≈53 km) and at 1 hPa (≈48 km) from 1980 to 2016. c): Summer mean values of NCEP/NCAR temperatures at 30 hPa (≈24.5 km) from 1948 to 2016. All time series show the average values in the region 47°–53°N and 0°–12°E. The temperatures in panel a) and b) have been detrended (more details see text). The main sinusoidal oscillations fitted to the data sets are shown as blue and green curves, respectively. The shaded areas display two times the 1σ uncertainties of the fit. (For interpretation of the references to color in this figure legend, the reader is referred to the Web version of this article.)

P = 27.0 ± 1.4 years and ϕ = 4.3 ± 1.0 years. In comparison to the former results the fitted oscillation shows nearly the same behavior as the oscillation of OH* temperatures and it is anticorrelated to the oscillation of PSH at the end of the time series. Taking into account the uncertainties the period and phase are the same as the ones for OH* temperatures and the shorter interval of PSH (see Table 1). When moving to the beginning of the PSH time series the anticorrelation to the NCEP/NCAR temperature oscillation weakens. A similar oscillation with a period of about 25 years can be fitted to the data at the surrounding pressure levels, for example, at 20 and 10 hPa (≈27.5 and 32 km) as well as at 50 and 70 hPa (≈21 and 18.5 km). These oscillations are partly accompanied by a linear increase/decrease of the temperature. When going down from 30 hPa (≈24.5 km) the amplitude of the oscillation decreases and the significance of the signal in the LSP decreases as well.

Since the highest level of NCEP/NCAR reanalysis data available is 10 hPa (≈32 km), we additionally analyzed MERRA2 reanalysis data from 1980 to 2016 to continue to higher altitudes. Unfortunately, the time interval is much shorter than that of NCEP/NCAR data. Nonetheless, an approximately 25 year oscillation can be found in the MERRA2 data in the mesosphere, too. Fig. 5a shows the pressure level of 0.5 hPa (≈53 km) as an example. As in the mesosphere a large temperature decrease during the time interval is observed, this has to be accounted for in the fitting. Thus, Eq. (1) expands to

$$\mathrm{T}(t) = \mathrm{A}\cdot\sin\left(\frac{2\pi}{\mathrm{P}}\cdot((t-1988.5)+\phi)\right) + \mathrm{b} + C_{\mathrm{linear}}\cdot(t-1988.5), \tag{2}$$

where C_{linear} gives the linear increase/decrease with time. The results are A = −0.75 ± 0.24 K, P = 21.9 ± 2.6 years, ϕ = 3.1 ± 2.0 years, and C_{linear} = −1.1 ± 0.2 K/decade. The oscillation is shown in Fig. 5a as a blue curve. The temperatures have been detrended using the linear term before displaying to focus on the oscillation only. The oscillation fitted to the temperatures at 0.5 hPa (≈53 km) shows a more or less anticorrelated behavior compared to the oscillation at 30 hPa (≈24.5 km) and to that of the OH* temperatures and it is in phase with that of PSH (see also Table 1). When going further up to the pressure levels 0.4, 0.3, and 0.1 hPa (≈55, 57, and 64.5 km) still an about 25-year oscillation can be observed together with a negative trend. But there is a slight shift of the phase such that the maxima and minima occur earlier. Since the linear decrease of the temperatures is large (up to about - 2.5 K/decade), this may influence the determination of the period and phase, if the decrease is not determined or described correctly, e.g., if it is not strictly linear. Nonetheless, these results strongly suggest that an oscillation similar to that observed for PSH can be observed in the whole mesosphere.

In the stratopause region the situation is not completely clear. Fig. 5b shows the temperature at 1 hPa (≈48 km) as example. The results of a fit to the data using Eq. (2) are A = −1.6 ± 0.3 K, P = 28.8 ± 2.7 years, ϕ = −0.4 ± 1.4 years, and C_{linear} = 0.7 ± 0.2 K/decade. The fit curve is shown in blue and the temperatures have also been detrended before displaying. Even though the period of the obtained oscillation is matching that of the other data sets (PSH, OH* temperatures, and NCEP/NCAR), there is a phase shift and the oscillation is neither completely in phase with that of PSH nor with that of OH* temperatures. When going further down the situation is even more complex. At 2 hPa (≈43.5 km) an about 28 year oscillation can be fitted to the data using Eq. (2) that is in close agreement with the oscillation at 30 hPa (≈24.5 km), whereas at 3 hPa (≈40.5 km) only an oscillation with a much smaller period of about 18 years can be obtained. Even further down at 4 and 5 hPa (≈38.5 and 37 km) oscillations in the period range 20–24 years can be seen, that are already more or less in phase with the oscillations in the mesosphere. Thus, it seems that this region is somehow a transition region with different oscillations.

3.4. *Weak influence of solar cycle*

As the LSPs for the time series of PSH and OH* summer mean values exhibit a peak in the range 10–15 years, the possible correlation of the summer mean values with the 11-year cycle of solar activity is analyzed. Thus, Eq. (1) is expanded to

$$\mathrm{T}(t)\text{ or }\mathrm{PSH}(t) = C_{\mathrm{solar}}\cdot\mathrm{SF} + \mathrm{A}\cdot\sin\left(\frac{2\pi}{\mathrm{P}}\cdot((t-1988.5)+\phi)\right) + \mathrm{b}, \tag{3}$$

where C_{solar} is the correlation coefficient and SF the average solar radio flux F10.7 cm in summer months (MJJ) in solar flux units (SFU).

The results of the fits are A = 2.9 ± 0.7 K, P = 22.5 ± 3.2 years, ϕ = 0.3 ± 2.0 years, and C_{solar} = 3.5 ± 1.5 K/(100 SFU) for OH* and A = −0.18 ± 0.05 km, P = 21.0 ± 2.7 years, ϕ = −0.3 ± 1.7 years, and C_{solar} = −0.16 ± 0.10 km/(100 SFU) for the 29-year time series of PSH. The two oscillations are nearly perfectly anticorrelated in the time interval, in which both observations exist. The results for the 58-year time series of PSH are A = −0.18 ± 0.04 km, P = 19.7 ± 0.8 years, ϕ = −1.2 ± 0.7 years, and C_{solar} = 0.098 ± 0.065 km/(100 SFU). Thus, although the solar radio flux is only quasi periodic and longer variations (e.g., not every maximum is of equal height) are included as well, the obtained oscillations when including this dependency are very similar to the ones before (compare Sect. 3.2 and Table 1 and uncertainties).

The significant (at 2σ level) value of 3.5 K/(100 SFU) for OH* temperatures is in very good agreement with the former studies of the Wuppertal time series of annual average OH* temperatures by Offermann et al. (2010) (3.5 K/(100 SFU)) and Kalicinsky et al. (2016) (4.1 K/(100 SFU)), and other studies of temperatures in the mesopause region (e.g., Beig, 2011a, b; Perminov et al., 2014). The negative correlation of PSH and solar radio flux is not significant at the 2σ level, but, however, this anticorrelation agrees well with the observed anticorrelation of the standard phase heights (SPH) derived from the same measurements and Lyman-alpha observations (Peters et al., 2017). Furthermore, the authors analyzed the correlation between the thickness temperature (mean temperature between stratopause and 81.8 km) and determined a coefficient of 2.3 K/(100 SFU), a value that is also close to the values observed for OH* temperatures.

In total the summer mean values of PSH and OH* temperatures are dominated by the quasi-bidecadal oscillation and the response to the 11-year solar cycle plays a minor role. This can already be seen by the different peak heights in the LSPs (see Fig. 4).

4. Discussion

In the next subsections we discuss the robustness of the quasi-bidecadal oscillation by analyzing different combinations of months to calculate mean values of PSH and OH* temperatures and we briefly discuss the situation in winter. Furthermore, we propose a mechanism that can lead to the anticorrelated long-term behavior of the two time series and, finally, we discuss possible causes for the quasi-bidecadal oscillation.

4.1. Robustness of oscillation

In order to test the robustness of the oscillations observed for the summer mean values (MJJ) we analyzed other combinations of months to calculate mean values of PSH and OH* temperatures. The combinations range from a complete half year (April to September) to combinations of two months such as May/June (MJ). We determined the main oscillation for each of these new time series by fitting Eq. (1) to the data. In the case of the PSH observations we calculated the fits for the two different time intervals 1959–2016 and 1988–2016 (same as OH* temperatures). Note here that no measurements of OH* temperatures after the end of July in the year 2013 exist. Thus, this year has to be excluded in the case of combinations that include the months August or September.

All results are summarized in Table 2. The use of other combinations of months does not lead to significant differences of the resulting amplitudes, phases or periods for each of the three different time intervals and/or observations. Thus, the conclusion is that the observed long-periodic oscillations is a robust result.

The comparison between the results for PSH and OH* in the time interval 1988–2016 shows that, taking into account the uncertainties, the periods and phases are not different for each different combination of months. As this is the case and the amplitudes for PSH and OH* have opposite sign, this clearly suggests the anticorrelated behavior of the oscillations at least in the last about 30 years.

4.2. Quasi-bidecadal oscillation in winter

We additionally analyzed the winter mean values (NDJ) of OH* temperatures to study wether there is a difference for the quasi-bidecadal oscillation and the solar correlation in different seasons. The LSP shows a peak at about 11 years and at about 25 years (not shown). But in contrast to the summer mean values (see Fig. 4) the peak at 11 years is larger than that at about 25 years. The fit results using Eq. (3) are $A = 1.6 \pm 0.5\,\mathrm{K}$, $P = 26.2 \pm 4.1$ years, $\phi = 1.3 \pm 2.7$ years and $C_{\mathrm{solar}} = 3.5 \pm 0.8\,\mathrm{K}/(100\ \mathrm{SFU})$. Thus, the correlation coefficient is the same for both seasons of the year, which shows that the sensitivity to the 11-year solar cycle is independent of the season. Furthermore, the periods of the oscillations in summer and winter agree within the given 1σ uncertainties (when using Eq. (3)). The amplitude of the long periodic oscillation in summer is almost twice as large as in winter. Because of this larger amplitude of the oscillation in summer, the oscillation explains the larger part of the variance compared to the 11-year cycle. In winter the situation is opposite. This opposite situation explains the difference in the peak heights in the LSPs.

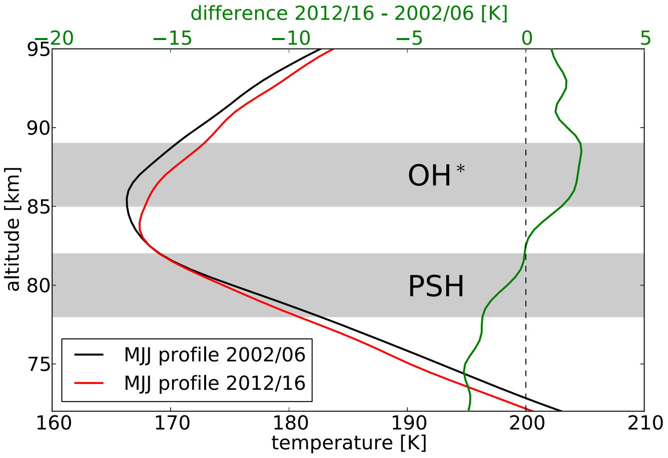

Fig. 6. Mean summer temperature profile (MJJ) derived from SABER observations in the region 47°–53°N and 0°–12°E in the time interval 2002–2006 (black) and in the time interval 2012–2016 (red). The gray horizontal bars show the center regions of OH* temperatures and PSH, respectively. Additionally, the difference between the profile of the second and the first interval is shown with a second axis on the top. (For interpretation of the references to color in this figure legend, the reader is referred to the Web version of this article.)

4.3. Anticorrelation of oscillation

The mean summer temperature profiles derived from SABER observations in the region 47°–53°N and 0°–12°E for the two time intervals 2002–2006 and 2012–2016 are shown in Fig. 6 as black and red curve, respectively. Both profiles show the same vertical structure with a negative vertical temperature gradient up to about 83–85 km, a temperature minimum in that region and increasing temperatures when going further up. But the red profile is more or less a downward shifted version of the black one. As in the center region of the OH* temperatures (marked by the upper horizontal gray bar) the red curve is below the black one, the OH equivalent temperatures in the second interval are larger than those in the first one, as it is observed from the station in Wuppertal (compare Figs. 2b and 3a). Below about 82 km the red curve is also located below the black one. Thus, in the center region of the PSH observations (marked by the lower horizontal gray bar) the temperature in the second interval is smaller than in the first interval (see

Table 2
Results for the fits using Eq. (1) to the different time series of mean values of OH* temperatures and PSH for different combinations of months.

	PSH 1959–2016			PSH 1988–2016			OH 1988–2016		
	A [km]	P [years]	ϕ [years]	A [km]	P [years]	ϕ [years]	A [K]	P [years]	ϕ [years]
MJJ	−0.18 ± 0.04	19.8 ± 0.8	−1.4 ± 0.7	−0.18 ± 0.05	24.1 ± 3.2	1.8 ± 2.3	3.1 ± 0.8	26.2 ± 3.8	2.7 ± 2.8
MJJA	−0.15 ± 0.04	20.0 ± 1.0	−1.1 ± 0.8	−0.16 ± 0.04	25.7 ± 4.2	3.1 ± 3.1	3.1 ± 1.0	29.2 ± 7.0	4.5 ± 5.1
AMJJAS	−0.13 ± 0.04	20.4 ± 1.0	−1.3 ± 0.9	−0.12 ± 0.04	26.3 ± 4.8	2.4 ± 3.5	2.3 ± 0.9	28.7 ± 7.2	3.7 ± 5.1
AMJ	−0.18 ± 0.04	19.6 ± 0.9	−1.5 ± 0.7	−0.14 ± 0.04	23.7 ± 3.6	1.9 ± 2.6	2.3 ± 0.8	28.4 ± 7.4	4.3 ± 5.5
JJA	−0.16 ±. 0.04	20.3 ± 1.0	−0.9 ±0.8	−0.15 ± 0.05	26.3 ± 5.0	3.3 ± 3.7	2.8 ± 1.1	29.6 ± 8.8	4.8 ± 6.4
MJ	−0.19 ± 0.05	19.7 ± 0.9	−1.4 ± 0.8	−0.20 ± 0.05	23.9 ± 3.1	1.8 ± 2.3	3.2 ± 0.8	27.2 ± 4.3	3.6 ± 3.1
JJ	−0.19 ± 0.05	20.1 ± 0.8	−1.3 ± 0.7	−0.18 ± 0.06	24.1 ± 3.4	1.3 ± 2.5	2.8 ± 0.9	24.7 ± 4.3	1.8 ± 3.0
JA	−0.12 ± 0.05	20.7 ± 1.4	−0.3 ± 1.1		no convergence		2.9 ± 1.2	31.5 ± 11.8	5.9 ± 8.6

also difference of both profiles: green curve in Fig. 6), which is also observed for PSH (compare Figs. 2c and 3b).

Thus, the SABER observations confirm the observation of the anticorrelated long-term temperature behavior at the different observation altitudes of PSH and OH* temperatures. When shifting the region, in which the SABER observations are averaged, by half the box size in all four directions (North, South, East, and West) the results are very similar and the opposite behavior at the two observation altitudes is present in all four cases (not shown). As already mentioned above, the mean solar radio flux F10.7 cm in the two time intervals is nearly identical. Thus, an additional influence of the 11-year cycle besides the quasi-bidecadal oscillation, which is the main interest, can be excluded.

Because of the different observation altitudes of OH* temperatures and PSH, which are located in regions with opposite vertical temperature gradients (above and below temperature minimum), a vertical shift of the whole temperature profile in any of the both directions (upward and downward) always leads to an opposite behavior of the temperatures at the different altitudes. Thus, a periodic vertical displacement of the profile with upward and downward shifts following each other then cause temperature oscillations which show an anticorrelated long-term behavior at the different altitudes. The MERRA2 reanalysis data strongly suggests that the long-term behavior of the temperature at the observation altitude of PSH persists downwards through the whole mesosphere. In the mid-stratosphere a similar long-term behavior of the temperature as that of OH* temperatures can be seen in NCEP/NCAR reanalysis data (see Sect. 3.3). Since the vertical temperature gradient in the mesosphere and mid-stratosphere are opposite, these two regions fit into the picture of the periodic vertical displacement of the profile as the mechanism. The situation in the region around the stratopause is not completely clear. Thus, we denoted this region as transition region.

Pisŏft et al. (2009) found disagreements between the occurrences of an approximate 8 year periodicity in temperature fields for NCEP/NCAR and ERA-40 reanalysis data and they concluded that this may be caused by the influence of the assimilation algorithms. Thus, we carried out some comparisons of different reanalysis data sets to obtain more confidence in the shown results. We additionally took ERA-Interim reanalysis data (e.g., Dee et al., 2011) for this purpose. At 30 hPa (the altitude shown in Fig. 5c) the correlation coefficient for the different comparisons of the three data sets is always larger 0.91, which shows a very good agreement of all three data sets at this altitude. Furthermore, at this altitude or surrounding altitudes the quasi-bidecadal oscillations has been extracted from the NCEP/NCAR data series by other scientists using different methods as EMD (Coughlin and Tung, 2004) and power spectrum plus fitting procedure (Qu et al., 2012). Therefore, we think that the results in this altitude range are very reliable as they are confirmed by different data sets and methods. At the altitude of 1 hPa the difference between ERA-Interim and MERRA2 is larger and the correlation coefficient decreases to 0.74. Nonetheless, a period of about 35 years can be determined from the ERA-Interim data, which shows some agreement with the 29-year oscillation observed for MERRA2. But as mentioned above the situation in this region is not clear anyway and we therefore denoted it as transition region. Unfortunately, above 1 hPa only the MERRA2 data are available and no such comparisons are possible.

4.4. *Possible causes of the oscillation*

As a definitive judgement of the cause for the quasi-bidecadal oscillation cannot be made with the analyzed data sets and this issue is beyond the scope of this paper, we only briefly discuss possible options here. Different types are plausible, external such as the sun and the ocean as well as internal by the atmosphere itself, or combinations of two or all of them.

The sun's polar magnetic field shows an approximately two decadal variation, the Hale cycle, with maxima during sunspot minimum and field reversal near sunspot maximum (e.g., Svalgaard et al., 2005; Thomas et al., 2014). Thus, there are zero crossings of the magnetic field, for example, at about 1990, 2000, and 2013 (compare partly Svalgaard et al., 2005, Fig. 1.). When one compares these zero crossings with the behavior of the oscillations obtained for PSH and OH* temperatures in the time interval 1988–2016 (see Fig. 3 and Sect. 3.2), it can be seen that the oscillations of PSH and temperature precede the reversal of the magnetic field by at least one or even more years. Most evident are the differences at the beginning and the end of the mentioned time interval. Since a response cannot precede the forcing or the cause, we tend to exclude the reversal of the solar polar magnetic field as a likely cause as we did before (Kalicinsky et al., 2016). Lower frequency components of the solar input may also play a role, but these should at least partly be accounted for in the correlation analysis using the solar radio flux F10.7 cm (see Sect. 3.4) unless the response of the atmospheric temperatures to these lower frequency components would be much larger.

The Pacific decadal oscillation (PDO) also exhibits a bidecadal component besides components with even lower frequencies (e.g., Biondi et al., 2001; Mantua and Hare, 2002; Gedalof et al., 2002). Thus, there is a possible connection to this variability in the ocean from below and a coupling between the ocean variability and atmospheric temperatures.

In the context of surface air temperatures internally-generated variability in the atmosphere (or the coupled ocean-atmosphere system) plays an important role on the multi-decadal time scale. This variability in the low frequency range can arise from various processes inside the system (e.g., Deser et al., 2012; Wallace et al., 2016, and references therein). Offermann et al. (2015) obtained self-exited oscillations with periods of several years (2 - 6 years) in the whole atmosphere (up to 110 km) over Central Europe from model simulations with fixed boundary conditions, that exhibit a similar vertical structure of correlation/anticorrelation. This vertical structure was also observed for much longer periods (> 20 years) by analyzing further model simulations indicating a vertical displacement of the profile (personal communication D. Offermann).

Even a combination of internal and external variabilities might be possible, which may lead to synchronisation of slightly different periods and phases of the variabilities. Thus, it is imaginable that the atmosphere itself can oscillate at various periods and together with a matching external forcing (e.g., same period) these internal oscillations are largely enhanced whereas oscillations at other periods are damped. An analysis of such interactions and the determination of the cause of the oscillation will rely on model simulations that enable the modification of the boundary conditions to perform different sensitivity studies.

5. Summary and conclusions

We found quasi-bidecadal oscillations at two different altitudes (about 87 km and 80 km) in the mesopause region in summer. Above the temperature minimum at about 87 km the OH* temperatures show a clear quasi-bidecadal oscillation with an amplitude of about 3 K. Below the temperature minimum at about 80 km the analysis of PSH also revealed such a long-periodic oscillation with an amplitude of about 180 m. The PSH oscillation is almost exactly 180° out-of-phase with that of the OH* temperatures, which means that the long-term temperature behavior is opposite at the two different altitudes. As the two observation altitudes are located in regions with opposite vertical temperature gradients, a periodic vertical displacement of the mean temperature profile with consecutive upward and downward shifts can explain this anticorrelated behavior. Temperature observations by the SABER instrument in the same region in summer confirm this mechanism.

MERRA2 reanalysis data show that a similar oscillation to that of PSH can be found in a large part of the mesosphere. In the mid-stratosphere (NCEP/NCAR reanalysis data) the phase of the oscillation is

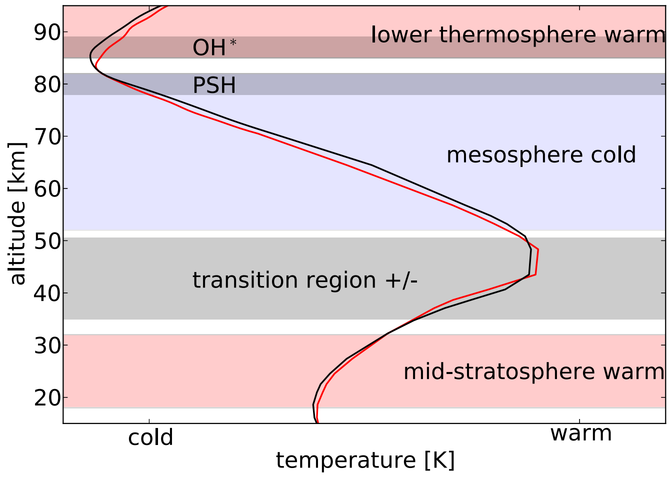

Fig. 7. Sketch of mean summer temperature profiles (MJJ) in two different time intervals (first in black and second in red) to illustrate the effect of a downward shift of the temperature profile in the regions: mid-stratosphere, mesosphere, and lower thermosphere. The temperature behavior at a constant altitude is given by the colored areas in blue for cold and red for warm. Additionally, the center regions of PSH and OH* temperatures are marked by darker dyed horizontal bars. (For interpretation of the references to color in this figure legend, the reader is referred to the Web version of this article.)

such that it is now in phase again with the long-term oscillation observed for OH* temperatures and opposite to that of PSH. This is in accordance with the periodic vertical displacement of the temperature profile, since the sign of the vertical temperature gradient is the same in both regions. A larger region around the temperature maximum in the stratopause region seems to be a transition region from one state to the other.

The whole situation is illustrated in Fig. 7 which shows the situation of a downward shift as example. Two temperature profiles for two time intervals are shown in the figure. The first one is displayed in black and second one in red. In the three regions (mid-stratosphere, mesosphere, and lower thermosphere) there is always a downward shift of the profile from the first to the second one. The temperature behaviors in these regions are marked by colored areas in blue (cold) and red (warm). In such a situation the mid-stratosphere and the lower thermosphere show the same behavior, as the sign of the vertical temperature gradients is the same. Since the gradient in the mesosphere is opposite to this, the temperature behavior as a response to the vertical shift is also opposite. The region around the temperature maximum in the stratopause region is marked as transition region, since responses in both directions can occur and the situation is not unambiguous (compare Sect. 3.3). An upward shift of the profile will lead to the opposite behavior in all regions. Thus, warm regions will turn cold and vice versa. Consequently, a periodic vertical displacement of the whole temperature profile with upward and downward shifts following each other will lead to the observed oscillations and the anticorrelated long term behavior at the different altitudes.

The cause for the quasi-bidecadal oscillation cannot be determined with the analyzed data sets. Such an analysis will require different model sensitivity studies with different boundary conditions for ocean, sun, greenhouse gases, etc. to possibly identify the underlying mechanism and, thus, the cause. This analysis will be future work.

Acknowledgements

This work was partly funded by the German Federal Ministry of Education and Research (BMBF) within the ROMIC (Role Of the Middle atmosphere In Climate) project MALODY (Middle Atmosphere LOng term DYnamics) under Grant no. 01LG1207A. The solar radio flux F10.7 cm data was obtained from the Natural Resources Canada, Space Weather Canada Web site: http://www.spaceweather.gc.ca/. NCEP/NCAR Reanalysis data provided by the NOAA/OAR/ESRL PSD, Boulder, Colorado, USA, from their Web site at http://www.esrl.noaa.gov/psd/ are greatly acknowledged. SABER data were provided by GATS Inc. and are freely available at http://saber.gats-inc.com. The MERRA-2 data used in this study/project have been provided by the Global Modeling and Assimilation Office (GMAO) at NASA Goddard Space Flight Center.

References

Baker, D.J., Stair Jr., A.T., 1998. Rocket measurements of the altitude distributions of the hydroxyl airglow. Phys. Scripta 37, 611. http://dx.doi.org/10.1088/0031-8949/37/4/021.

Beig, G., 2011a. Long term trends in the temperature of the mesosphere/lower thermosphere region: 1. Anthropogenic influences. J. Geophys. Res. 116, A00H11. http://dx.doi.org/10.1029/2011JA016646.

Beig, G., 2011b. Long term trends in the temperature of the mesosphere/lower thermosphere region: 2. Solar response. J. Geophys. Res. 116, A00H12. http://dx.doi.org/10.1029/2011JA016766.

Biondi, F., Gershunov, A., Cayan, D.R., 2001. North pacific decadal climate variability since 1661. J. Clim. 14, 5–10. http://dx.doi.org/10.1175/1520-0442(2001)014<0005:NPDCVS>2.0.CO;2.

Bittner, M., Offermann, D., Graef, H.H., 2000. Mesopause temperature variability above a midlatitude station in Europe. J. Geophys. Res. 105, 2045–2058. http://dx.doi.org/10.1029/1999JD900307.

Bittner, M., Offermann, D., Graef, H.H., Donner, M., Hamilton, K., 2002. An 18-year time series of OH* rotational temperatures and middle atmosphere decadal variations. J. Atmos. Sol. Terr. Phys. 64, 1147–1166. http://dx.doi.org/10.1016/S1364-6826(02)00065-2.

CIRA65, 1965. Cospar Working Group IV, Preparatory Group on the International Reference Atmosphere. North-Holland Pub. Co.

Coughlin, K.T., Tung, K.K., 2004. 11-Year solar cycle in the stratosphere extracted by the empirical mode decomposition method. Adv. Space Res. 34, 323–329. http://dx.doi.org/10.1016/j.asr.2003.02.045.

Cumming, A., Marcy, G.W., Butler, R.P., 1999. The lick planet search: detectability and mass thresholds. Astrophys. J. 526, 890–915. http://dx.doi.org/10.1086/308020.

Dee, D.P., Uppala, S.M., Simmons, A.J., Berrisford, P., Poli, P., Kobayashi, S., Andrae, U., Balmaseda, M.A., Balsamo, G., Bauer, P., Bechtold, P., Beljaars, A.C.M., van de Berg, L., Bidlot, J., Bormann, N., Delsol, C., Dragani, R., Fuentes, M., Geer, A.J., Haimberger, L., Healy, S.B., Hersbach, H., Hólm, E.V., Isaksen, L., Kållberg, P., Köhler, M., Matricardi, M., McNally, A.P., Monge-Sanz, B.M., Morcrette, J.-J., Park, B.-K., Peubey, C., de Rosnay, P., Tavolato, C., Thépaut, J.-N., Vitart, F., 2011. The ERA-Interim reanalysis: configuration and performance of the data assimilation system. Q. J. R. Meteor. Soc. 137, 553–597. http://dx.doi.org/10.1002/qj.828.

Deser, C., Phillips, A., Bourdette, V., Teng, H., 2012. Uncertainty in climate change projections: the role of internal variability. Clim. Dynam. 38, 527–546. http://dx.doi.org/10.1007/s00382-010-0977-x.

Entzian, G., 1967. Quasi-Phasenmessungen im Langwellenbereich (100–200 kHz) zur indirekten Bestimmung von Plasmaparametern in der Hochatmosphäre (60–90 km). Diss. Univ. Rostock.

García-Comas, M., López-González, M.J., González-Galindo, F., de la Rosa, J.L., López-Puertas, M., Shepherd, M.G., Shepherd, G.G., 2017. Mesospheric OH layer altitude at mid-latitudes: variability over the Sierra Nevada observatory in Granada, Spain (37°N, 3°W). Ann. Geophys. 35, 1151–1164. http://dx.doi.org/10.5194/angeo-35-1151-2017.

Gedalof, Z., Mantua, N.J., Peterson, D.L., 2002. A multi-century perspective of variability in the Pacific Decadal Oscillation: new insights from tree rings and coral. Geophys. Res. Lett. 29, 57-1–57-4. http://dx.doi.org/10.1029/2002GL015824. 2204.

Gelaro, R., McCarty, W., Suárez, M.J., Todling, R., Molod, A., Takacs, L., Randles, C.A., Darmenov, A., Bosilovich, M.G., Reichle, R., Wargan, K., Coy, L., Cullather, R., Draper, C., Akella, S., Buchard, V., Conaty, A., da Silva, A.M., Gu, W., Kim, G.-K., Koster, R., Lucchesi, R., Merkova, D., Nielsen, J.E., Partyka, G., Pawson, S., Putman, W., Rienecker, M., Schubert, S.D., Sienkiewicz, M., Zhao, B., 2017. The modern-era retrospective analysis for research and applications, version 2 (MERRA-2). J. Clim. 30, 5419–5454. http://dx.doi.org/10.1175/JCLI-D-16-0758.1.

Horne, J.H., Baliunas, S.L., 1986. A prescription for period analysis of unevenly sampled time series. Astrophys. J. 302, 757–763.

Kalicinsky, C., Knieling, P., Koppmann, R., Offermann, D., Steinbrecht, W., Wintel, J., 2016. Long-term dynamics of OH* temperatures over central Europe: trends and solar correlations. Atmos. Chem. Phys. 16, 15033–15047. http://dx.doi.org/10.5194/acp-16-15033-2016.

Kalnay, E., Kanamitsu, M., Kistler, R., Collins, W., Deaven, D., Gandin, L., Iredell, M., Saha, S., White, G., Woollen, J., Zhu, Y., Chelliah, M., Ebisuzaki, W., Higgins, W., Janowiak, J., Mo, K.C., Ropelewski, C., Wang, J., Leetmaa, A., Reynolds, R., Jenne, Roy, Joseph, Dennis, 1996. The NCEP/NCAR 40-year reanalysis project. Bull. Am. Meteorol. Soc. 77, 437–471. http://dx.doi.org/10.1175/1520-0477(1996)077<$0437:TNYRP>2.0.CO;2.

Kopp, M., Gerding, M., Höffner, J., Lübken, F.-J., 2015. Tidal signatures in temperatures derived from daylight lidar soundings above Kühlungsborn (54°N, 12°E). J. Atmos. Sol. Terr. Phys. 127, 37–50. http://dx.doi.org/10.1016/j.jastp.2014.09.002.

Lauter, E.A., 1974. Mesospheric properties as seen from D-region electron density behaviour. Z. Meteorol. 24, 65–79.

Lomb, N.R., 1976. Least-squares frequency analysis of unequally spaced data. Astrophys.

Space Sci. 39, 447–462.

Mantua, N.J., Hare, S.R., 2002. The pacific decadal oscillation. J. Oceanogr. 58, 35–44. http://dx.doi.org/10.1023/A:1015820616384.

Mlynczak, M.G., 1997. Energetics of the mesosphere and lower thermosphere and the SABER instrument. Adv. Space Res. 20, 1177–1183. http://dx.doi.org/10.1016/S0273-1177(97)00769-2.

Mulligan, F.J., Lowe, R.P., 2008. OH-equivalent temperatures derived from ACE-FTS and SABER temperature profiles – a comparison with OH*(3,1) temperatures from Maynooth (53.2°N, 6.4°W). Ann. Geophys. 26, 1–17. https://doi.org/10.5194/angeo-26-795-2008.

Noll, S., Kausch, W., Kimeswenger, S., Unterguggenberger, S., Jones, A.M., 2016. Comparison of VLT/X-shooter OH and O$_2$ rotational temperatures with consideration of TIMED/SABER emission and temperature profiles. Atmos. Chem. Phys. 16, 5021–5042. https://doi.org/10.5194/acp-16-5021-2016M.

Oberheide, J., Offermann, D., Russell III, J.M., Mlynczak, M.G., 2006. Intercomparison of kinetic temperature from 15 μm CO$_2$ limb emissions and OH*(3,1) rotational temperature in nearly coincident air masses: SABER, GRIPS. Geophys. Res. Lett. 33, L14811. http://dx.doi.org/10.1029/2006GL026439.

Offermann, D., Gusev, O., Donner, M., Forbes, J.M., Hagan, M., Mlynczak, M.G., Oberheide, J., Preusse, P., Schmidt, H., Russel III, J.M., 2009. Relative intensities of middle atmosphere waves. J. Geophys. Res. 114, D06110. http://dx.doi.org/10.1029/2008JD010662.

Offermann, D., Hoffmann, P., Knieling, P., Koppmann, R., Oberheide, J., Steinbrecht, W., 2010. Long-term trend and solar cycle variations of mesospheric temperature and dynamics. J. Geophys. Res. 115, D18127. http://dx.doi.org/10.1029/2009JD013363.

Offermann, D., Wintel, J., Kalicinsky, C., Knieling, P., Koppmann, R., Steinbrecht, W., 2011. Long-term development of short-period gravity waves in middle Europe. J. Geophys. Res. 116, D00P07. http://dx.doi.org/10.1029/2010JD015544.

Offermann, D., Goussev, O., Kalicinsky, C., Koppmann, R., Matthes, K., Schmidt, H., Steinbrecht, W., Wintel, J., 2015. A case study of multi-annual temperature oscillations in the atmosphere: middle Europe. J. Atmos. Sol. Terr. Phys. 135, 1–11. http://dx.doi.org/10.1016/j.jastp.2015.10.003.

Perminov, V.I., Semenov, A.I., Medvedeva, I.V., Zheleznov, Yu.A., 2014. Variability of mesopause temperature from hydroxyl airglow observations over mid-latitudinal sites, Zvenigorod and Tory, Russia. Adv. Space Res. 54, 2511–2517. http://dx.doi.org/10.1016/j.asr.2014.01.027.

Peters, D.H.W., Entzian, G., 2015. Long-term variability of 50 years of standard phase-height measurement at Kühlungsborn, Mecklenburg, Germany. Adv. Space Res. 55, 1764–1774. http://dx.doi.org/10.1016/j.asr.2015.01.021.

Peters, D.H.W., Entzian, G., Keckhut, P., 2017. Mesospheric temperature trends derived from standard phase-height measurements. J. Atmos. Sol. Terr. Phys. 163, 23–30. http://dx.doi.org/10.1016/j.jastp.2017.04.007.

Peters, D.H.W., Entzian, G., Chau, J., 2018. Phasenhöhen-Messungen über Europa während der letzten 5 solaren Zyklen - Langzeitvariabilität der Mesosphäre, Institutsbericht 2016/2017. Leibniz-Institut für Atmosphärenphysik e.V., Kühlungsborn. www.iap-kborn.de.

Pisŏft, P., Mikšovský, M., Žák, M., 2009. An analysis of the spatial distribution of approximate 8 years periodicity in NCEP/NCAR and ERA-40 temperature fields. Eur. Phys. J. Spec. Top. 174, 147–155. http://dx.doi.org/10.1140/epjst/e2009-01097-3.

Qu, W., Zhao, J., Huang, F., Deng, S., 2012. Correlation between the 22-year solar magnetic cycle and the 22-year quasicycle in the Earth's atmospheric temperature. Astron. J. 144 (6). http://dx.doi.org/10.1088/0004-6256/144/1/6.

Russell III, J.M., Mlynczak, M.G., Gordley, L.L., Tansock, J., Esplin, R.W., 1999. Overview of the SABER experiment and preliminary calibration results. Proc. SPIE 3756, 277–288. http://dx.doi.org/10.1117/12.366382.

Scargle, J.D., 1982. Studies in astronomical time series analysis. II. Statistical aspects of spectral analysis of unevenly spaced data. Astrophys. J. 263, 835–853.

Schwarzenberg-Czerny, A., 1998. The distribution of empirical periodograms: Lomb-Scargle and PDM spectra. Mon. Not. Roy. Astron. Soc. 301, 831–840. http://dx.doi.org/10.1111/j.1365-8711.1998.02086.x.

Smith, A.K., 1997. Stationary planetary waves in upper mesospheric winds. J. Atmos. Sci. 54, 2129–2145. http://dx.doi.org/10.1175/1520-0469(1997)054<2129:SPWIUM>2.0.CO;2.

Svalgaard, L., Cliver, E.W., Kamide, Y., 2005. Sunspot cycle 24: smallest cycle in 100 years? Geophys. Res. Lett. 32, L01104. http://dx.doi.org/10.1029/2004GL021664.

Taubenheim, J., 1974. Interpretation of diurnal variations of ionospheric characteristic heights. Z. Meteorol. 24, 102–105.

Thomas, S.R., Owens, M.J., Lockwood, M., 2014. The 22-year Hale cycle in cosmic ray flux – evidence for direct heliospheric modulation. Sol. Phys. 289, 407–421. http://dx.doi.org/10.1007/s11207-013-0341-5.

Townsend, R.H.D., 2010. Fast calculation of the Lomb-Scargle periodogram using graphics processing units. Astrophys. J. Suppl. 191, 247–253. http://dx.doi.org/10.1088/0067-0049/191/2/247.

von Cossart, G., Entzian, G., 1976. Ein Modell der Mesopausenregion zur Interpretation indirekter Phasenmessungen und zur Abschätzung von Ionosphären- und Neutralgasparametern. Z. Meteorol. 26, 219–230.

von Cossart, G., Taubenheim, J., 1986. Indications of a quasi-20-year cycle of middle atmosphere temperatures. Adv. Space Res. 6, 73–75.

von Savigny, C., Eichmann, K.-U., Llewellyn, E.J., Bovensmann, H., Burrows, J.P., Bittner, M., Höppner, K., Offermann, D., Taylor, M.J., Zhao, Y., Steinbrecht, W., Winkler, P., 2004. First near-global retrievals of OH rotational temperatures from satellite-based Meinel band emission measurements. Geophys. Res. Lett. 31, L15111. http://dx.doi.org/10.1029/2004GL020410.

von Savigny, C., 2015. Variability of OH(3-1) emission altitude from 2003 to 2011: long-term stability and the universality of the emission rate–altitude relationship. J. Atmos. Sol. Terr. Phys. 127, 120–128. http://dx.doi.org/10.1016/j.jastp.2015.02.001.

Wallace, J.M., Deser, C., Smoliak, B.V., Phillips, A.S., 2016. Attribution of climate change in the presence of internal variability. In: Climate Change: Multidecadal and Beyond. World Scientific Publishing Co. Pte. Ltd., Singapore, pp. 1–29.

Wei, M., Qiao, F., Deng, J., 2015. A quantitative definition of global warming Hiatus and 50-year prediction of global-mean surface temperature. J. Atmos. Sci. 72, 3281–3289. http://dx.doi.org/10.1175/JAS-D-14-0296.1.

Yee, J.H., Talaat, E.R., Christensen, A.B., Killeen, T.L., Russell III, J.M., Woods, T.N., 2003. TIMED instruments. Johns Hopkins APL Tech. Dig. 24, 156–164.

Zechmeister, M., Kürster, M., 2009. The generalised Lomb-Scargle periodogram - a new formalism for the floating-mean and Keplerian periodograms. Astron. Astrophys. 496, 577–584. http://dx.doi.org/10.1051/0004-6361:200811296.

Atmos. Meas. Tech., 13, 467–477, 2020
https://doi.org/10.5194/amt-13-467-2020

Atmospheric Measurement Techniques
Open Access

Determination of time-varying periodicities in unequally spaced time series of OH* temperatures using a moving Lomb–Scargle periodogram and a fast calculation of the false alarm probabilities

Christoph Kalicinsky, Robert Reisch, Peter Knieling, and Ralf Koppmann

Institute for Atmospheric and Environmental Research, University of Wuppertal, Wuppertal, Germany

Correspondence: C. Kalicinsky (kalicins@uni-wuppertal.de)

Received: 11 September 2019 – Discussion started: 30 September 2019
Revised: 18 December 2019 – Accepted: 6 January 2020 – Published: 5 February 2020

Abstract. We present an approach to analyse time series with unequal spacing. The approach enables the identification of significant periodic fluctuations and the derivation of time-resolved periods and amplitudes of these fluctuations. It is based on the classical Lomb–Scargle periodogram (LSP), a method that can handle unequally spaced time series. Here, we additionally use the idea of a moving window. The significance of the results is analysed with the typically used false alarm probability (FAP). We derived the dependencies of the FAP levels on different parameters that either can be changed manually (length of the analysed time interval, frequency range) or that change naturally (number of data gaps). By means of these dependencies, we found a fast and easy way to calculate FAP levels for different configurations of these parameters without the need for a large number of simulations. The general performance of the approach is tested with different artificially generated time series and the results are very promising. Finally, we present results for nightly mean OH* temperatures that have been observed from Wuppertal (51° N, 7° E; Germany).

1 Introduction

Many time series in atmospheric sciences are characterised by an unequal spacing of the data points, e.g. due to data gaps. OH or other airglow observations often have such data gaps in the measured time series (e.g. Espy et al., 1997; Das and Sinha, 2008; Reid et al., 2014). The OH* temperatures which have been observed from Wuppertal (51° N, 7° E) since the 1980s also exhibit an unequal spacing. The time series of nightly mean OH* temperatures repeatedly has data gaps mainly because of bad weather conditions during some nights that prevent useful measurements (see e.g. Bittner et al., 2000). Within a single night such data gaps can also occur when clouds move through the line of sight. The measurements before and after such a cloud contamination are useful. Typical methods such as the fast Fourier transformation (FFT) rely on a discrete sampling with equal spacing. Thus, a time series like that of OH* temperatures has to be manipulated, e.g. with interpolation techniques before the analysis (e.g. Espy et al., 1997; Bittner et al., 2000; Reid et al., 2014). The Lomb–Scargle periodogram (LSP; Lomb, 1976; Scargle, 1982) is a method that can handle this drawback, as it can be used for time series with unequal spacing. This method has been used in different studies analysing airglow observations (e.g. Espy et al., 1997; Takahashi et al., 2002; Gao et al., 2010; Reid et al., 2014; Egito et al., 2018; Franzen et al., 2018; Nyassor et al., 2018).

A second important point with respect to the analysis of periodicities is the variation of these periodicities with time, i.e. the period is not stable during the complete analysed time interval or the amplitude varies. In such cases many methods as the FFT and the LSP will lead to results of a mean state only. The wavelet transform is a method that is very useful as it delivers time-resolved information on the periodicities of the analysed time series and it is used in several studies analysing the temporal evolution of periodic signals in airglow observations (e.g. Das and Sinha, 2008; Takahashi et al., 2013; Reid et al., 2014; Nyassor et al., 2018). In the case of the Wuppertal OH* temperatures, Bittner et al. (2000) used the wavelet transform to analyse the variability of the nightly mean OH* temperatures after assimilation of the data gaps in the time series by use of the maximum entropy method (MEM). Similar to that, other studies also report that the time series have to be interpolated before the use of the wavelet transform (e.g. Das and Sinha, 2008; Reid et al., 2014) or the sampling is at least almost evenly distributed (Nyassor et al., 2018). The goal of the presented study is to avoid such an assimilation of the data gaps and still derive time-resolved information on the periodicities. Thus, we combined the LSP and the idea of a moving window to identify and characterise periodicities in unequally spaced time series even when the periodicities vary with time. Other airglow studies also use some kind of windowed LSP but for independent time windows following each other such as different parts of a night (Reid et al., 2014) or months of a year (Egito et al., 2018). Some studies analysing radar observations of winds report a periodogram analysis with a moving window (Yoshida et al., 1999, but without significance evaluation) or a LSP analysis for at least partly overlapping windows (Luo et al., 2000). However, our study combines the LSP with a moving window (moved with the minimum possible time step); additionally, we derive a fast and easy method to calculate the false alarm probabilities (FAPs) for different situations (length of time series, frequency range, data gaps) to identify significant results. The determination of the FAP levels is typically done with Monte Carlo simulations, which is very time-consuming (e.g. Cumming et al., 1999; Zechmeister and Kürster, 2009). Thus, our new empirically derived relationship to calculate the levels improves the application of the method.

The main intention of the paper is to describe the approach from a user perspective and to illustrate the capabilities of the approach with examples of artificial data sets as well as observations. The paper is structured as follows. In Sect. 2 the classical LSP and the new approach are explained. The evaluation of the significance of obtained results is made in Sect. 3. Finally, the method is applied to artificial data and observations of OH* temperatures in Sect. 4. A short summary is given in Sect. 5.

2 Methodology

2.1 Classical Lomb–Scargle periodogram

The Lomb–Scargle periodogram (LSP) was developed by Lomb (1976) and Scargle (1982). The periodogram is defined as

$$P_X(\omega) = \frac{1}{2} \left\{ \frac{\left[\sum_j X_j \cos\omega(t_j-\tau)\right]^2}{\sum_j \cos^2\omega(t_j-\tau)} + \frac{\left[\sum_j X_j \sin\omega(t_j-\tau)\right]^2}{\sum_j \sin^2\omega(t_j-\tau)} \right\}, \quad (1)$$

where X_j represents the measurements at the times t_j, ω is the angular frequency ($\omega = 2\pi f$), and the time offset τ is defined as

$$\tan(2\omega\tau) = \frac{\left(\sum_j \sin 2\omega t_j\right)}{\left(\sum_j \cos 2\omega t_j\right)}. \quad (2)$$

An advantage compared to other methods such as the FFT is that the LSP can handle unequally spaced time series. A prerequisite is that the time series has zero mean before the calculation of the periodogram powers. With the given definition, the LSP has two useful properties: (1) it is invariant to a shift of the origin of time, and (2) it is equivalent to the least squares fitting of sinusoids (e.g. Horne and Baliunas, 1986). Scargle (1982) showed that the definition of the periodogram is the same (except for a factor of $1/2$) as the reduction in sum of squares (sum of squares of data minus sum of squares of residual) when using least squares fitting of sinusoids (see Scargle, 1982, Appendix C). Thus, the maximum power in the periodogram occurs at that frequency that leads to a minimum of the sum of squares of the residuals when a sinusoid with this frequency is fitted to the time series.

2.2 Moving LSP

The approach used in the following analyses is based on the classical LSP, but the whole time series is analysed sequentially. The procedure is as follows.

A window size (time interval), which is typically much smaller than the length of the whole time series, is defined. Then the procedure starts at the beginning of the time series:

1. calculate LSP for the data points within the window (time interval),
2. move the window by one time step (minimum possible sampling step),
3. move to step one until the end of the times series is reached.

By executing this procedure, one single LSP is calculated for each possible part of the time series with the length of the window (time interval). By contrast to the LSP for the whole time series at once, this procedure delivers time-resolved information on the periodicities and amplitudes.

2.3 Normalisation of the LSP

There are different ways to normalise the periodogram: sample variance (or sum of squares), known variance of data, and variance of the residuals (see e.g. Cumming et al., 1999; Zechmeister and Kürster, 2009). Here we use the normalisation by the sample variance and sum of squares, respectively. These two only differ by a constant factor that relies on the number of data points N. The periodogram power can vary between 0 and $(N-1)/2$ when using the normalisation by the sample variance and between 0 and 1 when using the normalisation by sum of squares (when the factor $1/2$ is also considered; compare Sect. 2.1) (e.g. Cumming et al., 1999; Zechmeister and Kürster, 2009). As the height of a peak in the case of the normalisation by the variance depends on the number of data points N, the peak heights for the same sinusoid differ for different numbers of data points. Since the data gaps in the time series of nightly mean OH* temperatures are randomly distributed, the number of data points in different possible windows of same size can vary. In order to make the peak heights in these different windows comparable, we prefer the normalisation by the sum of squares. This type of normalisation has another useful property. Because of the equivalence to the reduction in sum of squares when fitting a sinusoid, the normalisation by the sum of squares leads to a normalised power that gives the contribution of the sinusoid to the total sum of squares, and therefore to the total variance. In this way it is a measure of the explained variance. Here non-correlation between different sinusoids and/or a sinusoid and the residual is assumed. This is, at least approximately (increasing with number of data points), the case for sinusoids with different periods and, thus, the variances of the individual parts (sinusoids) of the time series add up.

Alternatively, one can determine the amplitude of the sinusoid at each frequency. This is also based on the equivalence of the periodogram power and the reduction in sum of squares. Furthermore, the variance of a sinusoid is given by $A^2/2$, where A is the amplitude (e.g. Horne and Baliunas, 1986; Smith, 1997). With these two relationships, the amplitude can be calculated as

$$A(\omega) = \sqrt{\frac{4P_X(\omega)}{N-1}}. \tag{3}$$

In total the LSP delivers information on the periodicities together with a measure of the explained variance when a sinusoid is fitted to the data and the corresponding amplitude of the sinusoid. An example periodogram is shown in Fig. 1. The time series that is analysed is a combination of two sinusoids with different periods and amplitudes. The first one has a period of 10 d and an amplitude of 1 K, whereas the second sinusoid has a period of 35 d and an amplitude of 0.5 K. The total length of the time series is 60 d and the time series has equal spacing. Thus, the variance of the second sinusoid is only one-quarter of the variance of the first one. This can be seen in the normalised power (black curve in Fig. 1) where at 10 d a value of about 0.8 is reached and at 35 d a value of about 0.2 is reached. Because of the different amplitudes, the sinusoids contribute 80 % and 20 % to the total variance of the time series. And also the amplitudes themselves are well determined by using Eq. (3) (see red curve in Fig. 1).

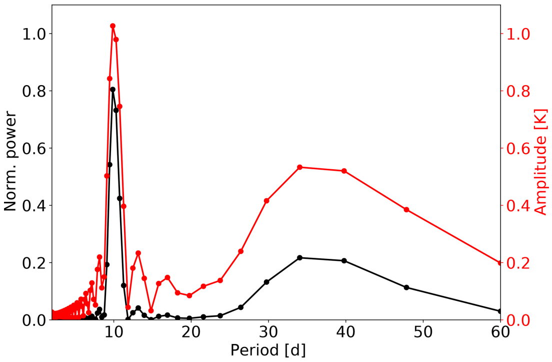

Figure 1. Example LSP for a time series composed of two sinusoids. The first one has a period of 10 d and an amplitude of 1 K and the second has a period of 35 d and an amplitude of 0.5 K. The normalised power is shown as a black curve and the amplitude as a red curve with a second axis to the right.

3 Significance evaluation

3.1 False alarm probability

An important quantity with respect to the LSP is the so-called false alarm probability (FAP). It gives the probability that a peak with a height above a certain level can occur just by chance, e.g. due to noise. The distribution of the periodogram powers and thus the description of the false alarm probability depends on the type of normalisation (see e.g. Cumming et al., 1999; Zechmeister and Kürster, 2009). In the case of the normalisation by the sample variance, the periodogram powers follow a beta distribution (Schwarzenberg-Czerny, 1998). As the variance and the sum of squares differ by a constant factor only, the type of distribution is the same. Hereafter, we only describe the situation for the normalisation by sum of squares. At a single frequency the probability that a peak height z exceeds a value of z_0 is given by

$$\mathrm{Prob}(z > z_0) = (1 - z_0)^{\frac{N-3}{2}}, \tag{4}$$

where N is the number of data points (Zechmeister and Kürster, 2009). Since periods in a frequency range are analysed, one is interested in the probability that one peak somewhere in the periodogram covering a frequency range Δf exceeds a certain value by chance, which is given by the FAP. The probability that all peaks in this frequency range are below or equal to a certain value is given by $(1 - \mathrm{Prob}(z > z_0))^{N_\mathrm{i}}$, where N_i is the number of independent frequencies (number of frequencies where potentially peaks can occur).

Then the FAP is

$$\mathrm{FAP} = 1 - \left(1 - \mathrm{Prob}(z > z_0)\right)^{N_\mathrm{i}}, \tag{5}$$

where N_i gives the number of independent frequencies (see e.g. Horne and Baliunas, 1986; Cumming et al., 1999; Zechmeister and Kürster, 2009, for some discussion on FAP). There is no analytical way to describe the number of independent frequencies, but a good way to determine N_i is the use of Monte Carlo simulations (see e.g. Cumming et al., 1999).

The procedure to determine N_i using simulations is as follows. As already pointed out by Scargle (1982) the cumulative distribution function (CDF) can be used to determine the FAP. We use a large number of samples of random values taken from a Gaussian distribution. Then we calculate the LSP for each sample and determine the height of the maximum peak within the analysed frequency range. From these maximum peak heights, we calculate the empirical CDF which gives the probability that the maximum peak and thus all other peaks in a periodogram have a height equal to or below a certain value. The CDF is then given by $(1 - \mathrm{Prob}(z > z_0))^{N_\mathrm{i}}$, and consequently the FAP is then 1−CDF. In the last step we determine N_i by fitting Eq. (5).

An example for the results of this procedure is shown in Fig. 2. The example shows the FAP derived from 10 000 samples of Gaussian noise, where each sample has 60 data points and a sampling of $1\,\mathrm{d}^{-1}$; thus, the complete time interval length is 60 d. The frequency range used for the analysis is $\Delta f = 1/2\text{–}1/60\,\mathrm{d}^{-1}$. The frequency sampling during these simulations (and all other simulations) is fixed with respect to the length of the time interval, thus the duration of observations T and the frequency range. We evaluated the LSP at N_freq equally spaced frequencies in the frequency range Δf, where $N_\mathrm{freq} = 4T\Delta f$, which was shown to be an adequate sampling to observe all possible peaks by Cumming et al. (1999). The blue circles show the results for $\mathrm{Prob}(z > z_0)$ at a single frequency. The theoretical curve of Eq. (4) is shown in magenta. The determined probability and the theoretical one match very well. The results for the FAP (1-CDF) are shown as black circles. The red curve is determined by fitting Eq. (5) to these data points. The number of independent frequencies N_i in this case is about 72. From this curve, different FAP levels can be determined. In the following we typically use a FAP level of 5 %, which means that in only 5 % of the noise samples the maximum peak in the complete frequency range exceeded the corresponding peak height value. In Fig. 2 the dashed horizontal line marks a FAP of 5 % and the intersection with the red curve gives the height of about 0.225 that corresponds to this level.

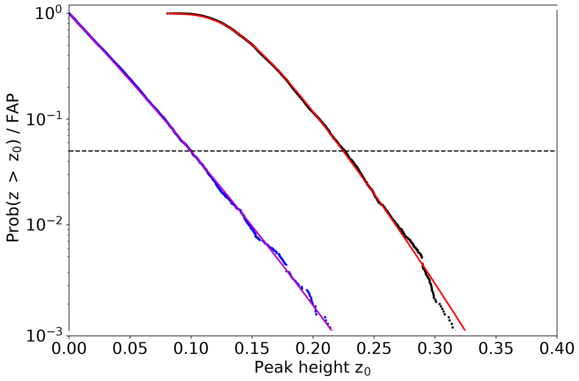

Figure 2. False alarm probability (FAP) and $\mathrm{Prob}(z > z_0)$ at a single frequency derived from 10 000 noise samples with 60 data points each. The data sampling was $1\,\mathrm{d}^{-1}$ and the analysed frequency range $\Delta f = 1/2\text{–}1/60\,\mathrm{d}^{-1}$. The derived $\mathrm{Prob}(z > z_0)$ is shown with blue circles and the theoretical curve (Eq. 4) is depicted in magenta. The determined FAP is shown by the black circles and the fit to these data points using Eq. (5) is displayed as red curve. The dashed horizontal line marks a FAP of 5 %.

3.2 Dependency of N_i and FAP

The number of independent frequencies N_i and the false alarm probability depend on different factors: the length of the analysed time interval T, the data gaps within the time interval, and the analysed frequency range Δf. Since different situations with respect to data gaps can occur during the analysis of the OH* temperatures and, additionally, the length of the window (time interval) and the frequency range can be chosen, one would have to perform simulations for all situations. As these simulations are much more time-consuming than the calculation of the LSP itself, we want to avoid these numerous simulations. Thus, we examined the different dependencies to find a faster and easier way to determine N_i and thus the FAP levels. The sampling of the time series used for these analyses was chosen to be $1\,\mathrm{d}^{-1}$, which is the same as for the nightly mean OH* temperatures without data gaps. For the different analyses, we varied only one parameter and kept the other two fixed. In all cases 10 000 noise samples were used to determine one N_i value.

Firstly, we analysed the dependency of N_i on the length of the time interval T. Here the frequency range was kept constant and the time series had no data gaps. As this is the case and the sampling is $1\,\mathrm{d}^{-1}$, the length of the time interval is equal to the number of data points N, i.e. a time interval of 60 d has 60 data points. The frequency range was fixed to $\Delta f = 1/2\text{–}1/60\,\mathrm{d}^{-1}$ for the first analysis. Since the width of a peak is inversely proportional to the length of the analysed time interval (see e.g. Cumming et al., 1999; Zechmeister and Kürster, 2009), the number of independent frequencies N_i for a fixed frequency range should linearly increase with increasing time interval length. Figure 3 shows the results for N_i for different time interval lengths T between 30 and 90 d (typical values used for the analysis of nightly mean OH* temperatures) as blue full circles. Obviously, the dependency is linear. A linear fit including an additional intercept leads to an intercept of about zero. Thus, we calculated a fit line that has to intersect the point (0, 0) and only determined the slope of this line, which is 1.208 ($\pm$0.004) d^{-1}. The fit is shown as a blue line in Fig. 3a. Since the number of data points N increases with increasing length of the time interval T, the probability that the power at a single frequency exceeds a certain value by chance decreases (compare Eq. 4). As this effect is larger than the opposite effect of the increase in N_i, the FAP levels also decrease. Figure 3b shows the levels of a FAP of 5 % for the different time interval lengths as blue full circles.

In a second analysis we varied the frequency range and repeated the analysis that was done before. The frequency ranges lay between 1/2–1/5 and 1/2–1/90 d^{-1}. A smaller frequency range should include a smaller number of independent frequencies. As the decrease in N_i for a reduction of Δf depends on the width of the peaks, and therefore on the length of the time interval T, the decrease in N_i for the same reduction of Δf has to be larger for larger T. This can be seen in Fig. 3a, where example results for the frequency ranges 1/2–1/5 and 1/2–1/10 d^{-1} are shown in black and red, respectively. For the smallest frequency range, the lowest values can be seen and the largest decrease in N_i is observed for the longest time interval T. Because of this dependency of the decrease in N_i on the time interval length, the fit lines are not shifted by a constant value, but the slopes of the fit lines change. Thus, the slopes depend on frequency range Δf. Figure 3c shows the dependency of the slopes on the frequency range Δf. Obviously, for the analysed frequency ranges this dependency can be described by a straight line. A fit to the data leads to the results for the slope of 2.92 ($\pm$0.02) $\mathrm{d\,d}^{-1}$ and for the intercept of -0.203 ($\pm$0.008) d^{-1}. The fit line is shown as black line. With the knowledge of these parameters the number of independent frequencies N_i can be determined for each combination within the analysed parameter range by

$$N_\mathrm{i} = \left(2.92\,\mathrm{d\,d}^{-1} \cdot \Delta f - 0.203\,\mathrm{d}^{-1}\right) \cdot T. \tag{6}$$

In the last analysis we evaluated the dependency of N_i on the number of data gaps in a fixed time interval. The frequency ranges for this analysis were $\Delta f = 1/2$–$1/5$, 1/2–1/10, and 1/2–1/60 d^{-1}. We took a time interval of 60 d and introduced 1 to 29 randomly distributed data gaps. We only removed data points inside the complete time interval, i.e. both end points were always there and the time interval length was always 60 d. Since the spectral width of the peaks depends on the length of the time interval, which is fixed, and not on the number of data points, the number of independent frequencies N_i is supposed to be almost the same for different numbers of data gaps. Figure 4a shows N_i as a function of the number of data gaps for different frequency ranges. In all cases only a slight decrease in N_i with increasing number of gaps can be seen. The decrease is slightly larger for those frequency ranges that lead to larger N_i values. But the relative decrease is very similar for all shown situations. The decrease in all cases is only of the order of a few percent for 50 % data gaps. This decrease is caused by an on average very small decrease in the resolution caused by a small increase in the peak width. Although the number of independent frequencies is nearly constant, this does not mean that the FAP levels stay the same. Since the number of data points N decreases with increasing number of data gaps, the probability that the power at a single frequency exceeds a certain value increases (compare Eq. 4). Thus, the FAP for a certain peak height also increases. This increase is shown

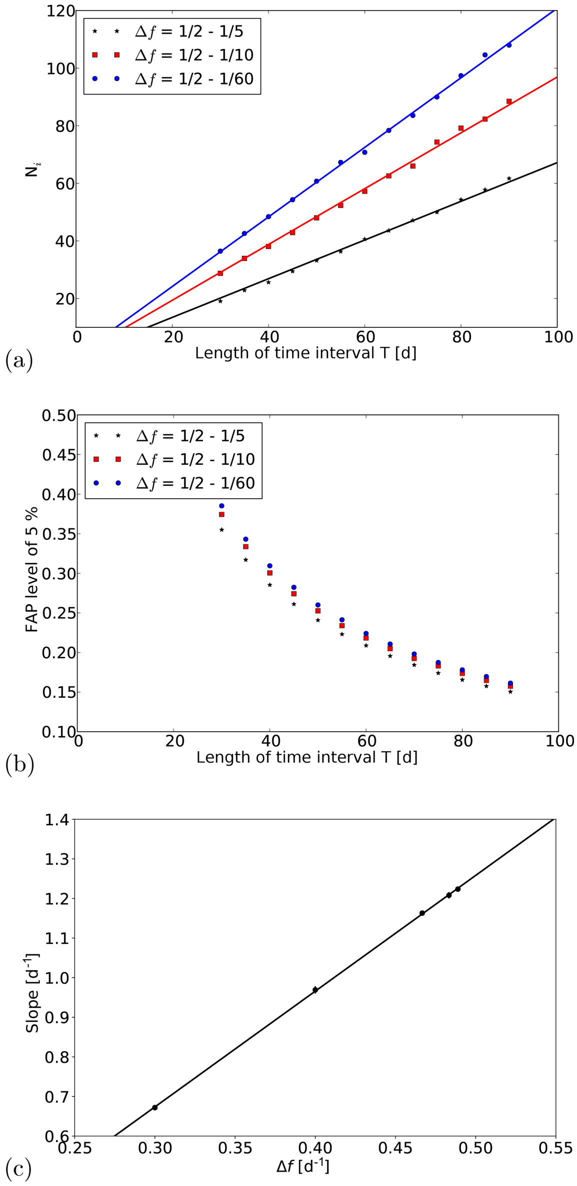

Figure 3. (a, b) Dependency of N_i and the FAP level of 5 % on the length of the time interval T and the frequency range. The analysed frequency ranges are 1/2–1/5, 1/2–1/10, and 1/2–1/60 d^{-1}, and the time series of the simulations have no data gaps. **(c)** Dependency of the slopes (lines from panel **a**) and additionally for the frequency ranges (1/2–1/30 and 1/2–1/90 d^{-1}) on the frequency range Δf. The error bars show 2 times the standard error of the slopes.

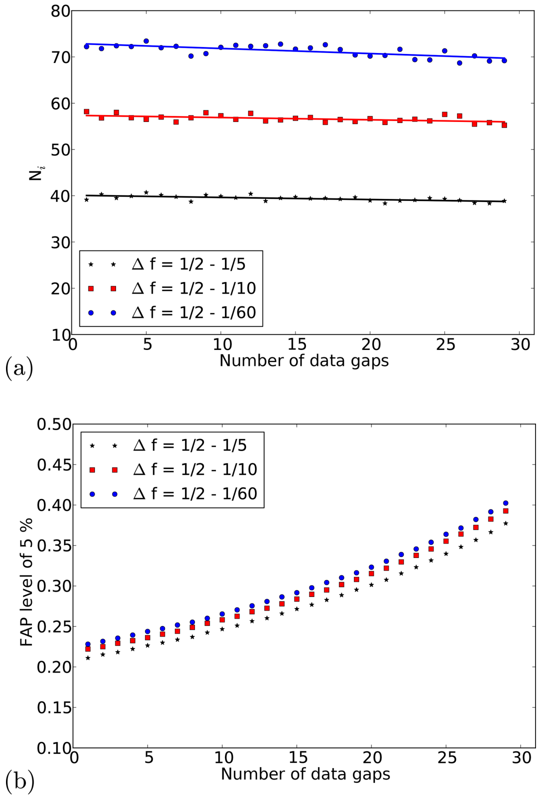

Figure 4. Dependency of N_i and the FAP level of 5 % on the number of data gaps in a fixed time interval of length T. The analysed frequency ranges are 1/2–1/5, 1/2–1/10, and 1/2–1/60 d^{-1}, and the time interval length is 60 d.

in Fig. 4b. The effect of the decrease in N_i on the FAP levels of 5 % is typically of the order of a few per mil (‰). Thus, a non-consideration of this decrease in N_i would lead to a very small change in the FAP levels. Furthermore, the change when considering the decrease would be negative, i.e. the FAP for the same height z would get smaller. Consequently, the FAP levels of 5 % also have smaller values. Thus, a non-consideration would not change the judgement if a signal is significant or not in a false way. When a signal exceeds a higher value it will certainly exceed a smaller value, too. Nonetheless, in the FAP levels shown later on, the effect of the data gaps on the N_i values is considered.

4 Data evaluation

4.1 Artificial data

In order to study the performance of the approach we analysed different time series of artificial data. In this section we present selected examples of these time series. The total length of the time series was always 1 year (365 d) and the sampling was 1 d^{-1}, which is the same as for the nightly mean OH* temperatures without data gaps.

The analysis of a single sinusoid is a very trivial problem and the approach delivers the expected results (not shown). As the approach shall be used in the case of non-stable periodicities, we focus here on such problems. The first example shows a time series of a periodic signal with a period that increases with time from approximately 8 to 16 d and an amplitude of 1 K. The time series is shown in Fig. 5a as a black curve. (The components signal (blue) and noise (green) are shown additionally in separate panels.) The results of the analysis are shown in Fig. 5b and c for the normalised power and the amplitude, respectively. The y axes of these two figures give the frequency and period, respectively, and the x axes show the centre days of the sequentially analysed time intervals. The normalised power and the amplitude are shown colour coded and the white contour lines mark the FAP level of 5 % (N_i was determined using Eq. 6). The results clearly show the change in the period with time and the normalised power is close to one. The small deviation from a value of one can be explained by the change in the period, which occurs on a smaller timescale than the interval size of 60 d. Thus, a sinusoid with a fixed period is not able to explain the complete variance in each of the analysed time intervals. The results for the amplitude show values close to 1 K, and thus also the expectation. The analysis was repeated for the same periodic signal with additional noise added to the time series and also data gaps that have been incorporated. The standard deviation of the noise was 0.5 times the standard deviation of the signal and thus the variance of the noise is one-quarter of that of the signal. Additionally, about 30 % of the data points have been randomly removed. The signal with gaps (blue curve), the noise (green curve), and the complete time series (sum of both; black curve) are shown in Fig. 5d. The corresponding results are shown in Fig. 5e and f. The displayed FAP level of 5 % was determined for each LSP individually with respect to the varying length of the time interval (when end points are missing) and the number of data points inside these time intervals. Additionally, the small decrease in N_i due to the data gaps was considered (see Sect. 3.2). The change in the period is still captured very well. In the case of noise and data gaps, the normalised power reduces to a value of about 0.8 as a part of the variance can be explained by the contribution of the noise (ratio 4 to 1 for signal to noise). The amplitude shows some fluctuations, but these fluctuations go around a value of 1 K. Additionally, the noisy behaviour at smaller periods is much better visible for the amplitudes compared to the powers, because the square root of the powers enters the calculation of the amplitudes (compare Eq. 3) and therefore differences with respect to the maximum amplitude get smaller. In total, the results clearly capture the main features of the time series with respect to period, amplitude, and explained variance.

We additionally present two further examples. The time series and the results of the analyses are shown in Fig. 6. The first time series is composed of a periodic signal with a period of 25 d, and an amplitude that varies between 0 and

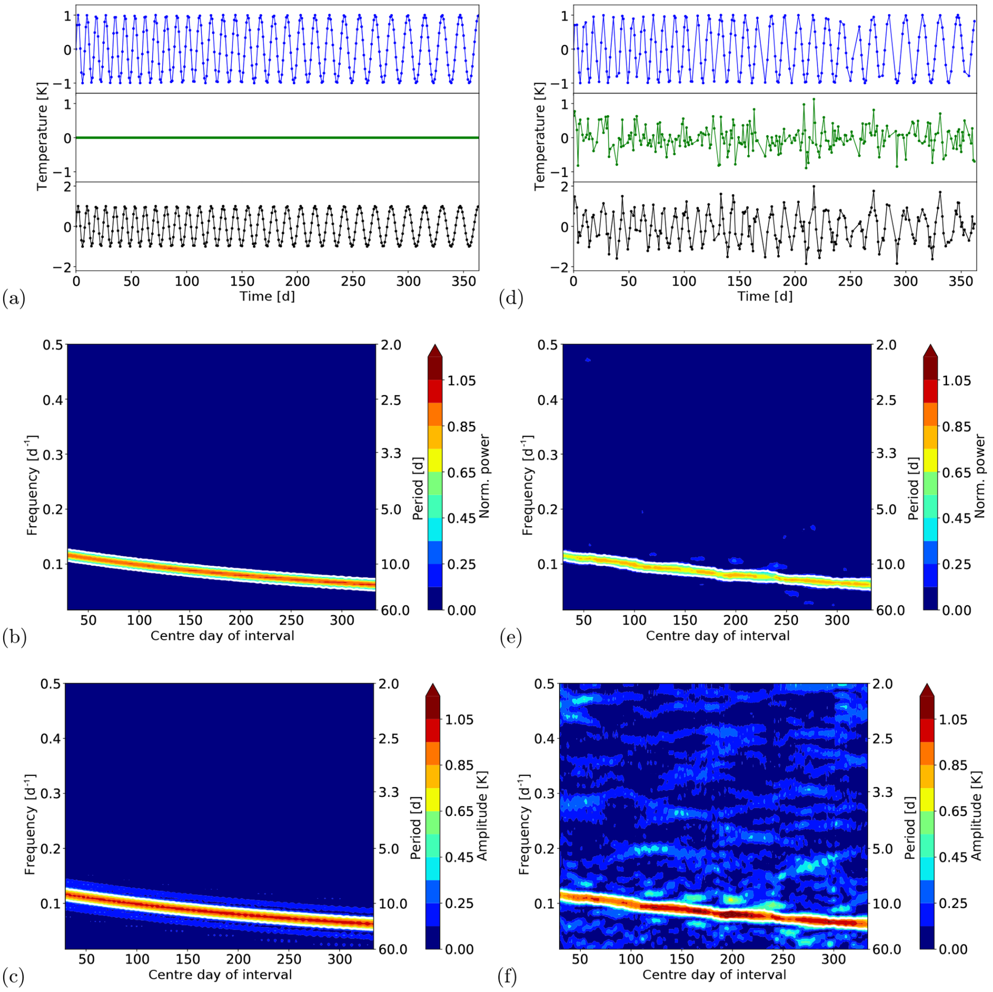

Figure 5. (a) Time series of a periodic signal with increasing period. The upper panel shows the signal, the middle panel the noise, and the lower panel the sum of both. **(b, c)** Results for the normalised power and amplitude. The results are displayed at the centre day of the corresponding time window. The length of the time window was 60 d. The white contours mark the significant results. **(d–f)** Same as for **(a–c)** with additional noise added to the time series and data gaps.

1 K (Fig. 6a blue curve in upper panel), and additional noise (Fig. 6a green curve in middle panel). The standard deviation of the noise was again 0.5 times the standard deviation of the signal and about 30 % of the data points have been removed. The complete time series is shown as a black curve in the lower panel of Fig. 6a. The results for the normalised power and the amplitude are shown in Fig. 6b and c, respectively. The normalised power shows an increasing value to the centre of the complete time interval. This behaviour is caused by the contribution of the noise to the total time series, which is much larger when the amplitude is small and decreases with increasing amplitude of the signal. The result for the amplitude nicely reflects the increase in the amplitude to the centre and the following decrease to the end of the time series. As the variation of the amplitude occurs on a smaller timescale than the chosen time interval for the analysis some kind of averaging occurs. Thus, the theoretical maximum of 1.0 K is not reached and the maximum value that is observed is about 0.9 K. In total, the main features of the signal are captured very well by the analysis and the correct period and the variation of the amplitude with time are detected. The last example shows the sum of the two former ones. Thus, the complete time series (Fig. 6d black curve in lower panel) is composed of a sinusoid with an amplitude of 1 K and an increasing period (Fig. 6d blue curve in upper panel), a periodic signal with a period of 25 d and an amplitude that varies between 0 and 1 K (Fig. 6d red curve in second panel), and noise (Fig. 6d green curve in third panel). The standard deviation of the noise and the number of data gaps are the same as before. The results for the normalised power and amplitude are presented in Fig. 6e and f, respectively. The first signal can significantly be detected during the whole time and the increase in the period from about 8 to 16 d is captured very well. As the amplitude of the second signal increases to the

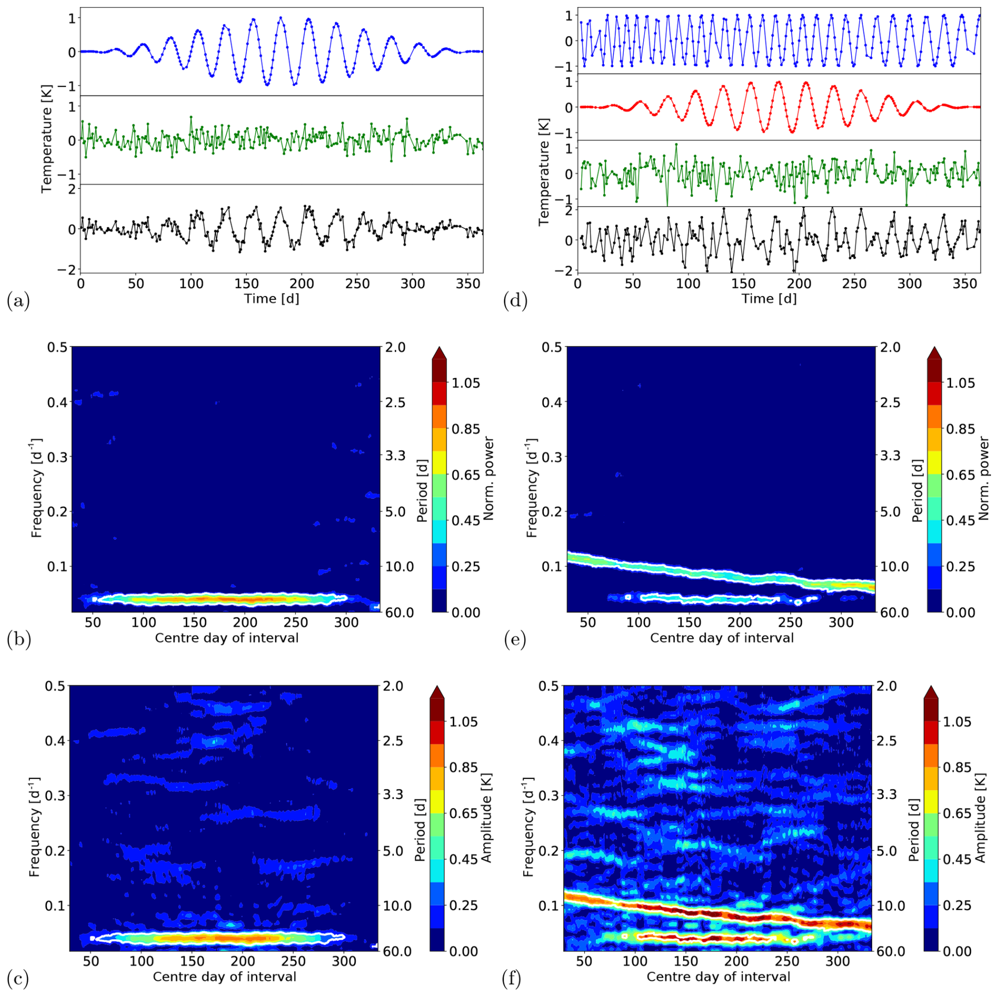

Figure 6. (a) Time series of a periodic signal with varying amplitude and additional noise and data gaps. The upper panel shows the signal, the middle panel the noise and the lower panel the sum of both. **(b, c)** Results for the normalised power and amplitude. The results are displayed at the centre day of the corresponding time window. The length of the time window was 60 d. The white contours mark the significant results. **(d)** Time series of a periodic signal with increasing amplitude plus a periodic signal with varying amplitude and additional noise and data gaps. The upper two panels show the two signals, the third panel the noise, and the lower panel the sum of all. **(e, f)** Same as for **(b, c)**.

centre of the complete time interval, this signal can only be significantly detected in the middle of the complete time interval. The normalised power reflects the different contributions of the two signals to the complete time series very well. In the middle of the complete time series, each single signal contributes to almost the same amount, as the amplitude is about 1 K in both cases. The remaining part of the total variance can be explained by the noise (variance of noise is 0.25 times variance of sum of signals). At the beginning and the end, only the first signal and additionally the noise contribute to the complete time series. The results for the amplitude also show the main features of the two signals. For the first signal, the amplitude stays at around 1 K during the whole time and the amplitude modulation of the second signal is also captured. Compared to the former example, the result for the amplitude is noisier because of the larger absolute noise in the last example.

In summary, the applied method is able to detect periodic signals that vary with time, i.e. the amplitude or the period changes with time. In cases where changes occur on much smaller timescales than the used time window, the results show some kind of averaging. Then the maximum values of the amplitude or the explained variance cannot be obtained and a mean value in the analysed time window is derived. The method is also very useful when noise is added to the time series and additionally data gaps are introduced. Although about 30 % of the data points have been removed, the results are very good and still reflect the behaviour of the signals. Thus, the presented method is well suited to analyse time-varying periodicities even in the case of unequally spaced time series.

4.2 Measurement data

The OH* temperatures are derived from measurements by a GRIPS (GRound-based Infrared P-branch Spectrometer) instrument operated in Wuppertal (51° N, 7° E; Germany). This GRIPS instrument measures three emission lines of the OH*(3,1) band, the P1(2), P1(3), and P1(4) lines. The relative intensities of these lines are used to derive rotational temperatures (Bittner et al., 2000, and references therein). The OH layer from which the emissions originate is located in the mesopause region. The mean altitude is about 87 km and the layer has a full width at half maximum (FWHM) of about 9 km (e.g. Baker and Stair Jr., 1998; Oberheide et al., 2006). Measurements are carried out every night, except for nights with bad weather conditions. The OH* temperatures have been continuously observed from Wuppertal since mid-1987 and a GRIPS instrument is still in operation to continue the observations. Until mid-2011 the measurements have been carried out by the GRIPS-II instrument (see Bittner et al., 2000, 2002, for an instrument description), and after that the GRIPS-N instrument (follow-up of GRIPS-II) is used to continue the observations (Kalicinsky et al., 2016).

Figure 7 shows the nightly mean OH* temperatures for the year 1989 as an example. This year was chosen because Bittner et al. (2000) analysed the same year with a different technique (wavelet transform); thus, the results of our approach can be compared to their results. The temperatures show the typical seasonal behaviour with a temperature minimum in summer and a maximum in winter. This behaviour can be described with three main components: an annual, a semi-annual, and a ter-annual cycle (Bittner et al., 2000). The red curve in the figure shows a least squares fit to the data that considers these three components. Such fits are typically used to determine the annual average OH* temperatures since a simple arithmetic mean is not advisable because of the data gaps (e.g. Bittner et al., 2002; Offermann et al., 2010; Perminov et al., 2014; Kalicinsky et al., 2016). The lower panel of Fig. 7 shows the residual temperatures, i.e. the OH* temperatures minus the determined fit curve. Bittner et al. (2000) already showed that such residual temperatures include statistically significant periodic fluctuations. We now analyse the residual temperatures with respect to such fluctuations using the moving LSP approach.

The results for the normalised power and the amplitude are shown in Fig. 8. Different events with significant periodic fluctuations can be detected when using the moving LSP approach. The largest event is detected at the beginning of the year. The determined period is about 40 d and the amplitude 6 to 7 K. This behaviour can also be seen in the residual temperatures just by eye (compare Fig. 7). It seems that the fluctuations continue with a slightly larger period and smaller amplitude, but the result cannot be judged as significant after a centre day of the interval of about 70 d. As can be seen in the residual temperatures, the number of observations between day 75 and 125 is very low and a lot of data gaps are present. The FAP levels for time windows including a large number of data gaps increase then and thus the results are not significant, although it is likely that the signal is still there and real. Additionally, the data gaps are responsible for the vertical structure that can be clearly observed in the amplitudes in this time region, because the gaps interrupt the continuity. Around a centre day of 250, a second significant result for a fluctuation with a period of about 50 d is detected, but the amplitude is smaller with 4 to 5 K. At the end of the year additional significant events with smaller periods of about 10 and 16 d can be seen. All of these significant fluctuations agree well with the findings of Bittner et al. (2000), where the authors analysed the same observations using a wavelet transform and assimilation technique based on the maximum entropy method to get rid of the data gaps. Our new method now enables a safe detection of such significant fluctuations without the need for processing the data before the analysis.

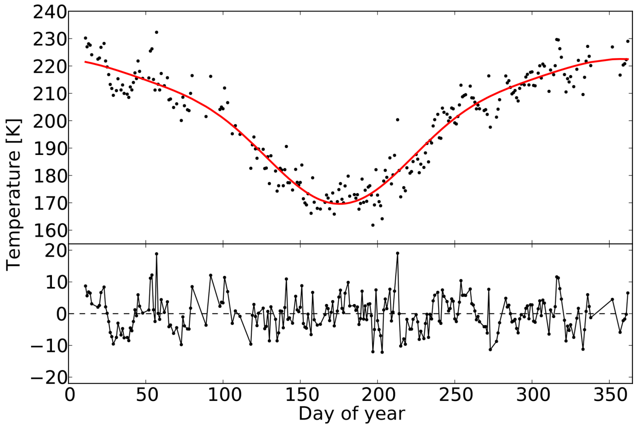

Figure 7. Nightly mean OH* temperatures observed from Wuppertal in the year 1989. The red curve shows the fit of the seasonal cycle including an annual, semi-annual, and ter-annual components. The residual temperatures (measurements minus fit) are shown in the lower panel.

5 Summary and conclusions

We present an approach to analyse time series with unequal spacing with respect to significant period fluctuations. The approach is also able to derive time-resolved information on the periods and amplitudes of the detected fluctuations. It is based on the classical Lomb–Scargle periodogram (LSP), a method that can handle unequally spaced time series. Additionally, it uses the idea of a moving window to enable the determination of time-resolved periods and amplitudes. The significance of the results is analysed with the typically used false alarm probability (FAP). As the determination of the FAP levels needs many simulations, we derived the dependencies of the FAP levels on the length of the analysed time interval T, the frequency range Δf, and the number of data

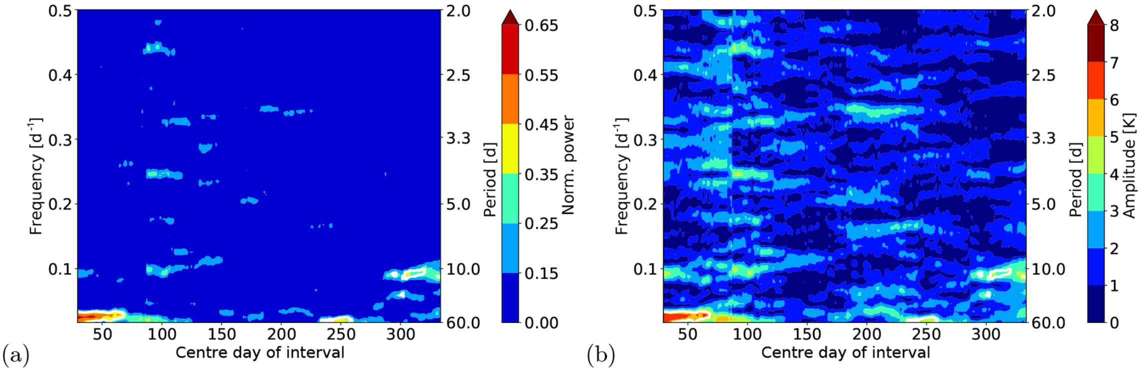

Figure 8. Results for the normalised power and amplitude for the analysis of the temperature residual of the GRIPS observations in 1989. The results are displayed at the centre day of the corresponding time window. The length of the time window was 60 d. The white contours mark the significant results.

gaps to find a fast and easy way to calculate the FAP levels in the used parameter range. Thus, we can avoid a large number of simulations. In the analysed parameter range, the number of independent frequencies N_i shows a linear dependency on the length of the time interval T, because the peak width is inversely proportional to T. Furthermore, the slope of the line that describes this dependency is different for different frequency ranges, where a smaller frequency range Δf reduces the slope. We used these two relationships to quickly calculate the FAP levels. The number of data gaps has only a very minor effect, because the peak width depends on the length of the time interval and not on the number of data points.

The approach was tested with different artificially generated time series. These time series include variations of the period and amplitude with time, and, additionally, noise is added and data gaps have been introduced. In all cases, the approach shows very good results and thus the approach is a suitable method for the time-resolved detection of periodic fluctuations, even in the case of unequal spacing. Finally, we analysed the nightly mean OH* temperatures that have been observed from Wuppertal (51° N, 7° E; Germany) in the year 1989. The results show several significant events with fluctuations that have periods in the range between 10 and 50 d and amplitudes between 3 and 7 K. These significant results agree very well with the results of a former study carried out by Bittner et al. (2000) without the need for processing the data before the analysis.

Data availability. The nightly mean OH* temperatures can be obtained by request to the corresponding author or to Peter Knieling (knieling@uni-wuppertal.de).

Author contributions. CK conceptualised the method. CK and RR performed the simulations and did the analyses under intensive discussion with RK. PK provided the OH* data. The article was written by CK with contributions from all coauthors.

Competing interests. The authors declare that they have no conflict of interest.

Acknowledgements. We thank the two reviewers for their useful comments that helped to improve the paper.

Financial support. This research has been supported by the Bundesministerium für Bildung und Forschung (ROMIC project MALODY (grant no. 01LG1207A)).

Review statement. This paper was edited by Lars Hoffmann and reviewed by two anonymous referees.

References

Baker, D. J. and Stair Jr., A. T.: Rocket measurements of the altitude distributions of the hydroxyl airglow, Phys. Scripta, 37, 611, https://doi.org/10.1088/0031-8949/37/4/021, 1998.

Bittner, M., Offermann, D., and Graef, H. H.: Mesopause temperature variability above a midlatitude station in Europe, J. Geophys. Res., 105, 2045–2058, https://doi.org/10.1029/1999JD900307, 2000.

Bittner, M., Offermann, D., Graef, H. H., Donner, M., and Hamilton, K.: An 18-year time series of OH* rotational temperatures and middle atmosphere decadal variations, J. Atmos. Sol.-Terr. Phy., 64, 1147–1166, https://doi.org/10.1016/S1364-6826(02)00065-2, 2002.

Cumming, A., Marcy, G. W., and Butler, R. P.: The lick planet search: detectability and mass thresholds, Astrophys. J., 526, 890–915, https://doi.org/10.1086/308020, 1999.

Das, U. and Sinha, H. S. S.: Long-term variations in oxygen green line emission over Kiso, Japan, from ground photometric observations using continuous wavelet transform, J. Geophys. Res., 113, D19115, https://doi.org/10.1029/2007JD009516, 2008.

Egito, F., Buriti, R. A., Fragoso Medeiros, A., and Takahashi, H.: Ultrafast Kelvin waves in the MLT airglow and wind, and their interaction with the atmospheric tides, Ann. Geophys., 36, 231–241, https://doi.org/10.5194/angeo-36-231-2018, 2018.

Espy, P. J., Stegman, J., and Witt, G.: Interannual variations of the quasi-16-day oscillation in the polar summer mesospheric temperature, J. Geophys. Res., 102, 1983–1990, https://doi.org/10.1029/96JD02717, 1997.

Franzen, C., Espy, P. J., Hibbins, R. E., and Djupvik, A. A.: Observation of quasi-periodic structures in the hydroxyl airglow on scales below 100 m, J. Geophys. Res.-Atmos., 123, 10935–10942, https://doi.org/10.1029/2018JD028732, 2018.

Gao, H., Xu, J., and Wu, Q.: Seasonal and QBO variations in the OH nightglow emission observed by TIMED/SABER, J. Geophys. Res., 115, A06313, https://doi.org/10.1029/2009JA014641, 2010.

Horne, J. H. and Baliunas, S. L.: A prescription for period analysis of unevenly sampled time series, Astrophys. J., 302, 757–763, 1986.

Kalicinsky, C., Knieling, P., Koppmann, R., Offermann, D., Steinbrecht, W., and Wintel, J.: Long-term dynamics of OH* temperatures over central Europe: trends and solar correlations, Atmos. Chem. Phys., 16, 15033–15047, https://doi.org/10.5194/acp-16-15033-2016, 2016.

Lomb, N. R.: Least-squares frequency analysis of unequally spaced data, Astrophys. Space Sci., 39, 447–462, 1976.

Luo, Y., Manson, A. H., Meek, C. E., Meyer, C. K., and Forbes, J. F.: The quasi 16-day oscillations in the mesosphere and lower thermosphere at Saskatoon (52° N, 107° W), 1980–1996, J. Geophys. Res., 105, 2125–2138, https://doi.org/10.1029/1999JD900979, 2000.

Nyassor, P. K., Buriti, R. A., Paulino, I., Medeiros, A. F., Takahashi, H., Wrasse, C. M., and Gobbi, D.: Determination of gravity wave parameters in the airglow combining photometer and imager data, Ann. Geophys., 36, 705–715, https://doi.org/10.5194/angeo-36-705-2018, 2018.

Oberheide, J., Offermann, D., Russell III, J. M., and Mlynczak, M. G.: Intercomparison of kinetic temperature from 15 µm CO_2 limb emissions and OH*(3,1) rotational temperature in nearly coincident air masses: SABER, GRIPS, Geophys. Res. Lett., 33, L14811, https://doi.org/10.1029/2006GL026439, 2006.

Offermann, D., Hoffmann, P., Knieling, P., Koppmann, R., Oberheide, J., and Steinbrecht, W.: Long-term trend and solar cycle variations of mesospheric temperature and dynamics, J. Geophys. Res., 115, D18127, https://doi.org/10.1029/2009JD013363, 2010.

Perminov, V. I., Semenov, A. I., Medvedeva, I. V., and Zheleznov, Yu. A.: Variability of mesopause temperature from the hydroxyl airglow observations over mid-latitudinal sites, Zvenigorod and Tory, Russia, Adv. Space Res., 54, 2511–2517, https://doi.org/10.1016/j.asr.2014.01.027, 2014.

Reid, I. M., Spargo, A. J., and Woithe, J. M.: Seasonal variations of the nighttime $O(^1S)$ and OH (8-3) airglow intensity at Adelaide, Australia, J. Geophys. Res.-Atmos., 119, 6991–7013, https://doi.org/10.1002/2013JD020906, 2014.

Scargle, J. D.: Studies in astronomical time series analysis. II. Statistical aspects of spectral analysis of unevenly spaced data, Astrophys. J., 263, 835–853, 1982.

Takahashi, H., Buriti, R. A., Gobbi, D., and Batista, P. P.: Equatorial planetary wave signatures observed in mesospheric airglow emissions, J. Atmos. Sol.-Terr. Phy., 64, 1263–1272, https://doi.org/10.1016/S1364-6826(02)00040-8, 2002.

Takahashi, H., Shiokawa, K., Egito, E., Murayama, Y., Kawamura, S., and Wrasse, C. M.: Planetary wave induced wind and airglow oscillations in the middle latitude MLT region, J. Atmos. Sol.-Terr. Phy., 98, 97–104, https://doi.org/10.1016/j.jastp.2013.03.014, 2013.

Smith, S. W.: The Scientist and Engineer's Guide to Digital Signal Processing, California Technical Publishing, San Diego, California, USA, 1997.

Schwarzenberg-Czerny, A.: The distribution of empirical periodograms: Lomb–Scargle and PDM spectra, Mon. Not. R. Astron. Soc., 301, 831–840, https://doi.org/10.1111/j.1365-8711.1998.02086.x, 1998.

Yoshida, S., Tsuda, T., Shimizu, A., and Nakamura, T.: Seasonal variations of $3.0 \sim 3.8$-day ultra-fast Kelvin waves observed with a meteor wind radar and radiosonde in Indonesia, Earth Planets Space, 51, 675–684, https://doi.org/10.1186/BF03353225, 1999.

Zechmeister, M. and Kürster, M.: The generalised Lomb–Scargle periodogram – A new formalism for the floating-mean and Keplerian periodograms, Astron. Astrophys., 496, 577–584, https://doi.org/10.1051/0004-6361:200811296, 2009.

JOURNAL OF GEOPHYSICAL RESEARCH, VOL. 116, D00P07, doi:10.1029/2010JD015544, 2011

Long-term development of short-period gravity waves in middle Europe

D. Offermann,[1] J. Wintel,[1] C. Kalicinsky,[1] P. Knieling,[1] R. Koppmann,[1]
and W. Steinbrecht[2]

Received 22 December 2010; revised 21 April 2011; accepted 26 April 2011; published 23 July 2011.

[1] The long-term development of short-period gravity waves is investigated using the analysis of temperature fluctuations in the mesosphere. The temperature fluctuations are quantified by their standard deviations σ based on data from OH measurements at Wuppertal (51°N, 7°E) and Hohenpeissenberg (48°N, 11°E) obtained from 1994 to 2009 at 87 km altitude. The temperatures are Fourier analyzed in the spectral regime of periods between 3 and 10 min. The resulting oscillation amplitudes correlate very well with the standard deviations. Shortest periods are taken as "ripples" that are indicative of atmospheric instabilities/breaking gravity waves. In consequence the standard deviations are used as proxies for gravity wave activity and dissipation. This data set is analyzed for seasonal, intradecadal, and interdecadal (trend) variations. Seasonal changes show a double peak structure with maxima occurring slightly before circulation turnaround in spring and autumn. This is found to be in close agreement with seasonal variations of turbulent eddy coefficients obtained from WACCM 3.5. The intradecadal variations show close correlations with the zonal wind and the annual amplitude of the mesopause temperature. The long-term trend (16 years) indicates an increase of gravity wave activity of 1.5% per year. Correspondences with dynamical parameters such as zonal wind speed and summer length are discussed.

Citation: Offermann, D., J. Wintel, C. Kalicinsky, P. Knieling, R. Koppmann, and W. Steinbrecht (2011), Long-term development of short-period gravity waves in middle Europe, *J. Geophys. Res.*, *116*, D00P07, doi:10.1029/2010JD015544.

1. Introduction

[2] Atmospheric gravity waves (GW) are known to be important parts of middle atmosphere dynamics. They have been intensively studied since the early work of Colin Hines [*Hines*, 1960] with respect to their influences on atmospheric structure and variability [e.g., *Andrews et al.*, 1987; *Fritts and Alexander*, 2003]. They are known to control the mesospheric circulation and its changes by dissipation and momentum deposition [e.g., *Fritts et al.*, 2006]. An extensive review on the voluminous literature on GW has been given by *Fritts and Alexander* [2003]. More recent developments are described e.g., by *Preusse et al.* [2006, 2008, 2009], *Ern et al.* [2004], *Jacobi et al.* [2006], *Krebsbach and Preuße* [2007], *Wu et al.* [2006], and the references given therein.

[3] Substantial amount of work has been spent on the question as to the origin of gravity waves in the mesosphere. There are many sources in the lower atmosphere (orographic structures, weather systems), and GW upward propagation in the middle atmosphere up to the mesopause has been extensively studied e.g., by ray tracing methods [*Preusse et al.*, 2009, and references therein]. Gravity waves are subject to many influences and modifications on their way up to the mesosphere and lower thermosphere, as for instance by wind filtering in the middle atmosphere [e.g., *Alexander*, 1998]. Wavelike oscillations are also known to be excited in situ in the mesosphere by breaking gravity waves and Kelvin-Helmholtz or convective instabilities. These have exceptionally short periods and wavelengths ("ripples"), and are investigated in detail by theory and imaging experiments [e.g., *Nakamura et al.*, 1999; *Horinouchi et al.*, 2002; *Hecht*, 2004, *Hecht et al.*, 2005, 2007; *Taylor et al.*, 1997, 2007; *Shiokawa et al.*, 2009]. Gravity wave–fine structure interactions, related Kelvin-Helmholtz instabilities, and turbulence production have also been numerically studied by *Fritts et al.* [2009, and references therein].

[4] Gravity wave amplitudes in the upper mesosphere are comparatively large. At the mesopause they appear to be the strongest of all types of waves (in temperature [*Offermann et al.*, 2009]). In the lower mesosphere and upper stratosphere their amplitudes are relatively small indicating considerable wave dissipation. Gravity waves therefore appear to be linked to turbulence production and hence to eddy diffusion in the mesosphere [e.g., *Rapp et al.*, 2004].

[5] Considering the general importance of gravity waves it is interesting to study possible long-term changes. Seasonal variations have been analyzed on many occasions, and sometimes with quite different results. Annual and

---

[1] Physics Department, Wuppertal University, Wuppertal, Germany.
[2] Meteorologisches Observatorium, Hohenpeissenberg, Germany.

0148-0227/11/2010JD015544

Table 1. List of Acronyms

Acronym	Definition
AMSU	Advanced Microwave Sounding Unit
AURA	NASA satellite, Earth science Projects Division
CRISTA	Cryogenic Infrared Spectrometers and Telescopes for the Atmosphere
DOY	Day Of Year
ESD	Equivalent Summer Duration
FFT	Fast Fourier Transform
GCM	General Circulation Model
GRIPS	Ground based Infrared P-branch Spectrometer
HIRDLS	High Resolution Dynamics Limb Sounder
LIMS	Limb Infrared Monitor of the Stratosphere
MLS	Microwave Limb Sounder
SABER	Sounding of the Atmosphere using Broadband Emission Radiometry
TIMED	Thermosphere, Ionosphere, Mesosphere, Energetics, and Dynamics
WACCM	Whole Atmosphere Community Climate Model

semiannual variations have been found with maxima at solstices or at equinox. The structures depend on the wave frequency, and can be different for different latitudes as well as different altitudes. Measurement parameter (wind, temperature) also appears to play a role. For details, see, e.g., *Manson et al.* [1999], *Jacobi et al.* [2006], *Dowdy et al.* [2007], *Offermann et al.* [2009], and *Preusse et al.* [2009], and the many references given therein. Interannual (intradecadal) and interdecadal (long-term trend) results are much more scarce. Considerable interannual variability has been observed, and there appear to be indications of solar cycle influences [e.g., *Jiang et al.*, 2006; *Jacobi et al.*, 2006]. An analysis of a limited data set at the station of Wuppertal (51°N, 7°E) was given by *Offermann et al.* [2006]. The latter data are substantially extended and analyzed in detail in the present paper.

[6] Gravity waves are extremely manifold as their wavelengths, periods, and propagation directions are considered. All these parameters vary with altitude, latitude, and specific location of the measurements. Data interpretation is therefore not easy, and a consistent climatology is obviously difficult to obtain. Furthermore ground based measurements lack horizontal and sometimes also vertical information. Satellite measurements are limited to gravity waves of longer wavelengths in the horizontal or vertical direction because of limited spatial resolution of limb sounders in the horizontal and nadir sounders in the vertical [e.g., *Alexander*, 1998; *McLandress et al.*, 2000; *Preusse et al.*, 2006]. These types of measurements have been performed by various satellites instruments such as MLS, LIMS, CRISTA, SABER, HIRDLS, and AMSU [*Wu and Waters*, 1996; *Fetzer and Gille*, 1994; *Eckermann and Preusse*, 1999; *Preusse et al.*, 2006, *Alexander and Ortland*, 2010; *Jiang et al.*, 2006]. (Explanation of the acronyms is given in Table 1.)

[7] Up to now the time intervals covered by satellite measurement series are rather limited. Much longer data series are available from various ground experiments. These include radar wind measurements, Lidar intensity or temperature measurements, and airglow spectral or imaging observations of temperature or intensity [e.g., *Fritts and Alexander*, 2003; *Scheer et al.*, 2006; *Jacobi et al.*, 2006; *Hoffmann et al.*, 2011, and references therein]. High time resolution can be obtained by these techniques. Particularly high resolution has been obtained by the OH technique. Mesospheric oscillations with periods of a few minutes have been observed by OH imaging experiments [e.g., *Taylor et al.*, 2007; *Hecht et al.*, 2007].

[8] In the present paper we discuss an OH data series covering 16 years of observation (1994–2009) with a time resolution of 1.3 min taken at the station of Wuppertal (51°N, 7°E, GRIPS II instrument). In addition, six years of data taken at Hohenpeissenberg (48°N, 11°E, GRIPS I, 2004–2009) are also included. This is a large amount of data, only part of which can be discussed here. The paper is organized as follows: Section 2 describes the data and their analysis. Section 3 compares oscillation amplitudes and the standard deviations σ_N from the nightly mean temperature as a proxy for mesospheric waves. In section 4 the seasonal variations of this parameter are discussed. This includes wave breaking and eddy coefficients K_{zz} as obtained from a recent atmospheric model WACCM 3.5. Section 5 analyzes intradecadal and interdecadal variations. Section 6 discusses the results and compares them with other data. Section 7 summarizes the results.

2. Data and Analysis

[9] The hydroxyl (OH) layer in the upper mesosphere is centered at about 87 km altitude and is 8 km wide (full width at half maximum) [e.g., *Bittner et al.*, 2002; *Oberheide et al.*, 2006; *Mulligan et al.*, 2009; *Offermann et al.*, 2010]. The exact layer altitude is not very important for the wave analyses presented here. The OH molecules are chemically excited and emit a broad spectrum of lines at visible and near infrared wavelengths. These emissions are widely used to determine atmospheric temperatures at this altitude [e.g., *Scheer et al.*, 2006]. Such measurements are also taken at the station of Wuppertal (51°N, 7°E) by a small grating spectrometer of moderate resolution (GRIPS II). With this instrument the intensities of three P band lines at wavelengths of 1.524 μm, 1.533 μm, and 1.543 μm are measured, from which the temperature is derived. Instrument and measurement technique are described in detail by *Bittner et al.* [2002] and *Offermann et al.* [2010]. A similar ("twin") instrument (GRIPS I) is operated at the station of Hohenpeissenberg (48°N, 11°E) about 360 km south of Wuppertal [*Offermann et al.*, 2010, 2011]. The measurements are taken during night to avoid stray light from the sun. The fields of view are tilted northward to avoid moon interferences. Cloud-free observations were used only. The three infrared lines of one spectrum are measured within 54 s. This should be fast enough to limit the distortion of the derived temperature value by haze possibly drifting into the field of view.

[10] The OH temperatures show strong variations on a wide range of time scales, reaching from minutes to decades. One recurrent variation with large amplitude is the seasonal change. An example for Wuppertal is shown in Figure 1. Mean nightly temperatures are given. They are low in summer and high in winter which is due to the large scale circulation. The seasonal variation is modeled by an harmonic analysis (solid line in Figure 1) with seven free parameters: mean temperature T_0, three amplitudes A_1,A_2, A_3 for annual, semiannual, and terannual components, and the corresponding phases. Figure 1 shows the data of 2005.

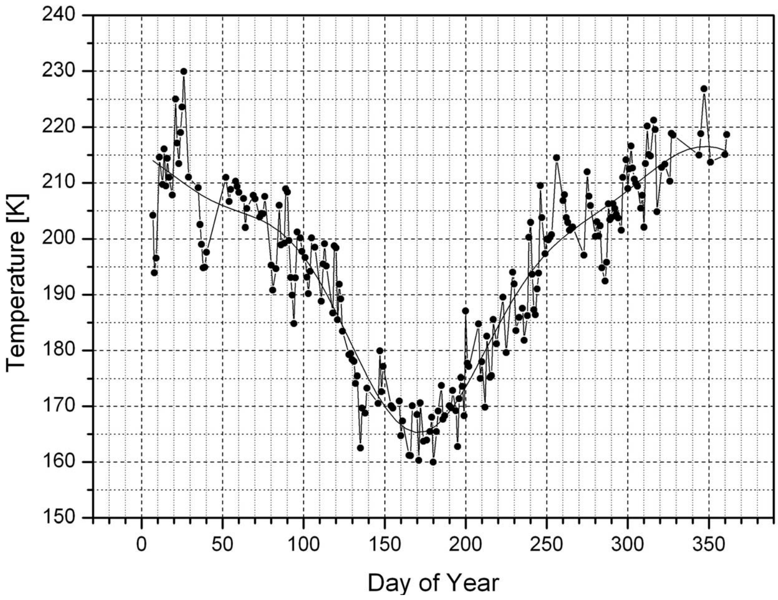

Figure 1. Seasonal variation of OH temperatures in 2005. Nightly mean values are given. The solid curve is a harmonic fit with annual, semiannual, and terannual components.

This year is chosen because it is near the middle of our data window analyzed and because the terannual component of the harmonic fit is well visible as relative increases around DOYs 100 and 250, respectively. Seasonal analyses for years 1987–2008 have been described by *Offermann et al.* [2010], and some long-term trends have been obtained.

[11] Here we analyze the temperature measurements from 1994 to 2009 for the fastest oscillations detectable by our technique. One infrared spectrum is taken every 1.3 min. As an example a data set resulting from 16 spectra in a 21 min interval is shown in Figure 2. Oscillation periods down to 2.6 min can be determined according to the Nyquist theorem.

[12] The data are analyzed on a nightly basis. Owing to the time resolution of our instrument the data are fairly noisy. This is partly due to the intensity fluctuations of the

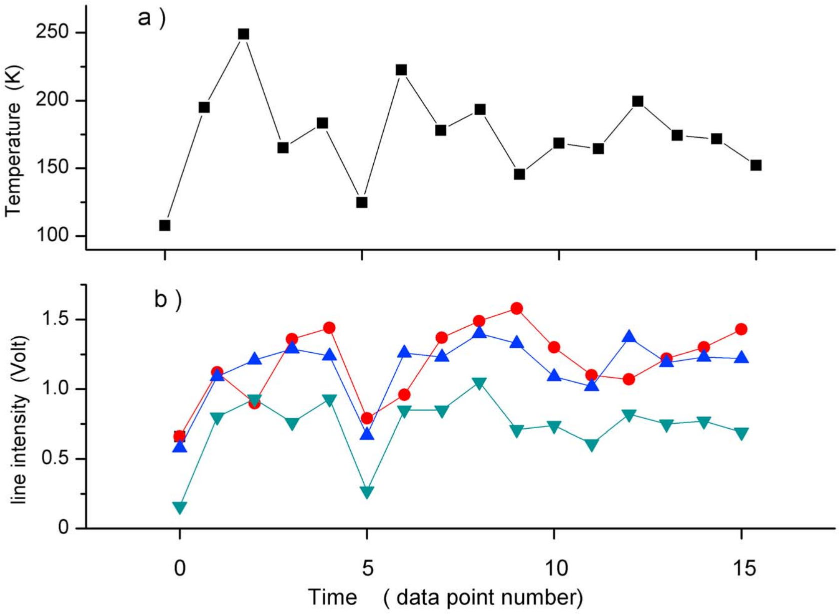

Figure 2. Data set of 21 min length. (a) Temperatures are derived from hydroxyl lines $P_1(2)$, $P_1(3)$, and $P_1(4)$ and (b) their intensities ($P_1(2)$, red; $P_1(3)$, blue; and $P_1(4)$, green). Time distance of data points is 1.3 min.

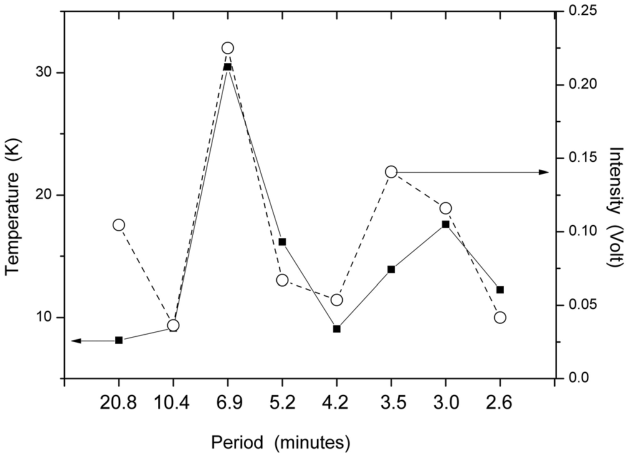

Figure 3. FFT spectra of the data shown in Figure 2. Temperature amplitudes are shown as squares (left ordinate), and mean intensity amplitudes are shown as circles (right ordinate) (see text).

three infrared lines used. Their noise is amplified by the nonlinear retrieval method used to determine the temperature [*Bittner et al.*, 2002]. As a measure of the temperature fluctuations we use the standard deviation σ_N from the nightly mean temperature. These σ_N values can be occasionally quite large (40 K). They contain both the noise and the atmospheric variations due to waves and “ripples” (see below).

[13] The objective of our analysis is to separate the waves from the noise. For this purpose we use a spectral analysis (FFT). As the noise can be much larger than the amplitudes of the atmospheric waves, it cannot be excluded that some noise fluctuations are mistaken as waves by the spectral analysis. To avoid a distortion of our results we use the following procedure: We perform an FFT analysis not only for the temperatures, but at the same time also for the intensities of all three infrared lines. A wave identified in the temperatures is accepted as valid only if it shows up in the intensities of the lines as well. An example is shown in Figure 2. For all subsequent analyses we use data sets of 16 data points, i.e., 16 measured intensity spectra for the FFT. The three FFT spectra of the three lines are averaged and compared to the temperature FFT spectrum. This is shown in Figure 3 for the temperature and intensity data of Figure 2. An FFT analysis of 16 data points yields amplitudes of eight spectral elements (21 min, 10.4 min, 6.9 min, 5.2 min, 4.2 min, 3.5 min, 3 min, and 2.6 min). We do not use the two end points of the spectrum. We count a wave event as valid only if (1) the temperature spectrum has a relative maximum at a given spectral position, i.e., the amplitude at this point is 5% larger than at its two neighbor positions, and (2) if the mean intensity spectrum has a corresponding maximum at the same spectral position. For the example given in Figure 3 this is the case at the period of 6.9 min. However, we also count an event as valid if the intensity maximum does not occur at the same spectral position as that of the temperature but at the neighbor position. In the example given in Figure 3 this occurs at 3 min and 3.5 min, respectively. The reason is the limited spectral resolution of our FFT. This may attribute a wave to a spectral position or to its neighbor if the wave period is about in the middle. Thus Figure 3 counts two maxima in total.

[14] Our analysis method is fairly conservative. It is justified as follows: If in the atmosphere there is a wave in the temperature this also causes a wave in the three intensity lines used by us. This is because temperature enters the equation of OH level excitation (exponentially). In general temperature variations and those of the intensities seen in the data may not be independent. There are three cases to consider: (1) If the mean of three intensity lines shows a wavelike structure and a temperature wave results (and vice versa) we count this as a valid event. (2) If there is an oscillation in the temperature but not in the intensities there are three possibilities: either the intensities have been disturbed too strongly (for instance by some noise) or the intensities have compensated to some extent, or there is no real wave in the temperature at all, i.e., it is accidental. In each of these cases the event/time interval considered is discarded as a candidate for containing a temperature wave. (3) There is an oscillation seen in the intensities, but not in temperature. This may for instance happen if the intensities are modulated in a wavelike form by some obstacle (cloud) in the field of view. In this case the three lines are changed by the same factor, and the retrieval algorithm does not yield a temperature change. Also this type of event is discarded.

[15] Our selection criterion thus is strict as quite a few (small) waves may be lost. It has, however, the advantage to exclude strong noise fluctuations in the temperature signal from being accidentally taken as real temperature waves. We have checked on this effect by dropping the requirement that an intensity maximum must be seen simultaneously with the temperature maximum. As expected the amplitudes given in Figure 4 below went up. The changes were moderate: between 10% and a factor 2.3.

[16] Our method thus yields lower limits for wave occurrence and wave amplitudes. It does not give a climatology as it is biased for instance toward high temperature

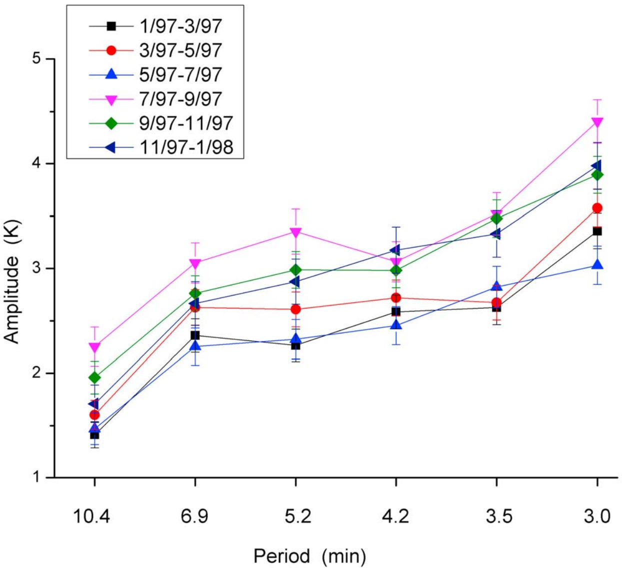

Figure 4. Mean temperature spectra in 3-monthly intervals in 1997.

amplitudes. This is, however, not a limitation for the present analysis as this studies relative variations, only.

[17] To obtain a general impression of the temperature spectra we have analyzed the data of all nights available in year 1997 which we use as a test year here. Again, data sets of 21 min length have been used. Amplitudes are very different and can be substantial (see Figure 3). We therefore calculate for a given oscillation period a mean amplitude per night which is weighted by the occurrence frequency. Resulting mean spectra are shown in Figure 4 for various times of the year 1997. The curves give means of three months each which are moved in steps of two months through the year (i.e., JFM, MAM, MJJ, JAS, SON, NDJ). The error bars are errors of the mean.

[18] The amplitudes are between 1 K and 5 K, which is typical also of other years. It is interesting to note an increase of amplitudes from long to short periods in Figure 4. This is essentially determined by the occurrence frequencies of the oscillation periods as the amplitudes are rather similar (±5%, decreasing from long to short periods). The increase is seen in a similar way in other years, too (1997–2009).

[19] Only part of the oscillations in Figure 4 can be gravity waves as these can exist only at periods longer than the Brunt-Väissällä period (5 min). Following suggestions by *Taylor and Hapgood* [1990], *Taylor et al.* [1997], *Hecht* [2004], and *Hecht et al.* [2007] we assume as a working hypothesis that our 3 min periods are "ripples" that are indicative of atmospheric instabilities. This is discussed in detail in section 6.1 below. The curves in Figure 4 indicate a seasonal variation of the amplitudes with greatest values in late summer and autumn. This will be discussed in detail below (section 4).

[20] We have checked whether the maximum criterion "5% larger than at its two neighbor positions" might be too weak. We have raised that value in steps up to 40%. This should decrease the mean amplitudes in Figure 4. It does as expected. The changes are, however, moderate. Up to a 20% criterion they are 7–25%. For the 40% criterion they are 50% to a factor 1.4. The relative form of the spectra remains about the same in all cases.

[21] We have also checked whether the increased maximum criteria affect the long-term correlation of the short-period proxy σ_a and the longer-period proxy σ_N discussed below (first and second paragraphs in section 4, and Figure 9). It is found that the long-term σ_a curve in Figure 9 is essentially unchanged in its relative structures. The correlation coefficients between σ_a and σ_N are slightly reduced by 4% in the 20% case and by 13% in the 40% case.

[22] It needs to be mentioned that the temperature changes shown in Figure 2a are very large, and high amplitudes result in Figure 3. This is not a common feature. These data rather were chosen to give a pronounced example. In general amplitudes larger than 25 K amount only to a few percent of occurrence for the periods shown in Figure 4. Temperature changes of 50 K or more within 1.3 min occur in less than 4% of the cases.

[23] The complexities of airglow wave structures in the upper mesosphere including line-of-sight cancellations have recently been demonstrated by *Snively et al.* [2010]. They show how difficult it is to analyze in detail spatial and temporal structures especially for measurements from a single station. We do not attempt this here but rather study the long-term stability or variation of our signatures.

3. Standard Deviations and Wave Amplitudes

[24] For a given time interval (e.g., one night) we calculate a mean temperature and the deviations from this mean. The corresponding standard deviation σ_N is a convenient parameter to estimate the magnitude of the temperature fluctuations in that time interval. These fluctuations contain contributions from genuine atmospheric noise, instrumental noise, gravity waves of various oscillation periods, and possibly other fast waves as tides and fast planetary waves. Figure 5 shows nightly standard deviations σ_N for the recent years in Wuppertal (black curve). The scatter of the σ_N data is fairly large and the data have therefore been smoothed by a 50-point Savitzky-Golay algorithm which has a good resolution [*Savitzky and Golay*, 1964]. This type of smoothing is used in all pictures given here if not stated differently. The error is estimated to ±0.7 K. The resulting values in Figure 5 are high and still quite variable. There are two major variations: a long-term change over several years, and a pronounced shorter variation during the course of the year which appears to recur in a similar manner each year. Either variation must have specific reasons beyond simple noise, because it is hard to believe that atmospheric and/or instrumental noise could have the time dependences shown. Especially interesting is the intra-annual variation which shows a pronounced peak in autumn and a smaller peak in spring. This pattern is seen in most of the years analyzed (see also Figure 9 below). To study whether this is a general structure or a feature specific to the Wuppertal measurement site, we have added a second data set to Figure 5 (red curve). It shows σ_N values measured by our twin instrument GRIPS I at Hohenpeissenberg. Note that this curve has been shifted upwards by 10 K to better distinguish it from the Wuppertal curve. The σ_N values at the two places are fairly similar, those at Hohenpeissenberg being somewhat larger. The intra-annual variations with the two peaks mentioned are found at Hohenpeissenberg, too. Hence, these features are general structures, indeed.

[25] Gravity wave activity is believed to influence the mesosphere and its circulation [e.g., *Holton*, 1983; *Jiang et al.*, 2006]. This should somehow be linked to our σ_N values. As gravity waves can have periods and wavelengths of very different magnitudes it needs to be determined which wave has which effect? We start here with the shortest periods we can measure as described in section 2. Afterwards we compare them with σ_N which covers somewhat longer periods.

[26] As mentioned before, we use the year 1997 as a test year. To express the amplitudes of the short periods in terms of standard deviations we calculate an equivalent standard deviation σ_a for the shortest oscillations. For this we calculate for each period i (i = 1–6) given in Figure 3 the mean amplitude $\bar{a}_i$ in a given night. Only nights with more than five data sets of 21 min available are considered. Parameter σ_a is then calculated from equation (1).

$$\sigma_a = \sqrt{\frac{1}{2}\sum_{i=1}^{6}\bar{a}_i^2} \qquad (1)$$

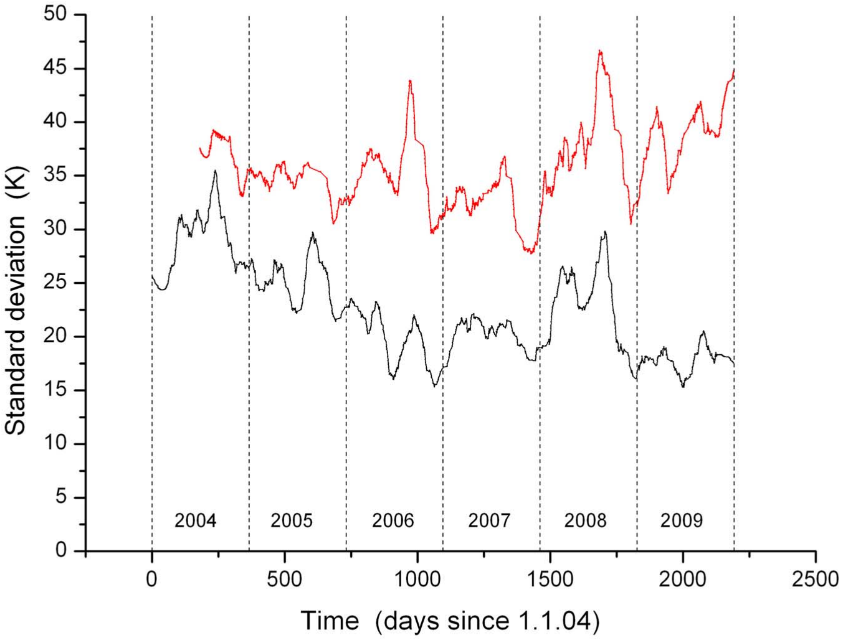

Figure 5. Nightly standard deviations σ_N from mean temperatures during the course of years 2004–2009. Data have been smoothed by a 50-point Savitzky-Golay algorithm. Black curve shows results from Wuppertal (51°N, 7°E, GRIPS II), and red curve shows those from Hohenpeissenberg (48°N, 11°E, GRIPS I). The red curve has been shifted upward by 10 K for clarity.

The resulting σ_a values are used as a measure of short-period wave/oscillation activity. These values are plotted for all nights in 1997 versus σ_N in Figure 6. A close correlation is obtained with a correlation coefficient r = 0.91. The slope of the regression line is 0.38 K/K. If the whole smoothed data set 1994–2009 discussed below is used, the respective numbers are r = 0.94 and slope = 0.40 K/K.

[27] The time dependence of σ_N and σ_a during the course of the year 1997 is shown in Figure 7. As shown by the slope of the line in Figure 6 σ_a amounts to about 40% of σ_N. A 20-point smoothing has been applied for the two curves. The two curves are nearly parallel, i.e., their relative variations are very similar. This indicates that the regression line

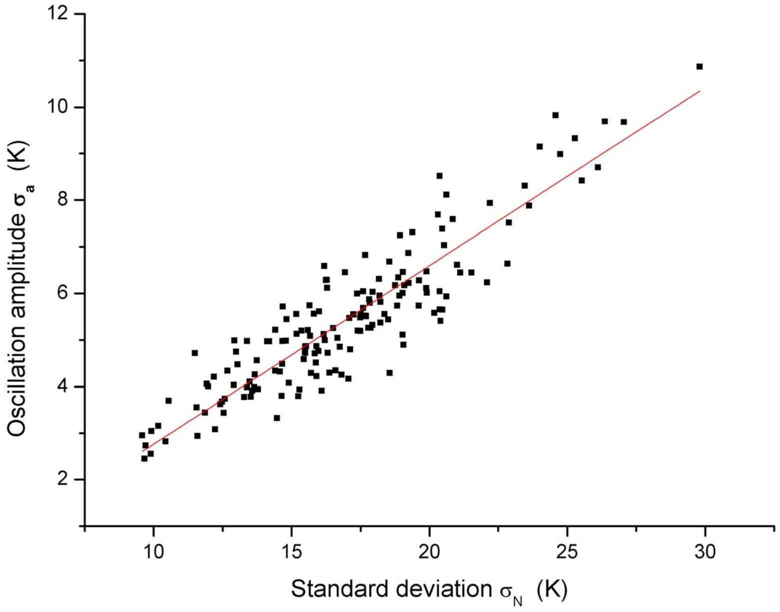

Figure 6. Short-period oscillation amplitudes σ_a compared to temperature standard deviations σ_N in 1997. Correlation coefficient is r = 0.91. Slope of regression line is (0.38 ± 0.012) K/K (see text).

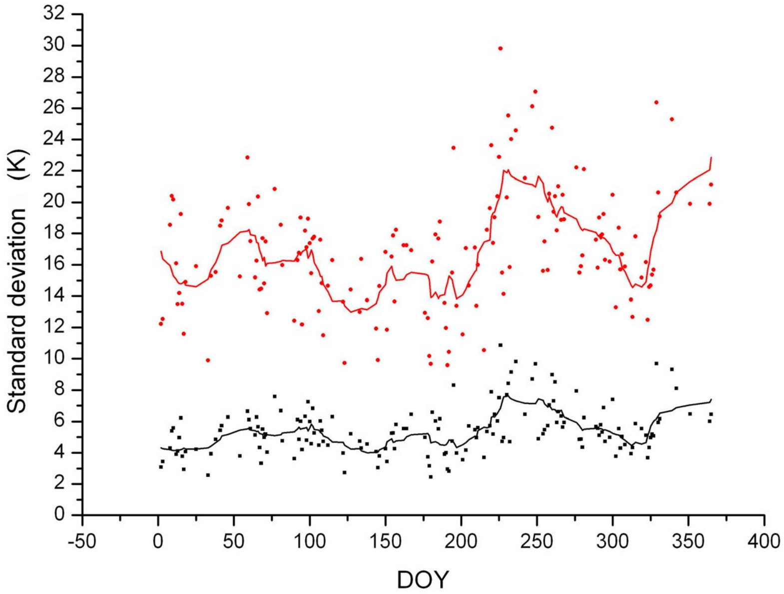

Figure 7. Time development of parameters σ_N (red) and σ_a (black) of Figure 6 during 1997. Solid curves show a 20-point smoothing.

in Figure 6 is representative of all parts of the year. The errors are about ±0.3 K for σ_a and ±0.7 K for σ_N.

[28] The parameter σ_a is a cumulative measure of the amplitudes of the six oscillation periods. It remains to be determined whether or not the amplitudes of the individual periods also behave similarly, or whether certain periods might show a peculiar behavior. This might happen because the shortest periods (3–4.2 min) may be of other origin than the longer periods (6.9–10.4 min) (ripples versus gravity waves, see section 6.1, 6.2). To check on this we plotted the amplitudes of the six periods similarly as in Figure 7 and smoothed them accordingly. These mean curves are shown in Figure 8 together with those of σ_a and σ_N as references. The estimated errors are ±0.7 K for σ_N, and between ±0.25 K and ±0.35 K for the other curves. The curves are quite similar and follow more or less the main features of σ_a and σ_N with their flat maximum in spring and a more pronounced maximum in late summer. Figure 8 shows that σ_a and also σ_N is a reasonable representation of the oscillation activity at these short periods.

[29] These results demonstrate a significant contribution of the very short period wavelike structures to the nightly data variance. About 40% of σ_N can be ascribed to them. The remaining variance must be due to other longer-period gravity waves, noise, etc. The importance of the short oscillations is further discussed in section 6.

4. Seasonal Variations

[30] Temperature standard deviations σ_N as shown in Figure 5 are available at Wuppertal back to 1994. This 16 year data record is shown in Figure 9. A 50-point smoothing has been used. Errors are as in Figure 5. The modulation structure with one or two peaks per year is seen in almost all of the years. Superimposed is a long-term increase 1994–2004 with an apparent trend break around 2004, and a decrease in the following years. The whole data set 1994–2009 shows a positive trend of (0.29 ± 0.02) K/a (dashed line in Figure 9). The size of the seasonal peaks is very variable (see also Figure 5).

[31] We have added in Figure 9 the long-term developments of σ_a (blue) and of the amplitudes of our shortest oscillation (3 min, red). This is because we want to check again on possible differences between the shortest oscillation (3 min) taken as an indication of ripples and the other oscillations contained in σ_a (see Sections 6.1, 6.2). The attribution of the 3 min period to ripples is discussed in Section 6.1 below. The errors of the two curves are ±0.2 K and ±0.25 K, respectively. There are several data gaps in these curves. They mostly occur because only nights with more than five data sets have been used for improved statistics. The curves follow the major structures of σ_N quite well. The correlation of σ_N with σ_a has a coefficient r = 0.94. The slope of the regression line is 0.40. The correlation coefficient of the 3 min amplitudes with σ_N is r = 0.88 (slope is 0.26). That of the 3 min amplitudes with σ_a is r = 0.94 (slope is 0.66). This close relationship of the three parameters is interesting and allows using one (σ_N) for the others. (If unsmoothed data are correlated the coefficients are between 0.57 and 0.88.) A trend of (0.12 ± 0.01) K/a is obtained by fitting a linear regression to the σ_a data (not shown in Figure 9). The corresponding numbers for the 3 min oscillation are (0.061 ± 0.008) K/a. The σ_N data series of Hohenpeißenberg (Figure 5) appears to show a trend different from that at Wuppertal. This series is, however, too short to draw significant conclusions.

[32] In an attempt to understand the nature and variability of the seasonal peaks of σ_N we have calculated a seasonal mean, i.e., the average of all years shown in Figure 9. The result is given in Figure 10. The data are again very variable and have therefore been smoothed by a 50-point running mean (red curve; the error is about three times the thickness

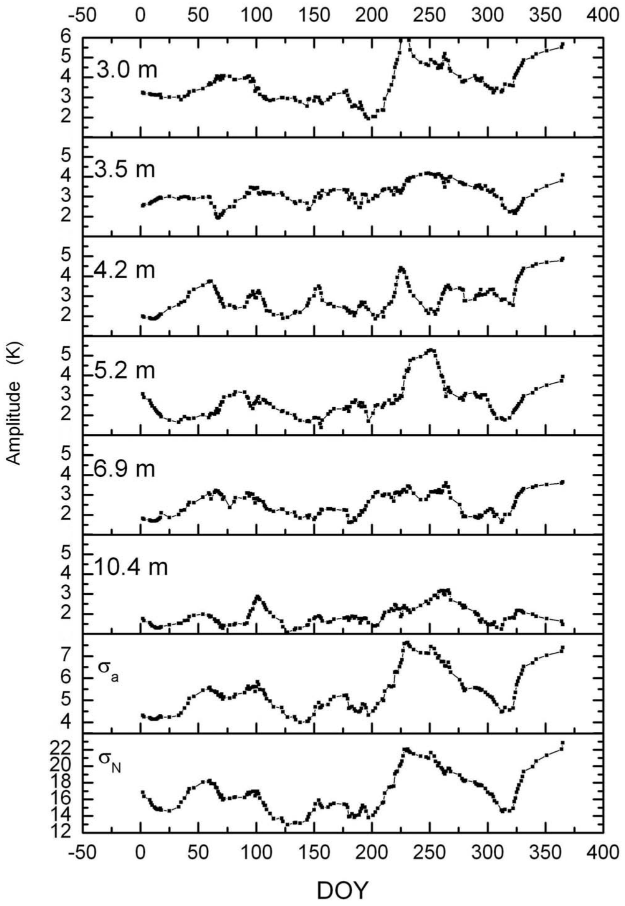

Figure 8. Amplitudes (K) of six oscillation periods given in Figure 3 during 1997. Parameters σ_a and σ_N from Figure 7 are shown for comparison. A 20-point smoothing has been applied. Periods 3.0 m, 3.5 m, and 4.2 m are believed to be "ripples," and longer periods could be "ripples" or gravity waves (see text).

of the line). This mean curve exhibits a seasonal structure as expected from the single years. There is a pronounced late summer peak around DOY 237 and a smaller and broader peak in spring around DOY 108.

[33] We have compared this to the turnaround times (times of zonal wind reversal) in the middle stratosphere (20 hPa altitude). The autumn reversal is at about DOY 244. The spring reversal shows a trend from DOY 110 to DOY 130 between 1988 and 2008. These times are indicated in Figure 10 by vertical dashed (black) lines and by a horizontal black arrow. These times are taken from *Offermann et al.* [2010, Figure 13]. Zonal wind reversal at the altitude of the OH measurements is of greater interest, but cannot be so easily determined. Radar wind measurements nearest to Wuppertal are taken at Juliusruh (55°N, 13°E). They are available at 94 km altitude [*Offermann et al.*, 2010, Figure 15] and show a spring reversal with a trend from DOY 148 to DOY 136 in the time interval 1993–2008. This is indicated by red dashed vertical lines and a red horizontal arrow in Figure 10. The mean value of the autumn turnaround of the radar winds near the mesopause is difficult to determine [*Offermann et al.*, 2010]. We therefore use corresponding radar data at somewhat lower altitude (80 km) from *Keuer et al.* [2007]. They find the autumn reversal near DOY 255 (red vertical dashed line in Figure 10) with a small tendency to shift toward later times.

[34] We thus find that the maxima of the temperature standard deviation σ_N occur before the circulation reversal in the stratosphere (at 20 hPa) as well in spring as in autumn. This applies even stronger to the mesosphere near the OH altitude. It should be noted that in the upper mesosphere the time of turnaround does not change much with altitude.

[35] It is widely believed that gravity waves propagating upwards in the middle atmosphere tend to break and produce turbulence in the 80–90 km altitude regime. This can be seen, for instance, in the recent WACCM 3.5 whole atmosphere model. This model uses a parameterization of both orographic and nonorographic GW. Details of the parameterization are described by *Garcia et al.* [2007]. The parameterization of nonorographic waves now includes variable GW sources that depend on frontal systems and convection calculated in the model [*Richter et al.*, 2010]. In the upper mesosphere parameterized GW dissipation leads to eddy diffusion of potential temperature and constituents which can be represented as vertical diffusion with coefficient K_{zz} (see *Garcia et al.* [2007, Appendix A4] for a description of the formulation). Figure 11 shows monthly mean K_{zz} averaged over a four-member ensemble of WACCM simulations over the period 1987 to 2005. These simulations were conducted as part of the Stratospheric Processes and their Relation to Climate 2nd Chemistry-Climate Model Validation (SPARC CCMVal-2) activity [*Eyring et al.*, 2010; *Morgenstern et al.*, 2010].

[36] The data in Figure 11 are from 19 years of free model runs for an altitude of 85 km. Results at 90 km and 95 km altitude look essentially the same, however, the values are somewhat larger. The eddy coefficients show a pronounced seasonal variation with a high peak in autumn and a slightly broader and smaller peak in spring. This structure is similar to that seen in the temperature standard deviations in Figure 10. The eddy peak values in April, May, and September in Figure 11 (DOYs 105, 135, and 258) are given in Figure 10 as vertical dash-dotted green lines. They occur near to the turnaround times and hence near to the σ_N maxima.

[37] In Figure 11 we have added for comparison the turbopause altitudes as derived by *Offermann et al.* [2007] (errors are a few km and are given in detail in their Figure 6). At a fixed observation height (e.g., 90 km) one would expect high gravity wave amplitudes if the turbopause is at low altitude, and vice versa. We have therefore reversed the scale in Figure 11 for better comparison with K_{zz}. A close correspondence of the two curves is seen. It suggests that around months 4, 5, and 9 there is considerable gravity wave activity leading to strong turbulence production.

[38] We have also compared the monthly eddy values in Figure 11 with monthly mean σ_N values computed from Figure 10. Again, the two curves are quite similar. The correlation coefficient is 0.71 at 99% significance. The similarity is important as data from a global model (WACCM) are compared here to measurements taken at a local station (Wuppertal). These results together with those of Figures 6–9 suggest that our σ_N parameter is related to gravity wave activity as well as gravity wave breaking, and

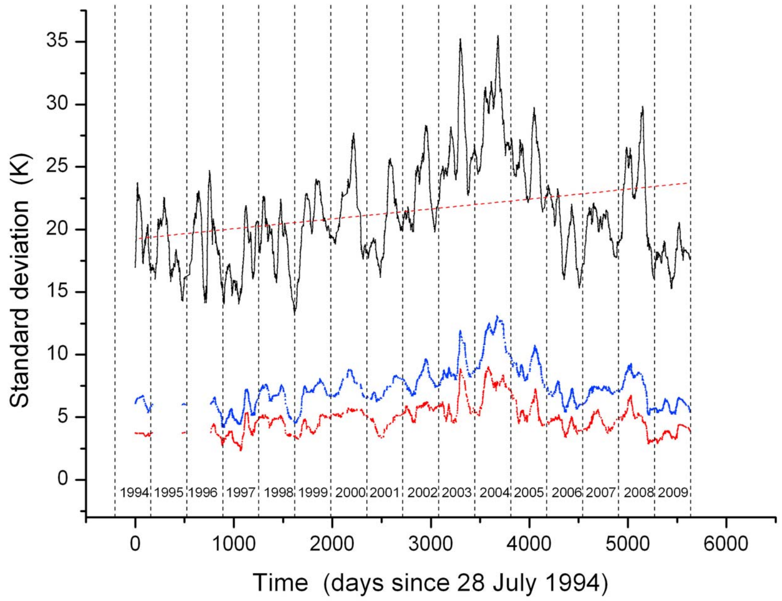

Figure 9. Temperature standard deviations (black) as in Figure 5, but for the extended time interval 1994–2009 at Wuppertal. For comparison, σ_a (blue) and 3 min amplitudes (red) are given (see text). A 50-point smoothing has been applied.

we will therefore tentatively use it as a corresponding proxy in the following. It should be mentioned that the very short period structures (ripples) are also expected to collapse into turbulence [e.g., *Hecht et al.*, 2007].

[39] It is interesting to note that there is a similar correspondence of our K_{zz} and σ values derived from SABER data [*Offermann et al.*, 2009, Figure 8] at lower altitudes (70–80 km). There is, however, only one seasonal K_{zz} maximum at these altitudes. It occurs in summer (July) and

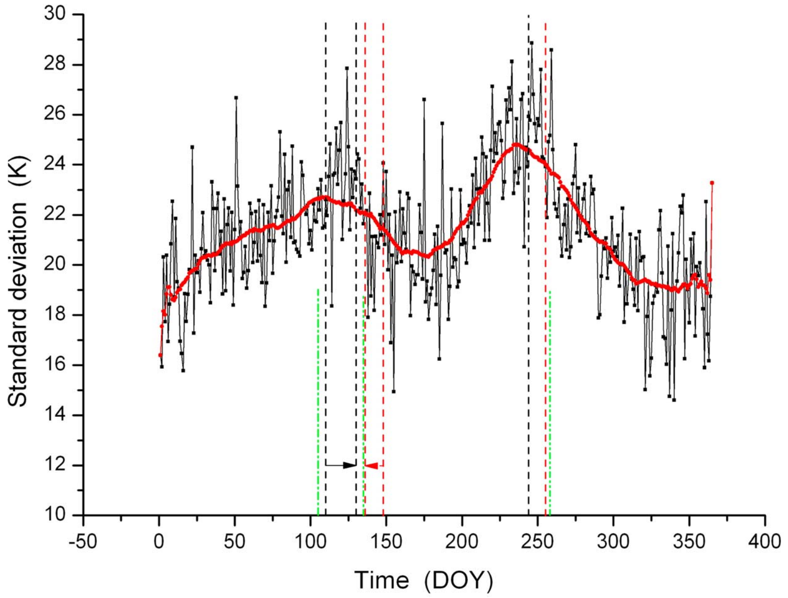

Figure 10. Mean temperature standard deviations σ_N for the years given in Figure 9 (1994–2009). The seasonal variation is shown by the red curve (50-point running mean). Vertical dashed lines indicate circulation turnaround in the stratosphere (black) and mesosphere (red). Black arrow indicates a trend in the stratosphere in the time interval 1988–2008. Red arrow indicates a trend in the mesosphere in the time interval 1993–2008. Green dash-dotted vertical lines indicate the maxima of eddy coefficients in Figure 11. For details see text.

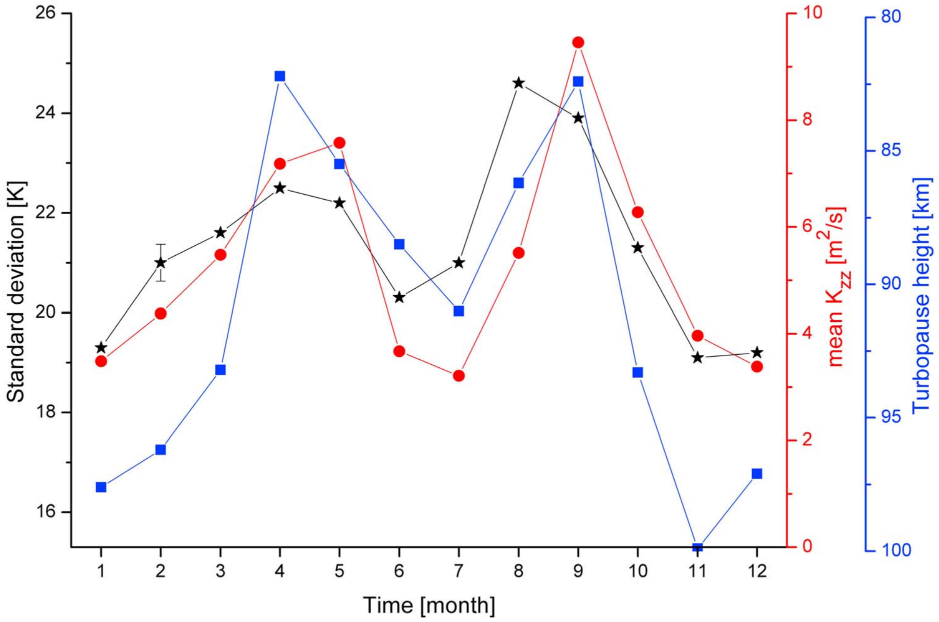

Figure 11. Turbulent eddy coefficients K_{zz} (red dots) as derived by the WACCM 3.5 model. Nineteen years of free model runs have been averaged, and resulting monthly means are shown for 85 km altitude. The turbopause height [*Offermann et al.*, 2007] is given for comparison (blue squares). Please note that its ordinate has been inverted (see text). Temperature standard deviations σ_N (black stars, left ordinate) are monthly means from 1994 to 2009 (87 km altitude). The error bar shown for February is the error of the mean and is typical of the other months.

meets a corresponding maximum in the SABER data, indeed. This shows that the seasonal structures are very variable with altitude which is discussed below (section 6.3).

5. Intradecadal and Interdecadal Variations

[40] In addition to the pronounced seasonal variations of the temperature standard deviations σ_N there are substantial long-term changes as shown by Figure 9. There is a decadal increase until 2003/2004 and a subsequent decrease toward 2009. In addition, there appear to be intradecadal variations superimposed. To separate these variations from the seasonal variations and to show the structures more clearly Figure 12 presents yearly mean values of σ_N. These are calculated from 1 January to 31 December and are plotted in the middle of the year in Figure 12. In order to increase the time resolution of this analysis we have shifted the data series by half a year and calculated corresponding yearly means from 1 July to 30 June of the next year.. These are plotted at the end of the year in Figure 12. For comparison Figure 12 shows corresponding annual amplitudes A_1 of the harmonic analyses described above (red curve).The error of σ_N is about double the size of the symbols. The error of A_1 is ±1.6 K according to *Offermann et al.* [2010, Figure 4].

[41] The increasing or decreasing trends of σ_N before and after 2004 are shown in Figure 12 by linear regression lines. Fit intervals are 1 July 1994 to 1 January 2004, and 1 January 2004 to 1 January 2009, respectively. The differences of the measured data points and the fit lines (residues) show values of several Kelvin and thus are relatively large.

[42] A linear fit line has also been drawn to the A_1 data in Figure 12 (1994–2009), and substantial residues are seen here, too. A weak trend break at 2004 is found in the A_1 data as well. It is, however, so weak that it is disregarded here.

[43] It is very interesting to note that the two types of residues in Figure 12 are in antiphase with each other, i.e., a positive residue in σ_N corresponds to a negative one in A_1, and vice versa. We have calculated the correlation coefficient to be r = −0.63 with a significance of 99%. The slope of the corresponding regression line is −0.47 K/K.

[44] If a fit is calculated for the whole σ_N data set in Figure 12 its slope is (0.32 ± 0.13) K/a. The slope of the corresponding A_1 fit line is −0.042 K/a. The correlation of these data is marginal with a correlation coefficient of −0.38. The gradient of the regression line is –0.17 K/K. It has the same sign as the corresponding value of the residues but is quite a bit smaller.

[45] We have increased the time resolution of the analysis of the whole σ_N data set by calculating trends on a monthly basis instead of an annual basis. The results are shown in Figure 13. The monthly trends are near the slope of the entire data set of 0.32 K/yr. They are, however, not constant during the year but show seasonal variations with a broad maximum in late summer/autumn and another one in spring/early summer (see the hatched areas in Figure 13; the horizontal bar from February to November is meant to guide the eye). There are pronounced minima in February and November. These structures are not too conclusive considering the error bars. Nevertheless, the two broad maxima may be interpreted as time periods of increasing gravity wave activity and hence of dynamical forcing, if we assume

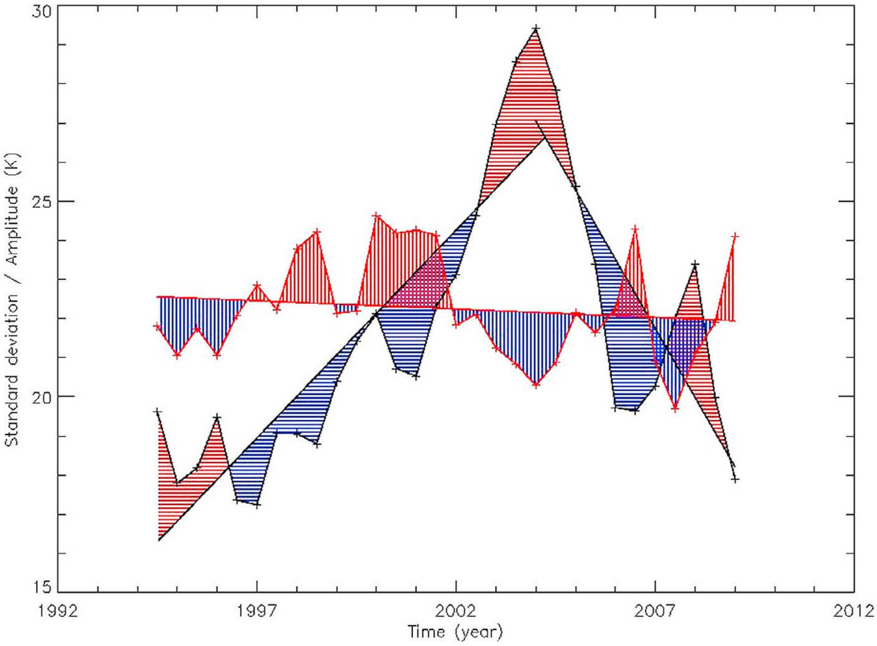

Figure 12. Comparison of yearly mean temperature standard deviations σ_N (black lines and pluses) and harmonic annual fit amplitudes A_1 (red lines and pluses). Data series have been shifted in addition by one half year for increased time resolution (see text). Straight lines are least square fits. Deviations from the fit lines (residues) are shaded red (blue) if positive (negative). Red and blue areas of the two parameters are anticorrelated (see text).

our standard deviations σ_N as proxies for wave breaking. The seasonal structure is similar to the general GW structure seen in Figure 10. To indicate this, the mesosphere turnaround times shown in Figure 10 are also shown in Figure 13 as red dashed vertical lines. It is apparent that the two maxima in Figure 13 occur at the same times or somewhat earlier than those in Figure 10. Hence, if our σ_N is indicative of GW breaking a large and increasing part of it occurs before turnaround.

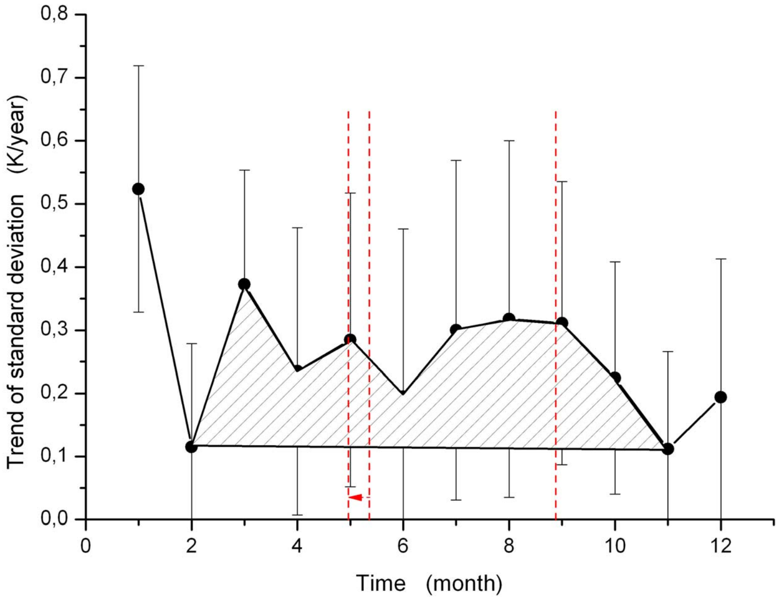

Figure 13. Long-term increase (trend) of temperature standard deviations σ_N on a monthly basis. Trend interval is 1994–2009. Vertical dashed red lines indicate circulation turnaround in the mesosphere and are taken from Figure 10. Red arrow indicates a shift in the time interval 1993–2008.

[46] We have checked whether the long-term trends would influence the seasonal variation of σ_N (Figure 10). Therefore we divided our data set in two subsets: 1994 to 2001 and 2002 to 2009, respectively. Corresponding seasonal variations were determined as in Figure 10 (not shown here). The curve of the later time interval is a few K above that of the earlier interval because of the trend increase in nine years. Otherwise the seasonal variation has not much changed in this time span. This was to be expected from Figure 13.

6. Discussion

6.1. Short-Period Spectra

[47] Waves with short periods and short horizontal wavelengths have been intensively studied in the recent years by various types of airglow imagers [e.g., *Hecht*, 2004; *Hecht et al.*, 2005, 2007; *Taylor et al.*, 2007; *Medeiros et al.*, 2007; *Nielsen et al.*, 2009; *Simkhada et al.*, 2009, and references therein]. Major wavelike structures observed are "bands" and "ripples." Band structures are larger than ripples, with horizontal scales on the order of 25 km versus 15 km [*Hecht*, 2004]. Time periods are on the order of 4–40 min for bands and 3–10 min for ripples. Even shorter periods down to below 1 min) have been occasionally reported as ripples [*Hecht*, 2004].

[48] The band structures are widely believed to show fast gravity waves traveling from the lower atmosphere to the mesopause and eventually breaking there. Vertical wavelengths are on the order of 35 km, i.e., much larger than the OH layer thickness [*Li et al.*, 2005].

[49] Ripples are thought to originate in situ from local nonlinear interactions of wind shears with gravity waves leading to Kelvin-Helmholtz instabilities, and from convective instabilities [*Taylor and Hapgood*, 1990; *Horinouchi et al.*, 2002; *Hecht*, 2004; *Li et al.*, 2005, *Hecht et al.*, 2005, 2007; *Fritts et al.*, 2009]. They are thus indicative of dissipating gravity waves. If these structures move or are transported with the wind through the field of view of an upward looking OH instrument like GRIPS they could have a wave-like appearance [e.g., *Hecht et al.*, 2007]. The apparent oscillation period would be influenced by the wind speed.

[50] In our spectra (Figures 3 and 4) with periods ranging from 3 to 10 min we could see short-period gravity waves as well as ripples. We cannot distinguish between them as imager measurements can do [e.g., *Taylor et al.*, 1997]. However, amplitudes at periods shorter than the Brunt-Väissällä frequency (5 min) can hardly be gravity waves (if we neglect Doppler shifting and evanescent waves [e.g., *Hecht et al.*, 1995, 2007; *Yue et al.*, 2010]). It needs to be mentioned that the period limitation to greater than 5 min is valid for the intrinsic frequencies. *Nielsen et al.* [2009] have shown, however, that the average distributions of observed and intrinsic periods of gravity waves are rather similar. This leads us to use apparent (observed) periods here.

[51] Many histograms of the occurrence of band and ripple periods have been published [e.g., *Taylor et al.*, 1997; *Nakamura et al.*, 1999, 2003; *Pautet et al.*, 2005; *Medeiros et al.*, 2007; *Suzuki et al.*, 2009]. Imagers find the shortest ripple periods to be well below shortest gravity wave (band) periods. Shortest ripple periods are found down to below 2.7 min by *Taylor et al.* [1997] and down to below 1 min by *Hecht* [2004]. In a detailed analysis of measurements with enhanced spatial resolution *Hecht et al.* [2007] identify the vast majority of features with periods below 4 min as ripples. They find wavelike structures down to periods below 2 min. The maximum of counted numbers of these ripples is found around periods of 3 min. These are observed periods that can be directly compared to our results (Figures 3 and 4). The increase of our amplitudes toward shorter periods in Figure 4 compares favorably with the results of *Hecht et al.* [2007, Figure 7]. It should be noted that *Hecht et al.* [2007] analyze intensity structures, only, whereas our oscillations are seen in temperature as well as in intensity.

[52] On the basis of the work cited we assume here as a working hypothesis that our oscillations at periods of 3 min are ripples. Our parameter σ_a is a superposition of gravity wave and ripple activity. We thus tentatively use our 3 min amplitudes as indication (proxy) of unstable (dissipating) gravity waves or atmospheric instability events involving gravity waves. The following analysis will show how far this assumption carries. The high correlation of the 3 min amplitudes with parameter σ_a obtained above (section 4) shows that σ_a is indicative of unstable gravity waves, too.

[53] Ripples are expected to mostly decay into turbulence [e.g., *Hecht et al.*, 2007]. The above shown high correlations of our 3 min amplitudes with our gravity wave proxy σ_N on the one hand, and of σ_N with the eddy coefficients K_{zz} on the other are in line with this expectation.

[54] Not much seems to be known about power spectra at these short periods because emphasis in the literature is mostly on structures with periods longer than the Brunt-Väissällä period [e.g., *Dewan et al.*, 1992; *Hecht et al.*, 2007]. It should be noted that our spectra (Figure 4) cannot be compared to standard power spectra directly because our analysis method emphasizes strong oscillations and we show weighted amplitudes.

6.2. Standard Deviations as Wave Proxies

[55] Our parameter σ_N is the temperature standard deviation in one night. It is used here as a proxy for gravity waves as has been done in many publications since the early work of *Fetzer and Gille* [1994] and *Wu and Waters* [1996]. In Figure 6 we demonstrate a very close correlation of the two parameters σ_a and σ_N, and in section 4 we find the same for the 3 min amplitudes and σ_N. If the 3 min amplitudes and σ_a are proxies for breaking gravity waves, this correlation means that some part of the gravity waves present in σ_N are unstable. This is not unreasonable at the altitude of 87 km as gravity waves are generally assumed to break in the 80–90 km regime. It is in line with Figure 11 which shows a close correlation of σ_N and the eddy coefficients K_{zz} at 85 km, as mentioned.

[56] The parameter σ_N is very useful to analyze various wave features in an easy way. It needs to be noticed, however, that it takes into account only short- and medium-period waves as it is restricted to the nightly measurement time of a few hours. The parameter σ_a is also highly selective (e.g., concerning the wavelength). It selects waves/oscillations that are visible in temperature and transport (i.e., intensity) simultaneously. One could thus suspect that the very short oscillations (3–10 min) might not be typical of the atmosphere. Figure 8 shows, however, that the seasonal

variations (in 1997) of the shortest periods, of σ_a, and of σ_N are quite similar. The correlation of the 3 min data with σ_N in Figure 8 yields, for instance, a coefficient r = 0.59. The slope of the regression line is 0.29 K/K. The corresponding numbers for the larger data set in Figure 9 are r = 0.88 and 0.26 K/K, respectively. This confirms the connection of ripples and general gravity waves if it is assumed that the 3 min data represent the former, and σ_N the latter.

[57] The slope of the regression line σ_a versus σ_N is 0.38 K/K in Figure 6 and 0.40 K/K in Figure 9. Hence, σ_N contains a substantial amount of fluctuations beyond the very short oscillations shown in Figure 4. These may be longer-period gravity waves. They could, however, also be some short-period features that were neglected because our analysis method yields lower limits, only.

6.3. Seasonal Variations

[58] Seasonal variations of gravity wave activity are interesting because the corresponding wave breaking is thought to control the large scale circulation in the mesosphere [*Holton*, 1983]. Gravity wave maxima in summer and in winter are believed to explain zonal wind turnaround in spring and autumn. Corresponding seasonal variations have been inferred by various model studies [see, e.g., *Fritts and Alexander*, 2003].

[59] Many wind measurements by ground based radars have been performed, and frequently found the above mentioned semiannual variation with gravity wave maxima at solstices, sometimes superimposed on an additional annual variation [e.g., *Manson et al.*, 1999; *Beldon and Mitchell*, 2009; *Placke et al.*, 2010, 2011, and references therein]. Details of this basic picture can be quite different at least at times as gravity waves are found to be strongly dependent on parameters like altitude, latitude, local station, and their period and wavelength. *Dowdy et al.* [2007] found a mixture of annual and semiannual variations that was different at 80 km and 90 km, depending on the wave periods. The relative share even reversed from the lower to the higher altitude. A peculiar altitude dependence was also seen by *Jacobi et al.* [2006], with an annual variation at lower altitudes, i.e., a summer solstice maximum that split and moved toward the equinoxes at the higher altitudes. It is interesting to note that annual and/or semiannual variations are frequent in mesospheric and lower thermospheric airglow intensity, and a similar transition from an annual variation at lower altitudes to a semiannual variation at higher altitudes was reported by *Liu et al.* [2008]. Much interannual variation of the seasonal gravity wave changes is also seen.

[60] Seasonal satellite measurements have also been reported by *Jiang et al.* [2006]. They analyzed MLS data measured on the AURA satellite at high latitudes (and 80 km altitude) and found a semiannual oscillation with maxima near solstices in the mesosphere and an annual variation in the upper stratosphere.

[61] The seasonal curves presented here (Figures 5 and 7–11) are different. The characteristic seasonal structure is a double peak with one maximum near spring turnaround and another one near autumn turnaround (Figure 10). However, it does not occur in every year. Sometimes the two peaks seem to be merged into one (summer) peak (Figure 9). Another difference is that at the end of most years there is a deep minimum and not a winter maximum as reported in much of the literature.

[62] Temperature measurements from SABER on the TIMED satellite have been analyzed by *Preusse et al.* [2009] and *Offermann et al.* [2009]. The latter authors find a double peak structure in the summer half of the year with maxima in April/May and July/August, respectively (at 50°N, Offermann et al.'s Figure 8). This is very similar to the double structure shown here in April and August (in Figures 10 and 11). An even better agreement is obtained between the mean curve in time interval 2002–2009 (see above Section 5, last paragraph) and Figure 6 of *Offermann et al.* [2009] (2002–2005, 88 km) which gives a closer comparison in altitude and time interval. The correlation coefficient of these two curves is 0.53 at 93% significance).

[63] The double peak structure is seen by *Offermann et al.* [2009] not only at 50°N and 88–90 km, but appears to be present in a similar form also at 70°N (90 km and 100 km, Offermann et al.'s Figure 8). It is important to note that at 50°N and different altitudes (10 km lower and higher than 90 km) the seasonal variations look fairly different (maxima near summer and winter solstices). The same applies to 70°N at lower altitudes (winter maxima only). Hence, the seasonal variation of gravity waves is quite variable with altitude and latitude. This may explain the variety of results reported in the literature.

[64] Another reason of the different experimental results may be the differences in measurement techniques. Radar wind data yield kinetic energies of gravity waves whereas OH temperature data yield potential energies. These different energies have sensitivity to different gravity wave frequencies as was shown by *Geller and Gong* [2010]. Different frequencies, however, may have different seasonal variations [e.g., *Dowdy et al.*, 2007]. Gravity wave results recently published by *Yang et al.* [2010] appear to fit this picture. They derived gravity wave activity from temperature perturbations and showed semiannual maxima near the equinoxes.(These lidar measurements were taken at 23°S.)

[65] Our gravity wave proxy σ_N is correlated with wave breaking and turbulence production. The close correspondence of σ_N (16 years of local OH temperature measurements), eddy coefficients (global GCM, 19 years), and the turbopause height (4 years of SABER data, Figure 11) yields a consistent picture even though the data sets are rather different. The physical relation between our two seasonal gravity wave maxima and the circulation turnaround times needs to be determined yet.

6.4. Decadal Variations and Trends

[66] Long-term variations of mesospheric winds and other parameters have frequently been discussed in the literature. This includes trend-like developments as well as frequent trend breaks [e.g., *Portnyagin et al.*, 2006; *Laštovička et al.*, 2008, 2010; *Laštovička*, 2009, and references therein]. Little seems to be known about long-term changes of gravity wave activity. *Jacobi et al.* [2006] report on solar cycle dependence of this activity (see also the references therein). No conclusive results appear to be available for longer-term trends. Considering the consequences of gravity waves for mesospheric energy and momentum budgets, a search for a trend appears to be important.

[67] Our long-term data are shown in Figure 9. Here, solar cycle influences, if present, should show up with the maximum around years 2000/2001 and the solar minima around 1996 and 2008/9. Variability of the data is high, however, and in consequence a solar cycle signature cannot be identified. A substantial long-term trend is seen, though, with a break in 2004 (Figure 12). If the data are fitted without a break the trend is still there, but much weaker (Figure 9).

[68] We interpret this trend as an increasing gravity wave activity with associated dissipation. If this is true there should be a corresponding change of mesospheric circulation. This is found, indeed, in the data of *Keuer et al.* [2007]. These authors analyzed radar wind measurements at Juliusruh (55°N, 13°E) and found a long-term increase of the zonal wind speed U in summer in the time frame 1993–2005 at altitudes 85 km and 90 km (Keuer et al.'s Figure 15). The mean trend at the two altitudes is (0.52 ± 0.03) m/s per year. It is a mean value for the whole summer from April to September. This compares to an increase of the gravity wave proxy σ_N of 0.32 K/year. We call the ratio of the two numbers a trend sensitivity S_t which then results to $S_t = 1.6$ (m/s)/K.

[69] Superimposed on the fit lines of *Keuer et al.* [2007] are several intradecadal fluctuations (residues with respect to the fit lines). The most pronounced ones are in the years 2001–2002 for low values of U and 2003–2005 for high values. The mean swing between these two intervals is 7.5 m/s. There are corresponding fluctuations (low/high) of our σ_N in the same time intervals, with a swing of 3.4 K (Figure 12). The resulting sensitivity of the residues is $S_r = 2.2$ (m/s)/K. Hence the two sensitivity values are close together and are essentially the same if the errors (±49%) are taken into account. We conclude that the intradecadal influence of the gravity waves on the circulation (U) is about the same as for the extradecadal trends with a mean sensitivity of S = 1.9 (m/s)/K. It should be noted that we compare here annual σ_N values with zonal winds in summer. This is, however, not a strong limitation because the winter winds have almost no trend.

[70] The seasonal temperature variation in the upper mesosphere (Figure 1) is closely linked to the atmospheric circulation. If there is a long-term change in the wind field one may expect changes in the seasonal temperature variation as well. We therefore compare the residues of the annual amplitudes A_1 with those of σ_N (Figure 12). As mentioned before, they are anticorrelated ($r = -0.63$). The corresponding sensitivity is $S_r = (-0.47 \pm 0.11)$ K/K. Hence, there appears to be a substantial influence of the gravity waves on the harmonic amplitude.

[71] The long-term trends of the two parameters are opposite as well (Figures 9 and 12). They are, however, fairly flat and have large errors. In this case, a trend sensitivity S_t is not very meaningful.

[72] Changes of the seasonal temperature variation suggest changes of the summer duration. The Equivalent Summer Duration (ESD) is the time interval in Figure 1 when the harmonic fit curve is below 198 K. It varies from year to year and shows a long-term increase of 1.2 days/year since 1988 [*Offermann et al.*, 2010]. The mean ESD is about 150 days. Hence, the increase is about 0.8%/year. The corresponding change rate of σ_N given above is 0.32 K/year, i.e., 1.5%/year. Although no direct conclusions can be drawn from these numbers it is interesting to note that they are on the same order of magnitude.

[73] The summer length can also be defined as the time difference between the zonal wind turnaround in spring and autumn [see *Offermann et al.*, 2010]. The turnaround method is in principle to be preferred to the ESD method because it is more objective. The spring turnaround data in the mesosphere are available from the measurements at the station of Juliusruh. They show a trend of about 0.8 days/year toward earlier times (at 94 km [*Offermann et al.*, 2010, Figure 15]). This compares well with the change rate of the spring point of the ESD analysis of about 0.9 days/year [*Offermann et al.*, 2010]. This shows that the two definitions of summer length yield similar results. However, the autumn turnaround data of the wind station are not available for a period sufficiently long to derive a trend. Hence the turnaround method cannot be applied directly. We therefore use estimated reversal times as a surrogate as follows.

[74] A change of the spring/autumn time difference can be roughly estimated from the long-term increase of the zonal wind velocity U. The zonal wind U increases from spring turnaround toward the middle of summer, and subsequently decreases again toward autumn turnaround. This is sketched in a very simplified manner in Figure 14 by assuming linear changes (87.5 km). The summer length is 2*SL (see Figure 14). The parameter u denotes the increase of the wind speed (for instance in one year). It is assumed here for simplicity that u is the same at all times of the summer. This leads to a shift sl of the turnaround point (U = 0) to earlier times in the first half of summer. From the geometry of Figure 14 it follows that $U_0/SL = u/sl$. Mid summer maximum wind speed U_0 is about 12 m/s, half of the summer length is SL = 62 days (data for 87.5 km from *Offermann et al.* [2011, Figure 6]). The increase rate u as derived above from *Keuer et al.* [2007] is u = 0.52 (m/s)/year. The resulting increase of the summer length is sl = 2.7 days/year (shift of spring turnaround toward earlier times), which is half of the total increase.

[75] This estimate is based on the approximate finding that there is almost no change of wind speed in winter [*Keuer et al.*, 2007]. The estimate is an overestimation because it assumes the same trend during all of summer. This is an oversimplification as the real trend increases toward the middle of summer [*Keuer et al.*, 2007] which leads to smaller sl values. Comparing this to the results given above [*Offermann et al.*, 2010] our surrogate yields the right direction and the right order of magnitude. These results suggest a physical relationship of the increase of summer duration and the increases of gravity waves and zonal wind.

[76] It is interesting to note that very similar changes of spring turnaround as discussed here (but with opposite sign) have been reported from measurements and modeling of the stratosphere in the Northern as well as the Southern Hemisphere [*McLandress et al.*, 2010; *Offermann et al.*, 2010].

[77] It has been noted in the literature that gravity wave increases may lead to increased atmospheric instability in the mesosphere [*Hecht*, 2004]. Measured changes of barotropic and baroclinic instabilities have been reported by *Offermann et al.* [2011]. They find a modification of the occurrence distribution of the Quasi-Two Day Waves (QTDW) in the summer mesosphere. For instance, instability appears to have increased in recent years in the middle

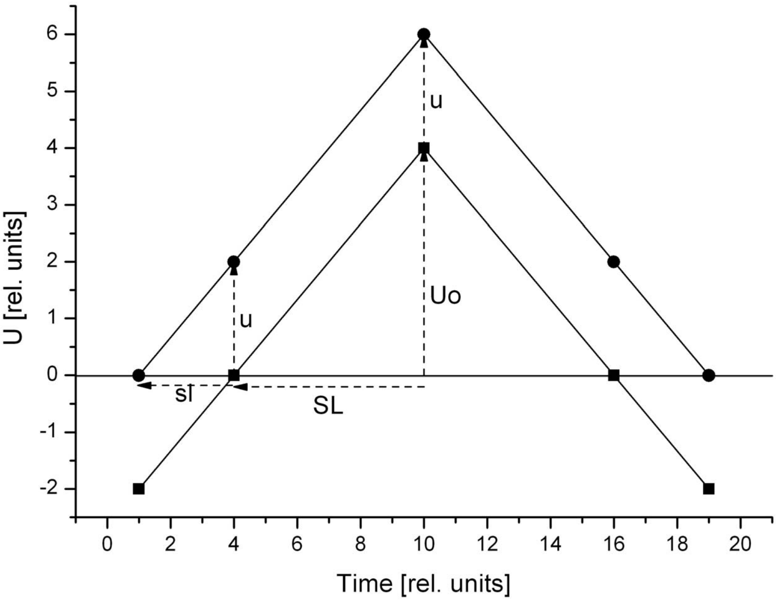

Figure 14. Sketch of zonal wind variation in summer (87.5 km; see text). Summer length is 2*SL. Increase of summer length is by 2*sl and results from an increase of zonal wind U by u.

of May and at the end of August (peaks of QTDW amplitudes, Offermann et al.'s Figure 12). These are times of substantial increases of our gravity wave proxy σ_N as shown in Figure 13. *Offermann et al.* [2011] also gave some quantitative estimate of the baroclinic instability in the mesosphere from radar wind measurements at Juliusruh. They found an increase especially in the early part of summer (DOY 100–140). The baroclinic instability increased by about a factor 1.6 (±6%) in seven years (using the intervals 1990–1995 and 1997–2002 for comparison, Offermann et al.'s Figure 13). This can be compared to our σ_N data in the same time interval (1993–2000). These increase by a factor 1.5 (±13%) according to the fit line in Figure 12. This is an interesting coincidence that suggests more detailed studies.

7. Summary and Conclusions

[78] Fluctuations of mesospheric temperature and winds have frequently been taken as proxies for atmospheric gravity waves. Here we use temperature standard deviations during the night (σ_N) as indicators of gravity wave activity. Hydroxyl (OH) temperature measurements at Wuppertal (51°N, 7°E) and Hohenpeissenberg (48°N, 11°E) are analyzed. Furthermore, data in windows of 21 min length are Fourier analyzed and yield oscillation amplitudes for periods between 3 and 10 min. These amplitudes are expressed by their equivalent standard deviation σ_a for comparison with σ_N. Standard deviations σ_a and σ_N are found closely correlated.

[79] The mean duration of the nightly measurements is approximately 5 h. Wave periods up to this length are therefore covered by σ_N. Hence, relatively short to very short waves/oscillations are analyzed here. The shortest periods (3 min) in their majority cannot be gravity waves as these mostly exist at periods longer than the Brunt-Väissällä period (5 min). They are therefore interpreted as "ripples" that result from atmospheric instabilities/gravity wave breaking. Parameter σ_a thus contains ripples and short-period gravity waves. There is a close correlation between the ripples (3 min amplitudes), σ_a, and σ_N. Therefore these parameters are taken here as proxies for gravity waves and breaking gravity waves. This is supported by a close relationship with turbulent eddy coefficients obtained from a general circulation model (WACCM 3.5). Hence, the picture suggested here is that gravity wave activity in general is accompanied by a certain amount of wave breaking/dissipation at the altitudes of our measurements. This leads us to use the standard deviations to study variations of the forcing of dynamics/circulation in the mesosphere.

[80] Time variations of σ_N (and $\sigma_{a,}$ 3 min amplitudes) are observed on seasonal, intradecadal, and interdecadal (trend) scales. Seasonal variations show on the mean two relative maxima near (somewhat before) circulation turnaround in spring and autumn. This has been found in 13 years of Wuppertal data and in very similar form in several years of simultaneous measurements at Hohenpeissenberg. A similar seasonal variation has recently been obtained from a gravity wave analysis of SABER data. A physical relationship of gravity wave maxima and times of circulation reversal needs to be determined, though.

[81] There is an extradecadal (trend) variation of σ_N seen as a long-term increase (16 years). Similar variations are found in the zonal wind speed and the annual component A_1 of the seasonal temperature variation. The intradecadal changes as well as the extradecadal variations of the zonal wind closely correlate with the parameter σ_N.

[82] The long-term increase of σ_N is 1.5%/year, which means a corresponding increase of long-term gravity wave activity. This appears to lead to an increase of zonal wind speed of 0.5 m/s per year at 87.5 km altitude and 55°N. This trend value allows estimating a change in summer length at

the mesopause. An increase results that is in qualitative agreement with an increase of the Equivalent Summer Duration (ESD) reported in the literature.

[83] In summary, we observe changes of several dynamical parameters that appear compatible with considerable variations and a long-term increase of the activity of short-period gravity waves in the mesosphere.

[84] **Acknowledgments.** We thank Dan Marsh (ACD, NCAR, Boulder, Colorado) for making the mesospheric eddy coefficients of WACCM 3.5 available to us. Many helpful discussions with P. Hoffmann (IAP, Kühlungsborn) are gratefully acknowledged.

References

Alexander, M. J. (1998), Interpretation of observed climatological patterns in stratospheric gravity wave variance, *J. Geophys. Res.*, *103*, 8627–8640, doi:10.1029/97JD03325.

Alexander, M. J., and D. Ortland (2010), Equatorial waves in High Resolution Dynamics Limb Sounder (HIRDLS) data, *J. Geophys. Res.*, *115*, D24111, doi:10.1029/2010JD014782.

Andrews, D. G., J. R. Holton, and C. B. Leovy (1987), *Middle Atmosphere Dynamics*, *Int. Geophys. Ser.*, vol. 40, Academic, San Diego, Calif.

Beldon, C. L., and N. J. Mitchell (2009), Gravity waves in the mesopause region observed by meteor radar, 2: Climatologies of gravity waves in the Antarctic and Arctic, *J. Atmos. Sol. Terr. Phys.*, *71*, 875–884, doi:10.1016/j.jastp.2009.03.009.

Bittner, M., D. Offermann, H.-H. Graef, M. Donner, and K. Hamilton (2002), An 18-year time series of OH rotational temperatures and middle atmosphere decadal variations, *J. Atmos. Sol. Terr. Phys.*, *64*, 1147–1166, doi:10.1016/S1364-6826(02)00065-2.

Dewan, E. M., W. Pendleton, N. Grossbard, and P. Espy (1992), Mesospheric OH airglow temperature fluctuations: A spectral analysis, *Geophys. Res. Lett.*, *19*, 597–600, doi:10.1029/92GL00391.

Dowdy, A. J., R. A. Vincent, M. Tsutsumi, K. Igarashi, Y. Murayama, W. Singer, and D. J. Murphy (2007), Polar mesosphere and lower thermosphere dynamics: 1. Mean wind and gravity wave climatologies, *J. Geophys. Res.*, *112*, D17104, doi:10.1029/2006JD008126.

Eckermann, S. D., and P. Preusse (1999), Global measurements of stratospheric mountain waves from space, *Science*, *286*, 1534–1537, doi:10.1126/science.286.5444.1534.

Ern, M., P. Preusse, M. J. Alexander, and C. D. Warner (2004), Absolute values of gravity momentum flux derived from satellite data, *J. Geophys. Res.*, *109*, D20103, doi:10.1029/2004JD004752.

Eyring, V., T. G. Shepherd, and D. W. Waugh (Eds.) (2010), SPARC CCMVal report on the evaluation of chemistry-climate models, *SPARC Rep. 4*, SPARC, Univ. of Toronto, Toronto, Ont., Canada. [Available at http://www.atmosp.physics.utoronto.ca/SPARC.]

Fetzer, E. J., and J. C. Gille (1994), Gravity wave variances in LIMS temperatures, I, Variability and comparison with background winds, *J. Atmos. Sci.*, *51*, 2461–2483, doi:10.1175/1520-0469(1994)051<2461:GWVILT>2.0.CO;2.

Fritts, D. C., and M. J. Alexander (2003), Gravity wave dynamics and effects in the middle atmosphere, *Rev. Geophys.*, *41*(1), 1003, doi:10.1029/2001RG000106.

Fritts, D. C., S. L. Vadas, K. Wan, and J. A. Werne (2006), Mean and variable forcing of the middle atmosphere by gravity waves, *J. Atmos. Sol. Terr. Phys.*, *68*, 247–265, doi:10.1016/j.jastp.2005.04.010.

Fritts, D. C., L. Wang, and J. Werne (2009), Gravity wave-fine structure interactions: A reservoir of small-scale and large scale turbulence energy, *Geophys. Res. Lett.*, *36*, L19805, doi:10.1029/2009GL039501.

Garcia, R. R., D. R. Marsh, D. E. Kinnison, B. A. Boville, and F. Sassi (2007), Simulation of secular trends in the middle atmosphere, 1950–2003, *J. Geophys. Res.*, *112*, D09301, doi:10.1029/2006JD007485.

Geller, M. A., and J. Gong (2010), Gravity wave kinetic, potential, and vertical fluctuation energies as indicators of different frequency gravity waves, *J. Geophys. Res.*, *115*, D11111, doi:10.1029/2009JD012266.

Hecht, J. H. (2004), Instability layers and airglow imaging, *Rev. Geophys.*, *42*, RG1001, doi:10.1029/2003RG000131.

Hecht, J. H., S. K. Ramsay Howat, R. L. Walterscheid, and J. R. Isler (1995), Observations of spectra of intensity fluctuations of the OH Meinel nightglow during ALOHA-93, *Geophys. Res. Lett.*, *22*, 2873–2876, doi:10.1029/95GL03020.

Hecht, J. H., A. Z. Liu, R. L. Walterscheid, and R. J. Rudy (2005), Maui Mesosphere and Lower Thermosphere (Maui MALT) observations of the evolution of Kelvin-Helmholtz billows formed near 86 km altitude, *J. Geophys. Res.*, *110*, D09S10, doi:10.1029/2003JD003908.

Hecht, J. H., A. Z. Liu, R. L. Walterscheid, S. J. Franke, R. J. Rudy, M. J. Taylor, and P.-D. Pautet (2007), Characteristics of short-period wavelike features near 87 km altitude from airglow and lidar observations over Maui, *J. Geophys. Res.*, *112*, D16101, doi:10.1029/2006JD008148.

Hines, C. O. (1960), Internal atmospheric gravity waves at ionospheric heights, *Can. J. Phys.*, *38*, 1441–1481, doi:10.1139/p60-150.

Hoffmann, P., M. Rapp, W. Singer, and D. Keuer (2011), Trends of mesospheric gravity waves at northern middle latitudes during summer, *J. Geophys. Res.*, doi:10.1029/2011JD015717, in press.

Holton, J. R. (1983), The influence of gravity wave breaking on the general circulation of the middle atmosphere, *J. Atmos. Sci.*, *40*, 2497–2507, doi:10.1175/1520-0469(1983)040<2497:TIOGWB>2.0.CO;2.

Horinouchi, T., T. Nakamura, and J. Kosaka (2002), Convectively generated mesoscale gravity waves simulated throughout the middle atmosphere, *Geophys. Res. Lett.*, *29*(21), 2007, doi:10.1029/2002GL016069.

Jacobi, C., N. M. Gavrilov, D. Kürschner, and K. Fröhlich (2006), Gravity wave climatology and trends in the mesosphere/lower thermosphere region deduced from low-frequency drift measurements 1984–2003 (52.1°N, 13.2°E), *J. Atmos. Sol. Terr. Phys.*, *68*, 1913–1923, doi:10.1016/j.jastp.2005.12.007.

Jiang, J. H., S. D. Eckermann, D. L. Wu, and D. Y. Wang (2006), Interannual variation of gravity waves in the Arctic and Antarctic winter middle atmosphere, *Adv. Space Res.*, *38*, 2418–2423, doi:10.1016/j.asr.2005.09.036.

Keuer, D., P. Hoffmann, W. Singer, and J. Bremer (2007), Long-term variations of the mesospheric wind field at mid-latitudes, *Ann. Geophys.*, *25*, 1779–1790, doi:10.5194/angeo-25-1779-2007.

Krebsbach, M., and P. Preuße (2007), Comparison of global distributions of zonal mean gravity wave variance inferred from different satellites measurements, *Geophys. Res. Lett.*, *34*, L03814, doi:10.1029/2006GL028040.

Laštovička, J. (2009), Global pattern of trends in the upper atmosphere and ionosphere: Recent progress, *J. Atmos. Sol. Terr. Phys.*, *71*, 1514–1528, doi:10.1016/j.jastp.2009.01.010.

Laštovička, J., R. A. Akmaev, G. Beig, J. Bremer, J. T. Emmert, C. Jacobi, M. J. Jarvis, G. Nedoluha, Y. I. Portnyagin, and T. Ulich (2008), Emerging pattern of global change in the upper atmosphere and ionosphere, *Ann. Geophys.*, *26*, 1255–1268, doi:10.5194/angeo-26-1255-2008.

Laštovička, J., P. Krizan, and M. Kozubek (2010), Long-term trends in the middle atmosphere dynamics at northern middle latitudes—One regime or two different regimes?, *Atmos. Chem. Phys. Discuss.*, *10*, 2633–2668, doi:10.5194/acpd-10-2633-2010.

Li, F., A. Z. Liu, G. R. Swenson, J. H. Hecht, and W. A. Robinson (2005), Observation of gravity wave breakdown into ripples associated with dynamical instabilities, *J. Geophys. Res.*, *110*, D09S11, doi:10.1029/2004JD004849.

Liu, G., G. G. Shepherd, and R. G. Roble (2008), Seasonal variations of the nighttime O(^{1}S) and OH airglow emission rate at mid-to-high latitudes in the context of the large- scale circulation, *J. Geophys. Res.*, *113*, A06302, doi:10.1029/2007JA012854.

Manson, A. H., C. E. Meek, C. Hall, W. K. Hocking, J. MacDougall, S. Franke, K. Igarashi, D. Riggin, D. C. Fritts, and R. A. Vincent (1999), Gravity wave spectra, directions and wave interactions: Global MLT-MFR network, *Earth Planets Space*, *51*, 543–562.

McLandress, C., M. J. Alexander, and D. L. Wu (2000), Microwave Limb Sounder observations of gravity waves in the stratosphere: A climatology and interpretation, *J. Geophys. Res.*, *105*, 11,947–11,967, doi:10.1029/2000JD900097.

McLandress, C., A. I. Jonsson, D. A. Plummer, M. C. Reader, J. F. Sinocca, and T. G. Shepherd (2010), Separating the dynamical effects of climate change and ozone depletion. Part I: Southern Hemisphere stratosphere, *J. Clim.*, *23*, 5002–5020, doi:10.1175/2010JCLI3586.1.

Medeiros, A. F., H. Takahashi, R. A. Buriti, J. Fechine, C. M. Wrasse, and D. Gobbi (2007), MLT gravity wave climatology in the South America equatorial region observed by airglow imager, *Ann. Geophys.*, *25*, 399–406, doi:10.5194/angeo-25-399-2007.

Morgenstern, O., et al. (2010), Review of the formulation of present-generation stratospheric chemistry-climate models and associated forcings, *J. Geophys. Res.*, *115*, D00M02, doi:10.1029/2009JD013728.

Mulligan, F. J., M. E. Dyrland, F. Sigernes, and C. S. Deehr (2009), Inferring hydroxyl layer peak heights from ground-based measurements of OH(6–2) band integrated emission rate at Longyearbyen (78°N, 16°E), *Ann. Geophys.*, *27*, 4197–4205, doi:10.5194/angeo-27-4197-2009.

Nakamura, T., A. Higashikawa, T. Tsuda, and Y. Matsushita (1999), Seasonal variations of gravity wave structures in OH airglow with a CCD imager at Shigaraki, *Earth Planets Space*, *51*, 897–906.

Nakamura, T., T. Aono, T. Tsuda, A. G. Admiranto, E. Achmad, and Suranto (2003), Mesospheric gravity waves over a tropical convective region observed by OH airglow imaging in Indonesia, *Geophys. Res. Lett.*, *30*(17), 1882, doi:10.1029/2003GL017619.

Nielsen, K., M. J. Taylor, R. E. Hibbins, and M. J. Jarvis (2009), Climatology of short-period mesospheric gravity waves over Halley, Antarctica (76°S, 27°W), *J. Atmos. Sol. Terr. Phys.*, *71*, 991–1000, doi:10.1016/j.jastp.2009.04.005.

Oberheide, J., D. Offermann, J. M. Russell III, and M. G. Mlynczak (2006), Intercomparison of kinetic temperature from 15 μm CO_2 limb emissions and OH*(3,1) rotational temperature in nearly coincident air masses: SABER, GRIPS, *Geophys. Res. Lett.*, *33*, L14811, doi:10.1029/2006GL026439.

Offermann, D., M. Jarisch, M. Donner, W. Steinbrecht, and A. I. Semenov (2006), OH temperature re-analysis forced by recent variance increases, *J. Atmos. Sol. Terr. Phys.*, *68*, 1924–1933, doi:10.1016/j.jastp.2006.03.007.

Offermann, D., M. Jarisch, H. Schmidt, J. Oberheide, K. U. Grossmann, O. Gusev, J. M. Russell III, and M. G. Mlynczak (2007), The “wave turbopause,” *J. Atmos. Sol. Terr. Phys.*, *69*, 2139–2158, doi:10.1016/j.jastp.2007.05.012.

Offermann, D., O. Gusev, M. Donner, J. M. Forbes, M. Hagan, M. G. Mlynczak, J. Oberheide, P. Preusse, H. Schmidt, and J. M. Russell III (2009), Relative intensities of middle atmosphere waves, *J. Geophys. Res.*, *114*, D06110, doi:10.1029/2008JD010662.

Offermann, D., P. Hoffmann, P. Knieling, R. Koppmann, J. Oberheide, and W. Steinbrecht (2010), Long-term trends and solar cycle variations of mesospheric temperature and dynamics, *J. Geophys. Res.*, *115*, D18127, doi:10.1029/2009JD013363.

Offermann, D., P. Hoffmann, P. Knieling, R. Koppmann, J. Oberheide, D. M. Riggin, V. M. Tunbridge, and W. Steinbrecht (2011), Quasi 2 day waves in the summer mesosphere: Triple structure of amplitudes and long-term development, *J. Geophys. Res.*, *116*, D00P02, doi:10.1029/2010JD015051.

Pautet, P.-D., M. J. Taylor, A. Z. Liu, and G. R. Swenson (2005), Climatology of short-period gravity waves observed over northern Australia during the Darwin Area Wave Experiment (DAWEX) and their dominant source regions, *J. Geophys. Res.*, *110*, D03S90, doi:10.1029/2004JD004954.

Placke, M., G. Stober, and C. Jacobi (2010), Gravity wave momentum fluxes in the MLT–Part I: Seasonal variation at Collm (51.3°N, 13.0°E), *J. Atmos. Sol. Terr. Phys.*, *73*, 904–910, doi:10.1016/j.jastp.2010.07.012.

Placke, M., P. Hoffmann, E. Becker, Ch. Jacobi, W. Singer, and M. Rapp (2011), Gravity wave momentum fluxes in the MLT–Part II: Meteor radar investigations at high and midlatitudes in comparison with modeling studies, *J. Atmos. Sol. Terr. Phys.*, *73*, 911–920, doi:10.1016/j.jastp.2010.05.007.

Portnyagin, Y. I., E. G. Merzlyakov, T. V. Solovjova, C. Jacobi, D. Kürschner, A. Manson, and C. Meek (2006), Long-term trends and year-to-year variability of mid-latitude mesosphere/lower thermosphere winds, *J. Atmos. Sol. Terr. Phys.*, *68*, 1890–1901, doi:10.1016/j.jastp.2006.04.004.

Preusse, P., et al. (2006), Tropopause to mesopause gravity waves in August: Measurement and modeling, *J. Atmos. Sol. Terr. Phys.*, *68*, 1730–1751, doi:10.1016/j.jastp.2005.10.019.

Preusse, P., S. D. Eckermann, and M. Ern (2008), Transparency of the atmosphere to short horizontal wavelength gravity waves, *J. Geophys. Res.*, *113*, D24104, doi:10.1029/2007JD009682.

Preusse, P., S. D. Eckermann, M. Ern, J. Oberheide, R. H. Picard, R. G. Roble, M. Riese, J. M. Russell III, and M. G. Mlynczak (2009), Global ray tracing simulations of the SABER gravity wave climatology, *J. Geophys. Res.*, *114*, D08126, doi:10.1029/2008JD011214.

Rapp, M., B. Strelnikov, A. Müllemann, and F.-J. Lübken (2004), Turbulence measurements and implications for gravity wave dissipation during the MaCWAVE/MIDAS rocket program, *Geophys. Res. Lett.*, *31*, L24S07, doi:10.1029/2003GL019325.

Richter, J. H., F. Sassi, and R. R. Garcia (2010), Toward a physically based gravity wave source parameterization in a general circulation model, *J. Atmos. Sci.*, *67*, 136–156, doi:10.1175/2009JAS3112.1.

Savitzky, A., and M. J. E. Golay (1964), Smoothing and differentiation of data by simplified least squares procedures, *Anal. Chem.*, *36*, 1627–1639, doi:10.1021/ac60214a047.

Scheer, J., E. R. Reisin, O. Gusev, W. J. R. French, G. Hernandez, R. Huppi, P. Ammosov, G. A. Gavrilyeva, and D. Offermann (2006), Use of CRISTA mesopause region temperatures for the intercalibration of ground-based instruments, *J. Atmos. Sol. Terr. Phys.*, *68*, 1698–1708, doi:10.1016/j.jastp.2005.12.009.

Shiokawa, K., Y. Otsuka, and T. Ogawa (2009), Propagation characteristics of nighttime mesospheric and thermospheric waves observed by optical mesosphere thermosphere imagers at middle and low latitudes, *Earth Planets Space*, *61*, 479–491.

Simkhada, D. B., J. B. Snively, M. J. Taylor, and S. J. Franke (2009), Analysis and modeling of ducted and evanescent gravity waves observed in the Hawaiian airglow, *Ann. Geophys.*, *27*, 3213–3224, doi:10.5194/angeo-27-3213-2009.

Snively, J. B., V. P. Pasko, and M. J. Taylor (2010), OH and OI airglow modulation by ducted short-period gravity waves: Effects of trapping altitude, *J. Geophys. Res.*, *115*, A11311, doi:10.1029/2009JA015236.

Suzuki, S., K. Shiokawa, K. Hosokawa, K. Nakamura, and W. K. Hocking (2009), Statistical characteristics of polar cap mesospheric gravity waves observed by an all-sky airglow imager at Resolute Bay, Canada, *J. Geophys. Res.*, *114*, A01311, doi:10.1029/2008JA013652.

Taylor, M. J., and M. A. Hapgood (1990), On the origin of ripple-type wave structure in the OH nightglow emission, *Planet. Space Sci.*, *38*, 1421–1430, doi:10.1016/0032-0633(90)90117-9.

Taylor, M. J., W. R. Pendleton Jr., S. Clark, H. Takahashi, D. Gobbi, and R. A. Goldberg (1997), Image measurements of short-period gravity waves at equatorial latitudes, *J. Geophys. Res.*, *102*, 26,283–26,299, doi:10.1029/96JD03515.

Taylor, M. J., W. R. Pendleton, P.-D. Pautet, Y. Zhao, C. Olsen, H. K. Surendra Babu, A. F. Medeiros, and H. Takahashi (2007), Recent progress in mesospheric gravity wave studies using nightglow imaging system, *Rev. Bras. Geofis.*, *25*, suppl. 2, 49–58, doi:10.1590/S0102-261X2007000600007.

Wu, D. L., and J. W. Waters (1996), Gravity-wave-scale temperature fluctuations seen by the UARS MLS, *Geophys. Res. Lett.*, *23*, 3289–3292, doi:10.1029/96GL02924.

Wu, D. L., P. Preusse, S. D. Eckermann, J. H. Jiang, M. de la Torre Juarez, L. Coy, and D. Y. Wang (2006), Remote sounding of atmospheric gravity waves with satellite limb and nadir techniques, *Adv. Space Res.*, *37*, 2269–2277, doi:10.1016/j.asr.2005.07.031.

Yang, G., B. Clemesha, P. Batista, and D. Simonich (2010), Seasonal variations of gravity wave activity and spectra derived from sodium temperature lidar, *J. Geophys. Res.*, *115*, D18104, doi:10.1029/2009JD012367.

Yue, J., T. Nakamura, C.-Y. She, M. Weber, W. Lyons, and T. Li (2010), Seasonal and local time variability of ripples from airglow imager observations in US and Japan, *Ann. Geophys.*, *28*, 1401–1408, doi:10.5194/angeo-28-1401-2010.

C. Kalicinsky, P. Knieling, R. Koppmann, D. Offermann, and J. Wintel, Physics Department, Wuppertal University, Gauss-Strasse 20, D-42097 Wuppertal, Germany. (offerm@uni-wuppertal.de)

W. Steinbrecht, Meteorologisches Observatorium, D-82383 Hohenpeissenberg, Germany.

Journal of Atmospheric and Solar-Terrestrial Physics 135 (2015) 1–11

Contents lists available at ScienceDirect

Journal of Atmospheric and Solar-Terrestrial Physics

journal homepage: www.elsevier.com/locate/jastp

A case study of multi-annual temperature oscillations in the atmosphere: Middle Europe

D. Offermann [a,*], O. Goussev [b], Ch. Kalicinsky [a], R. Koppmann [a], K. Matthes [c,1], H. Schmidt [d], W. Steinbrecht [e], J. Wintel [a]

[a] University of Wuppertal, Germany
[b] DLR Oberpfaffenhofen, Germany
[c] GEOMAR Helmholtz Centre for Ocean Research Kiel, Germany
[d] MPI Meteorology, Hamburg, Germany
[e] DWD, Hohenpeißenberg Observatory, Germany

ARTICLE INFO

Article history:
Received 14 January 2015
Received in revised form
18 September 2015
Accepted 2 October 2015

Keywords:
Multi-annual oscillations
Atmospheric temperatures
CCM simulations
Self-sustained oscillations
Synchronization

ABSTRACT

SABER temperature measurements from 2002 to 2012 are analyzed from 18 to 110 km altitude in Middle Europe. Data are complemented by radiosonde measurements in the altitude range from 0 to 30 km. Low frequency oscillations with periods of about 2.4–2.2 yr, 3.4 yr, and 5.5 yr are seen in either data set. Surprising vertical structures in amplitudes and phases are observed with alternating minima and maxima of amplitudes, steep phase changes (180°) at the altitudes of the minima, and constant phase values in between. HAMMONIA CCM simulations driven by boundary conditions for the years 1996–2006 are analyzed for corresponding features, and very similar structures are found. Data from another CCM, the CESM-WACCM model, are also analyzed and show comparable results.

Similar oscillation periods have been reported in the literature for the ocean. A possible forcing of the atmospheric oscillations from below was therefore tested with a special HAMMONIA run. Here, climatological boundary conditions were used, i.e. the boundaries in all eleven years were the same. Surprisingly also in this data set the same atmospheric oscillations are obtained. We therefore conclude that the oscillations are intrinsically forced, self-sustained in the atmosphere. The oscillations turned out to be quite robust as they are still found in a HAMMONIA run with strongly reduced vertical resolution. Here only the form of the vertical amplitude and phase profile of the 2.2 yr feature is lost but the oscillation itself is still there, and the two other oscillations are essentially unchanged.

Similar oscillations are seen in the earth surface temperatures. Global Land Ocean Temperature Index data (GLOTI) reaching back to 1880 show such oscillations during all that time. The oscillations are also seen in parameters other than atmospheric temperature. They are found in surface data such as the North Atlantic Oscillation Index (NAO) and in zonal winds in the troposphere and lower stratosphere. The oscillations found are tentatively discussed in terms (of synchronization) of self-sustained non-linear oscillators, as many of their properties resemble such oscillators described in the literature.

1. Introduction

Atmospheric oscillations with periods of a few years have been observed and frequently discussed in the literature. Undoubtedly, the most prominent of such oscillations is the Quasi-Biennial Oscillation (QBO; Andrews et al., 1987; Baldwin et al., 2001) in the tropical stratosphere. Much longer periods near 11 years and 5.5 years are occasionally seen at higher altitudes in the upper mesosphere and lower thermosphere, and have been attributed to influences of the solar cycle and its harmonics (e.g., Khomich et al., 2013). Solar cycle signals are also seen in the stratosphere and troposphere (e.g., Gray et al., 2010). A period of about 3.5 years was observed in total ozone in the lower stratosphere and troposphere (Wang et al., 2011) and was attributed to the El Nino-Southern Oscillation (ENSO). Oscillations of atmospheric angular momentum (AAM) with periods in a band between three and five years have been analyzed in the troposphere and lower stratosphere by Abarca del Rio et al. (2000), and a survey on related work is given therein. Various wave modes with periods between two years and eleven years have been observed and described in the ocean, and are discussed in the context of ENSO (e.g. White et al. 2003; White and Liu, 2008a,b; Chen et al., 2010). Self-

---

[*] Corresponding author.
[1] Christian-Albrechts Universität zu Kiel, Kiel, Germany.

http://dx.doi.org/10.1016/j.jastp.2015.10.003
1364-6826/

excitation of such oscillations are also discussed by these authors. Synchronization of non-linear oscillations has been described for instance by Pikovsky et al. (2003).

In the present paper we discuss three major periods of Multi-Annual Oscillations (MAO) in atmospheric temperature resulting from our analysis. They are near 2.2–2.4 years, 3.4 years, and 5.5 years, and are the most prominent periods at most altitudes. They are similar to oceanic oscillations (see the above references), and are analyzed for a possible relationship. The analysis is a case study for European mid latitudes. This study presents an exploratory approach to determine the nature and scope of these oscillations.

The paper is organized as follows: Section 2 describes the data used, and the analysis method employed. Section 3 shows the vertical structures obtained from the measured temperature data. Section 4 gives corresponding results from experiments with two different state-of-the art chemistry-climate models (CCMs) (HAMMONIA CCM and CESM-WACCM). Section 5 analyzes similar oscillations in other atmospheric parameters. Section 6 discusses the results and Section 7 gives a summary and some conclusions.

2. Data and methods

An analysis of atmospheric oscillations requires a data set as homogeneous and complete in space and time as possible. In the present study we therefore use data from the SABER instrument on the TIMED satellite (Remsberg et al., 2008). Version 1.07 temperatures are used from 2002 to 2012 in the altitude range from 18 km to 110 km. As a first step data above Central Europe (45°N–55°N; 4°W–16°E) are used in this exploratory study.

The SABER data cover a time interval that might appear somewhat short for the analysis of the periods cited. There is, however, no longer homogeneous data series available in this altitude regime. Hence, if one wants to perform this type of analysis at all, one has to use these data. The results should be considered as a first approximation.There is still another argument for relatively short analysis intervals. The oscillations analyzed here change their amplitudes fairly quickly and quite substantially. An example is discussed in Section 6.1 with a factor of 5 change in about a decade. Hence, longer analysis intervals will smooth or decrease the resulting amplitudes. The interval length chosen is therefore a compromise between the accuracy of the oscillation periods and their amplitudes.

Derivation of temperatures by a limb scanning technique (as that of SABER) becomes increasingly difficult at low altitudes, and ends at 18 km in the present case. To complement the SABER temperature profiles at lower altitudes we use radiosonde data from the ground to an altitude of 10 hPa (30 km). Monthly mean temperatures from eight radiosonde stations in Germany were averaged. The resulting annual mean temperature profiles over Germany then complement the SABER data and were the basis for our analysis.

A spectral analysis was performed in several steps. The SABER measurements in an area of 20° latitude by 20° longitude were yearly averaged. The resulting eleven data points (2002–2012) at a given altitude were smoothed by a five- point running mean. With this procedure a possible long term trend can be removed. These smoothed data were subtracted from the original data, and the residues were further analyzed. Detrending also included a correction for possible influences of the solar flux and its variations during a solar cycle, which was achieved by a linear correlation between the temperatures and the 10.7 cm solar radio flux density. The procedure was not iterated as previously described by Offermann et al. (2010) and thus is an approximate solution, only. Below an altitude of 55 km no significant influence of the solar activity could be found. Therefore, the solar flux correction was only applied for all altitudes above 55 km. We have checked the quality of our detrending and found it a good procedure. Estimated accuracy is on the order of a few percent. It should be noted that the following data interpretation analyzes relative variations, mostly. Thus, small absolute inaccuracies are not important in a first approximation.

As a first approach to a spectral analysis we performed an FFT analysis of the data at a given altitude. It yielded – despite the few data points – three dominant periods of about 2.4, 3.4, and 5.5 years, two of which appeared at almost all altitude levels. In order to investigate these oscillations further, we performed harmonic analyses using Origin Pro 8G. In a second step an optimum harmonic function was fitted to the data set. Its period was found near to one of these periods and used as a result. In a third step this harmonic function was subtracted from the original data, the residue was formed, and another harmonic function was fitted to this residue. This gave a second period near to the FFT results. This procedure yielded periods, amplitudes, and phases of two major oscillations at almost all altitude levels.

In a fourth step, the amplitude and phase of the missing third period were determined in an independent harmonic analysis of the original data set. As it is shown in Section 3, the oscillation amplitudes vary substantially with altitude. Hence, it frequently occurs that one of the three periods has a very small amplitude at a given altitude (often with a phase jump of 180° near this altitude). In this case it does not show up in step 2 or step 3. Therefore in the 4th step we use a prescribed period as an input to a harmonic function that is fitted to the original data set. Although small, its amplitude can be estimated this way. The prescribed period is estimated (as a mean) from the other altitudes at which the third period has high amplitudes. It is also near to one of the FFT periods.

It may appear somewhat questionable to derive three independent oscillations from a data set as short as eleven points. Therefore, the third period must be considered with caution. In the Figures shown below the periods resulting from steps 2 and 3 are identifiable by their error bars, whereas periods resulting from step 4 do not carry error bars as they are prescribed, and can thus be recognized.

The errors of the phases are twice the size of the symbols shown.

These spectral analyses were performed at altitude steps of 2 km. In the case of the numerical simulations the steps were 3 km. The model data are available on a pressure grid and were interpolated to geometric altitudes. By the procedure described we determined three major periods that were found near 2.4 yr, 3.4 yr, and 5.5 yr. This became possible because the three amplitudes varied with altitude and hence each of the periods was seen in steps 2 or 3 of the analysis at several altitudes. It turned out that the periods do not change much with altitude. This and the fact that very similar values were obtained also from other data sets led us to the interpretation in terms of non-linear, self-sustained oscillators (see below).

3. Vertical structures of the oscillations

The results of the spectral analyses of the SABER and radiosonde data for the three major oscillations are shown in Fig.1a–c. The graphs give the vertical distributions of amplitudes (left), periods (middle), and phases (right) up to an altitude of 110 km. As the error bars indicate, results at the uppermost levels are increasingly uncertain.

Amplitudes obtained from the SABER and radiosonde data are plotted in one picture to show how the data agree (note the

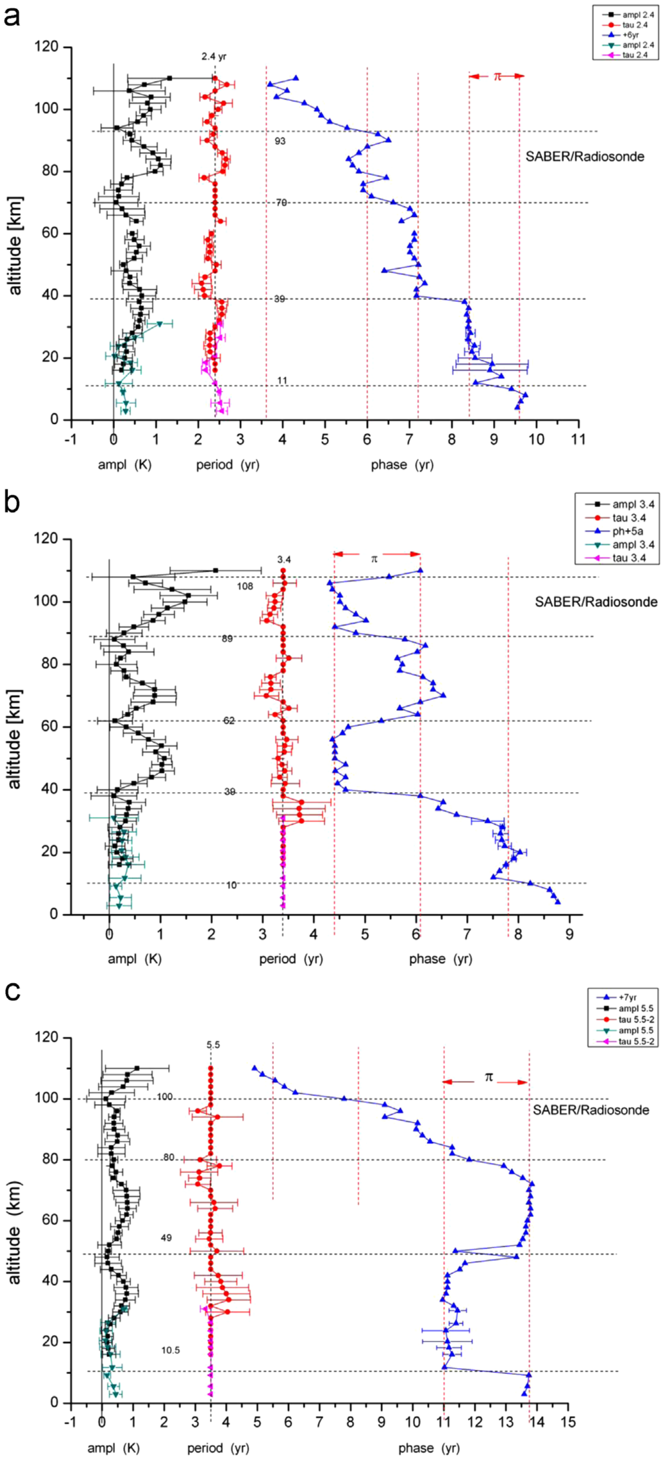

Fig. 1. a. Harmonic analysis of SABER/Radiosonde data (2002–2012). Amplitudes and phases of oscillation periods near 2.4 yr are shown in the left and right columns. Periods are given in the middle. Period symbols without error bars indicate that periods have been prescribed at 2.4 yr. The abscissa is in relative units. It is in years for the periods and phases, and in Kelvin for the amplitudes. The phases have been shifted horizontally by +6 years to accommodate them in the figure and use a common abscissa. Corresponding shifts have also been applied in the other pictures. A vertical straight line is given with the period data at 2.4 yr, as indicated on top of the line. It is meant to guide the eye and show that this number is a close fit to the data. For the other straight dashed lines see text. b. Harmonic analysis of SABER/Radiosonde data (2002–2012). Amplitudes and phases of oscillation period near 3.4 yr are shown in the left and right columns. Periods are given in the middle. Period symbols without error bars indicate that periods have been prescribed at 3.4 yr. The abscissa is in relative units. It is in years for the periods and phases, and in Kelvin for the amplitudes. A vertical straight line is given with the period data at 3.4 yr, as indicated on top of the line. It shows that this number is a close fit to the data. For the other straight dashed lines see text. c. Harmonic analysis of SABER/Radiosonde data (2002–2012). Amplitudes and phases of oscillation periods near 5.5 yr are shown in the left and right columns. Periods are given in the middle. Period symbols without error bars indicate that periods have been prescribed at 5.5 yr. The abscissa is in relative units. It is in years for the periods and phases, and in Kelvin for the amplitudes. A vertical straight line is given with the period data at 5.5 yr, as indicated on top of the line. It shows that this number is a close fit to the data. For the other straight dashed lines see text. The period profile has been shifted to the left by two years for clarity. (For interpretation of the references to color in this figure, the reader is referred to the web version of this article.)

Table 1
Periods of Multi-Annual Oscillations (MAO).

SABER	2.37 ± 0.15 yr	3.39 ± 0.15 yr	5.53 ± 0.21 yr
HAMMONIA run Hhi-trans-free	2.21 ± 0.04 yr	3.39 ± 0.18 yr	5.48 yr*
HAMMONIA run Hhi-max	2.20 ± 0.08 yr	3.42 ± 0.11 yr	5.5 yr*
HAMMONIA run Hlo-max	2.22 ± 0.08 yr	3.38 ± 0.09 yr	5.5 yr*
CESM-WACCM	2.28 ± 0.08 yr	3.38 ± 0.16 yr	5.48 ± 0.14 yr*

Mean altitude values are shown. Values with asterix* are biased as they have been prescribed at many altitudes.

Table 2
List of Acronyms.

Acronym	Definition
CCM	Chemistry climate model
CESM-WACCM	Community earth system model – whole atmosphere community climate model
GEOS CCM	Goddard earth observing system chemistry-climate model
HAMMONIA	HAMburg model of the neutral and ionized atmosphere
SABER	Sounding of the atmosphere using broadband emission radiometry
TIMED	Thermosphere, ionosphere, mesosphere, energetics, and dynamics
QBO	Quasi-Biennial Oscillation

different colors). The same was done for the periods. The data agree well within their error bars. The presentation of the phases is somewhat different: mean values of SABER and radiosonde data are presented for altitudes where data are available. The bar shown together with the mean gives the maximum and minimum at this altitude.

The middle curves in Fig. 1 show the periods found at different altitude levels. They are somewhat scattered, but do not indicate any systematic deviation from their mean values and are close to the values mentioned above. These means (based on the SABER data) are 2.37 ± 0.15 yr (Fig. 1a), 3.39 ± 0.15 yr (Fig. 1b), and 5.53 ± 0.21 yr (Fig. 1c) (see also Table 1 and 2). Vertical straight lines are given with the data to guide the eye. They are at a) 2.4 yr, b) 3.4 yr, and c) 5.5 yr and show that these numbers fit well to the data, and that there is no apparent vertical trend. The mean values are slightly biased towards these values as there are a number of prescribed periods used that are shown by symbols without error bars. The 2.4 yr period agrees with the QBO period (27 months) within the error bar, which is discussed below.

The amplitudes obtained from the harmonic analyses as plotted on the left sides of Fig. 1 reach values of about 1 K. They do not show an increase with altitude as it would be the case for freely upward propagating waves.Although the error bars are relatively large, an undulated structure is obvious with pronounced maxima and minima at quasi-regular altitude distances.

The phases are shown on the right sides of Fig. 1. Given are relative values (in years), because only relative phase variations are discussed here. The curves have been shifted horizontally to accommodate them in the figures and use a common abscissa.

The vertical phase distributions show an intriguing structure. Phases tend to be constant in a given altitude interval. Going further upward (or downward) the phase values change abruptly to higher or lower values, and then remain constant again. In Fig. 1a this has a staircase appearance, whereas in Fig. 1b and c it has a square wave appearance.This step-like behavior is demonstrated by the vertical red (dashed) lines in Fig. 1. At higher altitudes the step structure has a tendency to dissolve.

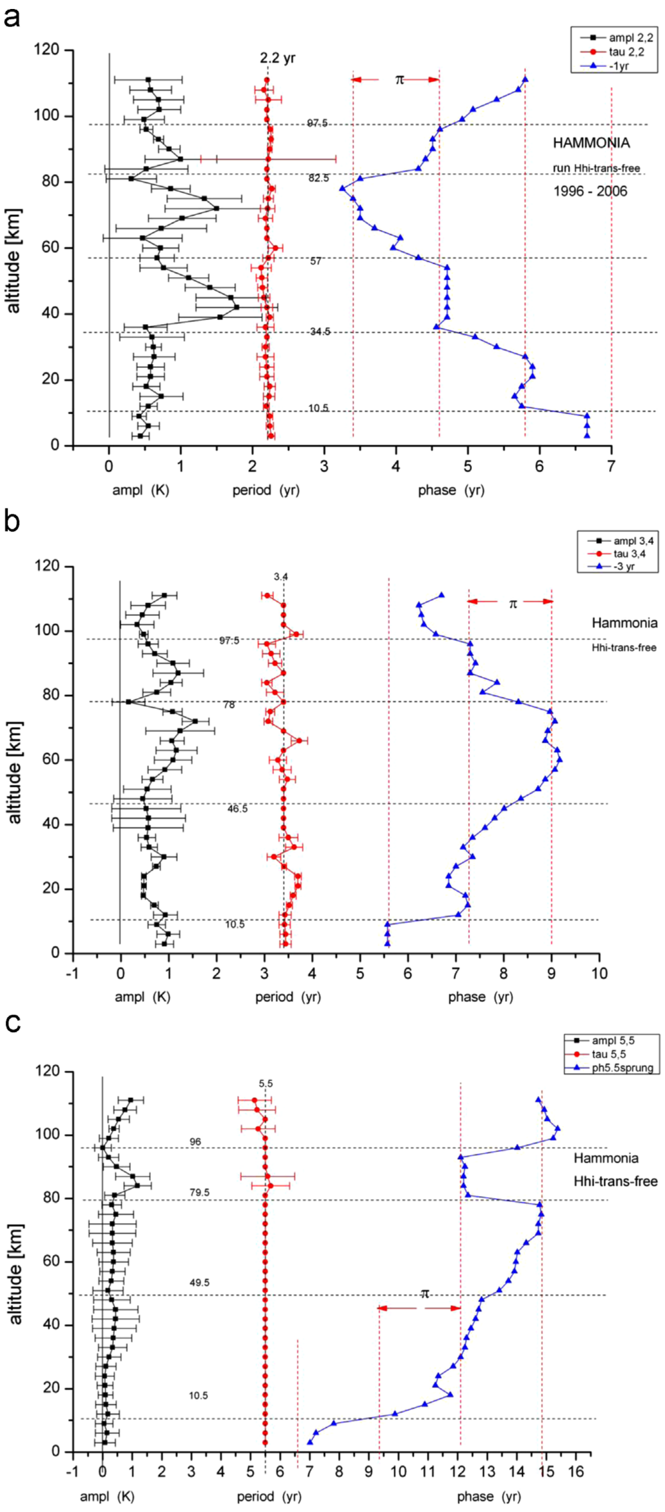

Fig. 2. a. Harmonic analysis as in Fig. 1a, but for HAMMONIA model data (run Hhi-trans-free, 1996–2006). Periods are near to 2.2 yr (see text). b. Harmonic analysis as in Fig. 1b, but for HAMMONIA model data (run Hhi-trans-free, 1996–2006). Periods are near to 3.4 yr (see text). c. Harmonic analysis as in Fig. 1c, but for HAMMONIA model data (run Hhi-trans-free, 1996–2006). Periods are near to 5.5 yr (see text).

The phase steps contain an ambiguity if they are 180° wide. Such a step could go upwards as well as downwards. In all figures shown here we have used the smallest phase difference between two adjacent points and connected them by straight lines. As Fig. 1 shows, there is some scatter in the phase data. The error bars are small, typically twice the symbol size. This scatter makes the choice of the step direction (upward or downward) sometimes ambiguous: the step direction is not compelling in some cases. Hence, the form of the vertical phase profiles shown in this paper (i.e. “stair case” or “square wave”) is not very significant. What counts are the jumps of the phase and the phase constancy in between.

There are two important features in the step-like phase structures. 1) The phase changes are very steep ("phase jumps"), and they occur in most cases at or close to those altitudes where the amplitudes have a pronounced minimum. This is indicated in Fig. 1 by horizontal dashed lines. 2) The magnitude of the phase jumps have a special value for all three periods. They amount to half of the length of the oscillation period (180° or π), i.e. the oscillation is in anti-phase at neighboring step levels. This is shown by the vertical dashed (red) lines in Fig. 1. These phase structures are very characteristic for these multi-annual oscillations (MAO). The altitudes at which the steps occur are different for the three periods.

4. Model experiments/simulations

The amplitude and phase structures of the observed multi-annual oscillations are quite surprising. They would gain considerable credibility if they could be reproduced in an atmospheric model. This might also help to elucidate their nature.

4.1. Hammonia

The Hamburg Model of the Neutral and Ionized Atmosphere (HAMMONIA; Schmidt et al., 2006) is used here in a first step. It is based on the ECHAM5 general circulation model (Roeckner et al., 2006) but vertically extended to cover an altitude range up to about 250 km and coupled to the MOZART3 chemistry module (Kinnison et al., 2007). While the model is described by Schmidt et al. (2006) we use the same naming of specific model simulations as used by Schmidt et al. (2013). In this section we use simulation "Hhi-trans-free", which is a transient simulation driven by boundary conditions (e.g. greenhouse gas concentrations, solar irradiance, and SSTs) as observed or reconstructed for the period 1960–2006. The model internally generates a QBO, which is in general not in phase with the observed QBO. For the comparison to SABER data we use data for a model grid column located in Central Europe (50°N, 7°E) and a time slab of 11 years length as close to the SABER data as possible (1996–2006). These data were analyzed in the same way as described for the SABER data above. The results are remarkable. Again three oscillations are found, which are shown in Fig. 2. The figure is organized as Fig. 1. Fig. 2a shows the shortest period with a value of 2.21 ± 0.04 yr (see also Table 1). This is somewhat shorter than for the measured data, but it agrees within the combined error bars. The middle period is shown in Fig. 2b. Its mean value is 3.39 ± 0.18 yr and hence agrees with the measured period within the single error bar. The longest period is shown in Fig. 2c. Its mean value is 5.48 yr, i.e. close to 5.5 yr. This period could be determined directly only in the upper altitudes because of the smallness of the amplitudes. As it was found close to 5.5 yr this value was used to prescibe the periods at the other altitudes.

There is close agreement of the modeled periods with those of the measured data. Also the simulated amplitudes are of the same magnitudes as the measured ones and show a similar variation with height.

The phases are different from those shown in Fig. 1 as they are also relative values, and the reference is arbitrary. Nevertheless, we find phase jumps similar as in Fig. 1. Again,they approximately coincide with the amplitude minima. This is clearly seen in Fig. 2a for the 2.2 yr period. Adjacent altitude levels with nearly constant phase values again are about in anti-phase.

Phase jumps of 180° between altitude regimes of constant phases are also seen in the two other oscillations (Fig. 2b and c). They are, however, not as pronounced as for the 2.2 yr oscillation. In the stratosphere they appear to be missing at all.

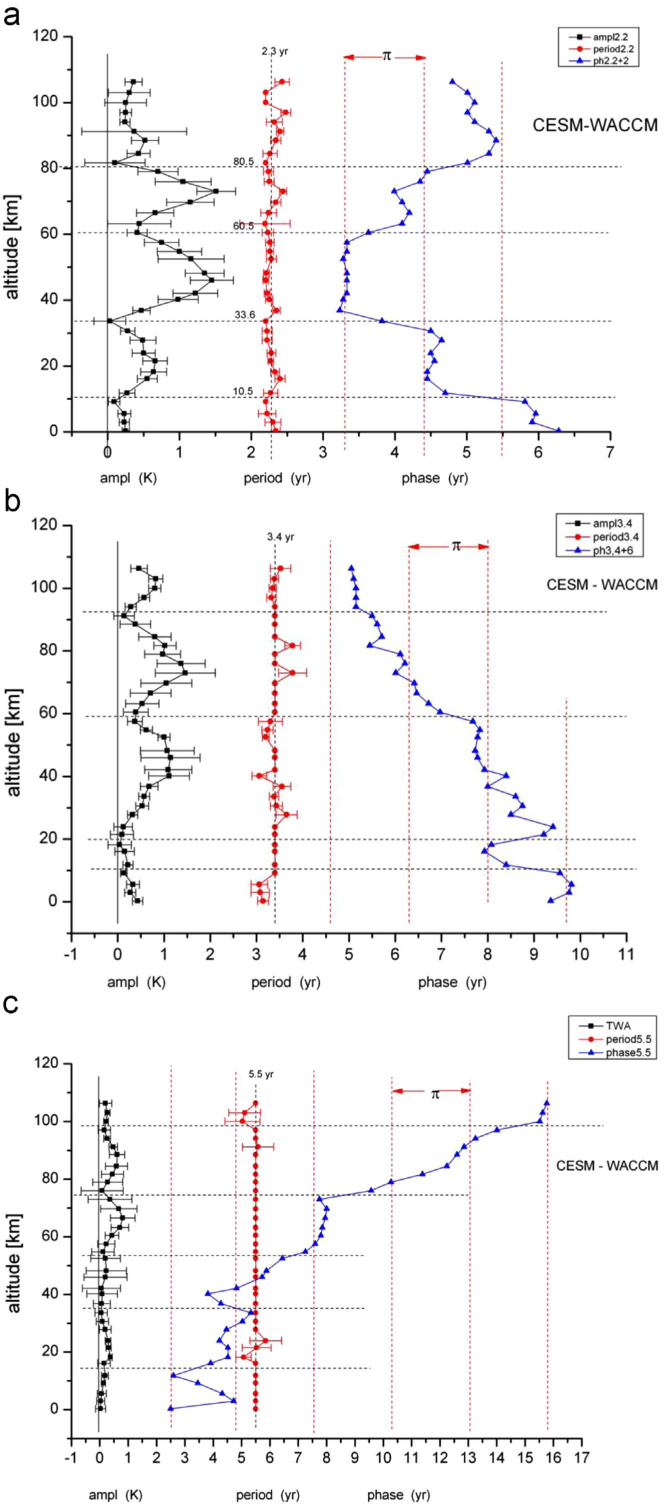

Fig. 3. a. Harmonic analysis as in Fig. 1a, but for CESM-WACCM model data. Mean oscillation periods are near to 2.3 yr (see text). The phases have been shifted by 2 yr for clarity. b. Harmonic analysis as in Fig. 1b, but for CESM-WACCM model data. Mean oscillation periods are near to 3.4 yr (see text). The phases have been shifted by 6 yr for clarity. c. Harmonic analysis as in Fig. 1c, but for CESM-WACCM model data. Mean oscillation periods are near to 5.5 yr (see text). Periods are given by red dots, phases by blue triangles. (For interpretation of the references to color in this figure legend, the reader is referred to the web version of this article.)

In summary, the HAMMONIA data in Fig. 2 basically confirm the atmospheric amplitude and phase structures revealed by SABER and radiosonde measurements. We conclude that the

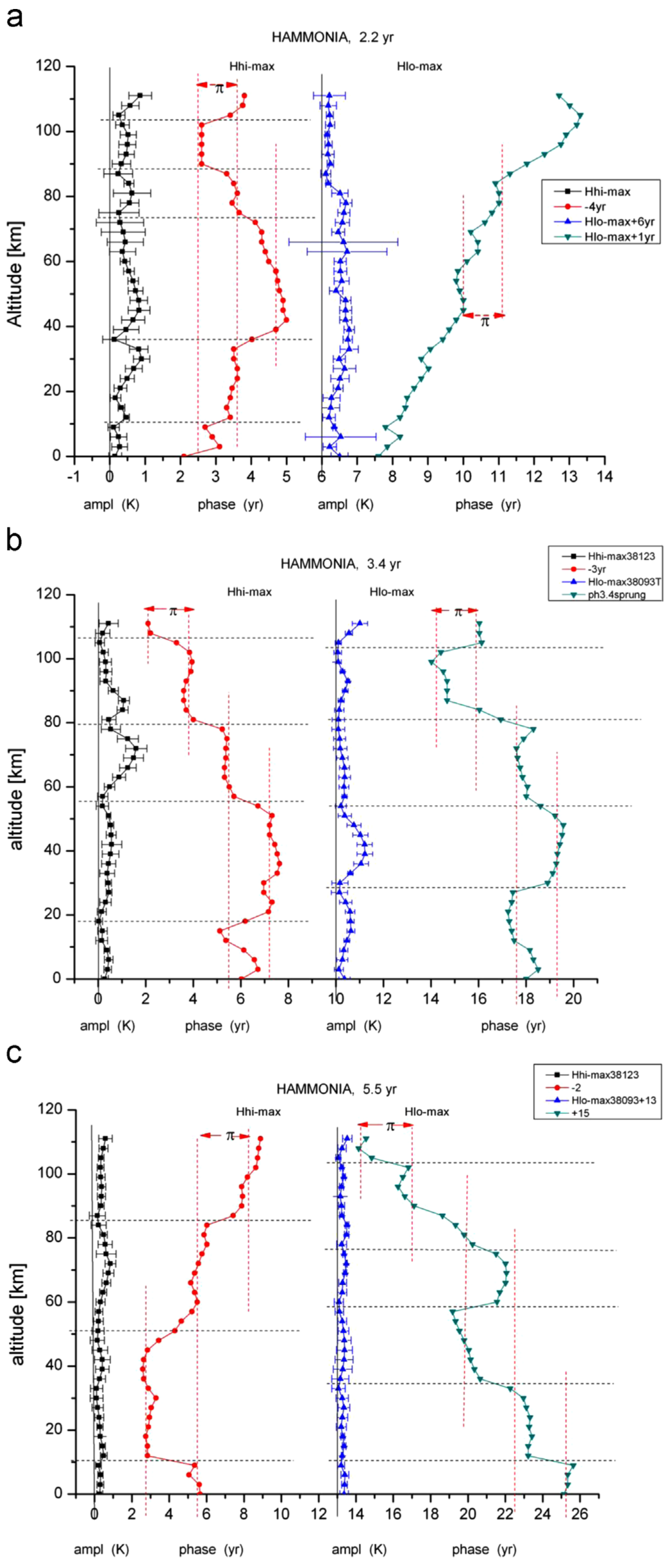

Fig. 4. a Harmonic analysis for HAMMONIA run Hhi-max (left) and run Hlo-max (right). Run Hhi-max: climatological boundaries; Run Hlo-max: reduced vertical resolution The picture is structured as Fig.2a except that the period profile is omitted (see text). Periods are near to 2.2 yr. Abscissa is in relative units as in Fig. 1. For the straight dashed lines see text. The phase profiles are relative profiles without fixed reference points. The zero point of run Hlo-max amplitudes is at 6 rel. units. b Harmonic analysis for HAMMONIA run Hhi-max (left) and run Hlo-max (right). Run Hhi-max: climatological boundaries; Run Hlo-max: reduced vertical resolution The picture is structured as Fig.2b except that the period profile is omitted (see text). Periods are near to 3.4 yr. Abscissa is in relative units as in Fig. 1b. For the straight dashed lines see text. The phase profiles are relative profiles without fixed reference points. The zero point of run Hlo-max amplitudes is at 10 rel. units. c Harmonic analysis for HAMMONIA run Hhi-max (left) and run Hlo-max (right). Run Hhi-max: climatological boundaries; Run Hlo-max: reduced vertical resolution The picture is structured as Fig.2c except that the period profile is omitted (see text). Periods are near to 5.5 yr. Abscissa is in relative units as in Fig. 1c. For the straight dashed lines see text. The phase profiles are relative profiles without fixed reference points. The zero point of run Hlo-max amplitudes is at 13 rel.units.

measured structures are real, indeed. It should be noted that the boundary conditions used for HAMMONIA do not exactly match the period of the SABER and radiosonde measurements but differ by 6 yr. Additionally, the meteorology of the model is internally produced and hence does not match the actually observed meteorology for a given date. Therefore, differences in the detailed altitude profiles could be due to this if the structures should change with time or depend on actual meteorology.

4.2. *CESM-WACCM*

For a further comparison we have studied a run of NCAR's Community Earth System Model-Whole Atmosphere Community Climate Model (CESM-WACCM; Marsh et al., 2013). CESM is a state-of-the-art coupled atmosphere-ocean model system which is based upon the Community Climate System Model (CCSM4) (Gent et al., 2011). Here, CESM was used with the atmospheric component WACCM, version 4 (CESM1-WACCM) (Marsh et al., 2013), a fully interactive chemistry-climate model which extends from the Earth's surface to 140 km altitude (Garcia et al., 2007; Richter et al., 2010) and is used here on a horizontal grid of 1.9° × 2.5° (latitude × longitude) and on 66 vertical levels. Chemistry is calculated interactively in the chemistry module based on version 3 of the Model for OZone And Related chemical Tracers (MOZART) (Kinnison et al., 2007). WACCM is not able to generate a self-consistent QBO, it therefore uses a nudging technique to closely follow the observed QBO (Matthes et al., 2010). The CESM-WACCM experiment has been integrated from 1955 through 2099 using observed increases in GHGs and ozone depleting substances as well as observed solar forcing. Details of the "GHG" simulation are described in Hansen et al. (2014). HAMMONIA and CESM-WACCM are comparable CCMs except for the representation of the QBO (prescribed in CESM-WACCM, internally generated in HAMMONIA) and the ocean (interactively calculated in CESM-WACCM, prescribed SSTs in HAMMONIA). A time slab between 2002 and 2012 was analysed in the way described above, coinciding with the SABER time slab.

Three oscillation periods are identified also in this model: at 2.28 ± 0.08 yr, 3.38 ± 0.16 yr, and 5.48 ± 0.14 yr (see Table 1). These periods agree within the single error bars with those of SABER and HAMMONIA run "Hhi-trans-free", which is quite remarkable. They are shown in Fig. 3 and are approximated by 2.3 yr, 3.4 yr, and 5.5 yr lines. The error value of the 5.48 yr period is approximate because at many altitudes this period had been prescribed (see Fig. 3c).

These oscillations are shown in Fig. 3 in the same manner as in Figs.1 and 2. The middle curves closely follow straight lines with the periods cited. The amplitudes are on the same order of magnitude as in Figs. 1 and 2. They show a pronounced minimum/maximum structure again. The phase profile of the shortest period (Fig. 3a) has well developed phase jumps of nearly 180° except at the highest altitudes. The jumps nicely coincide with deep minima in the amplitude profile. The corresponding altitudes are given together with the horizontal dashed lines. They are not far from the jump levels indicated in the HAMMONIA data shown in Fig. 2a. Fig. 3a thus confirms the picture of multi-annual oscillations (MAO) with very special structures in amplitudes and phases.

The phase profiles of the 3.4 yr and 5.5 yr periods in Fig. 3b and c differ, however, from Fig. 1. The staircase or square wave structure is not seen. There are a few indications of phase steps, but mostly in an unclear manner. It is interesting to note that the step structure in the 3.4 yr and 5.5 yr oscillations of HAMMONIA (Fig. 2b and c) also are less clear than for the short period. It needs to be analyzed whether the steps in Fig. 3b and c become clearer if a WACCM run with internal (self-sustained) QBO is used.

4.3. *Climatological boundaries*

A possible explanation of the MAO in observations and simulations are variations in surface conditions, in particular sea surface temperatures (SST). In atmospheric models this can be tested using SSTs that are not transient as in the HAMMONIA simulation "Hhi-trans-free" but have a fixed annual cycle. Such simulations

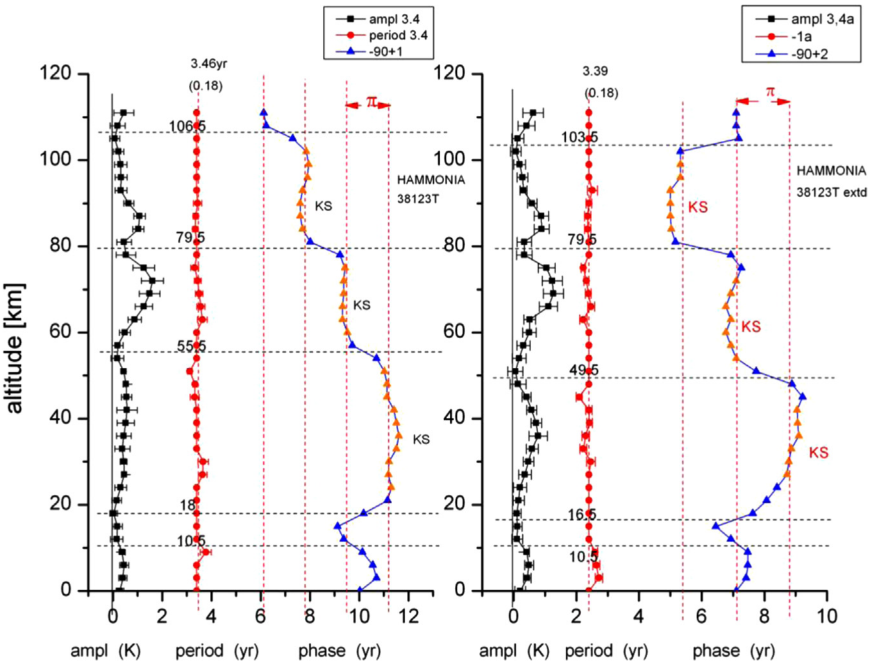

Fig. 5. Harmonic analysis for two HAMMONIA runs Hhi-max with different analysis windows. The left hand side shows the results for an eleven years window, the right hand side for a 17 yr window. The picture compares the amplitudes, periods, and phases. The amplitudes are highly correlated with a correlation coefficient of 0.89. The mean periods are close to the values 3.46 ± 0.18 yr and 3.39 ± 0.18 yr as indicated above the vertical dashed lines. Both of the phase profiles show three areas (steps KS) of almost constant phase values (indicated by red triangles). Both of the profiles show five phase jumps, and they occur at very similar altitudes. The right hand period profile has been shifted to the left by one year for clarity. The zero points of the phase profiles are arbitrary. The picture shows that the difference in window length yields only minor changes of the harmonic analysis. (For interpretation of the references to color in this figure legend, the reader is referred to the web version of this article.)

with HAMMONIA have been described and analysed by Schmidt et al. (2010, 2013). The simulation used here is named “Hhi-max”, where besides fixed SSTs also all other boundary conditions are set to constant values. Hence, any oscillation occurring in this simulation is obviously internally produced.

We analyzed a time slab of eleven years from the middle of this run. To our surprise all three oscillations are still there, and their periods are very similar to the values obtained in simulation “Hhi-trans-free” with transient boundary conditions (see Table 1). The agreement is within the single error bars.

The corresponding amplitudes and phases are given in Fig. 4a–c in the same order as in Fig. 2: a) period 2.2 yr, b) 3.4 yr, and c) 5.5 yr. For the errors see Table 1. Fig. 4 is organized as Fig. 2, except that the period profiles have been omitted because they show nothing new. Results of model run “Hhi-max” are shown in the left hand side of the figures.

The amplitude and phase profiles of run “Hhi-max” are quite similar to run “Hhi-trans-free” (Fig. 2). The amplitudes are up to about 1 K and vary between maxima and minima. The phase profiles show a step-like structure as in Fig. 2, with the phase jumps at the altitudes of the amplitude minima. The altitudes of the jumps are, however, different from Fig. 2. Also their direction (to higher or lower values) is different. In summary, however, the profiles of Fig. 4 and Fig. 2 are surprisingly similar. The step structure of oscillation periods 3.4 yr and 5.5 yr appears to be even clearer in Fig. 4 than in Fig. 2.

The three oscillations and their intriguing amplitude and phase structures are obviously not initiated by the boundary conditions. This leads us to the surprising result that they must stem from inside the atmosphere. This means that they are due to some self-sustained mechanism in the atmosphere. Such mechanisms are known to exist in the ocean (e.g. White and Liu, 2008b) and appear to exist in the atmosphere, too. Indeed, the QBO in the lower stratosphere is known to be of this nature (e.g. Andrews et al., 1987).

4.4. Reduced vertical resolution

As mentioned earlier, the observed and simulated period of sligthly more than two years is very close to the QBO period. In order to test whether the two phenomena are actually related, we analyze HAMMONIA run “Hlo-max” that has a very similar set up to “Hhi-max”, but a reduced vertical resolution in the stratosphere with in total 67 instead of 119 vertical model layers (see Schmidt et al. (2010) for more details on the two simulations). As in other GCMs (e.g. Giorgetta et al., 2002) also in HAMMONIA a relatively high vertical resolution is necessary to sufficiently represent wave-mean flow interactions for an internal production of the QBO. In simulation “Hlo-max”, the tropical stratosphere does not show such an oscillation.

An eleven- year time slab from the middle of the “Hlo-max” run was analyzed in the same way as of the other runs. The results of the amplitudes and phases are shown in Fig. 4 (right hand side of the figure). The periods found are: a) 2.22 ± 0.08 yr; b) 3.38 ± 0.09 yr, and c) 5.5 yr. They again agree with the other runs within their error bars (see Table 1). The short period MAO is still present even in the absence of the QBO. Differences, however, are now found in the amplitude and phase profiles. The magnitude of the amplitudes is still about the same. The maximum/minimum modulation is still seen in Fig. 4b, but much smaller in Fig. 4c, and has disappeared in the shortest period (Fig. 4a). A similar behavior is seen in the phases. For the longer periods of 3.4 yr and 5.5 yr the step-like structures are clearly visible. They appear somewhat smoothed. For the 2.2 yr period (Fig. 4a), however, the steps have more or less disappeared, and an almost continuous increase of the phase with altitude is observed.

In summary, the three MAOs with periods of 2.2–2.4 yr, 3.4 yr, and 5.5 yr and their vertical amplitude and phase profiles are intrinsic atmospheric structures that are surprisingly robust. Further climate model experiments seem to be necessary to reveal their physical nature.

4.5. Period accuracy

The data window of the SABER data is 11 years long, and so were the selected model windows. The question arises whether the window length influences the periods obtained from the spectral analysis. This question cannot be answered by the SABER data set because it is too short. The HAMMONIA data, however, turn out to be a reasonable proxy for the measured data. We have therefore used an extended data window of 17 years length from the HAMMONIA run “Hhi-max” and compared it to the standard window of 11 years. In order not to bias the results by those altitudes where the periods are prescibed we use only those altitudes where the periods are directly derived from the harmonic analysis. The results obtained for the 2.2 yr and 3.4 yr periods are the same in the standard window and the extended window within single error bars (2.23 ± 0.10 yr versus 2.15 ± 0.06 yr, and 3.46 ± 0.18 yr versus 3.39 ± 0.18 yr, respectively). Prescribed values were not included in the means. The magnitudes of the amplitudes are also similar, and the phase profiles show similar jumps. The numbers of jumps in the standard and extended runs are the same, and the altitudes at which the jumps occur are quite similar. The ”directions” ($+\pi$ or $-\pi$) of the phase jumps are mostly different, but this can be attributed to the arbitrariness of such phase jumps, as discussed in Section 3. Fig. 5 shows as an example the standard and the extended run for the periods of about 3.4 yr.

A comparison of the period 5.5 yr of the two runs is not meaningful as at most altitudes prescribed values are used. Amplitude and phase profiles of the two runs, however, are similar as with the shorter periods. In summary, the difference in window length yields only minor changes of the spectral analyses.

It should again be remembered what was said before: that our analysis is a first approximation, only. The “third period” possibly questionable can be recognized in the pictures by the fact that these values do not carry error bars.

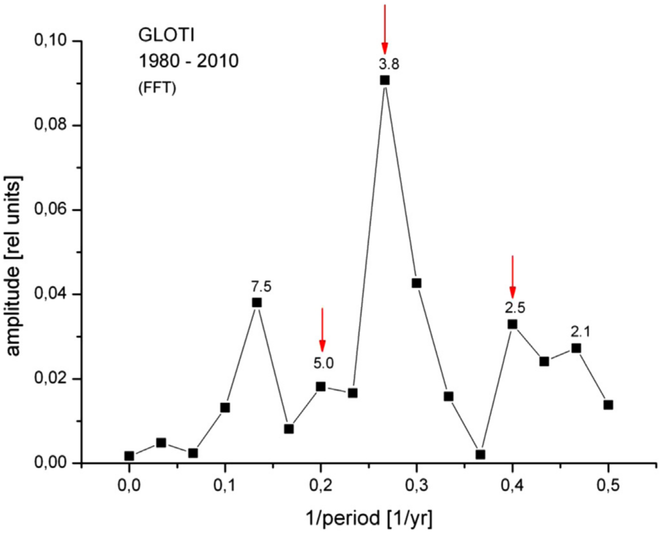

Fig. 6. FFT spectrum of Global Land Ocean Temperature Index (GLOTI) data. Time interval is 1980–2010. Numbers given with the peaks are periods in years.

5. Other parameters

The question arises whether the oscillatory structures are a temperature phenomenon only, or whether they are present in other atmospheric parameters as well. We discuss here three short examples.

5.1. Global Land Ocean Temperature Index (GLOTI)

A large set of surface temperatures is available as Global Land Ocean Temperature Index data that cover the period 1880–2010 (Hansen et al., 2010). The data are global mean values. They show oscillations during the time with periods near 2.2 yr, 3.5 yr, and 5.5 yr, and with changing amplitudes. As an example, Fig. 6 shows a FFT spectrum of the time interval 1980–2010. The annual mean GLOTI data have been detrended by a five-point running mean. The numbers shown with the peaks are the estimated periods in years. Corresponding harmonic analyses yield very similar values. Again the periods (see the red arrows) are not far from our main values given above (2.5 yr versus 2.4 yr, 3.8 yr versus 3.4 yr, and 5.0 yr versus 5.5 yr).

5.2. North Atlantic Oscillation Index (NAO)

The North-Atlantic Oscillation Index (NAO Index) is of major importance for the northern hemisphere dynamics and is therefore considered here. Fig. 7 shows an FFT spectrum of the NAO index in the time interval 1980–2013. (The data were taken from NCEP/NOAA, reference see below). Annual mean data were derived from monthly values and detrended by a five-point running mean. Numbers given together with the spectral peaks are the corresponding periods in years. It is interesting to see that all of the higher peaks except one (4.3 yr) have periods that are near to our major periods (red arrows). The periods shown are estimates, of course. A more detailed harmonic analysis gives very similar results.

5.3. Zonal winds

From the radiosondes used above for temperatures, also wind profiles are available. The zonal wind speeds (2002–2012) have been analyzed from 0 to 30 km in the same manner as the temperatures. The results look similar as in Fig.1 with periods near to 2.4 yr, 3.4 yr, and 5.5 yr. Amplitudes are small and rather variable at these low altitudes. Phases show jumps by 180° at 14 km altitude except for the 3.4 yr oscillation where the phase increase is fairly smooth.

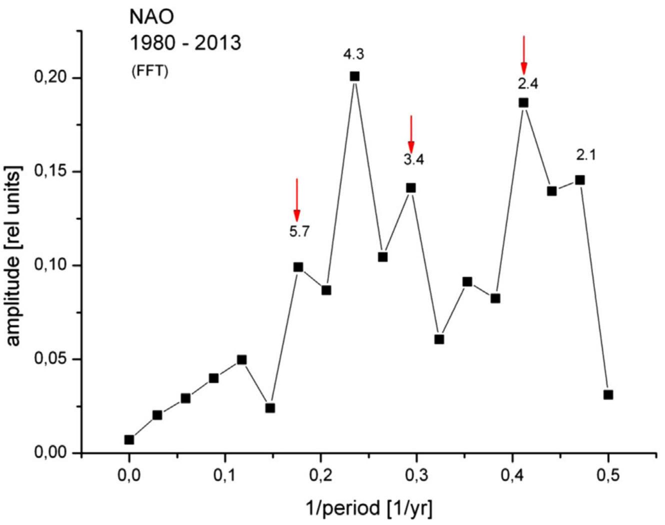

Fig. 7. FFT spectrum of North Atlantic Oscillation Index (NAO) data. Time interval is 1980–2013. Numbers given with the peaks are periods in years.

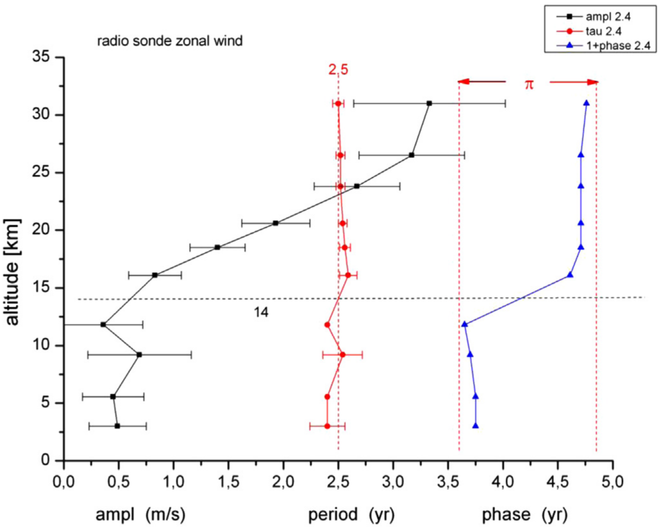

Fig. 8. Zonal wind speed analyzed for a 2.4/2.5 yr oscillation. The picture corresponds to Fig. 1a (radio sonde data). Phases have been shifted by 1 yr towards higher values for better readability.

There are two deviations from the general picture which are seen in Fig. 8. The shortest MAO period is not 2.4 yr, but closer to 2.5 yr. Furthermore the amplitude is low in the troposphere, but increases strongly in the stratosphere. This suggests some relation to the QBO. Such amplitude dependence is not analyzed for the other two periods.

The phase jump of the 2.4 resp. 2.5 yr oscillation is clearly seen at 14 km. Hence, it occurs at somewhat higher altitude than in the temperature in Fig. 1a. Generally speaking, the wind parameter suggests an oscillatory structure quite similar to the temperatures.

In summary the three examples show that the long period oscillations (MAO) are not restricted to temperatures. They may rather be expected in various other atmospheric parameters, too.

6. Discussion

6.1. Phenomenology

Multi-annual oscillations (MAO) of atmospheric parameters have been mentioned in a few earlier studies. However, except the QBO, not too much seems to be known about their origin. Wang et al. (2011) have analyzed total column ozone (TO_3) from eight stations and found an oscillation period of 3.5 years. They were able to support this by computer modeling with the GEOS CCM. The TO_3 stations used are located at mid latitudes (36–52°), and mostly in the European sector. Three stations are at more western and eastern longitudes (about $-80°$, $+140°$). This suggests that these oscillations are a global phenomenon. Wang et al. relate their oscillations to the ENSO signal. However, our results from HAMMONIA run “Hhi-max” (Fig. 4) do not support this.

In Central Europe measurements of phase heights of reflected LF radiowaves have been performed since 1959 (Peters et al., 2006/2007). These allow an estimate of long- term changes of atmospheric densities near 70 km altitude. A spectral analysis yields a pronounced oscillation at 3.4 yr period. This shows that many atmospheric parameters are affected by the MAO. It also suggests a more detailed analysis of atmospheric density at other altitudes (for instance in the thermosphere). It furthermore suggests that MAO are a more or less permanent phenomenon in the atmosphere.

The same is shown by the GLOTI data discussed in Section 5.1. Spectra of these surface temperatures exhibit our MAO periods during the entire time interval of 130 years (not shown here). Hence, we conclude that our MAO periods are a general and, as shown by the models, at least partly intrinsic property of the atmosphere. Of course, simultaneous occurrence of intrinsic oscillations and those of the coupled atmosphere/ocean system (as ENSO) is always a possibility.

Multi-year oscillations have also been observed in a quite different atmospheric parameter: the Atmospheric Angular Momentum (AAM, Abarca del Rio et al., 2000). These authors find oscillations in a band 3 to 5 years in the troposphere and lowest stratosphere at low to moderate latitudes. The data show a pronounced latitudinal structure at these altitudes. Hence a latitudinal analysis of the MAO at higher altitudes and at sufficient spectral resolution should be very interesting.

The shortest periods analyzed here (2.2–2.4 yr) are similar to that of the Quasi Biennial Oscillation (QBO, 27 months, e.g. Andrews et al., 1987). It is, however, not clear whether these are really the same. To approach this point we have analyzed surface GLOTI temperatures and HAMMONIA “Hhi-trans-free” temperatures at 45 km altitude at 2.2 yr period. Either data set shows a steep amplitude decrease in the time interval 1993–2008 and 1999–2004, respectively (order of factor 5). For comparison we have analyzed Singapore zonal winds (30 hPa) and find an amplitude decrease in the similar time interval 1995–2007 (on the order of 10%). The detailed relationship of these different parameters at different altitudes and latitudes remains to be determined.

6.2. *Structure and origin*

SABER measurements and several computer simulations show three different multi-annual oscillation periods (MAO) that are surprisingly similar in the observations and the simulations. Also the amplitudes are on the same order of magnitude (1 K).

The basic structure of our MAO is as follows: a) stable periods are about constant up to beyond 100 km, b) amplitudes vary (undulate) between minima and maxima in the vertical direction, they clearly do not show an exponential increase with altitude, c) step-like phase changes occur in the vertical, d) the structures are intrinsic, i.e. they originate from self-excitation, as experiments with climate models show, e) the structures are quite robust as the same experiments show.

Self-sustained (self-excited) oscillations are described and analysed in textbooks on non-linear dynamics (e.g. Pikovsky et al. (2003) and references given therein). Following this text, two such oscillators – if they are similar- can synchronize their periods. Here we tentatively assume that adjacent horizontal atmospheric layers (of 2–3 m thickness) are such oscillators. If they synchronize their periods this could explain the more or less constant vertical profiles of periods in our above figures. Self-sustained oscillators can also synchronize their phases, and this can occur in- phase or in anti-phase. This might possibly explain the steplike structures of many of our phase profiles. Self-sustained oscillators are especially robust against disturbances. Also this feature appears to be similar to our findings. Finally non-linear oscillators of periods T1 and T2 can show higher order synchronization if the periods obey the equality $m\mathrm{T1}=n\mathrm{T2}$ with m, n integers. It is interesting to note that the shortest of our periods and the middle one have about the ratio 2 : 3, and the middle and longest have this ratio, too. Hence, this might possibly be interpreted as higher order synchronization.

The assumption of two interacting layers is, of course, an oversimplification as the atmosphere is a continuous medium. In such media, however, synchronization of the kind described occurs, too, and it especially occurs in “clusters” or “clumps” (see Pikovsky et al., 2003). This appears to resemble our altitude regions with constant phase. Hence there are interesting similarities between our results and non-linear oscillators as described in the literature. In order to prove that the MAO are non-linear oscillators one would, however, have to actively interfere with the dynamical system (Pikovsky et al., 2003). This can hardly be done with the real atmosphere, but could possibly be achieved in the atmospheric model simulations. This is a complicated task, though, and beyond the scope of this paper.

It should be noted that the oscillations shown by the SABER data (Fig. 1) could, of course, be due to self-excitation as well as to influences from the ocean below. The same is true for the simulations by HAMMONIA “Hhi-trans-free” (Fig. 2) and CESM-WACCM (Fig. 3).

The two models are different in two important aspects. 1) The QBO is prescribed in CESM-WACCM, and is internally generated in HAMMONIA. 2) The SST are interactively calculated in CESM-WACCM (Fig. 3) and prescribed in HAMMONIA Hhi-max (Fig. 4). Nevertheless the periods are very similar in the two cases, and also the vertical structures of the phase profiles show similarities. This may be attributed to the robustness of self-sustained oscillators.

Multi-annnual oscillations are well known in the coupled atmosphere-ocean system. ENSO is unquestionably the most prominent example. Some of the oscillation periods are quite close to those discussed here (White et al., 2003; White and Liu, 2008a, b; Chen et al., 2010). Self-excitation of ocean waves or excitation by internal noise are discussed by White and Liu (2008b, see also references therein). These authors also describe a non-linear oscillator (Duffing oscillator) with near 11-yr period that forces (non-linearly) 3rd and 5th harmonics near 3.6- and 2.2-yr period. We have looked for long oscillation periods in our data and found, indeed, periods of about 10.2 yr ± 1.3 yr in the SABER temperatures and in HAMMONIA run “Hhi-max” with similar vertical phase profiles. The accuracy of these results is, however, questionable as the period length and the length of the data window are about the same. It should be remembered that our MAO oscillations in Fig. 4 (HAMMONIA Hhi-max and Hlo-max) do not stem from the ocean, as climatological boundary conditions have been used here.

The 5.5 yr oscillation in the upper atmosphere has frequently been discussed as the first (linear) harmonic of the solar cycle period of 11 yr (e.g. Khomich et al., 2013, and references therein). Our data are not in contradiction to this. They show, however, that the sun is not necessarily the origin of this oscillation. Self-excitation as seen in the HAMMONIA run “Hhi-max”with fixed boundaries (Fig. 4c) is an alternative. It remains an interesting and difficult question to determine the relative share of the two mechanisms in a given data set.

7. Summary and conclusions

Multi-annual oscillations (MAOs) with periods of 2.2–2.4 yr, 3.4 yr, and 5.5 yr are found in SABER and radiosonde temperatures between 0 and 110 km. Surprisingly, the periods are about constant with altitude. Also the amplitudes do not increase exponentially with altitude but show a modulated vertical structure of maxima and minima. The phases are constant in altitude steps, and change in steep jumps of 180° in between.

Similar oscillations are found in two numerical models of the atmospheric general circulation. One of the models (HAMMONIA) is therefore used as a proxy for the atmosphere and for experiments that are impossible with the atmosphere itself. The major experiment was to use climatological boundary conditions, which means to switch off all long-term influences from above and below (sun and ocean). This was because oscillations with the periods described are also seen in the ocean, and we suspected the atmospheric oscillations to be initiated by the ocean. Our MAO did, however, not disappear this way! We therefore must conclude that our oscillations are excited internally in the atmosphere ("self-sustained", "self-excited"). Self-excited non-linear oscillators are well known in the ocean (e.g. the Duffing oscillator). To our knowledge they are suggested here for the first time in the atmosphere in this large altitude range.

Self-sustained oscillators are known to be very robust. Our constant periods and the step-wise constant phases observed might be interpreted as synchronization effects that are typical of non-linear oscillators. The periods found in our data closely follow the ratio 3:2. This might be interpreted as higher order synchronization that is also a property of non-linear oscillators. These similarities of our results with synchronizations described in the literature are, however, not a proof. Our seeming synchronization effects could, rather, be fortuitous (Pikovsky et al., 2003). In order to prove them one would have to actively interfere with the basic non-linear dynamicl system. This is impossible for the real atmosphere. It might, however, become possibly in the future by using a general circulation model as an atmospheric proxy.

The results presented open a wide area of questions. Possible variations in latitude and longitude could be studied. The altitude range of the analysis (0–110 km) should be extended to the thermosphere. The GLOTI data indicate that MAOs with periods found in our studies are present globally since 130 yrs. This would motivate a detailed analysis from the ground to higher altitudes. The stability of MAO in time is an important question. MAO signatures should be looked for in other parameters beyond temperature (e.g. densities and winds). Higher order parameters are also of major interest (e.g. wave momentum flux, flux divergence etc). Analysis of these and other aspects will hopefully elucidate the structure of these oscillations and eventually reveal their nature.

Acknowledgments

North Atlantic Oscillation Indices (NAO) data were down- loaded from http://www.cpc.ncep.noaa.gov/products/precip/Cwlink/pna/norm.n…, and are gratefully acknowledged.

Global Land Ocean Temperature Index (GLOTI) data were down-loaded from http://data.giss.nasa.gov/gistemp/tabledata_v3/GLB.Ts+dSST.txt and are gratefully acknowledged.

HAMMONIA simulations were performed at and supported by the German Climate Computing Center (DKRZ).

Model intergrations of the CESM-WACCM Model have been performed at the Deutsches Klimarechenzentrum (DKRZ) Hamburg, Germany. The help of Sebastian Wahl in preparing the CESM-WACCM data is greatly appreciated.

Part of this work was funded in the framework of the MALODY project within the ROMIC program of the German Ministry of Education and Research, Grant no. 01LG1207A.

References

Abarca del Rio, R., Gambis, D., Salstein, D.A., 2000. Interannual signals in length of day and atmospheric angular momentum. Ann. Geophys. 18, 347–364.

Andrews, D.G., Holton, J.R., Leovy, C.B., 1987. Middle atmosphere dynamics. Academic Press Inc., Orlando, San Diego, New York, Austin, Boston, London, Sydney, Tokyo, Toronto.

Baldwin, M.P., et al., 2001. The quasi-biennial oscillation. Rev. Geophys. 39, 179–229.

Chen, G., Shao, B., Han., Y., Ma, J., Chapron, B., 2010. Modality of semiannual to multidecadal oscillations in global sea surface temperature variability. J. Geophys. Res. 115, C03005. http://dx.doi.org/10.1029/2009JC005574.

Garcia, R.R., Marsh, D.R., Kinnison, D.E., Boville, B.A., Sassi, F., 2007. Simulation of secular trends in the middle atmosphere,1950–2003. J. Geophys. Res. 112, D09301. http://dx.doi.org/10.1029/2006JD007485.

Giorgetta, M.A., Manzini, E., Roeckner, E., 2002. Forcing of the quasi-biennial oscillation from a broad spectrum of atmospheric waves. Geophys. Res. Lett. 29 (1245), 86-1–86-4. http://dx.doi.org/10.1029/2002GL014756.

Gent, P.R., et al., 2011. The community climate system model version 4. J. Clim. 24 (19), 973–4991. http://dx.doi.org/10.1175/2011JCLI4083.1.

Gray, L.J., et al., 2010. Solar influences on climate. Rev. Geophys. 48, RG4001. http://dx.doi.org/10.1029/2009RG000282.

Hansen, J., Ruedy, R., Sat, M., Lo, K., 2010. Global surface temperature change. Rev. Geophys. 48, RG4004. http://dx.doi.org/10.1029/2010RG000345.

Hansen, F., Matthes, K., Petrick, C., Wang, W., 2014. The influence of natural and anthropogenic factors on major stratospheric sudden warmings. J. Geophys. Res. Atmos 119, 8117–8136, http://dx.doi.org/10.1002/2013JD021397.

Khomich, V., Yu., A.I., Semenov, N.N., Shefov, 2013. Airglow as an Indicator of Upper Atmospheric Structure and Dynamics. Springer, Dordrecht, Heidelberg, New York, London.

Kinnison, D.E., Brasseur, G.P., Walters, S., Garcia, R.R., Marsh, D.R., Sassi, F., Harvey, V.L., Randall, C.E., Emmons, L., Lamarque, J.F., Hess, P., Orlando, J.J., Tie, X.X., Randel, W., Pan, L.L., Gettelmann, A., Granier, C., Diehl, T., Niemeier, U., Simmons, A.J., 2007. Sensitivity of chemical tracers to meteorological parameters in the MOZART-3 chemical transport model. J. Geophys. Res. 112 (D20302), 1–24. http://dx.doi.org/10.1029/2006JD007879.

Marsh, D., Mills, M.J., Kinnison, D.E., Lamarque, J.-F., Calvo, N., Polvani, L.M., 2013. Climate change from 1850 to 2005 simulated in CESM1(WACCM). J. Clim. 26, 7372–17391. http://dx.doi.org/10.1175/JCLI-D-12-00558.1.

Matthes, K., Marsh, D.R., Garcia, R.R., Kinnison, D.E., Sassi, F., Walters, S., 2010. Role of the QBO in modulating the influence of the 11 year solar cycle on the atmosphere using constant forcings. J. Geophys. Res. 115, D18110. http://dx.doi.org/10.1029/2009JD013020.

Origin Pro 8G,Copyright Origin Lab Corporation, Northhampton, USA.

Peters, D.H.W., Bremer, J., Entzian, G., Wecke, B., von Rein, R., 2006/7. Zur Langzeit-Variabilität der Elektronendichte in der Mesosphäre, Institutsbericht 2006/2007. Leibnitz-Institut für Atmosphärenphysik e.V. an der Universität Rostock, Kühlungsborn, Germany.

Pikovsky, A., Rosenblum, M., Kurths, J., 2003. Synchronization – A universal concept in nonlinear science. Cambridge Universit Press, Cambridge, UK.

Offermann, D., Hoffmann, P., Knieling, P., Koppmann, R., Oberheide, J., Steinbrecht, W., 2010. Long-term trends and solar cycle variations of mesospheric temperature and dynamics. J. Geophys. Res. 115, D18127. http://dx.doi.org/10.1029/2009JD013363.

Remsberg, E.E., et al., 2008. Assessment of the quality of the Version 1.07 temperature-versus-pressure profiles of the middle atmosphere from TIMED/SABER. J. Geophys. Res. 113, D17101. http://dx.doi.org/10.1029/2008JD010013.

Richter, J.H., Sassi, F., Garcia, R.R., 2010. Toward a physically based gravity wave source parameterization in a general circulation model. J. Atmos. Sci 67 (1), 136–156, http://dx.doi.org/10.1175/2009JAS3112.1.

Roeckner, E., Brokopf, R., Esch, M., Giorgetta, M., Hagemann, S., Kornblueh, L., Manzini, E., Schlese, U., Schulzweida, U., 2006. Sensitivity of simulated climate to horizontal and vertical resolution in the ECHAM5 atmosphere model. J. Clim. 19, 3771–3791.

Schmidt, H., Brasseur, G.P., Charron, M., Manzini, E., Giorgetta, M.A., Diehl, T., Fomichev, V.I., Kinnison, D., Marsh, D., Walters, S., 2006. The HAMMONIA chemistry climate model: sensitivity of the mesopause region to the 11-year solar cycle and CO_2 doubling. J. Clim. 19, 3903–3931. http://dx.doi.org/10.1175/JCLI3829.1.

Schmidt, H., Brasseur, G.P., Giorgetta, M.A., 2010. Solar cycle in a general circulation and chemistry model with internally generated quasi-biennial oscillation. J. Geophys. Res. 115, D1. http://dx.doi.org/10.1029/2009JD012542.

Schmidt, H., Kieser, J., Misios, S., Gruzdev, A.N., 2013. The atmospheric response to solar variability: Simulations with a General Ciculation and Chemistry Model for the Entire Atmosphere. In: Lübken, F.-J. (Ed.), Climate and Weather of the Sun-Earth System (CAWSES). Springer Atmospheric Sciences, Dordrecht, Heidelberg, New York, London, pp. 585–603, doi: 10/1007/ 978-94-007-4348-9.

Wang, J., Pawson, St, Tian, B., Liang, M.-Ch, Shia, R.-L., Yung, Y.L., Jiang, X., 2011. El Nino-Southern Oscillation in tropical and midlatitude column ozone. J. Atmos. Sci. 68, 1911–1921.

White, W.B., Liu, Z., 2008a. Resonant excitation of the quasi-decadal oscillation by the 1-year signal in the Sun's irradiation. J. Geophsy. Res. 113, C01002. http://dx.doi.org/10.1029/2006JC004057.

White, W.B., Liu, Z., 2008b. Non-linear alignment of El Nino to the 11-yr solar cycle. Geophys. Res. Lett. 35, L19607. http://dx.doi.org/10.1029/2008GL034831.

White, W.B., Tourre, Y.M., Barlow, M., Dettinger, M., 2003. A delayed action oscillator shared by biennial, interannual, and decadal signals in the Pacific basin. J. Geophys. Res. 108 (C3), 3070. http://dx.doi.org/10.1029/2002JC001490.

Atmos. Chem. Phys., 21, 1593–1611, 2021
https://doi.org/10.5194/acp-21-1593-2021

Atmospheric Chemistry and Physics
Open Access

Very long-period oscillations in the atmosphere (0–110 km)

Dirk Offermann[1], **Christoph Kalicinsky**[1], **Ralf Koppmann**[1], **and Johannes Wintel**[1,a]

[1]Institut für Atmosphären – und Umweltforschung, Bergische Universität Wuppertal, Wuppertal, Germany
[a]now at: Elementar Analysensysteme GmbH, Langenselbold, Germany

Correspondence: Dirk Offermann (offerm@uni-wuppertal.de)

Received: 30 January 2020 – Discussion started: 20 May 2020
Revised: 18 December 2020 – Accepted: 18 December 2020 – Published: 5 February 2021

Abstract. Multi-annual oscillations have been observed in measured atmospheric data. These oscillations are also present in general circulation models. This is the case even if the model boundary conditions with respect to solar cycle, sea surface temperature, and trace gas variability are kept constant. The present analysis contains temperature oscillations with periods from below 5 up to more than 200 years in an altitude range from the Earth's surface to the lower thermosphere (110 km). The periods are quite robust as they are found to be the same in different model calculations and in atmospheric measurements. The oscillations show vertical profiles with special structures of amplitudes and phases. They form layers of high or low amplitudes that are a few dozen kilometres wide. Within the layers the data are correlated. Adjacent layers are anticorrelated. A vertical displacement mechanism is indicated with displacement heights of a few 100 m. Vertical profiles of amplitudes and phases of the various oscillation periods as well as their displacement heights are surprisingly similar. The oscillations are related to the thermal and dynamical structure of the middle atmosphere. These results are from latitudes and longitudes in central Europe.

1 Introduction

Multi-annual oscillations with periods between 2 and 11 years have frequently been discussed for the atmosphere and the ocean. Major examples are the Quasi-Biennial Oscillation (QBO), solar-cycle-related variations near 11 and 5.5 years, and the El Niño–Southern Oscillation (ENSO). (For references see for instance Offermann et al., 2015.)

Self-excited oscillations in the ocean of such periods have been described for instance by White and Liu (2008). Oscillations in the atmosphere with periods between 2.2 and 5.5 years have been shown in a large-altitude regime by Offermann et al. (2015). Their periods are surprisingly robust; i.e. there is little change with altitude. They are also present in general circulation models, the boundaries of which are kept constant.

Oscillations of much longer periods in the atmosphere and the ocean have also been reported. Biondi et al. (2001) found bi-decadal oscillations in local tree ring records that date back several centuries. Kalicinsky et al. (2016, 2018) recently presented a temperature oscillation near the mesopause with a period near 25 years. Low-frequency oscillations (LFOs) on local and global scales in the multi-decadal range (50–80 years) have been discussed several times (e.g. Schlesinger and Ramankutty, 1994; Minobe, 1997; Polyakov et al., 2003; Dai et al., 2015; Dijkstra et al., 2006). Some of these results were intensively discussed as internal variability of the atmosphere–ocean system, for instance as the internal interdecadal modes AMV (Atlantic Multidecadal Variability) and PDO/IPO (Pacific Decadal Oscillation/Interdecadal Pacific Oscillation) (e.g. Meehl et al., 2013, 2016; Lu et al., 2014; Deser et al., 2014; Dai et al., 2015.) Multidecadal variations (40–80 years) in Arctic-wide surface air temperatures were, however, related to solar variability by Soon (2005). Some of these long-period variations have been traced back for 2 or more centuries (Minobe, 1997; Biondi et al., 2001; Mantua and Hare, 2002; Gray et al., 2004). Multidecadal oscillations have also been discussed extensively as internal climatic variability in the context of the long-term climate change (temperature increase) in the IPCC AR5 Report (e.g. Flato et al., 2013).

Even longer periods of oscillations in the ocean and the atmosphere have also been reported. Karnauskas et al. (2012) find centennial variations in three general circulation models of the ocean. These variations occur in the absence of external forcing; i.e. they show internal variabilities on the centennial timescale. Internal variability in the ocean on a centennial scale is also discussed by Latif et al. (2013) on the basis of model simulations. Measured data of a 500-year quasi-periodic temperature variation are shown by Xu et al. (2014). They analyse a more than 5000-year-long pollen record in East Asia. Very long periods are found by Paul and Schulz (2002) in a climate model. They obtain internal oscillations with periods of 1600–2000 years.

All long-period oscillations cited here refer to temperatures of the ocean or the land–ocean system. It is emphasized that by contrast the multi-annual oscillations described by Offermann et al. (2015) and those discussed in the present paper are properties of the atmosphere and exist in a large-altitude regime between the ground and 110 km altitude. They are not related to the ocean (see below).

In the present paper the work of Offermann et al. (2015) is extended to multi-decadal and centennial periods. Oscillations in the atmosphere are studied in three general circulation models. The analysis is locally constrained (central Europe) but vertically extended up to 110 km. The model boundary conditions (sun, ocean, trace gases) are kept constant. The results of model runs with HAMMONIA, WACCM, and ECHAM6 were made available to us. They simulate 34, 150, and 400 years of atmospheric behaviour, respectively. The corresponding results are compared to each other. Most of the analyses are performed for atmospheric temperatures.

For comparison, long-duration measured data series are also analysed. There is a data set taken at the Hohenpeißenberg Observatory (47.8° N, 11.0° E) since 1783. Long-term data have been globally averaged by Hansen et al. (2010) and published as GLOTI data (Global Land Ocean Temperature Index).

In Sect. 2 of this paper the three models are described and the analysis method is presented. In Sect. 3 the oscillations obtained from the three models are compared. The vertical structures of the periods, amplitudes, and phases of the oscillations are described. In Sect. 4 the results are discussed. Section 5 gives a summary and some conclusions.

2 Model data and their analysis

2.1 Long-period oscillations and their vertical structures

In an earlier paper (Offermann et al., 2015) multi-annual oscillations with periods of about 2–5 years were described at altitudes up to 110 km. These were found in temperature data of HAMMONIA model runs (see below). They were present in the model even if the model boundary conditions (solar irradiance, sea surface temperatures and sea ice, boundary values of greenhouse gases) were kept constant. The periods were found to be quite robust as they did not change much with altitude.The oscillations showed particular vertical structures of amplitudes and phases. Amplitudes did not increase exponentially with altitude as they do with atmospheric waves. They rather varied with altitude between maximum and near-zero values in a nearly regular manner. Phases showed jumps of about 180° at the altitudes of the amplitude minima and were about constant in between. There were indications of synchronization of amplitudes and phases.

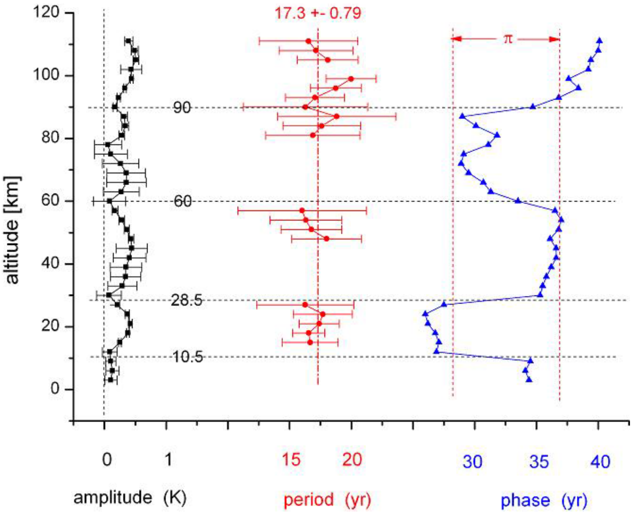

Figure 1. Vertical structures of long-period oscillations near 17.3 ± 0.8 years from HAMMONIA temperatures. Missing period values could not be derived from the data. They were prescribed as the mean value of 17.3 years (dash–dotted vertical red line; see text and Sect. 3.2). Phases are relative values.

The periods analysed in the earlier paper have been restricted to below 5.5 years. Much longer periods have been described in the literature. It is therefore of interest to see whether such longer periods could also be found in the models and what their origin might be.

Figure 1 shows an example of such temperature structures for an oscillation with a period of 17.3 ± 0.8 years obtained from the HAMMONIA model discussed below. This picture is typical of the oscillations in Offermann et al. (2015) and of the oscillations discussed in the present paper. The periods at the various altitudes are close to their mean value even though the error bars are fairly large. There is no indication of systematic altitude variations, and therefore the mean is taken as a first approximation. At some altitudes the periods could not be determined (see Sect. 3.3). In these cases the periods were prescribed by the mean of the derived periods (dash–dotted red vertical line, 17.3 years) to obtain approximate amplitudes and phases at these altitudes (see Offermann et al., 2015). Details of the derivation of periods, amplitudes, and phases are given in Sect. 3.2.

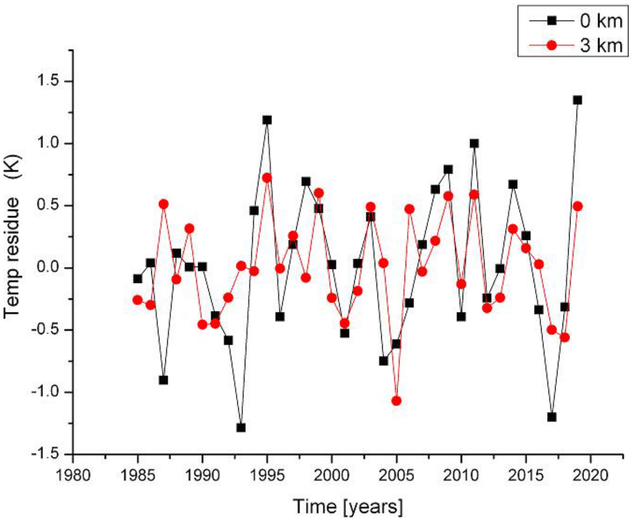

Figure 2. HAMMONIA temperature residues at 0 and 3 km altitude with fixed boundary conditions (see text). Mean temperatures of 281.89 K (0 km) and 266.04 K (3 km) have been subtracted from the model temperatures. Data are for 50° N, 7° E.

2.2 HAMMONIA

The HAMMONIA model (Schmidt et al., 2006) is based on the ECHAM5 general circulation model (Röckner et al., 2006) but extends the domain vertically to 2×10^{-7} hPa and is coupled to the MOZART3 chemistry scheme (Kinnison et al., 2007). The simulation analysed here was run at a spectral resolution of T31 with 119 vertical layers. The relatively high vertical resolution of less than 1 km in the stratosphere allows an internal generation of the QBO. Here we analyse the simulation (with fixed boundary conditions, including aerosol, ozone climatology) that was called "Hhi-max" in Offermann et al. (2015), but instead of only 11 we use 34 simulated years. Further details of the simulation are given by Schmidt et al. (2010).

As concerns the land parameters, part of them were also kept constant (vegetation parameters as leaf area, wood coverage) and so was ground albedo. Others were not (e.g. snow and ice on lakes). Hence, some influence on our oscillations is possible.

An example of the HAMMONIA data is given in Fig. 2 for 0 and 3 km altitudes. The HAMMONIA data were searched for long-period oscillations up to 110 km. The detailed analysis is described below (Sect. 3.2). Nine oscillations were identified with periods between 5.3 and 28.5 years. They are listed in Table 2a. The oscillation shown in Fig. 1 (17.3 years) is from about the middle of this range.

2.3 WACCM

Long runs with chemistry–climate models (CCMs) having restricted boundary conditions are not frequently available. A model run much longer than 34 years became available from the CESM-WACCM4 model. This 150-year run was analysed from the ground up to 108 km. The model experiments are described in Hansen et al. (2014). Here, the experiment with monthly varying constant climatological sea surface temperatures (SSTs) and sea ice has been used; i.e. there is a seasonal variation, but it is the same in all years. Other boundary conditions such as greenhouse gases (GHGs) and ozone-depleting substances (ODPs) were kept constant at 1960 values.

Solar cycle variability, however, was not kept constant during this model experiment. Spectrally resolved solar irradiance variability as well as variations in the total solar irradiance and the F10.7 cm solar radio flux were used from 1955 to 2004 from Lean et al. (2005). Thereafter solar variations from 1962–2004 were used as a block of proxy data and added to the data series several times to reach 150 years in total. Details are given in Matthes et al. (2013).

The WACCM data were analysed for long-period oscillations in the same manner as the HAMMONIA data. Here, the emphasis is on longer periods. Besides many shorter oscillations, nine oscillations with periods of more than 20 years were found. These results are included in Table 2a.

2.4 ECHAM6

The longest computer run available to us, covering 400 years, is from ECHAM6. ECHAM6 (Stevens et al., 2013) is the successor of ECHAM5, the base model of HAMMONIA. Major changes relative to ECHAM5 include an improved representation of radiative transfer in the solar part of the spectrum, a new description of atmospheric aerosol, and a new representation of the surface albedo. While the standard configuration of ECHAM5 used a model top at 10 hPa, this was extended to 0.01 hPa in ECHAM6. As the atmospheric component of the Max Planck Institute Earth System Model (MPI-ESM; Giorgetta et al., 2013), it has been used in a large number of model intercomparison studies related to the Coupled Model Intercomparison Project phase 5 (CMIP5). The ECHAM6 simulation analysed here was run at T63 spectral resolution with 47 vertical layers (not allowing for an internal generation of the QBO). All boundary conditions were fixed to constant values, taken as an average of the years 1979 to 2008.

The temperature data were analysed as the other data sets described above. Seventeen oscillation periods longer than 20 years were obtained (Table 2a). The ECHAM6 results in this paper are considered an approximate extension of the HAMMONIA results.

A summary of the model properties is given in Table 1. All analyses in this paper are for central Europe. The vertical model profiles are for 50° N, 7° E.

Table 1. Properties of the GCM simulations. All data are for central Europe (50° N, 7° E). For various details see text.

	HAMMONIA	WACCM4	ECHAM6
Horizontal resolution	T31	1.9° × 2.5° (lat/long)	T63
Vertical resolution	119 levels 1 km (stratosphere)	66 levels	47 levels
Altitude range	0–110 km	0–108 km	0–78 km
Length of simulation	34 years	150 years	400 years
Time resolution of data used	annual/monthly	annual	annual
Boundary conditions:			
– sun	fixed	variable (see text)	fixed
– ocean	climatological SST and sea ice	climatological SST and sea ice	climatological SST and sea ice
– greenhouse gases	fixed	fixed (1960 values)	fixed
References	Schmidt et al. (2010)	Hansen et al. (2014)	Stevens et al. (2013)

3 Model results

3.1 Vertical correlations of atmospheric temperatures

Figure 1 indicates that there are some vertical correlation structures in the atmospheric temperatures. This was studied in detail for the HAMMONIA and ECHAM6 data.

Ground temperature residues from the HAMMONIA run 38123 (34 years) are shown in Fig. 2 (black squares). The mean temperature is 281.89 K, which was subtracted from the model data. The boundary conditions (sun, ocean, greenhouse gases, soil humidity, land use, vegetation) have been kept constant, as discussed above. The temperature fluctuations thus show the atmospheric variability (standard deviation is $\sigma = 0.62$ K). This variability is frequently termed "(climate) noise" in the literature. It will be checked whether this notion is justified in the present case.

Also shown in Fig. 2 are the corresponding HAMMONIA data for 3 km altitude. The mean temperature is 266.04 K; the standard deviation is $\sigma = 0.41$ K. The statistical error of these two standard deviations is about 12 %. Hence the internal variances at the two altitudes are statistically different. This suggests that there may be a vertical structure in the variability that should be analysed.

The data sets in Fig. 2 show large changes within short times (2–4 years). Sometimes these changes are similar at the two altitudes. The variability of HAMMONIA thus appears to contain an appreciable high-frequency component and thus also needs to be analysed for vertical and for spectral structures.

Temperatures at layers 3 km apart in altitude were therefore correlated with those at 42 km as a reference altitude (near the stratopause). The results are shown in Fig. 3 for the HAMMONIA model run up to 105 km (red dots). A corresponding analysis for the much longer model run of ECHAM6 is also shown (black squares, up to 78 km). Two important results are obtained: (1) there is an oscillatory vertical structure in the correlation coefficient r with a maximum in the upper mesosphere and lower thermosphere and two minima in the lower stratosphere and in the mesosphere (for HAMMONIA). The correlations are highly significant near the upper three of these extrema (see the 95 % lines in Fig. 3). (2) The correlations in the two different data sets are nearly the same above the troposphere. This is remarkable because the two sets cover time intervals very different in length (34 years vs. 400 years). Therefore, the correlation structure appears to be a basic property of the atmosphere (see below).

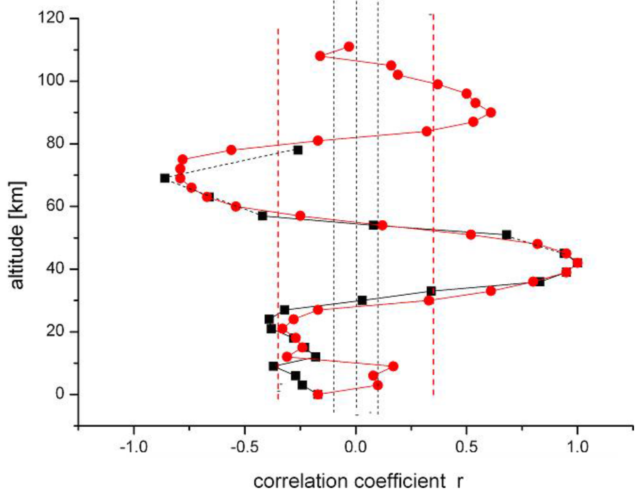

Figure 3. Vertical correlation of temperatures in HAMMONIA (red dots) and ECHAM6 (black squares). Reference altitude is 42 km ($r = 1$). Vertical dashed lines show 95 % significance for HAMMONIA (red) and ECHAM6 (black).

The correlations suggest that the fluctuations in the atmosphere (or part of them) are somehow "synchronized" at adjacent altitude levels. A vertical (layered) structure might therefore be present in the magnitude of the fluctuations, too. This was studied by means of the standard deviations σ of the temperatures T; the result is shown in Fig. 4. There is indeed a vertical structure with fairly pronounced layers.

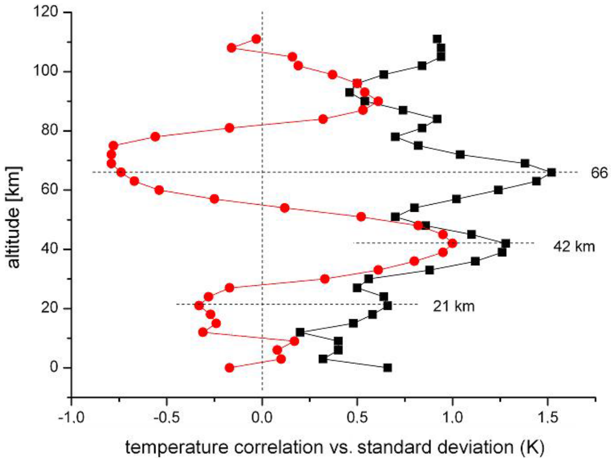

Figure 4. HAMMONIA temperatures: comparison of standard deviations (black squares, multiplied by 2 for easier comparison) and correlation coefficients (red dots, see Fig. 3). For details see text.

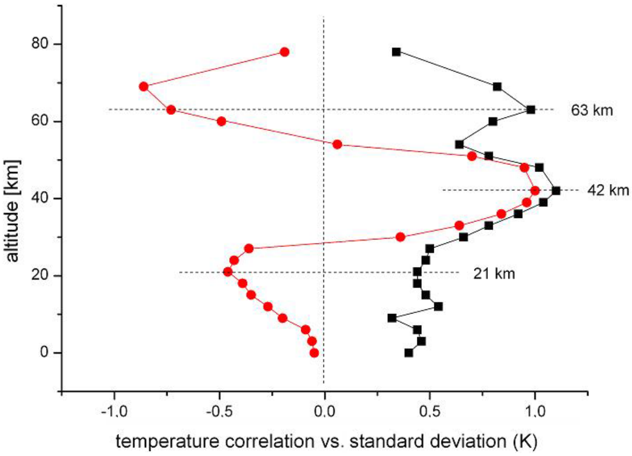

Figure 5. ECHAM6 temperatures: comparison of standard deviations (black squares, multiplied by 2) and correlation coefficients (red dots). For details see text.

The HAMMONIA data used for Fig. 4 were annual data that have been smoothed by a four-point running mean. This was done to reduce the influence of high-frequency "noise" mentioned above, which is substantial (a factor of 2). The correlation calculations were repeated with the unsmoothed data. The results are essentially the same. The same applies to the standard deviations.

The layered structures shown in Figs. 3 and 4 are not unrelated. This can be seen in Fig. 4, which also gives the vertical correlations r (Fig. 3) for comparison. The horizontal dashed lines indicate that the maxima of the standard deviations occur near the extrema of the correlation profile in the stratosphere and lower mesosphere. This suggests that the fluctuations in adjacent σ maxima (and in adjacent layers) are anticorrelated. Surprisingly these anticorrelations are also approximately seen in the amplitude and phase profiles of Fig. 1 that are typical of all oscillations (see below).

The ECHAM6 data have been analysed in the same way as the HAMMONIA data, including a smoothing by a four-point running mean. The data cover the altitude range of 0–78 km for a 400-year simulation. The results are very similar to those of HAMMONIA. This is shown in Fig. 5, which gives vertical profiles of standard deviations and of vertical correlations of the smoothed ECHAM6 data and is to be compared to the HAMMONIA results in Fig. 4. The two upper maxima of standard deviations are again anticorrelated.

It is apparently a basic property of the atmosphere's internal variability to be organized in some kind of "layers", and that adjacent layers are anticorrelated. It appears therefore questionable whether the internal variability may be termed noise, as is frequently done in the literature.

3.2 Time structures

The correlations or anticorrelations concern temporal variations in temperatures. This suggests a search for some kind of regular (ordered) structure in the time series, as well. Therefore in a first step, FFT (fast Fourier transform) analyses have been performed for all HAMMONIA altitude levels (3 km apart). The results are shown in Fig. 6, which gives amplitudes for the period range of 4–34 years versus altitude. Also in this picture, the amplitudes show a layered structure. In addition an ordered structure in the period domain is also indicated. There are increased or high amplitudes near certain period values, for instance at the left- and right-hand side and in the middle of the picture. A similar result is obtained for the ECHAM6 data shown in Fig. 7 for the longer periods of 10–400 years. The layered structure in altitude is clearly seen, and so are the increased amplitudes near certain period values. Obviously, the computer simulations contain periodic temperature oscillations, the amplitudes of which show a vertically layered order.

The amplitudes shown in Figs. 6 and 7 are relative values, and the resolution of the spectra is quite limited. Therefore a more detailed analysis is required. For this purpose the Lomb–Scargle periodogram (Lomb, 1976; Scargle, 1982) is used. As an example Fig. 8 shows the mean Lomb–Scargle periodogram in the period range 20–100 years for the ECHAM6 data. For this picture Lomb–Scargle spectra were calculated for all ECHAM6 layers separately, and the mean spectrum of all altitudes was determined. The power of the periodogram gives the reduction in the sum of squares when fitting a sinusoid to the data (Scargle, 1982); i.e. it is equivalent to a harmonic analysis using least-square fitting of sinusoids. The power values are normalized by the variance of the data to obtain comparability of the layers with different variance. Quite a number of spectral peaks are seen

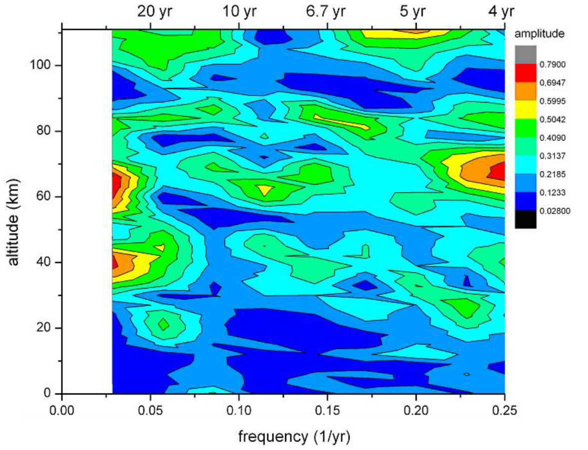

Figure 6. Long-period temperature oscillations in the HAMMONIA model. FFT amplitudes are shown in dependence on altitude and frequency (periods 4–34 years). Colour code of amplitudes is in arbitrary units.

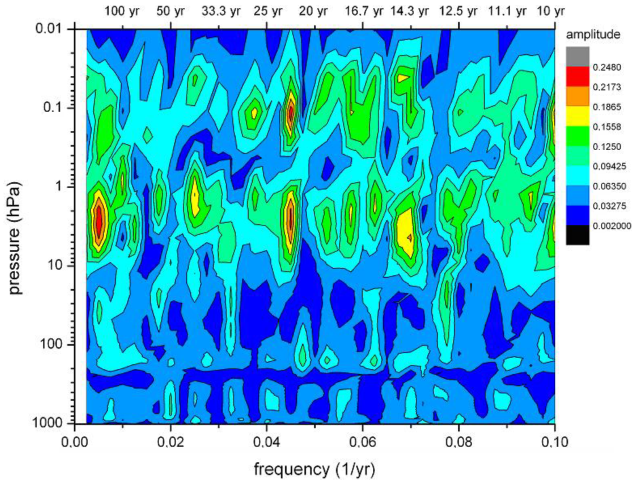

Figure 7. Long-period temperature oscillations in the ECHAM6 model. FFT amplitudes are shown in dependence on altitude and frequency (periods 10–400 years). Colour code of amplitudes is in arbitrary units.

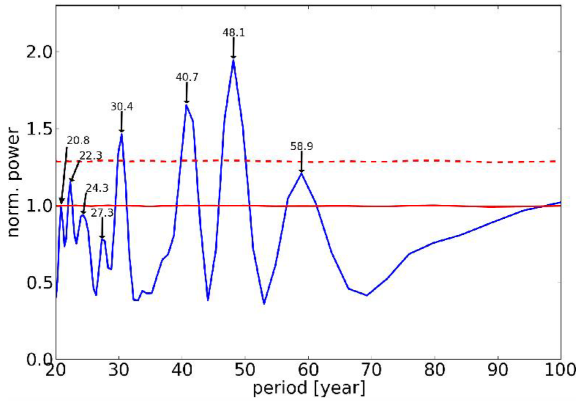

Figure 8. Long-period temperature oscillations in the ECHAM6 model Lomb–Scargle periodogram is given for periods of 20–100 years. Dashed red line indicates significance at the 2σ level. For straight red line see text.

between 20- and 60-year periods. Further oscillations appear to be present around 100 years and at even longer periods (not shown here as they are not sufficiently resolved).

We compared the mean result for the ECHAM6 data with 10 000 representations of noise. One representation covers 47 atmospheric layers. For each representation we took noise from a Gaussian distribution for each atmospheric layer independently and calculated a mean Lomb–Scargle periodogram for every representation in the same way as for the ECHAM6 data.

It might be considered appropriate to use red noise instead of white noise in this analysis. We therefore calculated the sample autocorrelation at a lag of 1 year for the different ECHAM6 altitudes. These values were found to be very close to zero and, thus, we used Gaussian noise in our analysis.

The red line in Fig. 8 shows the average of all of these mean periodograms. As expected for the average of all representations, the peaks cancel, and one gets an approximately constant value for all periods. A single representation typically shows one or several peaks above this mean level. The red dashed line gives the upper 2σ level, i.e. the mean plus 2σ. As the mean Lomb–Scargle periodogram for the ECHAM6 data shows several peaks clearly above this upper 2σ level, this mean periodogram is significantly different from that of independent noise. Therefore, the conclusion is that independent noise at the different atmospheric layers alone cannot explain the observed periodogram showing large remaining peaks after averaging.

The period values shown in Fig. 8 agree with those given for ECHAM6 in Table 2a which are from the harmonic analysis described next. The agreement is within the error bars given in Table 2a (except for 24.3 years).

A spectral analysis such as that in Fig. 8 was also performed for the HAMMONIA temperatures. It showed the periods of 5.3 and 17.3 years above the 2σ level. These values agree within single error bars with those given in Table 2a. All peaks found to be significant (in different analyses) are marked by heavy print in Table 2a.

The Lomb–Scargle spectra (in their original form) do not reveal the phases of the oscillations. We have therefore applied harmonic analyses to our data series. This was done by stepping through the period domain in steps 10 % apart. In each step we looked for the largest nearby sinus oscillation peak. This was done by means of an ORIGIN search algorithm (ORIGIN Pro 8G, Levenberg–Marquardt algorithm) that yielded optimum values for period, amplitude, and phase. The algorithm starts from a given initial period

Table 2. Periods of temperature oscillations from harmonic analyses. **(a)** Periods are numbered according to increasing values. Periods (in years) are given with their standard deviations. Modelled periods are from the HAMMONIA, WACCM, and ECHAM6 models, respectively. Additional periods are from Hohenpeißenberg measurements and from the Global Land Ocean Temperature Index (GLOTI). HAMMONIA periods are limited to 28.5 years as the model run covered 34 years, only. WACCM periods are given for less than 147 years from a model run of 150 years. ECHAM6 periods are from a 400-year run. Short periods (below 20 years) are not shown for WACCM, ECHAM6, and GLOTI as they are not used in the present paper. Hohenpeißenberg and GLOTI data after 1980 are not included in the analyses because of their steep increase in later years. Periods given in bold type refer to **(b)**. **(b)** Comparative periods (in years).

(a) No.	HAMMONIA (119 layers) (years)	WACCM (years)	ECHAM6 (47 years) (years)	Hohenpeißenberg 1783–1980 (years)	GLOTI 1880–1980 (years)
1	**5.34 ± 0.10**			5.48 ± 0.21	
2	**6.56 ± 0.24**			6.16 ± 0.20	
3	**7.76 ± 0.29**			7.83 ± 0.26	
4	9.21 ± 0.53			9.50 ± 0.65	
5	10.8 ± 0.34			10.85 ± 0.38	
6	**13.4 ± 0.68**			13.6 ± 0.80	
7	**17.3 ± 1.05**			18.02 ± 1.08	
8			20.0 ± 0.35	19.9 ± 1.00	20.2 ± 1.36
9			20.9 ± 0.15		
10	22.8 ± 1.27	21.7 ± 1.02	**22.1 ± 0.23**	21.9 ± 0.94	
11			23.8 ± 0.42		
12		25.82 ± 0.86	**25.3 ± 0.46**	25.1 ± 0.62	25.5 ± 2.0
13	28.5 ± 1.63		27.3 ± 0.41		
14		31.56 ± 1.42	**30.2 ± 0.49**	29.8 ± 0.66	
15			33.3 ± 0.84		
16		38.1 ± 0.82	36.9 ± 1.17	36.01 ± 1.28	35.4 ± 2.42
17		41.89 ± 0.95	**41.4 ± 0.97**		
18			**48.4 ± 1.73**		
19				52.06 ± 1.61	53.4 ± 11.4
20		57.64 ± 1.69	**58.3 ± 1.77**		
21		66.95 ± 7.31	64.9 ± 2.98		
22			77.5 ± 3.94	81.6 ± 4.18	
23		97.27 ± 5.06	95.5 ± 5.86		
24		147 ± 14.9	129.4 ± 14.5		
25			206.7 ± 16.3		
26				238.2 ± 11.8	

(b) No.	Period (years) from HAMMONIA/ ECHAM6 (numbers refer to Table 2a)	Accuracy/significance (SSA: singular spectrum analysis; ASA: autocorrelation spectral analysis; DFA: detrended fluctuation analysis)	Source/corresponding period
1	5.34 ± 0.1	2σ SSA	Lomb–Scargle periodogram as in Fig. 8 (not shown here) Plaut et al. (1995): 5.2 years
2	6.56 ± 0.24	1σ	Lomb–Scargle periodogram as in Fig. 8 (not shown here); see also CH_4 analysis (Table 3): 6.43 ± 0.26 years
3	7.76 ± 0.29	SSA ASA (80 %) DFA	Plaut et al. (1995): 7.7 years Schönwiese (1992): 7.5 years Meyer and Kantz (2019): 7.6 ± 1.8 years
6	13.4 ± 0.68	SSA ASA (95 %) 2σ	Plaut et al. (1995): 14.2 years Schönwiese (1992): 13 years Lomb–Scargle periodogram as in Fig. 8 (not shown here); see also CH_4 analysis (Table 3): 13.73 ± 0.93 years
7	17.3 ± 1.05	2σ	Lomb–Scargle periodogram as in Fig. 8 (not shown here)
10	21.1 ± 0.23	1σ	Lomb–Scargle periodogram: 22.3 years, see Fig. 8
12	25.3 ± 0.46	SSA	Plaut et al. (1995): 25.0 years
14	30.2 ± 0.49	2σ	Lomb–Scargle periodogram: 30.4 years, see Fig. 8
17	41.4 ± 0.97	2σ	Lomb–Scargle periodogram: 40.7 years, see Fig. 8
18	48.4 ± 1.73	2σ	Lomb–Scargle periodogram: 48.1 years, see Fig. 8
20	58.3 ± 1.77	1σ	Lomb–Scargle periodogram: 58.9 years, see Fig. 8

and looks for a major oscillation in its vicinity. For this it determines period, amplitude , and phase, including error bars. If in this paper the term "harmonic analysis" is used, this algorithm is always meant. The results are a first approximation, though, because only one period was fitted at a time, instead of the whole spectrum. Furthermore, the 10 % grid may be sometimes too coarse. Also small-amplitude oscillations may be overlooked.

This analysis was performed for all altitude levels available. Figure 1 shows an example for the HAMMONIA temperatures from 3–111 km for periods around 15–20 years. The middle track (red dots) shows the periods with their error bars, the left side shows the amplitudes, and the right side shows the phases. The mean of all periods is 17.3 ± 0.79 years. There are several altitudes where the harmonic analysis does not give a period. This may occur if an amplitude is very small or if there is a nearby period with a strong amplitude that masks the smaller one. At these altitudes the periods were interpolated for the fit (dash–dotted vertical line). The mean of the derived periods (17.3 years) is used as an estimated interpolation value. This is because the derived periods do not deviate too much from the mean value. This procedure allows us to obtain estimated amplitude and phase values for instance in the vicinity of the amplitude minima. That is important because at these altitudes large phase changes are frequently observed. The Levenberg–Marquardt algorithm calculates an amplitude and phase if a prescribed (estimated) period is provided.

The right track in Fig. 1 shows the phases of the oscillations. The special feature about this vertical profile is its step-like structure with almost constant values in some altitudes and a subsequent fast change somewhat higher to some other constant level. These changes are about 180° (π); i.e. the temperatures above and below these levels are anticorrelated. At these levels the temperature amplitudes (left track) are at a minimum, with maxima in between. These maxima occur near the altitudes of the maxima of the temperature standard deviations in Fig. 4 that are anticorrelated in adjacent layers. The phase steps in Fig. 1 approximately fit this picture. They suggest that the layer anticorrelation discussed above corresponds at least in part to the phase structure of the long-period oscillations in the atmosphere.

This important result was checked by an analysis of other oscillations contained in the HAMMONIA data series. Nine oscillations with periods between 5.34 and 28.5 years were obtained by the analysis procedure described above. They are listed in Table 2a, and all show vertical profiles similarly as in Fig. 1.

Figure 1 shows that at different altitudes the periods are somewhat different. They cluster, however, quite closely about their mean value of 17.3 years. This clustering about a mean value is found for almost all periods listed in Table 2a. This is shown in detail in Figs. 9 and 10, which give the number of periods found at different altitudes in a fixed period interval. The clusters are separated by major gaps, as is indicated by vertical dashed lines (black). This suggests using a mean period value as an estimate of the oscillation period representative of all altitudes. The mean period values are given above each cluster in red, together with a red solid line. A few clusters are not very pronounced, and hence the corresponding mean period values are unreliable (e.g. those beyond 20 years; see the increased standard deviations in Table 2a).

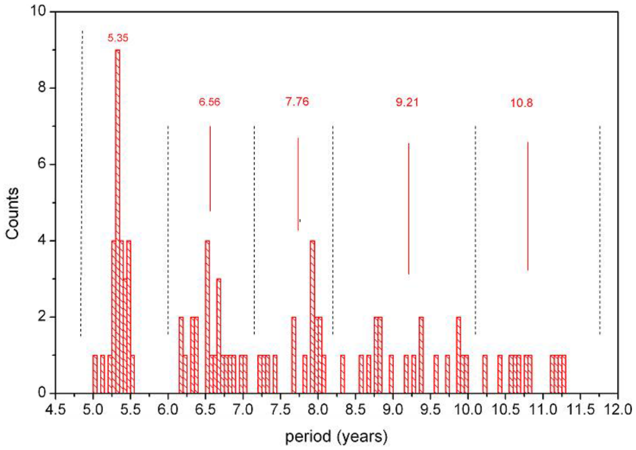

Figure 9. Number of oscillations counted in a fixed period interval at periods 4.75–11.75 years. Interval is 0.05 years (HAMMONIA).

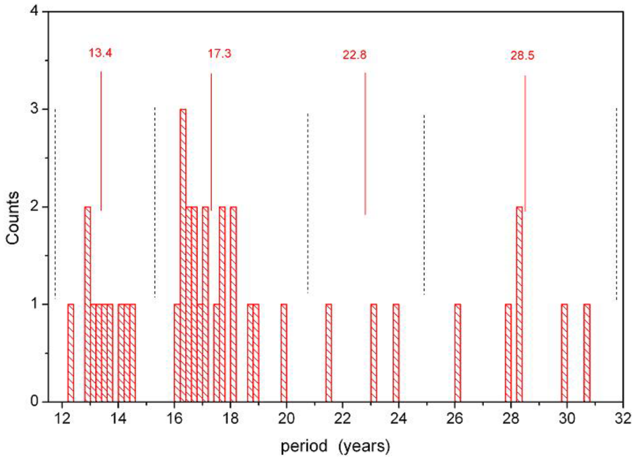

Figure 10. Number of oscillations counted in a fixed period interval at periods 11.75–31.75 years. Interval is 0.2 years (HAMMONIA).

In determining the mean oscillation periods we have avoided subjective influences as follows: periods obtained at various altitudes were plotted versus altitude as shown in Fig. 1 (middle column, red). When covering the period range of 5 to 30 years, nine vertical columns appeared. The definition criterion of the columns was that there should not be any overlap between adjacent columns. It turned out that such an attribution was possible. To make this visible we have plotted the histograms in Figs. 9 and 10. The pictures show that the column values form the clusters mentioned, which are separated by gaps. The gaps that are the largest ones in the neighbourhood of a peak are used as boundaries (except at 7.15 years). It turns out that if an oscillation value near a boundary is tentatively shifted from one cluster to the neighbouring one, the mean cluster values experience only minor changes. Figure 10 shows that our procedure comes to its limits, however, for periods longer than 20 years (for HAMMONIA). This is seen in Table 2a from the large error bars. We still include these values for illustration and completeness.

It is important to note that all HAMMONIA values in Table 2a (except 28.5 years) agree with the Hohenpeißenberg values within the combined error bars. The Hohenpeißenberg data are ground values and hence not subject to our clustering procedure. Furthermore also all other model periods in Table 2a have been derived by the same cluster procedure. The close agreement discussed in the text suggests that this technique is reliable.

ECHAM6 data are used in the present paper to analyse much longer time windows (400 years) than of HAMMONIA (34 years). Results shown in Figs. 3, 5, and 7 are quite similar to those of HAMMONIA. Harmonic analysis of long oscillation periods was performed in the same way as for HAMMONIA. Seventeen periods were found to be longer than 20 years and have been included in Table 2a. Shorter periods are not shown here as that range is covered by HAMMONIA. The amplitude and phase structures of these are very similar to those of HAMMONIA. The cluster formation about the mean period values is also obtained for ECHAM6 and looks quite similar to Figs. 9 and 10.

The vertical amplitude and phase profiles of the mean periods given in Table 2a all show intermittent amplitude maxima or minima and step-like phase structures. In general, they look very similar to Fig. 1. We have calculated the accumulated amplitudes (sums) from all of these profiles at all altitudes. They are shown in Fig. 11a for HAMMONIA. They clearly show a layered structure similar to the temperature standard deviations in Fig. 4, with maxima at altitudes close to those of the standard deviation maxima. The figure also closely corresponds to the amplitude distribution shown in Fig. 1, with maxima and minima occurring at similar altitudes in either picture.

Accumulated amplitudes have also been calculated for the ECHAM6 periods, and similar results are obtained as for HAMMONIA (see Fig. 11b). The similarity is already indicated in Fig. 3 above 15 km. The correlation of the HAMMONIA and ECHAM6 curves above this altitude has a correlation coefficient of 0.97. This and Fig. 11 support the idea that all of our long-period oscillations have a similar vertical amplitude structure.

The phase jumps in the nine oscillation vertical profiles of HAMMONIA also occur at similar altitudes. Therefore the mean altitudes of these jumps have been calculated and are shown in Fig. 11a as blue horizontal arrows. They are seen to be close to the minima of the accumulated amplitudes and thus confirm the anticorrelations between adjacent layers. Figures 4, 1, and 11 thus show a general structure of temperature correlations or anticorrelations between different layers of the HAMMONIA atmosphere and suggest the phase structure of the oscillations as an explanation. The same is valid for ECHAM6.

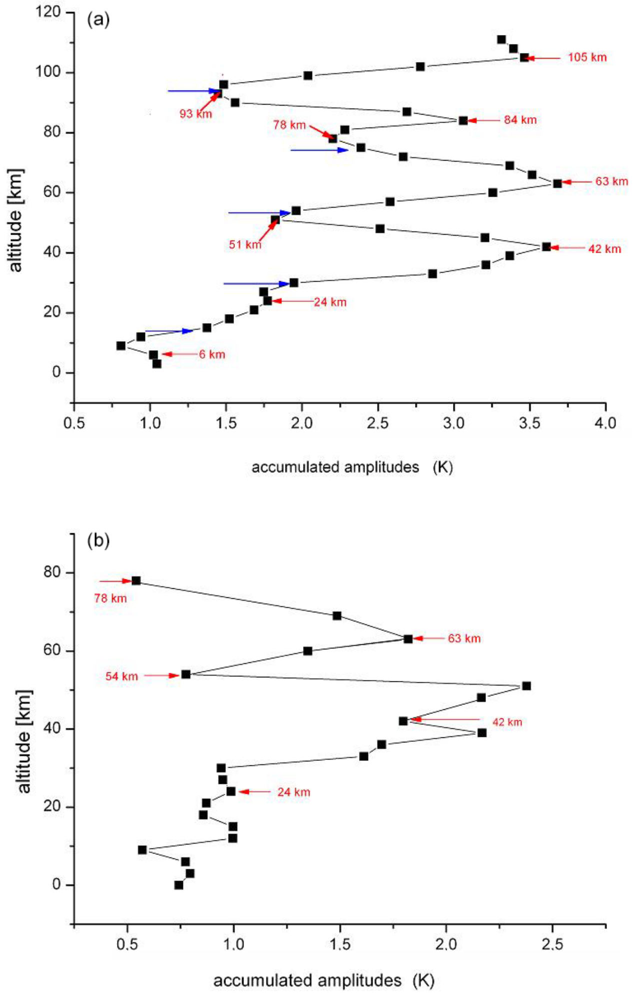

Figure 11. **(a)** Long-period temperature oscillations in the HAMMONIA model. Accumulated amplitudes are shown vs. altitude for periods of 5.3–28.5 years (see Table 2a). Blue horizontal arrows show mean altitudes of phase jumps. Red arrows indicate altitudes of maxima and minima. **(b)** Long-period temperature oscillations in the ECHAM6 model. Accumulated amplitudes are shown vs. altitude for the periods given in Table 2a. Red arrows indicate altitudes of maxima and minima.

Altogether HAMMONIA and ECHAM6 consistently show the same type of variability and oscillation structures. This type occurs in a wide time domain of 400 years. As mentioned, we do not believe that these ordered structures are adequately described by the term “noise”, as this notion is normally used for something occurring at random.

3.3 Intrinsic oscillation periods

Three different model runs of different lengths have been investigated by the harmonic analysis described. The HAMMONIA model covered 34 years, the WACCM model covered 150 years, and the ECHAM6 model covered 400 years. The intention was to study the differences resulting from the different nature of the models, and from the difference in the length of the model runs.

The oscillation periods found in these model runs are listed in Table 2a. These periods are vertical mean values as described for Figs. 1 and 9–10. Periods are given in order of increasing values in years together with their standard deviations. Only periods longer than 5 years are shown here. The maximum period cannot be longer than the length of the computer run. Therefore, the number of periods to be found in a model run can – in principle – be larger the longer the length of the run is. Table 2a preferentially shows periods longer than 20 years (except for HAMMONIA and Hohenpeißenberg) as the emphasis is on the long periods here. Of course, periods comparable to the length of the data series need to be considered with caution.

The periods shown here at a given altitude are from the Levenberg–Marquardt algorithm (at 1σ significance). The values obtained at different altitudes in a given model have been averaged as described above, and the corresponding mean and its standard error are given in Table 2a.

Table 2a also contains two columns of periods and their standard deviations that were derived from *measured* temperatures. These are data obtained on the ground at the Hohenpeißenberg Observatory (47.8° N, 11.0° E) from 1783 to 1980 and are globally averaged GLOTI data (Hansen et al., 2010). The data are annual mean values smoothed by a 16-point running mean and will be discussed below. Data after 1980 are not included in the harmonic analyses because they steeply increase thereafter ("climate change"). The periods are determined as for the data of the other rows of Table 2a (see Sect. 3.2).

The Hohenpeißenberg and GLOTI periods show several close agreements with the HAMMONIA and ECHAM6 results. Further comparisons with other data analyses are given below. A summary is given in Table 2b. Different techniques have been used, such as singular spectrum analysis (SSA), autocorrelation spectral analysis (ASA), and detrended fluctuation analysis (DFA), and yield similar results. They are also shown in Table 2b. For the accuracy and significance of these techniques the reader is referred to the corresponding papers. The periods listed in Table 2b are given in bold type in Table 2a.

There are some empty spaces in the lists of Table 2a. It is believed that this is because these oscillations are not excited in that model run or that their excitation is not strong enough to be detected or that the spectral resolution of the data series is insufficient (strong changes in amplitudes strengths are, for instance, seen in Fig. 1). For the *measured* data in Table 2a it needs to be kept in mind that they were under the influence of varying boundary conditions.

Table 3. Period comparison of two different HAMMONIA runs: temperature and CH_4. Periods (in years) are given together with their standard deviations. HAMMONIA run Hhi-max (temperature and CH_4 mixing ratios) uses 119 altitude layers and covers 34 years; run Hlo-max uses 67 layers and covers 20 years.

No.	Hhi-max (temperature)	Hlo-max (temperature)	CH_4
1	2.06 ± 0.02	2.07 ± 0.04	
2	2.16 ± 0.02	2.15 ± 0.02	
3	2.33 ± 0.04	2.36 ± 0.03	
4	2.51 ± 0.04	2.43 ± 0.02	
5	2.79 ± 0.08	2.78 ± 0.07	
6	3.11 ± 0.08	3.20 ± 0.09	
7	3.52 ± 0.12	3.44 ± 0.15	3.56 ± 0.15
8	3.96 ± 0.08	3.90 ± 0.12	4.02 ± 0.17
9	4.48 ± 0.21	4.27 ± 0.21	4.57 ± 0.17
10	5.34 ± 0.10	5.48 ± 0.29	5.41 ± 0.29
11	6.56 ± 0.24	6.57 ± 0.29	6.43 ± 0.26
12	7.76 ± 0.29	8.02 ± 0.12	7.90 ± 0.45
13	9.21 ± 0.53	9.16 ± 0.33	9.38 ± 0.47
14	10.8 ± 0.34	11.05 ± 0.46	10.93 ± 0.61
15	13.4 ± 0.68	13.02 ± 0.83	13.73 ± 0.93
16	17.3 ± 1.05		16.75 ± 0.90
17	22.8 ± 1.27	22.68 ± 1.11	

The model runs shown in Table 2a have different altitude resolutions. The best resolution (1 km) is available in HAMMONIA (119 vertical layers, run Hhi-max in the earlier paper of Offermann et al., 2015). The very long run of ECHAM6 uses only 47 layers. Data on a 3 km altitude grid are used here. In the earlier paper it was shown on the basis of a limited data set (HAMMONIA, Hlo-max) that a decrease in the number of layers affected the vertical amplitude and phase profiles of the oscillations found. It did, however, not change the oscillation periods. For a more detailed analysis a 20-year-long run of Hlo-max (67 layers) is now compared to the 34-year-long run of Hhi-max (119 layers). The resulting oscillation periods are shown in Table 3 (together with their standard deviations). Sixteen pairs of periods are listed that all agree within the single error bars (except no. 4). Hence it is confirmed that the periods of the oscillations are quite robust with respect to changes in altitude resolution. The periods of the ECHAM6 run can therefore be regarded as reliable, despite their limited altitude resolution.

When comparing the periods in Table 2a to each other several surprising agreements are observed. It turns out that all periods of the HAMMONIA and WACCM models find a counterpart in the ECHAM6 data (not vice versa). These data pairs always agree within their combined error bars and mostly even within single error bars. The difference between the members of a pair is much smaller than the distance to any neighbouring value with a higher or lower ordering num-

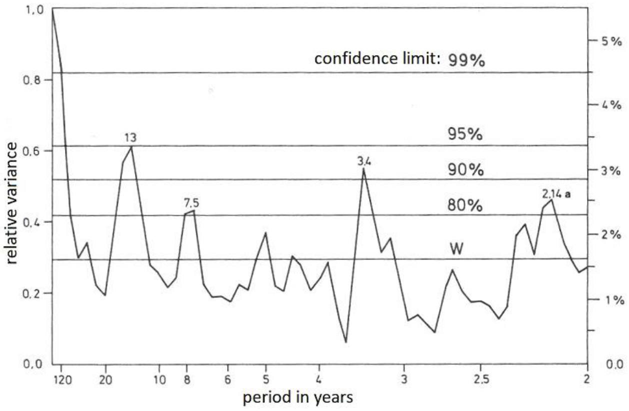

Figure 12. Periodogram (2 to 120 years) of measured Hohenpeißenberg temperatures from Schönwiese (1992, Fig. 57). Results are from an autocorrelation spectral analysis ASA.

ber in Table 2a. From this it is concluded that the different models find the same oscillations. Their periods are obviously quite robust.

A similar agreement is seen for the periods found in the measured Hohenpeißenberg data. These have been under the influence of variations in the sun, ocean, and greenhouse gases. A spectral analysis (autocorrelation spectral analysis) of these data is shown in Fig. 12. It was taken from Schönwiese (1992). The important peak at 3.4 years is not contained in Table 2 but was found in Offermann et al. (2015). The two peaks near 7.5 and 13 years are close to the values of 7.76 ± 0.29 and 13.4 ± 0.68 years in Table 2a.

A 335-year-long data set of central England temperatures (CETs) is the longest measured temperature series available (Plaut et al., 1995). A singular spectrum analysis was applied by these authors for interannual and interdecadal periods. Periods of 25.0, 14.2, 7.7, and 5.2 years were identified. All of these values nearly agree with numbers given for HAMMONIA, WACCM, and/or ECHAM6 in Table 2a (within the error bars given in the table).

Meyer and Kantz (2019) recently studied the data from a large number of European stations by the method of detrended fluctuation analysis. They identified a period of 7.6 ± 1.8 years, which again is in agreement with the HAMMONIA results given in Table 2a (and also agrees with Fig. 12 and with Plaut et al., 1995).

Also the GLOTI data in Table 2a are in agreement with some of the other periods, even though they are global averages. It will be shown below that such results are not limited to atmospheric temperatures alone but are, for instance, also seen in methane mixing ratios.

3.4 Oscillation amplitudes

In an attempt to learn more about the nature of the long-period oscillations we analyse their oscillation amplitudes. The calculation of absolute amplitudes is difficult and beyond the scope of the present paper. However, interesting results can be obtained from their relative values. One of these results is related to the vertical gradients of the atmospheric temperature profiles.

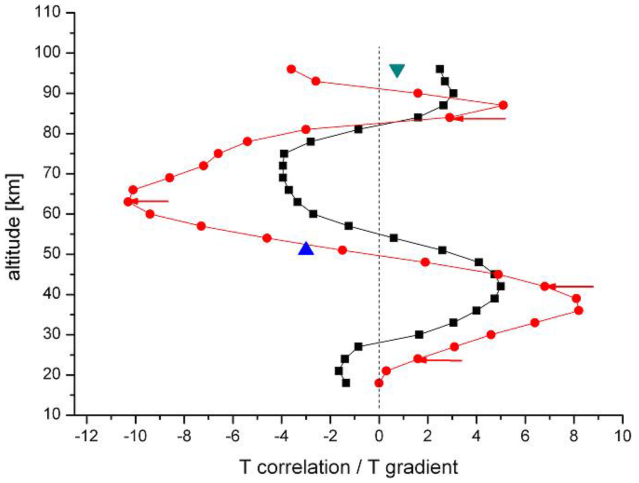

Figure 13. Comparison of HAMMONIA vertical correlations from Fig. 3 (black squares) with vertical temperature gradients (red dots). Data are from annual mean temperatures. Correlation coefficients are multiplied by 5. Temperature gradients are approximated by the differences in consecutive temperatures (K per 3 km). Two additional gradients are given for monthly mean temperature curves: blue triangle for January, green inverted triangle for July. Red arrows show the altitudes of the maxima of the accumulated amplitudes in Fig. 11a.

The HAMMONIA model simulates the atmospheric structure as a whole. The annual mean vertical profile of HAMMONIA temperatures can be derived and is seen to vary between a minimum at the tropopause, a maximum at the stratopause, and another minimum near the mesopause (not shown here). In consequence the vertical temperature gradients change from positive to negative and to positive again. This is shown in Fig. 13 (red dots) between 18 and 96 km. The temperature gradients are approximated by the temperature differences in consecutive levels.

Also shown in Fig. 13 is the correlation profile of HAMMONIA from Fig. 3 (black squares here). The two curves are surprisingly similar. The similarity suggests some connection of the oscillation structure and the mean thermal structure of the middle atmosphere. This is shown more clearly by the accumulated amplitudes of the long-period oscillations in Fig. 11a. The maxima of these occur at altitudes near the extrema of the temperature gradients as is shown by the red arrows in Fig. 13. The mechanism connecting the oscillations and the thermal structure appears to be active throughout the whole altitude range shown (except the lowest altitudes).

A possible mechanism might be a vertical displacement of air parcels. If an air column is displaced vertically by some distance D (“displacement height”), a seeming change in mixing ratio is observed at a given altitude. This is a relative change only, not a photochemical one. It can be estimated by the product D times mixing ratio gradient. If the vertical movement is an oscillation, the trace gas variation is an oscillation as well, assuming that D is a constant. Such transports may be best studied by means of a trace gas like CH_4.

HAMMONIA methane mixing ratios have therefore been investigated for oscillation periods in the same way as described above for the temperatures. Results are briefly summarized here.

Indeed, 10 periods have been found between 3.56 and 16.75 years by harmonic analyses and are shown in Table 3. These periods are very similar to those obtained for the temperatures in Tables 2a and 3. The agreement is within the single error bars. Hence it is concluded that the same oscillations are seen in HAMMONIA temperatures and CH_4 mixing ratios.

The CH_4 oscillations support the idea that a displacement mechanism is active. The corresponding displacement heights D were estimated from the CH_4 amplitudes and the vertical gradients of the mean HAMMONIA CH_4 mixing ratios.

The values D obtained from the different oscillation periods are about the same, though they show some scatter. This makes us presume that the displacement mechanism may be the same for all oscillations. The values D appear to follow a trend in the vertical direction. The displacements are below 100 m in the lower stratosphere and slowly increase with height to above 200 m.

Thus the important result is obtained that the our long-period oscillations are related to a vertical displacement mechanism that is altitude dependent but appears to be the same for all periods. A more detailed analysis is beyond the scope of this paper.

3.5 Seasonal aspects

Our analysis has so far been restricted to annual mean values. Large temperature variations on much shorter timescales are also known to occur in the atmosphere, including vertical correlations (e.g. seasonal variations). This suggests the question of whether these might be somehow related to the long-period oscillations. Our spectral analysis is therefore repeated using monthly mean temperatures of HAMMONIA.

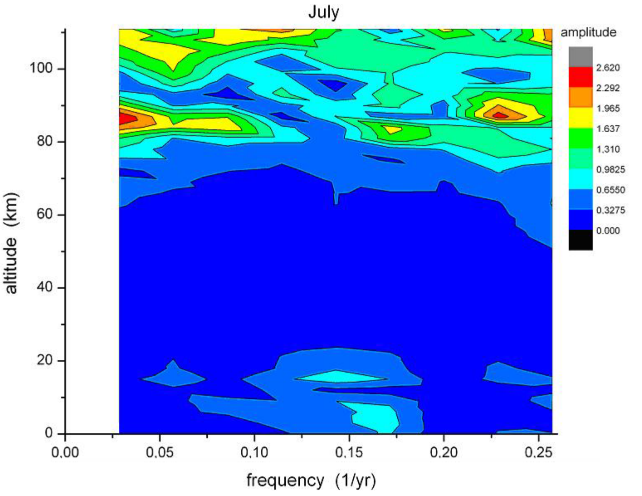

Figure 14. Long-period temperature oscillations in the month of July in HAMMONIA. Amplitudes are shown in dependence of altitude and frequency (periods 3.9–34 years). Colour code of amplitudes is in arbitrary units.

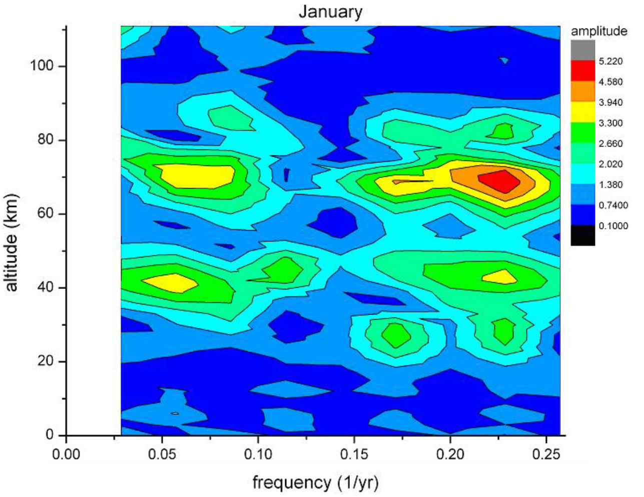

Figure 15. Long-period temperature oscillations as in Fig. 14 but for the month of January.

Results are shown in Figs. 14 and 15, which give the amplitude distribution vs. period and altitude of FFT analyses for the months of July and January. These two months are typical of summer (May–August) and winter (November–March), respectively. In July oscillation amplitudes are seen essentially at altitudes above about 80 km and some below about 20 km. In the regime in between, oscillations are obviously very small or not excited. The opposite behaviour is seen in January: oscillation amplitudes are now observed in the middle-altitude regime where they had been absent in July. This is to be compared to Figs. 6 and 11 that give the annual mean picture. In Fig. 11 the structures (two peaks) above 80 km appear to represent the summer months (Fig. 14). The structures between 80 and 30 km, on the other hand, apparently are representative of the winter months (Fig. 15).

The monthly oscillations appear to be related to the wind field of the HAMMONIA model. Figure 16 shows the monthly zonal winds of HAMMONIA from the ground up to 111 km (50° N). Comparison with Figs. 14 and 15 shows that oscillation amplitudes are obviously not observed in an easterly wind regime. Hence, the long-period oscillations and their phase changes are apparently related to the dynamical structure of the middle atmosphere. A change from high to

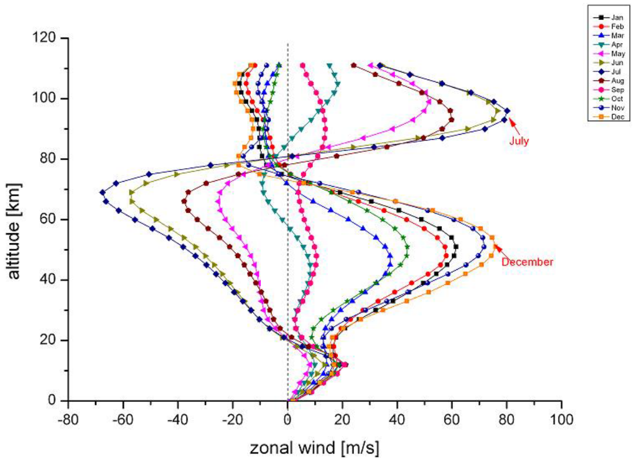

Figure 16. Vertical distribution of zonal wind speed in the HAMMONIA model.

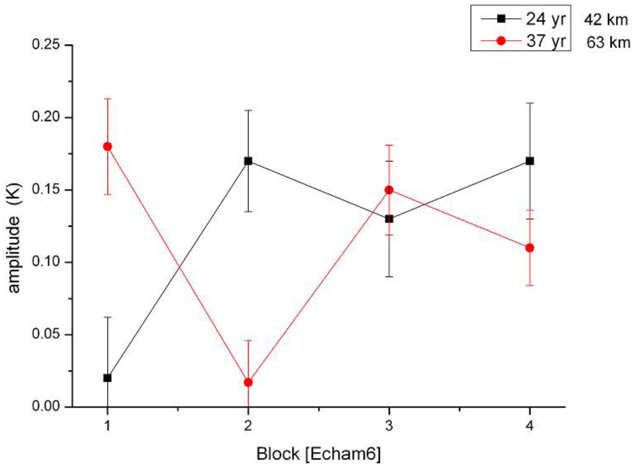

Figure 17. Amplitudes of 24 and 37 years oscillations in four subsequent equal time intervals (blocks) of the 400-year data set of ECHAM6.

low oscillation activity in the vertical direction appears to be related to a wind reversal.

This correspondence does not, however, exist in all details. In the regimes of oscillation activity there are substructures. For instance in the middle of the July regime of amplitudes above 80 km, there is a “valley” of low values at about 95 km. A similar valley is seen in the January data around 55 km. Near these altitudes there are phase changes of about 180° (see the blue arrows in Fig. 11a). Contrary to our expectation sketched above, these are altitudes of large westerly zonal wind speeds without much vertical change (see Fig. 16). However, the two valleys are relatively close to altitudes where the vertical temperature gradients are small (see Fig. 13). As the gradients from the annual mean temperatures used for the curves in Fig. 13 may differ somewhat from the corresponding monthly values, two monthly gradients have been added in Fig. 13 for January (at 51 km) and for July (at 96 km). They are small, indeed, and could explain low oscillation amplitudes by the above-discussed vertical displacement mechanism.

3.6 Oscillation persistence

It is an important question whether the excitation of our oscillations is continuous or intermittent. To check on this we have subdivided the 400-year data record of ECHAM6 in four smaller time intervals (blocks) of 100 years each. In each block we performed harmonic analyses for periods of 24 years (frequency of 0.042/year) and 37 years (frequency of 0.027/year), respectively, at the altitudes of 42 km (1.9 hPa) and 63 km (0.11 hPa). These are altitudes and periods with strong signals as seen in Fig. 7. Results for the two altitudes and two periods are given in Fig. 17.

The results show two groups of amplitudes: one is around 0.15 K; the other is very small and compatible with zero. The two groups are significantly different as is seen from the error bars. This result is compatible with the picture of oscillations being excited and not excited (dissipated) at different times. The non-excitation (dissipation) for the 24-year oscillation (black squares) occurs in the first block (century), that for the 37-year oscillation (red dots) in the second block. The 24-year profile at 63 km altitude is similar as that at 24 km. Likewise, the 37-year profile at 24 km is similar to that at 63 km. Hence it appears that the whole atmosphere (or a large part of it) is excited (or dissipated) simultaneously. (The two profiles in Fig. 17 appear to be somehow anticorrelated for some reason that is unknown as yet.)

For the analysis of shorter periods, the 400-year data set of ECHAM6 may be subdivided into a larger number of time intervals. Figure 18 shows the results for periods of 5.4 and 16 years, for various altitudes. An FFT analysis

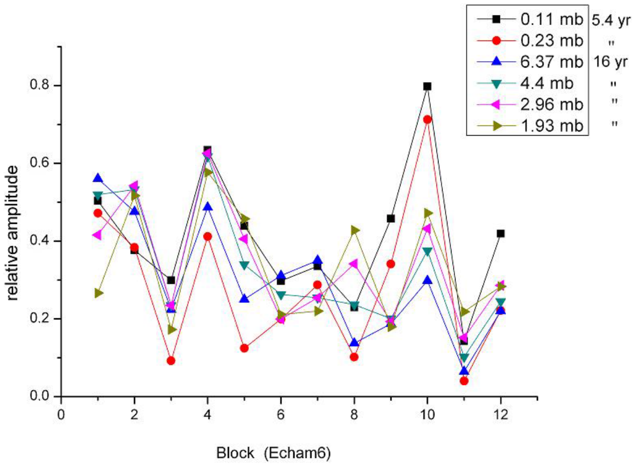

Figure 18. FFT amplitudes of 5.4- and 16-year oscillations in 12 equal time intervals (32-year blocks) of the ECHAM6 400-year data set.

was performed at 12 equal time intervals (blocks of 32-year length) in the altitude regime 0.01–1000 hPa and the period regime 4–40 years. The corresponding 12 maps look similar to Fig. 15; i.e. there are pronounced amplitude hotspots at various altitudes and periods. (Of course, the values near the 40-year boundary are not really meaningful.) In subsequent blocks these hotspots may shift somewhat in altitude and/or period, and hence the profiles taken at a fixed period and altitude such as those of Fig. 18 show some scatter. Nevertheless, there is a strong indication of the occurrence of coordinated high maxima and deep minima of amplitudes in blocks 3 and 4 and blocks 10 and 11, respectively. These maxima are interpreted as strong oscillation excitation, whereas the minima are believed to show (at least in part) the dissipation of the oscillations.

It should be mentioned that in the FFT analysis the 5.4-year period is an overtone of the 16-year period. Hence the two period data in Fig. 18 may be related somehow.

4 Discussion

The long-period oscillations are seen in measurements as well as in model calculations.

The nature and origin of them are as yet unknown. We therefore collect here as many of their properties as possible.

4.1 Oscillation properties and possible self-excitation

The oscillations exist in computer models even if the model boundaries for the influences of the sun, the ocean, and the greenhouse gases are kept constant. Therefore one might suspect that they are self-generated. The oscillation periods are robust, which is typical of self-excited oscillations. However, external excitation by land surface processes is a possibility.

Further oscillation properties are as follows: the periods cover a wide range from 2 to more than 200 years (at least). The different oscillations have similar vertical profiles (up to 110 km) of amplitudes and phases. This may indicate three-dimensional atmospheric oscillation modes. To clarify this, latitudinal and longitudinal studies of the oscillations are needed in a future analysis.

4.2 Vertical layered amplitude structures and displacement mechanism

The accumulated oscillation amplitudes show a layer structure with alternating maxima and minima and correlations or anticorrelations in the vertical direction. These appear to be influenced by the seasonal variations in temperature and zonal wind in the stratosphere, mesosphere, and lower thermosphere. Table 4 summarizes the results shown in Sect. 3.5. Maxima of oscillation amplitudes appear to be associated with westerly (eastward) winds together with large temperature gradients (positive or negative). Amplitude minima are associated with either easterly (westward) winds or with near-zero temperature gradients. The latter feature is compatible with a possible vertical displacement mechanism. Indeed, such displacements can be seen in the CH_4 data of the HAMMONIA model. The mechanism summarized in Table 4 appears to be a basic feature of the atmosphere that influences many different parameters such as temperature and mixing ratios. Vertical displacements of measured temperature profiles have been discussed for instance by Kalicinsky et al. (2018).

4.3 Oscillations are not noise!

The amplitudes found for the long-period oscillations are relatively small (Fig. 1). The question therefore arises whether these oscillations might be spurious peaks, i.e. some sort of noise. We tend to answer the question in the negative for the following reasons:

a. An accidental agreement of periods as close together as those shown in Table 2a for different model computations appears very unlikely. This also applies to the Hohenpeißenberg data in Table 2a, and several of these periods are even found in the GLOTI data.

   If the period values were accidental, they should be evenly distributed over the period-space. To study this the range of ECHAM6 periods is considered. Table 2a shows that the error bars (standard deviations) of ECHAM6 cover approximately half of this range. If the periods of this and some other data set occur at random, half of them should coincide with the ECHAM6 periods within the ECHAM6 error bars, and half of them should not. This is checked by means of the WACCM model data, the Hohenpeissenberg measured data, and three further measurements sets that reach back to 1783 (Innsbruck, 47.3° N, 11.4° E; Vienna, 48.3° N, 16.4° E; Stockholm, 59.4° N, 18.1° E). The result is that about two-thirds of the periods coincide with ECHAM6 periods within the ECHAM6 error bars. This is far from an even distribution.

   It is important to note that the data sets used here are quite different in nature: they are either model simulations with fixed or partially fixed boundaries, or they are real atmospheric measurements at different locations.

   A further argument against noise is the distribution of the data in Figs. 9 and 10. If our oscillations were noise, the counts in these figures should be evenly distributed with respect to the period scale. However, the distribution is highly uneven, with high peaks and large gaps, which is very unlikely to result from noise.

b. The periods given in Table 2a were all calculated by means of harmonic analyses (Levenberg–Marquardt algorithm). This was done to support the reliability of the comparison of the three models and four measured data sets. There could be, however, the risk of a "common

Table 4. Maxima or minima of accumulated amplitudes of temperature oscillations and associated structures (see Fig. 11a) (stratosphere, mesosphere, lower thermosphere).

Altitude (km)	Accumulated amplitudes	Zonal wind	Temperature gradient
105	max	westerly (summer)	large (positive)
93	min	westerly (summer)	near zero
84	max	westerly (summer)	large (positive)
78	min	easterly (except Sep)	medium (negative)
63	max	westerly (winter)	large (negative)
51	min	westerly (winter)	near zero
42	max	westerly (winter)	large positive

mode failure”. The harmonic analysis results are therefore checked and are confirmed by the Lomb–Scargle analysis and ASA shown in Figs. 8 and 12 and by the above-cited results of Plaut et al. (1995) and Meyer and Kantz (2019). There is, however, no one-to-one correspondence of these numbers and those in Table 2a. In general the number of oscillations found by the harmonic analysis is larger. Hence several of the Table 2a periods might be considered questionable. It is also not certain that Table 2a is exhaustive. Nevertheless, the large number of close coincidences is surprising.

c. The layered structure of the occurrence of the oscillations (e.g. Fig. 11a) and the corresponding anticorrelations appears impossible to reconcile with a noise field. These correlations extend over about 20 km (or more) in the vertical, which is about three scale heights. Turbulent correlation would, however, be expected over one transport length, i.e. one scale height, only.

d. The apparent relation of the oscillations to the zonal wind field and the vertical temperature structure (Table 4) would be very difficult to explain by noise.

e. The close agreement (within single error bars) of the oscillation periods in temperatures and in CH_4 mixing ratios would also be very difficult to explain by noise.

In summary it appears that many of the oscillations are intrinsic properties of the atmosphere that are also found in sophisticated simulations of the atmosphere.

4.4 Other atmospheric parameters

The long-period oscillations are studied here mainly for atmospheric temperatures. They show up, however, in a similar way in other parameters such as winds, pressure, trace gas densities, and NAO (Offermann et al., 2015). Some of the periods in Table 2a appear to be similar to the internal decadal variability of the atmosphere–ocean system (e.g. Meehl et al., 2013, 2016; Fyfe et al., 2016). One example is the Atlantic Multidecadal Oscillation (AMO) as discussed by Deser et al. (2010) with timescales of 65–80 years and with its “precise nature… still being refined”. Variability on centennial timescales and its internal forcing were recently discussed by Dijkstra and von der Heydt (2017). It needs to be emphasized that the oscillations discussed in the present paper are not caused by the ocean as they occur even if the ocean boundaries are kept constant.

4.5 Relation to “climate noise”

The long-period oscillations obviously are somehow related to the “internal variability” discussed in the atmosphere–ocean literature at 40–80-year timescales (“climate noise”; see, e.g., Deser et al., 2012; Gray et al., 2004, and other references in Sect. 1). The particular result of the present analysis is its extent from the ground up to 110 km, showing systematic structures in all of this altitude regime. These vertical structures lead us to hope that the nature of the oscillations and hence of (part of) the internal variability can be revealed in the future.

4.6 Time persistency

It appears that the time persistency of the long-period oscillations is limited. Longer data sets are needed to study this further.

4.7 Relation to climate change

The internal variability in the atmosphere–ocean system “makes an appreciable contribution to the total… uncertainty in the future (simulated) climate response” (Deser et al., 2012). Similarly our long-period oscillations might interfere with long-term (trend) analyses of various atmospheric parameters. This includes slow temperature increases as part of the long-term climate change and needs to be studied further.

5 Summary and conclusions

The atmospheric oscillation structures analysed in this paper occur in a similar way in different atmospheric climate models and even when the boundary conditions of sun, ocean, and greenhouse gases are kept constant. They also occur in long-term temperature measurements series. They are characterized by a large range of period values from below 5 to beyond 200 years.

As we do not yet understand the nature of the oscillations we try to assemble as many of their properties as possible. The oscillations show typical and consistent structures in their vertical profiles. Temperature amplitudes show a layered behaviour in the vertical direction with alternating maxima and minima. Phase profiles are also layered with 180° phase jumps near the altitudes of the amplitude minima (anticorrelations). There are also indications of vertical transports suggesting a displacement mechanism in the atmosphere. As an important result we find that for all oscillation periods the altitude profiles of amplitudes and phases as well as the displacement heights are nearly the same. This leads us to suspect an atmospheric oscillation mode.

These signatures are found to be related to the thermal and dynamical structure of the middle atmosphere. All results presently available are local; i.e. they refer to the latitude and longitude of central Europe. In a future step horizontal investigations need to be performed to check on a possible modal structure.

Most of the present results are for temperatures at various altitudes (up to 110 km). Other atmospheric parameters indicate a similar behaviour and need to be analysed in detail in the future. Also, the potential of the long-period oscillations to interfere with trend analyses needs to be investigated.

Appendix A: List of abbreviations

Abbreviations	Definition
CCM	Chemistry–climate model
CESM-WACCM	Community Earth System Model – Whole Atmosphere Community Climate Model
ECHAM6	ECMWF/Hamburg
GLOTI	Global Land Ocean Temperature Index
HAMMONIA	HAMburg Model of the Neutral and Ionized Atmosphere
IPCC	Intergovernmental Panel on Climate Change

Data availability. The HAMMONIA, WACCM, and ECHAM6 data were obtained from the sources cited in Sects. 2.2–2.4 and from the scientists listed in the acknowledgement. They are available from these upon request.

Author contributions. DO performed data analysis and prepared the paper and figures with contributions from all co-authors. JW managed data collection and performed FFT spectral analyses. CK performed Lomb–Scargle spectral and statistical analyses RK provided interpretation and editing of the paper, figures, and references.

Competing interests. The authors declare that they have no conflict of interest.

Acknowledgements. Global Land Ocean Temperature Index (GLOTI) data were downloaded from http://data.giss.nasa.gov/gistemp/tabledata_v3/GLB.Ts+dSST.txt (last access: November 2011) and are gratefully acknowledged.

We thank Katja Matthes (GEOMAR, Kiel, Germany) for making available the WACCM4 data, and for helpful discussions. Model integrations of the CESM-WACCM Model have been performed at the Deutsches Klimarechenzentrum (DKRZ) Hamburg, Germany. The help of Sebastian Wahl in preparing the CESM-WACCM data is greatly appreciated.

HAMMONIA and ECHAM6 simulations were performed at and supported by the German Climate Computing Centre (DKRZ). Many helpful discussions with Hauke Schmidt (MPI Meteorology, Hamburg, Germany) are gratefully acknowledged.

We are grateful to Wolfgang Steinbrecht (DWD, Hohenpeißenberg Observatory, Germany) for the Hohenpeißenberg data and many helpful discussions.

Part of this work was funded within the project MALODY of the ROMIC program of the German Ministry of Education and Research under grant no. 01LG1207A.

We thank the editor and three referees for their detailed and helpful comments.

Financial support. This research has been supported by the Bundesministerium für Bildung und Forschung (grant no. 01LG1207A).

Review statement. This paper was edited by Heini Wernli and reviewed by Christian von Savigny and two anonymous referees.

References

Biondi, F., Gershunov, A., and Cayan, D. R.: North Pacific Decadal Climate Variability since 1661, J. Climate 14, 5–10, 2001.

Dai, A., Fyfe, J. C., Xie, S.-P., and Dai, X.: Decadal modulation of global surface temperature by internal climate variability, Nat. Clim. Change, 5, 555–559, 2015.

Deser, C., Alexander, M. A., Xie, S. P., and Phillips, A. S.: Sea surface temperature variability: patterns and mechanisms, Annu. Rev. Mar. Sci., 2, 115–143, 2010.

Deser, C., Phillips, A., Bourdette, V., and Teng, H.: Uncertainty in climate change projections: the role of internal variability, Clim. Dynam., 38, 527–546, 2012.

Deser, C., Phillips, A. S., Alexander, M. A., and Smoliak, B. V.: Projecting North American climate over the next 50 years: Uncertainty due to internal variability, J. Climate, 27, 2271–2296, 2014.

Dijkstra, H. A. and von der Heydt, A. S.: Basic mechanisms of centennial climate variability, Pages Magazine, 25, 150–151, 2017.

Dijkstra, H. A., te Raa, L., Schmeits, M., and Gerrits, J.: On the physics of the Atlantic Multidecadal Oscillation, Ocean Dynam., 56, 36–50, 2006.

Flato, G., Marotzke, J., Abiodun, B., Braconnot, P., Chou, S. C., Collins, W., Cox, P., Driouech, F., Emori, S., Eyring, V., Forest, C., Gleckler, P., Guilyardi, E., Jakob, C., Kattsov, V., Reason, C., and Rummukainen, M.: Evaluation of Climate Models, in: Climate Change 2013: The Physical Science Basis, Contribution of Working Group I to the Fifth Assessment Report of the Intergovernmental Panel on Climate Change, edited by: Stocker, T. F., Qin, D., Plattner, G.-K., Tignor, M., Allen, S. K., Doschung, J., Nauels, A., Xia, Y., Bex, V., and Midgley, P. M., Ch. 9, https://doi.org/10.1017/CBO9781107415324.020, IPCC, Cambridge Univ. Press, UK and New York, NY, USA, 2013.

Fyfe, J. C., Meehl, G. A., England, M. H., Mann, M. E., Santer, B. D., Flato, G. M., Hawkins, E., Gillett, N. P., Xie, S. P., Kosaka, Y., and Swart, N. C.: Making sense of the early-2000s warming slowdown, Nat. Clima. Change, 6, 224–228, 2016.

Giorgetta, M. A., Jungclaus, J., Reick, C. H., Legutke, S., Bader, J., Böttinger, M., Brovkin, V., Crueger, T., Esch, M., Fieg, K., Glushak, K., Gayler, V., Haak, H., Hollweg, H.-D., Ilyina, T., Kinne, S., Kornblueh, L., Matei, D., Mauritsen, T., Mikolajewicz, U., Mueller, W., Notz, D., Pithan, F., Raddatz, T., Rast, S., Redler, R., Roeckner, E., Schmidt, H., Schnur, R., Segschneider, J., Six, K. D., Stockhause, M., Timmreck, C., Wegner, J., Widmann, H., Wieners, K.-H., Claussen, M., Marotzke, J., and Stevens, B.: Climate and carbon cycle changes from 1850 to 2100 in MPI-ESM simulations for the coupled model intercomparison project phase 5, J. Adv. Model. Earth Sy., 5, 572–597, https://doi.org/10.1002/jame.20038, 2013.

Gray, S. T., Graumlich, L. J., Betancourt, J. L., and Pederson, G. T.: A tree-ring based reconstruction of the Atlantic Multidecadal Oscillation since 1567 A.D., Geophys. Res. Lett., 31, L12205, https://doi.org/10.1029/2004GL019932, 2004.

Hansen, F., Matthes, K., Petrick, C., and Wang, W.: The influence of natural and anthropogenic factors on major stratospheric sudden warmings. J. Geophys. Res.-Atmos., 119, 8117–8136, 2014.

Hansen, J., Ruedy, Sato, M., and Lo, K.: Global Surface Temperature Change, Rev. Geophys., 48, 1–29, 2010.

Kalicinsky, C., Knieling, P., Koppmann, R., Offermann, D., Steinbrecht, W., and Wintel, J.: Long-term dynamics of OH* temperatures over central Europe: trends and solar correlations, Atmos. Chem. Phys., 16, 15033–15047, https://doi.org/10.5194/acp-16-15033-2016, 2016.

Kalicinsky, C., Peters, D. H. W., Entzian, G., Knieling, P., and Matthias, V.: Observational evidence for a quasi-bidecadal oscillation in the summer mesopause region over

Western Europe, J. Atmos. Sol.-Terr. Phys., 178, 7–16, https://doi.org/10.1016/j.jastp.2018.05.008, 2018.

Karnauskas, K. B., Smerdon, J. E., Seager, R., and Gonzalez-Rouco, J. F.: A pacific centennial oscillation predicted by coupled GCMs, J. Climate, 25, 5943–5961, https://doi.org/10.1175/JCLI-D-11-00421.1, 2012.

Kinnison, D., Brasseur, G. P., Walters, S., Garcia, R. R., and Marsh, D. R.: Sensitivity of chemical tracers to meteorological parameters in the MOZART-3 chemical transport model, J. Geophys. Res., 112, D20302, https://doi.org/10.1029/2006JD007879, 2007.

Latif, M., Martin, T., and Park, W.: Southern ocean sector centennial climate variability and recent decadal trends, J. Climate, 26, 7767–7782, 2013.

Lean, J., Rottman, G., Harder, J., and Knopp, G.: SOURCE contributions to new understanding of global change and solar variability, Sol. Phys. 230, 27–53, https://doi.org/10.1007/S11207-005-1527-2, 2005.

Lomb, N. R.: Least-squares frequency analysis of unequally spaced data, Astrophys. Space Sci., 39, 447–462, 1976.

Lu, J., Hu, A., and Zeng, Z.: On the possible interaction between internal climate variability and forced climate change, Geophys. Res. Lett., 41, 2962–2970, 2014.

Mantua, N. J. and Hare, S. R.: The Pacific Decadal Oscillation, J. Oceanography, 58, 35–44, 2002.

Matthes, K., Kodera, K., Garcia, R. R., Kuroda, Y., Marsh, D. R., and Labitzke, K.: The importance of time-varying forcing for QBO modulation of the atmospheric 11 year solar cycle signal, J. Geophys. Res., 118, 4435–4447, 2013.

Meehl, G. A., Hu, A., Arblaster, J., Fasullo, J., and Trenberth, K. E.: Externally forced and internally generated decadal climate variability associated with the Interdecadal Pacific Oscillation, J. Climate, 26, 7298–7310, 2013.

Meehl, G. A., Hu, A., Santer, B. D., and Xie, S.-P.: Contribution of Interdecadal Pacific Oscillation to twentieth-century global surface temperature trends, Nat. Clim. Change, 6, 1005–1008, https://doi.org/10.1038/nclimate3107, 2016.

Meyer, P. G. and Kantz, H.: A simple decomposition of European temperature variability capturing the variance from days to a decade, Clim. Dynam., 53, 6909–6917, doi.org/10.1007/s00382-019-04965-0, 2019.

Minobe, S.: A 50–70 year climatic oscillation over the North Pacific and North America, Geophys. Res. Lett., 24, 683–686, 1997.

Offermann, D., Goussev, O., Kalicinsky, C., Koppmann, R., Matthes, K., Schmidt, H., Steinbrecht, W., and Wintel, J.: A case study of multi-annual temperature oscillations in the atmosphere: Middle Europe, J. Atmos. Sol.-Terr. Phys., 135, 1–11, 2015.

Plaut, G., Ghil, M., and Vautard, R.: Interannual and interdecadal variability in 335 years of Central England Temperatures, Science, 268, 710–713, 1995.

Paul, A. and Schulz, M.: Holocene climate variability on centennial-to-millenial time scales: 2. Internal and forced oscillations as possible causes, in: Climate development and history of the North Atlantic realm, edited by: Wefer, G., Berger, W., Behre, K.-E., and Jansen, E., Springer, Berlin, Heidelberg, 55–73, 2002.

Polyakov, I. V. Berkryaev, R. V., Alekseev, G. V., Bhatt, U. S., Colony, R. L., Johnson, M. A., Maskshtas, A. P., and Walsh, D.: Variability and trends of air temperature and pressure in the Maritime Arctic, 1875–2000, J. Climate, 16, 2067–2077, 2003.

Roeckner, E., Brokopf, R., Esch, M., Giorgetta, M., Hagemann, S., Kornblueh, L., Manzini, E., Schlese, U., and Schulzweida, U.: Sensitivity of simulated climate to horizontal and vertical resolution in the ECHAM5 atmosphere model, J. Climate, 19, 3771–3791, 2006.

Scargle, J. D.: Studies in astronomical time series analysis. II. Statistical aspects of spectral analysis of unevenly spaced data, Astrophys. J., 263, 835–853, 1982.

Schlesinger, M. E. and Ramankutty, N.: An oscillation in the gobal climate system of period 65–70 years, Nature, 367, 723–726, 1994.

Schmidt, H., Brasseur, G. P., Charron, M., Manzini, E., Giorgetta, M. A., Diehl, T., Fomichev, V. I., Kinnison, D., Marsh, D., and Walters, S.: The HAMMONIA chemistry climate model: Sensitivity of the mesopause region to the 11-year solar cycle and CO_2 doubling, J. Climate, 19, 3903–3931, https://doi.org/10.1175/JCLI3829.1, 2006.

Schmidt, H., Brasseur, G. P., and Giorgetta, M. A.: The solar cycle signal in a general circulation and chemistry model with internally generated quasi-biennial oscillation, J. Geophys. Res., 115, D00I14, https://doi.org/10.1029/2009JD012542, 2010.

Schönwiese, C.-D.: Praktische Statistik für Meteorologen und Geowissenschaftler, 2.Auflage, Gebrüder Borntraeger, Berlin, Stuttgart, Abb. 57, p. 185, available at: https://www.borntraeger-cramer.de/9783443010294 (last access: 2 February 2021), 1992 (in German).

Soon, W. W.-H.: Variable solar irradiance as a plausible agent for multidecadal variations in the Arctic-wide surface air temperature record of the past 130 years, Geophys. Res. Lett., 32, L16712, https://doi.org/10.1029/2005GL023429 2005.

Stevens, B., Giorgetta, M., Esch, M., Mauritsen, T., Crueger, T., Rast, S., Salzmann, M., Schmidt, H., Bader, J., Block, K., Brokopf, R., Fast, I., Kinne, S., Kornblueh, L., Lohmann, U., Pincus, R., Reichler, T., and Roeckner, E.: The atmospheric component of the MPI-M earth system model: ECHAM6, J. Adv. Model. Earth Sy., 5, 1–27, 2013.

White, W. B. and Liu, Z.: Non-linear alignment of El Nino to the 11-yr solar cycle, Geophys. Res. Lett., 35, L19607, https://doi.org/10.1029/2008GL034831, 2008.

Xu, D., Lu, H., Chu, G., Wu, N., Shen, C., Wang, C., and Mao, L.: 500-year climate cycles stacking of recent centennial warming documented in an East Asian pollen record, Sci. Rep.-UK, 4, 3611, https://doi.org/10.1038/srep03611, 2014.